EXPERIMENTAL AND COMPUTATIONAL EXPLORATION OF LAYERED ELECTRIDES: AS 2D MATERIALS AND AS ELECTRODES FOR ELECTRON-ANION EXCHANGE

Daniel Lawrence Druffel

A dissertation submitted to the faculty of the University of North Carolina at Chapel Hill in partial fulfillment of the requirements for the degree of Doctor of Philosophy in the Department of Chemistry.

Chapel Hill
2019

Approved by:

Scott C. Warren

Joanna M. Atkin

James F. Cahoon

Gerald J. Meyer

Wei You

©2019
Daniel Lawrence Druffel
ALL RIGHTS RESERVED

ABSTRACT

Daniel Lawrence Druffel: Experimental and Computational Exploration of Layered Electrides: As 2D Materials and as Electrodes for Electron-Anion Exchange
(Under the direction of Scott C. Warren)

Here, we describe new chemistries that utilize electrides' electrons. First, we demonstrate experimentally that Ca_2N, a layered electride in which layers of atoms are separated by layers of a 2D electron gas (2DEG), can be exfoliated into two-dimensional (2D) nanosheets using liquid exfoliation. The 2D flakes are stable in a nitrogen atmosphere or in select organic solvents for at least one month. Electron microscopy and elemental analysis reveal that the 2D flakes retain the crystal structure and stoichiometry of the parent 3D Ca_2N. In addition, the 2D flakes exhibit metallic character and an optical response that agrees with DFT calculations. Together these findings provide the first experimental demonstration of an electride as a 2D material, which we call an "electrene".

Second, we show from first-principles that stacking electrenes with other 2D materials forms donor–acceptor heterostructures with interlayer distances 1 Å less than van der Waals layered materials but 1 Å more than covalent or ionic bonds. We show how these unusual bonding interactions have tunable polarities and strengths and that these "bonds" can be understood by drawing on familiar concepts from molecular orbital theory. We also demonstrate several useful properties of 2D donor–acceptor heterostructures, including superlubricity, ultralow work functions, and greatly improved voltages for lithium-ion batteries.

Through our efforts to understand layered electrides, we also discovered an analogous halide, Y_2CF_2, which is the first known transition metal carbide fluoride. Using both experimental and computational techniques, we determine its crystal structure and electronic structure, which reveal Y_2CF_2 to be an indirect band gap (1.7 eV) semiconductor with a low work function ($\sim$2.6 eV).

Lastly, we introduce a fundamentally new mechanism of ion-insertion, one in which electron transfer is not accompanied by reduction or oxidation. We show that when an anion such as F^- inserts into an electride such as Y_2C, F^- simply replaces e^-, occupying the same site without oxidizing or reducing the lattice. We provide first-principle calculations, which suggest insertion/deinsertion can occur at room temperature, and

demonstrate experimentally that this exchange can occur at the lowest temperatures (< 500 °C) yet reported. We introduce the name "electrochemical electron-anion exchange" to describe this mechanism and lay the intellectual framework for what is likely to be a large and important field of materials for electrochemistry, energy science, and electronics.

To those who seek to understand the fundamental laws of nature, that my work may prove a nominal contribution to our collective understanding.

ACKNOWLEDGEMENTS

I would like to thank my fiancée, Laura. What are not described in these pages are the meals that you cooked for me when I was tired, the gifts of coffee and sweets that you gave to me that powered me through late nights and early mornings, and the unwavering encouragement you provided when I felt daunted. You have believed in me even when I found it hard to and have inspired me as a scientist and as a person. I am excited and honored to spend a lifetime with you.

To my family, especially my parents Stephen and Donna and my brother Michael, I want to thank you for your love and support during this process and throughout my life. I cannot say enough how important and wonderful your presence, your wisdom, your strength, and your love have been to me. You're the best. I wish I could print your names on the front cover with mine.

I would also like to thank my advisor Scott Warren for his mentoring over my years at UNC and for encouraging me to push the boundaries of chemistry in creative and original ways. I would like to thank the current and former members of the Warren lab—especially Adam Woomer and Jun Hu who taught me an immeasurable amount in my first years of graduate school and Jacob Pawlik and Jack Sundberg who helped develop a lot of the techniques and computational abilities used in my thesis. I want to thank the other students for helping to build an environment fertile for creative thought.

I would like to thank Francis Alcorn and Katie Scott, who worked with me as undergraduate researchers. You are both awesome scientists and awesome people. It was a pleasure to work along side of you.

Last, I would like to thank my friends, especially Adam, Jason and Evan, for keeping me sane and motivated through this undertaking, for sharing countless conversations over burritos, burgers, and Chinese food, and for the unforgettable memories outside of the lab.

TABLE OF CONTENTS

LIST OF TABLES xii

LIST OF FIGURES xiii

LIST OF ABBREVIATIONS xvi

CHAPTER 1 – INTRODUCTION 1

1.1 The development of electrides and their properties 1

1.1.1 Discovery of layered electrides 2

1.1.2 Crystal structures of layered electrides 3

1.1.3 Mechanical properties of layered electrides 6

1.1.4 Electronic structures and properties 7

1.1.5 Chemical properties of electrides 10

1.1.6 Applications of electrides 11

1.1.6.1 Chemical synthesis and catalysis 11

1.1.6.2 Solid-state dopants 12

1.1.6.3 Batteries 12

1.1.6.4 Transparent conductors 13

1.2 Overview of the research described in this thesis 13

1.2.1 Electrenes 13

1.2.1.1 The synthesis of electrenes 14

1.2.1.2 Donor–acceptor heterostructures 14

1.2.2 Electride-halide analogs and electron-anion exchange 15

1.2.2.1 Electrochemical electron-anion exchange 15

1.2.2.2 Discovery of Y_2CF_2 16

CHAPTER 2 – METHODS FOR PREPARATION AND CHARACTERIZATION OF ELECTRIDES 18

2.1 Introduction 18

2.2 Synthesis of electrides and related phases 18

2.2.1 Preparation of reagents 19

2.2.2 Ampoules, containers, and crucibles for high-temperature reactions 20

2.2.2.1 Molybdenum and tantalum as crucibles and ampoules 22

2.2.3 Furnaces and rates of heating 24

2.2.4 Synthesis of bulk Ca_2N 24

2.2.5 Synthesis of Y_2CF_2 25

2.2.6 Arc-melting as a synthetic scheme 25

2.3 X-ray powder diffraction 28

2.3.1 Theory of diffraction 28

2.3.2 Experimental conditions for X-ray diffraction 33

2.3.2.1 X-ray diffractometer 33

2.3.2.2 Diffractometer geometry 33

2.3.3 Analysis of PXRD data 35

2.3.3.1 Phase identification 35

2.3.3.2 Whole pattern fitting by Rietveld refinement 36

2.4 Density functional theory 40

2.4.1 Basic principles of DFT 40

2.4.1.1 Approximations to the exchange correlation functional 42

2.4.1.2 Approximations made in implementing DFT 44

2.4.2 Calculating properties using DFT 46

2.4.2.1 Work function and ionization potential 48

2.4.2.2 Binding energy 49

2.4.2.3 The potential energy surfaces for sliding 50

2.4.2.4 Geometry optimization of 2D heterostructures 51

CHAPTER 3 – EXPERIMENTAL DEMONSTRATION OF AN ELECTRIDE AS A 2D MATERIAL 52

3.1 Introduction 52

3.2 Results and Discussion 53

3.2.1 The synthesis of 2D Ca_2N by liquid exfoliation 53

3.2.2 Characterizing electride nanosheets by electron microscopy 55

3.2.3 Understanding the composition of 2D Ca_2N 57

3.2.4 Analyzing the electronic structure of 2D Ca_2N 58

3.3 Conclusions 60

CHAPTER 4 – BONDING IN 2D DONOR–ACCEPTOR HETEROSTRUCTURES 62

4.1 Introduction 62

4.2 Results and Discussion 64

4.2.1 Creating heterostructures with donor–acceptor interactions 64

4.2.2 Understanding sterics and energetics of donor–acceptor heterostructures 66

4.2.3 Donor–acceptor analogy 68

4.2.4 Understanding the polarity of quasi-bonds 71

4.2.5 Applications of donor–acceptor heterostructures 72

4.3 Conclusions 75

CHAPTER 5 – THE SYNTHESIS AND ELCTRONIC STRUCTURE OF Y_2CF_2: A CRYSTALLINE STACK OF MXENE SHEETS 76

5.1 Introduction 76

5.2 Results and discussion 77

5.2.1 Synthesis and crystal structure 77

5.2.2 Composition and purity 80

5.2.3 Electronic structure of Y_2CF_2 81

5.2.4 Sensitivity to oxygen 83

5.3 Conclusion 88

CHAPTER 6 – ELECTROCHEMICAL ELECTRON-ANION EXCHANGE: A NEW MECHANISM OF ION-INSERTION AND ITS APPLICATION IN FLUORIDE-ION BATTERIES 89

6.1 Introduction 89

6.2 Results and Discussion 90

6.2.1 Electron analog pair 90

6.2.2 Activation barrier for F^- diffusion 92

6.2.3 Experimental evidence for electron-anion exchange 94

6.2.4 Storage of electrochemical energy 96

6.3 Conclusions 99

APPENDIX A –SUPPORTING INFORMATION FOR CHAPTER 3 101

A.1 3D Ca_2N synthesis and characterization 101

A.2 DFT calculations of Ca_2N and graphite 101

A.3 Screening solvents for liquid exfoliation of Ca_2N 103

A.4 Transmission electron microscopy experiments and simulations 104

A.5 Photoemission experiments of 2D and 3D electrides 105

A.6 Optical response of 2D Ca_2N 109

APPENDIX B –SUPPORTING INFORMATION FOR CHAPTER 4 114

B.1 Requirements for electron transfer between materials 114

B.2 Overview of density functional theory methods using CASTEP 115

B.3 Structural optimization of electrene and 2DM heterostructures 116

B.4 Bader charge analysis and hybrid functionals 116

B.5 Bond length assessment from the Materials Project 118

B.6 Electronic structure of donor–acceptor heterostructures 119

B.7 Binding energy 119

B.8 Sliding energy in donor-acceptor heterostructures 120

B.9 Work functions and potential energy 121

APPENDIX C –SUPPORTING INFORMATION FOR CHAPTER 5 129

C.1 The synthesis of Y_2CF_2 129
C.2 X-ray diffraction experiments of Y_2CF_2 130
C.3 Microscopy and spectroscopy of Y_2CF_2 131
REFERENCES 137

LIST OF TABLES

1.1 Selected bond lengths and interlayer distances for alkaline earth sub-pnictogenides 4

1.2 Selected bond lengths and interlayer distances for metal subcaribdes 5

3.1 XPS Binding Energies (eV) of Ca 2p Electrons from Ca_2N 58

5.1 Refinement of the structure of Y_2CF_2 78

5.2 Atomic distance in the crystal structure of Y_2CF_2 79

5.3 X-ray photoemission spectra from samples of Y_2CF_2 kept in different environments 84

6.1 Atomic distances in the crystal structures of Y_2C and Y_2CF_2 91

6.2 Bader charges on the atoms of Y_2C and Y_2CF_2 91

B.1 Lattice matching, interlayer distances, and strain on the 2DM and electrene components after structural optimizations 117

B.2 Electron transfer in donor-acceptor heterostructures calculated from bader charge analysis ... 117

B.3 Electron transfer for two donor-acceptor heterostructures using hybrid functionals 118

B.4 Binding energies for the donor-acceptor heterostructures 120

LIST OF FIGURES

1.1 The progression from solvated electrons to electrenes 1

1.2 The crystal structure of layered electrides with the common anti-$CdCl_2$-type structure 4

1.3 Binding energy of layered electrides 6

1.4 Comparison of carrier density and work functions for alkaline earth sub-pnictogenides 8

3.1 Liquid exfoliation of Ca_2N. 54

3.2 Morphology and crystallinity of exfoliated Ca_2N. 56

3.3 Photoemission spectra of calcium nitride species and related oxidized species. 58

3.4 Optical properties of 2D Ca_2N. 59

4.1 Illustration of a donor–acceptor heterostructure constructed from graphene and an electrene. . 63

4.2 Bonding and electron transfer in molecular compounds, van der Waals materials, and donor–acceptor heterostructures. 66

4.3 Orbital projections, electron density, and interlayer interaction energies in donor–acceptor heterostructures. 69

4.4 Donor–acceptor analogy to rationalize electron transfer in e-BN. 70

4.5 Atomic density deformation of donor–acceptor heterostructures and common materials. 72

4.6 Applications of donor–acceptor heterostructures. 74

5.1 X-ray diffraction pattern for Y_2CF_2 78

5.2 Crystal structure, bonding polyhedral, and lattice constants for Y_2CF_2 79

5.3 Comparison of the crystal structure of Y_2CF_2 to Y_2CCl_2 80

5.4 Optical properties of Y_2CF_2. 82

5.5 Photographs of Y_2CF_2 before grinding and after grinding. 83

5.6 X-ray photoemission spectroscopy experiments of Y_2CF_2. 85

5.7 Band alignment of Y_2CF_2. 87

6.1 Comparison of the crystal structures of Y_2C and Y_2CF_2. 92

6.2 Activation barrier for the diffusion of F^- in Y_2CF_2. 93

6.3 The effect of stacking sequence of R$\bar{3}$m Y_2C (ABC) and P$\bar{3}$m1 Y_2CF_2 (AA) on the stability of Y_2CF_x. 93

6.4 Activation barrier for the diffusion of F^- in ABC-stacked Y_2CF. 94

6.5 Powder X-ray diffraction pattern of Y_2CF_2 dehalogenated by chemical reduction using lithium metal at 500 °C. 95

6.6 Storage of electrochemical potential energy using the Y_2CF_2/Y_2C system 97

A.1 Powder X-ray diffraction of Ca_2N. 101

A.2 Electronic structure of mono- and bilayer Ca_2N. 103

A.3 Powder X-ray diffraction of Ca_2N exposed to THF for 24 hours. 104

A.4 Low-resolution transmission electron microscopy images of flakes of 2D Ca_2N. 105

A.5 Simulated diffraction pattern of 2D Ca_2N. 106

A.6 XPS spectra of core C 1s electrons for 2D Ca_2N, deliberately oxidized 2D Ca_2N, and $Ca(OH)_2$. 107

A.7 Photoemission spectroscopy of a thick film of 2D Ca_2N on a platinum-coated silicon wafer. 108

A.8 Differential charging of samples of 2D Ca_2N 110

A.9 Absorbance of 2D Ca_2N as a function of concentration. 111

A.10 Relationship of band structure and joint density of states of Ca_2N. 112

A.11 Measurements of optical response with 2D Ca_2N inside integrating sphere. 113

B.1 Electron transfer models in molecular systems and solids using band alignment and density of states 122

B.2 Optimized structure of the donor-acceptor heterostructures 123

B.3 Electronic structure of the e-C donor-acceptor heterostructure 123

B.4 Electronic structure of the e-BN donor-acceptor heterostructure 124

B.5 Electronic structure of the e-P donor-acceptor heterostructure 124

B.6 Electronic structure of the e-ZrS2(c) donor-acceptor heterostructure 125

B.7 Determining the binding energy of e-BN 125

B.8 Binding energy of donor-acceptor heterostructures per unit cell of acceptor 125

B.9 Binding energy of donor-acceptor heterostructures per acceptor atom nearest the electrene ... 126

B.10 Binding energy of donor-acceptor heterostructures in Joules per square meter 126
B.11 Potential energy surface for sliding in donor-acceptor heterostructures 126
B.12 Potential energy diagram and work function of e-ZrS2(a) 127
B.13 Potential energy diagram and work function of e-ZrS_2(b) 127
B.14 Potential energy diagram and work function of e-ZrS_2(c) 127
B.15 Potential energy diagram and work function of e-BN 128
B.16 Potential energy diagram and work function of e-C 128
B.17 Potential energy diagram and work function of e-P 128

C.1 Powder X-ray diffraction pattern of Y_2CF_2 synthesized from Y_2C. 131
C.2 Micrograph of Y_2CF_2 and corresponding EDS analysis and mapping. 132
C.3 Micrographs of Y_2CF_2. 132
C.4 Spectra collected from clean facets of Y_2CF_2 in a microspectrophotometer 133
C.5 Absorbance spectra of Y_2CF_2 133
C.6 Micrographs of Y_2CF_2 ball-milled to $<$ 5 µm particles 134
C.7 Powder X-ray diffraction pattern of Y_2CF_2 ball-milled to $<$ 5 µm particles 134
C.8 Specular reflection measurements of Y_2CF_2 ball-milled to $<$ 5 µm particles 135
C.9 Photographs of unoxidized and oxidized Y_2CF_2 135
C.10 X-ray diffraction patterns of Y_2CF_2 exposed to air for 3 weeks and before exposure 136
C.11 Reflectivity of Y_2CF_2 exposed to air for 1 month and images of the corresponding crystals . . 136

LIST OF ABBREVIATIONS

2D	two-dimensional
A	area
AA-stacked	crystallographic stacking sequence associated with P$\bar{3}$m1 space group
ABC-stacked	crystallographic stacking sequence associated with R$\bar{3}$m space group
ARPES	angle-resolved photoelectron spectroscopy
[C_4C_1im][OTf]	1-butyl-3-methylimidazolium trifluoromethanesulfonate
COD	Crystallography Open Database
D	crystallite size
DFT	density functional theory
DFT-D	density functional theory with Grimme's correction
e^-	electron
E_F	Fermi level
EDS	energy-dispersive x-ray spectroscopy
E_{ox}	oxidation potential
E_{red}	reduction potential
ΔF_{form}	Enthalpy of formation
F	Faraday's constant
FFT	fast Fourier transform
FWHM	full width at half maximum
GGA	generalized gradient approximation
ΔG	Gibbs free energy
I	current
ICSD	International Crystal Structure Database
ID	inner diameter
IP	ionization potential
IPA	isopropyl alcohol
IR	infrared
k_B	Boltzmann constant

LDA	local density approximation
LUMO	lowest unoccupied molecular orbital
M_2V	alkaline earth sub-pnictogenides
MP grid	Monkhorst-Pack grid
n	electron concentration
NEB	nudged elastic band
NFEG	nearly free electron gas
NIR	near infrared
OD	outer diameter
PXRD	X-ray powder diffraction
SCF	self-consistent field
SEM	scanning electron microscope
THF	tetrahydrofuran
TS-vdw	Tkatchenko and Scheffler
USPEX	Universal Structure Predictor: Evolutionary Xtallography
UV	ultraviolet
V	voltage
vdw	van der Waals
WF	work function
XRD	X-ray diffraction
XPS	X-ray photoelectron spectroscopy

CHAPTER 1–INTRODUCTION

"Th[is] negative ion constitutes a new species of anion. It consists of a negative charge, an electron . . . "

- Charles Kraus, 1908, *Solutions of Metals in Non-Metallic Solvents*[1]

1.1 The development of electrides and their properties

The classic concept of an ionic solid is a crystal made of oppositely charged ions, like NaCl, but in electrides, the negative "ion" is just an electron that lacks an atomic nucleus. While traditional ionic solids are hard, brittle, and electrically insulating, electrides can be soft, malleable, and among the most conductive materials known. To explain the unusual properties of electrides, I outline the historical development of their principles, learned through a century of research.

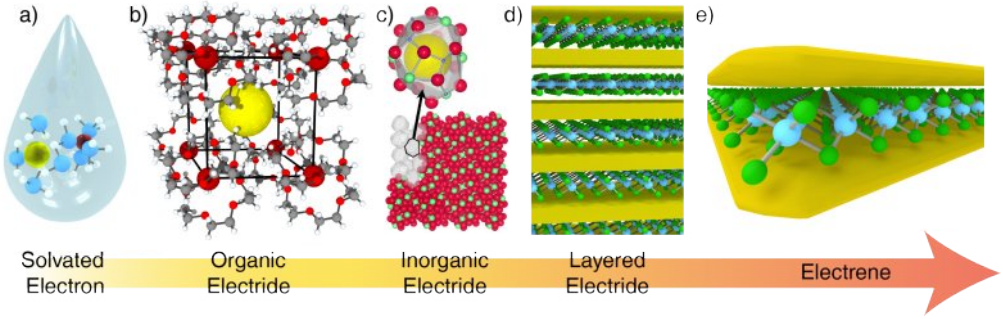


Figure 1.1: The progression of anionic electrons from a) solvated electrons to b) organic electrides[2] to c) inorganic electrides[3] to d) layered electrides to e) electrenes. (c) Reprinted by permission from Macmillan Publishers Ltd: *Nature Communications* 2013, **4** 2378. Copyright 2013.

The concepts that explain the properties of electrides originate from the history of solvated electrons (Figure 1.1a) and color centers.[4] In the 1900s, Kraus[1,5–9] introduced the idea of anionic electrons in his explanation of the dissolution of metals in liquid ammonia, "The negative ion constitutes a new species of

Portions of this chapter reproduced from Druffel, D. L.; Woomer, A. H.; Kuntz, K. L.; Pawlik, J. T.; Warren, S. C. Electrons on the surface of 2D materials: from layered electrides to 2D electrenes. *Journal of Materials Chemistry C* **2017**, *5*, 11196-11213. Copyright 2017 The Royal Society of Chemistry.

anion, . . . an electron, surrounded by an envelope of solvent molecules."[6] Mounting evidence corroborated the idea of an anionic electron solvated in fluid.[10] Then, researchers explored many of the same ideas in solids. Mott and de Boer rationalized color centers—crystal defects that cause transparent crystals like NaCl to absorb visible light—to be point defects in the crystal consisting of trapped anionic electrons or cationic holes.[11,12] The most famous of these is the F-center, in which an electron fills an anion vacancy.[13]

Because an F-center is a defect and not a periodic component of the crystal, the concentration of anionic electrons in a solid with F-centers is usually low.[13] In the early 1980s, however, Dye demonstrated that the compound, $Cs^+(18\text{-crown-}6)_2{\cdot}e^-$, had anionic electrons at a stoichiometric concentration equal to that of Cs metal.[14–17] The unpaired, anionic electrons reside in periodic spherical cavities between the complexed cations (Figure 1.1b). He called this type of solid an "electride."

Despite the successful synthesis of an electride, Dye's organic electrides decomposed at room temperature and prompted many to believe that electrides are unstable compounds. A breakthrough came in 2003, when Matsuishi succeeded in synthesizing a thermally stable electride, in which an inorganic lattice hosts the anionic electrons (Figure 1.1c).[18] Through high-temperature treatment with calcium metal, Matsuishi replaced the oxygen anions in mayenite, $[Ca_{24}Al_{28}O_{64}]^{4+}(2O^{2-})$, with electrons to form an electride, $[Ca_{24}Al_{28}O_{64}]^{4+}(4e^-)$. The synthesis of large single crystals of $[Ca_{24}Al_{28}O_{64}]^{4+}(4e^-)$ allowed measurements of intrinsic properties like electrical mobility[19–21] and demonstrated that electrides can be stable materials.[22]

While research on the properties of thermally stable, inorganic electrides gained momentum, Dye came to an important generalization about the structure of electrides: the electron density distribution resembles the available atomic void space.[23] In the organic electrides, the atomic void space is determined by the location of the van der Waals surfaces of the organic molecules.[4] In the inorganic electrides, the atomic void space is determined by the atomic crystal lattice. By engineering the crystal lattice, almost any geometry of atomic void space, and therefore almost any geometry of anionic electron density, is possible. Thus, by 2015, zero-, one-, and two-dimensional electron density distributions were demonstrated.[18,24–26]

1.1.1 Discovery of layered electrides

In the 1950s and 1960s, researchers synthesized layered crystals (Ba_2N,[27] Sr_2N[27] and Ca_2N[28]) that possess a two-dimensional (2D) void space.[25,29] The layered structures had surprisingly large interlayer distances (*e.g.* 3.85 Å in Ca_2N). To account for the large interlayer distance in Ca_2N, Keve et al. speculated that "excess electrons [are] situated in the large gaps between layers".[25] This speculation was not widely

accepted at first. For example, Brice et al. suggested that Sr_2N was, in fact, Sr_2NH.[30] But neutron diffraction experiments later ruled out the presence of H (*e.g.*, as a hydride) in Sr_2N[31] and Ca_2N.[32] Brese et al. proposed another hypothesis that Sr_2N could have oxidation states of +1.5 (Sr) and -3 (N) rather than +2 (Sr), -3 (N), and -1 (an anionic electron).[31] In 2000, careful electronic structure calculations showed that electrons existed between layers of atoms,[33] which agreed with X-ray and ultraviolet photoemission spectroscopy.[34] Because of the layered lattice, the anionic electrons are confined to a 2D void space.

The confinement of the anionic electrons into a 2D plane profoundly affects how the electrons behave. Density functional theory (DFT) calculations indicate that the anionic electrons partially delocalize into a 2D electron gas.[26,33,35] Experimental evidence supports this description. Low magnetic susceptibility, consistent with weak Pauli paramagnetism, indicates that the anionic electrons are paired.[31,32] The strongest evidence of the 2D electron gas confined between planes of atoms is the observation of metallic conduction with high in-plane electrical mobility and low out-of-plane mobility.[26] In a groundbreaking work, Hosono and coworkers performed electrical and photoemission experiments on single crystals of layered electrides and demonstrated, in addition to high in-plane electrical mobility, strong anisotropy in the magnetoresistance and work function, which further support the designation as a 2D electron gas.[26]

1.1.2 Crystal structures of layered electrides

The simplest model of the structure of layered electrides considers the crystal as layers of electron gas separated by slabs of atoms. The slabs of atoms carry a net positive charge and these slabs are held together by electrostatic forces. The layers of electrons carry a net negative charge and are partially delocalized into an electron gas.[35]

The most common crystal structure of layered electrides is the anti-$CdCl_2$-type structure (space group $R\bar{3}m$, #166) (Figure 1.2a). To represent this class of crystal for the alkaline earth sub-pnictogenides, we use the notation M_2V (M = Ca, Sr, Ba; V = N, P, As) for Ca_2N, Sr_2N, Ba_2N, Sr_2P, Ba_2P, and Ba_2As. Edge-sharing VM_6 octahedra form layers (Figure 1.2c). Because of the large electronegativity difference, we consider the interactions within the layers to be ionic. The observation that the M-V distances are nearly the sum of the respective ionic radii supports this designation (Table 1.1). Considering integer oxidation states for the ions (M = +2, V = -3), each M_2V formula unit carries a charge, regarded as $[M_2V]^+$. To balance the positive charges on the $[M_2V]^+$ layer, anionic electrons reside in the interlayer space.

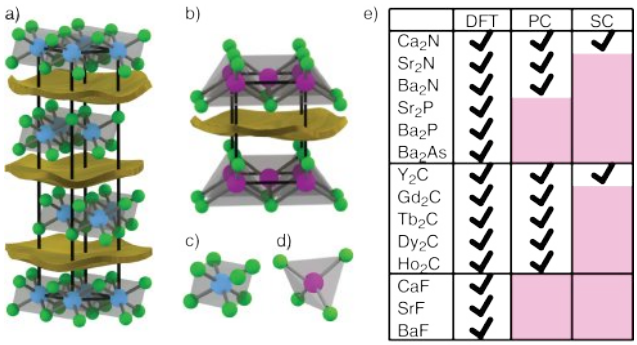


Figure 1.2: The crystal structure of a) layered alkaline earth sub-pnictogenides and layered rare earth sub-carbides and b) alkaline earth monofluorides. The electron gas is represented in gold. The space-filling polyhedra show nearest neighbors of the c) sub-pnictogenides and sub-carbides and d) monofluorides. e) A summary of the investigation of each compound using density functional theory (DFT), and experimentation on polycrystalline (PC) and single crystalline (SC) samples.

The interlayer distance in these compounds is quite large (*e.g.* ~3.85 Å in Ca_2N).[26] Interlayer metal-metal ($M\text{-}M^{inter}$) (Table 1.1) distances are greater than those in the respective elemental metal ($M\text{-}M^{metal}$), which rules out direct metal-metal bonding between layers. The interlayer metal-metal distances are more comparable to the van der Waals distances of the metal.[36] However, anionic electrons reside in the interlayer gap. Therefore, the dominant force in the out-of-plane direction is the Coulombic attraction between the metal cations and anionic electrons.

Table 1.1: Selected bond lengths and interlayer distances for alkaline earth sub-pnictogenides. These values are compared to the bond lengths for elemental metals (Ca, Sr, Ba) ($M\text{-}M^{metal}$),[37] the sum of the ionic radii ($M\text{-}V^{ionic\ radii}$),[38] and to the bond lengths of other alkaline earth pnictogenides, such as Sr_3P_4,[39] SrP,[40] Ba_3P_4,[39] Ba_3As_{11},[41] and $Ba_4As_{2.6}$[42] ($M\text{-}V^{other\ crystals}$). All distances are in Å.

	Ca_2N	Sr_2N	Sr_2P	Ba_2N	Ba_2P	Ba_2As
$M\text{-}M^{intra}$	3.27, 3.63	3.52, 3.86	4.06, 4.46	3.78, 4.03	4.36, 4.66	4.45, 4.77
$M\text{-}M^{inter}$	4.39	4.73	4.99	5.05	5.38	5.39
$M\text{-}M^{metal}$	3.94	4.30	4.30	4.34	4.34	4.34
M-V	2.44	2.61	3.01	2.77	3.19	3.27
$M\text{-}V^{ionic\ radii}$	2.46	2.64	2.98	2.81	3.15	3.50
$M\text{-}V^{other\ crystals}$			3.08–3.28		3.13–3.45	3.32–3.63
Interlayer Dist.	3.85	4.17	4.27	4.48	4.66	4.63

Like the alkaline earth sub-pnictogenides, layered metal sub-carbides crystallize in the anti-$CdCl_2$-type structure (Figure 1.2a). The bonding is ionic, which is supported by the metal-carbon distances that equal the sum of the ionic radii of M^{3+} (M = Y, Tb, Dy, Ho, Gd) and C^{4-} (Table 2). Considering the oxidation states of the ions (M = +3 and C = -4), a M_2C layer is expected to carry a +2 charge with 2 e^- per formula unit in the

Table 1.2: Selected bond lengths and interlayer distances for Y_2C,[43] Gd_2C,[44] Tb_2C,[45] Dy_2C,[46] and Ho_2C.[47] These values are compared to the bond lengths for elemental metals (Y, Gd, Tb, Dy, Ho)[37] and to the sum of the ionic radii.[38] Some interatomic distances are not known for Gd_2C. All distances are in Å.

	Y_2C	Gd_2C	Tb_2C	Dy_2C	Ho_2C
M-M^{intra}	3.42, 3.63	3.64	3.38, 3.58	3.41, 3.58	3.42, 3.58
M-M^{inter}	3.89		3.93	3.86	3.77
M-M^{metal}	3.56	3.57	3.52	3.50	3.49
M-C	2.49		2.46	2.47	2.47
M-$C^{ionic\ radii}$	2.42	2.46	2.46	2.43	2.42
Interlayer Dist.	3.28		3.34	3.25	3.17

interlayer space. In actuality, fewer than two electrons per formula unit reside in the interlayer space. The structure is better described as $[Y_2{}^{1.9+}C^{2-}]\cdot 1.8e^-$.[48] (See electronic properties, below.)

The additional charge density in the cationic layer and electron layer causes greater Coulombic attraction between planes. This results in interlayer distances (3.17–3.34 Å) that are much shorter than in the alkaline earth sub-pnictogenides and comparable to van der Waals distances.[48] The interlayer metal-metal distances are slightly greater (0.3–0.4 Å) than the interatomic distances in the respective elemental metal. Therefore, weak cation-cation bonding may be present. The stronger Coulombic attraction, weak cation-cation bonding, and van der Waals forces impart different mechanical and electronic properties to the layered metal sub-carbides than other layered electrides.

When considering the structure of layered electrides, it is tempting to consider the anionic electron as a sphere with an "ionic" radius. In the literature, the ratio of ionic radii has been used to justify why some compounds form electrides and others do not.[49] The reasoning derives from Pauling's First Rule for rationalizing crystal structures, which considers ions as rigid spheres and calculates a minimum ratio of radii for which the cation contacts a maximum number of anions.[50] The extreme similarity in the structure of sub-pnictogenide electrides to sub-pnictogenide halides (*e.g.* Ca_2N to Ca_2NCl) also attracts interesting comparisons between the crystals.[49,51–53] For example, the host sub-nitride lattice barely changes upon incorporation of Cl^-.[51] However, the anionic electrons in a layered electride do not behave like rigid spheres, like Cl^-. The electrons delocalize in the interlayer gap and that electron gas is compressible. Moreover, halides of some alkaline earth sub-pnictogenides are known (Mg_2NCl, Ca_2PI, Ca_2AsI) with the same layered structure ($R\bar{3}m$) as Ca_2NCl, but the corresponding electrides (Mg_2N, Ca_2P, Ca_2As) do not exist, which shows that the ratio of radii of M^{2+} to V^{3-} does not determine whether an electride forms. Therefore, we avoid the concepts of hard sphere-packing for rationalizing and predicting the crystal structures of electrides.

1.1.3 Mechanical properties of layered electrides

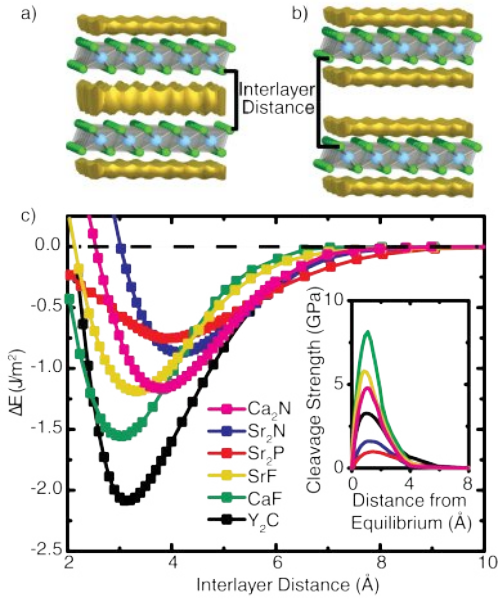


Figure 1.3: An illustration of the change in interlayer distance at a) equilibrium and b) large distances. c) The change in energy per unit interfacial area versus interlayer distance for the layered electrides. The inset shows cleavage strength, which is the first derivative of the binding energy. The DFT calculations were performed using the CASTEP code[54] with plane-wave basis set approximations[55] and a 400 eV cut-off energy. Ultrasoft pseudopotentials[56] were used to describe core electrons. A GGA PBE functional[57] was used for the exchange-correlation contribution to total energy and Grimme's DFT-D correction[58] was used for van der Waals forces. A Monkhorst-Pack grid[59] of 26×26×4 was used. Calculations were convergent with dE/dE_{cut} less than 0.01 meV/atom. Each unit cell was relaxed prior to calculations of the binding energy, resulting in lattice constants similar to those reported previously.[49] The relaxed structure was then used to calculate the effects of interlayer distance on the energy of the system.

For an ionic crystal, qualitative descriptions such as "malleable",[60] "graphitic",[61] and "easily cleaved"[26] are unusual, yet these are the descriptions of layered electrides. The anisotropy in the interlayer and intralayer forces causes anisotropy in the mechanical properties. For example, Ca_2N, Sr_2N, and Ba_2N are twice as compressible out-of-plane as they are in-plane.[62] Theoretical studies of Y_2C calculate a small bulk modulus (∼68 GPa),[63] suggesting that Y_2C has high compressibility for an ionic material, likely because of the electron gas layer. At the same time, a moderate Young's modulus (104.5 GPa) and Poisson ratio (0.24)[63] suggest that Y_2C is stiff and brittle, because of the ionic intralayer bonding. Moreover, because of the weak Coulombic attraction between the positively charged ionic slabs and electron gas, the planes of Ca_2N easily slide with a low energy barrier, comparable to van der Waals materials like graphite.[64]

Within the layered electrides, the strength of the interlayer Coulombic attraction influences the mechanical properties as evidenced by the differences in binding energy. The binding energy is the energy difference between the state in which the planes are at their equilibrium bulk separation (Figure 1.3a) and the state in which the planes are separated infinitely as approximated by a 15-Å thick vacuum-gap (Figure 1.3b). We reported calculations for Ca_2N[61] and calculations for Sr_2N, Sr_2P, Y_2C, CaF, and SrF (Figure 1.3c).[65] For all of the layered electrides, the change in energy at large interlayer distances is small. As the layers move closer together, the change in energy is negative because the layers interact favorably. At short interlayer distances, the nuclei and electrons experience repulsion and the energy increases. Of the layered electrides that we studied, Sr_2N and Sr_2P have the smallest binding energies and Y_2C and CaF have the largest binding energies. The low binding energies of Sr_2N and Sr_2P suggest that their interlayer forces are weaker than those of other layered electrides. In addition, the cleavage strength, which is the first derivative of binding energy with respect to distance, is low for Sr_2N and Sr_2P. Therefore, Sr_2N and Sr_2P are strong candidates for exfoliation. On the other hand, the high binding energy of Y_2C and CaF indicates stronger interlayer forces. We expect these crystals are difficult to exfoliate.

1.1.4 Electronic structures and properties

The electronic structure of layered electrides has been studied extensively. I refer the curious reader to a review[65] that describes the electronic structure of layered electrides in more detail than is warranted here. Here I will summarize the key concepts, which inform an understanding of the rest of the thesis.

The highest occupied state for all of these materials is a nearly free electron gas (NFEG) band (shown partially in gold in Figure 3.4f). The orbital projection of this band within thermal energy of the Fermi level (E_F) shows that this electron is spatially confined to the 2D space between ionic layers (Figure 3.4b,c). While this is a defining feature of the electronic structure of the layered electrides, the degree of delocalization of the anionic electron depends on the space group and compound.

For the alkaline earth sub-pnictogenides (Ca_2N, Sr_2N, Ba_2N, Sr_2P, Ba_2P, and Ba_2As) the NFEG band passes through E_F.[35,49] Because the NFEG states are close in energy and have appropriate symmetry, they are partially hybridized with the *p* states of the pnictogen. Below the NFEG band are ionic bonding states between the pnictogen *p* states and alkaline earth *s* and *d* states. Above the NFEG band are fully unoccupied bands, which consist of empty *d* states of the alkaline earth metal.

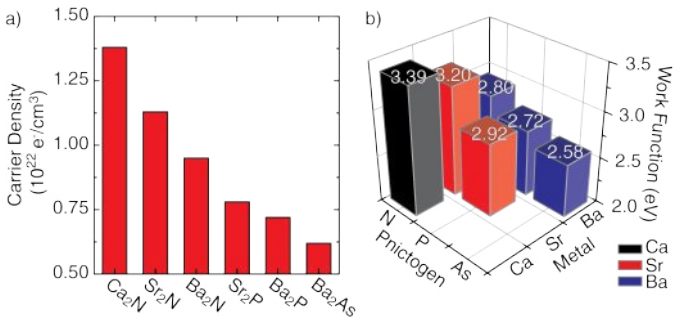


Figure 1.4: a) The theoretical carrier densities of the alkaline earth sub-pnictogenides predicted from their crystal structure assuming one carrier per formula unit. b) The work functions of the (001) surface of the alkaline earth sub-pnictogenides calculated by DFT, which decrease down the group IIA elements and down the pnictogens.[49]

Interestingly, integration of the partial electron density within the interlayer gap totals less than 1 e^- per formula unit of M_2V (0.5 e^- to 0.8 e^- depending on how the electron density is integrated).[49,61] Therefore, a fraction of electron density resides in the ionic slab. Despite this, the experimentally determined carrier concentration of Ca_2N (1.39×10^{22} e^- cm^{-3})[26] matches the carrier concentration (1.38×10^{22} e^- cm^{-3}) predicted from one electron per formula unit. This is because the remaining fraction of electron density is found on nitrogen *p* states near the E_F.

Because of the 2D confinement of the NFEG, the Fermi surface is approximately cylindrical. Angle-resolved photoelectron spectroscopy (ARPES) spectra of a cross section of the Fermi surface in the k_{xy} plane confirm a circular shape.[66] However, the electrons are not fully localized along the *z*-direction as evidenced by the finite dispersion of the anionic electron band in the *z*-direction (Figure 3.4f along path Γ–A).[67]

The properties that result from this electronic structure are exciting. From Hall measurements, Ca_2N has a very high in-plane mobility of 520 cm^2 V^{-1} s^{-1} at low temperatures (2 to 100 K for single crystalline samples).[26] Using the Drude model, researchers calculated an exceptionally long mean free path length of 120 nm and a scattering time of 0.6 ps for Ca_2N single crystals. In addition, because the electrons are only loosely bound to the crystal, layered electrides have very low and anisotropic work functions (Figure 1.4b). For example, the work function for the (100) plane of Ca_2N is ∼2.6 eV while that of the (001) plane is ∼3.5 eV.[26]

Within the class of the alkaline earth sub-pnictogenides, the electronic structure differs subtly. The bandwidth of the NFEG band depends on the elemental composition, and ranges from 2.0–1.5 eV for Ca_2N and Ba_2As, respectively.[35,49] Calculations of the maximum carrier density (n_o) for alkaline earth

sub-pnictogenides, assuming one electron per formula unit, range from *ca.* 1.38×10^{22} e^- cm^{-3} to 0.64×10^{22} e^- cm^{-3} for Ca_2N and Ba_2As, respectively (Figure 1.4a). The carrier density varies because of ionic size, where combinations of larger alkali earth metals and pnictogens result in larger lattice constants and larger unit-cell volumes. For the (001) surface, the work function decreases both down the group IIA elements and down the pnictogens (Figure 1.4b).[49] We attribute this to the decreasing electron affinity of the alkaline earth metal and increasing ionic radii; as the electron affinity of the alkaline earth metal decreases, the electrostatic potential between the anionic electron and cation decreases resulting in a lower work function. Furthermore, the increasing ionic radius of the pnictogen group results in larger lattice constants, interlayer distances, and cation-cation distances, which weakens the bound potential of the anionic electron.

The electronic structure of layered sub-carbides (Y_2C, Gd_2C, Tb_2C, Dy_2C, and Ho_2C) is similar to that of the alkaline earth sub-pnictogenides with an anionic electron band at E_F.[68] As mentioned previously, the oxidation states of the sub-carbide electrides suggest *ca.* 2.0 anionic electrons per formula unit. As a result, the anionic electron band is either filled or nearly filled. The expectation may be that the layered sub-carbides are insulators, but this is not the case. Overlap in energy but not momentum of the anionic electron band with a second conduction band (a hybridization of anionic electron and metal states) makes these materials semimetals.[48,69] I direct the reader to a beautiful graphical representation of the band structure published by Horiba *et al.*.[70] ARPES spectra of the Fermi surface of Y_2C agrees with DFT calculations.[70] Because of the overlap between unoccupied *d* states and the anionic electron band, the Fermi surface of Y_2C is a perturbed cylinder, in contrast to that of Ca_2N. Compared to the pnictogenides, the dispersion of the anionic electron band is smaller with a higher effective mass.[48,69] We attribute this to the smaller cation-cation distance and the larger oxidation state for the rare earth and transition metals, which partially localize the anionic electron to octahedral vacancy sites, as opposed to the disperse NFEG plane in alkaline earth sub-pnictogenides. The anionic electron in Y_2C is found closer to the metal atoms, which is attributed to greater electrostatic potential between the anionic electron and cation.

Y_2C shows large anisotropy in electrical properties for in-plane and out-of-plane directions. The out-of-plane resistance is four orders of magnitude larger than the in-plane resistance,[71] which is consistent with our description of the sub-carbides as alternating ionic and NFEG slabs. The electronic structure of the sub-carbide electrides gives rise to electronic properties different from the sub-pnictogenides. For the sub-carbide electrides, in which the molecular formula is $[M_2X]^{n+} \cdot ne^-$ and *n* is a value from 1.8 e^- to 2.0 e^-, one expects the carrier density to be approximately double that of the alkaline earth sub-pnictogenides.

However, Hall measurements of Y_2C show n_o to be 4.37×10^{21} e^- cm^{-3}, an order of magnitude lower than values predicted using only integer oxidation states. In addition, the mobility of Y_2C (5.6 cm^2 V^{-1} s^{-1} at 2 K) measures two orders of magnitude less than Ca_2N.[48] The electrons in Y_2C are more localized and have a larger effective mass compared to the NFEG states of the sub-pnictogenides. Furthermore, the work function for the (001) surface of the sub-carbides (*e.g.* 3.72 eV for Y_2C[48]) is greater than that of the sub-pnictogenides.

These examples illustrate both the similarities and differences between layered electrides. It reveals that the overlap in energy of the anionic electron band with bands made of atomic states perturbs the NFEG. Consequently, the degree to which the NFEG defines the properties of layered electrides spans a continuum, though in all cases, remains the defining feature of the material.

1.1.5 Chemical properties of electrides

The anionic electrons largely determine the chemical properties of layered electrides. As suggested by the low work functions, these materials readily donate their electrons, which makes them strong reducing agents. For rough comparison, layered electrides behave like alkali metals; they react exothermically with water, oxidize in air within seconds,[32] and must be handled cautiously under oil or in a glovebox.

Researchers have investigated the reactivity of anionic electrons in the form of solvated electrons. Because of the limited data on layered electrides and electrenes, we use results from solvated electrons[72] to inform our expectations for their reactivity. Solvated electrons can reduce all metal cations apart from alkali, alkaline earth, and bivalent rare earth metal ions. Anions with filled valence shells do not react. In addition, some nonmetallic oxo-anions ($B_4O_7^{2-}$, CO_3^{2-}, HCO_3^-, ClO_4^-, PO_4^{3-}, SO_4^{2-}) do not react, while many others (MnO_4^-, $Cr_2O_7^{2-}$) are highly reactive. Saturated hydrocarbons, amines, and ethers show little tendency to react with solvated electrons, while olefins, aldehydes, and ketones react. Aromatic hydrocarbons can react because they have a low lying LUMO that can accept an additional electron. Halogenated hydrocarbons react rapidly with anionic electrons. Hydrogen, nitrogen, and noble gases are inert to solvated electrons.[72]

Despite these similarities in the reactivity of solvated electrons and electrides,[61,73–75] there are some notable differences. One exception is that electrides degrade in triethylamine over time.[61] That observation merits a second study to ensure that the amine, and not contaminants like water, are responsible for the decomposition. A second notable exception is the observation that layered electrides degrade in tetrahydrofuran (THF), but not the related 1,3-dioxolane.[61] These results suggest that the chemistry of electrenes differs subtly from solvated electrons.

A additional difference in the reactivity of layered electrides is their ability to uptake hydrogen. Ca_2N begins to absorb hydrogen at 150 °C.[76] Hydrogen intercalates into the interlayer gap forming a hydride and slightly distorting the ionic lattice. At higher temperatures, the layered crystal reorganizes into Ca_2NH with a diamond-type structure ($Fd\bar{3}m$). Sr_2N also absorbs hydrogen, which intercalates into the interlayer gap, by at least 375 °C.[77–79] The intercalation results in only a small change to the Sr_2N lattice, and no reorganization is known at higher temperatures. Y_2C also absorbs hydrogen at 350 °C[80] and the hydrogen atoms intercalate into the interlayer gap. Though the lattice shows no expansion, the uptake of hydrogen transforms the yttrium sublattice and shifts the planes of Y_2C relative to each other. Interestingly, Kitano et al. reported that partially hydrogenated dicalcium nitride hydride, $[Ca_2N]^+H^-_x \cdot e^-_{x-1}$, offers a lower work function than either Ca_2N or the saturated Ca_2NH.[76] This suggests that the surfaces of the layered electrides have rich chemistries when perturbed by adsorbed species.

The experimentally synthesized layered electrides (Ca_2N, Sr_2N, Ba_2N, and Y_2C) are stable in argon and nitrogen atmospheres at room temperature. At higher temperatures (>260 °C), the layered nitrides can react with nitrogen gas.[81] For example, Ca_2N can react with N_2 to form Ca_3N_2 and Sr_2N can uptake N_2 as an intercalation compound to form Sr_4N_3, SrN, or SrN_2.[82]

1.1.6 Applications of electrides

Layered electrides and electrenes are already finding applications that leverage their unique properties. Among those that have been proposed are applications in synthesis, catalysis, and electronics. Use in these applications is not without challenges. The chemical reactivity of these materials requires innovations in storage and encapsulation techniques to prevent their decomposition in air.

1.1.6.1 Chemical synthesis and catalysis

Electrides show good catalytic activity for the synthesis of ammonia from N_2 and H_2 when paired with nanoparticles of iron or ruthenium.[76,83–85] This pairing helps in two ways: 1) charge transfer from the electride reduces the barrier for dissociation of N_2 on the surface of the nanoparticles, and 2) the electride suppresses the deactivation of iron or ruthenium surfaces when exposed to H_2 gas. The mechanism involves reversible storage of H^- in the interstitial space of the electride, decreasing the concentration of hydrogen on the nanoparticle surface. Unlike traditional catalysts, the rate-determining step in these catalytic reactions is

not the breaking of N≡N bonds, which has been the bottleneck for decades, but the association of N and H atoms on the surface of the Ru nanoparticle.[84]

Layered electrides can also serve as reducing agents. For example, Kim *et al*. demonstrated good activity for bulk Ca_2N for the pinacol coupling of *p*-chlorobenzaldehyde to form 1,2-*vic*-diols with up to a >99% yield.[74] Moreover, these reductions can occur at room temperature in an organic solvent. A key component to facilitate the electron transfer is the presence of a proton source, like methanol. In an organic solvent alone, such as THF, no intended products form. Layered electrides have also served as reducing agents for hydrogenation of alkynes and alkenes as well as hydrodehalogenation of organic halides.[74,75]

1.1.6.2 Solid-state dopants

Because of their low work functions, layered electrides can act as solid-state dopants. When two solid-state materials come into contact, charge transfers to equilibrate the chemical potentials. For example, by mixing layered electrides and carbon nanotubes, the electrides dope the nanotubes n-type, increasing the carrier density by an order of magnitude.[86]

Layered electrides can donate electrons to van der Waals semiconductors as well. A mechanically exfoliated sample of bulk Ca_2N can dope a thick flake of $MoTe_2$ to such a high degree (at least 2.2×10^{21} e^- cm^{-3}) that the $MoTe_2$ undergoes a phase transition.[87] Moreover, the depth of doping and long-range lattice symmetry change (∼100 nm) far exceeds the expected screening length (∼1 nm) of traditional metal-semiconductor junctions. As such, layered electrides appear to be unique solid-state dopants that may allow degenerate doping beyond conventional Debye lengths.

1.1.6.3 Batteries

Employing layered electrides in batteries capitalizes on both the layered morphology and high energy-density of the anionic electrons. First-principle calculations predict storage capacities of monolayer Ca_2N and Y_2C for Na ions as 1138 and 564 mA h g^{-1}, respectively.[88,89] The adsorption of Na and K atoms to the electride surface is spontaneous when compared to other metals. The 2D electron gas is retained until the surface becomes saturated with Na. Experimentally, a Ca_2N Na-ion battery claimed good initial discharge capacity (1110 mA h g^{-1}) but relatively poor reversible discharge capacity (320 mA h g^{-1}). Similar discharge capacities were seen for $Ca(OH)_2$, suggesting that these capacities may not be solely due to the electride.

Because of the high energy density and layered morphology, layered electrides merit further investigation as battery materials.

1.1.6.4 Transparent conductors

Electrides may have application as transparent conducting materials. Because the conduction electrons are outside of the plane of atoms, there is minimal nuclear scattering. This affords a high electrical mobility (520 cm^2 V^{-1} s^{-1}), long mean free path lengths (120 nm), and long scattering times (0.6 ps).[26] Many electrides possess high carrier concentrations as well. Combined with the high electrical mobility, these carrier densities afford electrical conductivity comparable to aluminum.

A distinguishing feature of the layered electrides is their remarkable transparency. The maximum attenuation coefficient in the visible spectrum for exfoliated Ca_2N was measured to be 10^5 cm^{-1}.[61] With this attenuation coefficient, a 10-nm thick film transmits 97% of light at visible wavelengths, while also having a theoretical maximum sheet resistance of just 4 Ω/□.[61]

1.2 Overview of the research described in this thesis

In this thesis, I detail efforts to use electride's unique electrons to accomplish new chemistries. My efforts involved finding ways to interact with the electrons—by exposing the electrons to the surface of 2D materials, by studying the interactions of surface-exposed electrons with 2D materials, and by intercalating ions into electrides. This has resulted in the development of exciting, new concepts, those of donor-acceptor heterostructures and electrochemical electron-anion exchange.

1.2.1 Electrenes

The unique properties of 2D materials motivate the exploration of layered solids and their 2D forms. In monolayer graphene, the emergence of a Dirac cone at the Fermi level drives research that exploits its high electrical mobility.[90–93] In some of the layered metal dichalcogenides, such as MoS_2, the transition from an indirect semiconductor in bulk to a direct semiconductor as a monolayer inspires investigation into their optoelectronic properties.[94–96] Many other materials are under study. Among these is the exceptional class of the layered electrides.

DFT calculations predict that a single layer of Ca_2N—just three atoms thick—can exist and, astonishingly, still has an electron gas on both sides of the layer. We call this 2D form of an electride, an "electrene". We realized that electrenes, with their exceptional ratio of surface area to volume and access to the anionic electrons, could offer advantages over bulk crystals. In all of the applications for which electrides are proposed—as catalysts, as reducing agents, as solid-state dopants, as electrodes in batteries, and as transparent conductors—the high surface area of electrenes gives them a distinct advantage.

1.2.1.1 The synthesis of electrenes

We sought to synthesize electrenes experimentally. Drawing on research ideas from the community exploring 2D materials, we recognized that we could exfoliate layered electrides because of their relatively weak interlayer binding. We chose the liquid-exfoliation methodology in which, a layered crystal is immersed in a compatible solvent and ultrasonic frequencies break the crystal preferentially along in the direction of the 2D planes. This method has yielded ultrathin graphene,[97] black phosphorus,[98] and other 2D materials[99,100] and produces scalable quantities of 2D materials.[99]

In chapter 3, I describe how I used this methodology to experimentally demonstrate electrenes. By thinning the crystal down to nanometer-thick flakes, we can interact—electronically, optically, magnetically, and chemically—with the 2D electron gas in ways that were not possible with bulk materials. In this way, electrenes bridge the gap between bulk electride crystals, in which most electrons are buried deep within the crystal, and solvated electrons, in which every electron is accessible. We expect that electrenes will serve as a testing ground for developing physical theories and will find use in a host of applications from chemical synthesis to electronics.

1.2.1.2 Donor–acceptor heterostructures

In 2013, Geim and Grigorieva[101] articulated a vision of designed solids made of stacked 2D materials, called heterostructures. In these heterostructures the layers are encoded one-by-one to enable atomic-scale control over physical properties. This vision transformed the field of 2D materials. It led to beautiful articles describing the use of heterostructures—to observe picosecond photoresponses,[102] to build atomically thin light-emitting diodes,[103] and the ability to control magnetoresistance electronically[104,105]—to name a few of the seminal works in this subject. While the field has examined the sequence and orientation of stacks of 2D materials in heterostructures, little attention has been given to the interlayer distance. And yet, we

know from many theoretical approaches, such as Pauling's bond orders and resonance,[106] Mulliken's overlap populations,[107] or Hückel and Hoffmann's linear combination of atomic orbitals[108,109] that nearly every material property, from color to conductivity to chemical reactivity, is influenced by the distance between atoms.

In chapter 4, my coworkers and I explore the creation of donor–acceptor heterostructures that, for the first time, offer a route to control the interlayer spacing and distance between atoms in stacks of 2D materials. We reasoned that the transfer of electrons from a 2D donor to a 2D acceptor could form strong bond-like interactions between layers and modulate the distance. Using the electrenes and their surface-bound electrons as 2D donors, we form donor–acceptor heterostructures with interlayer distances 1 Å less than van der Waals heterostructures and demonstrate several useful properties, including superlubricity, ultralow work functions, and greatly improved voltages for lithium-ion batteries

1.2.2 Electride-halide analogs and electron-anion exchange

As mentioned in section 1.1.2, the extreme similarity in the structure of sub-pnictogenide electrides to sub-pnictogenide halides (*e.g.* Ca_2N to Ca_2NCl) attracts interesting comparisons between the crystals.[49,51–53] For example, the host sub-nitride lattice barely changes upon incorporation of Cl^-.[51]

Many electrides have analogous halides. For example, Ca_2N is isostructural to Ca_2NX (X=Cl,Br); Sr_2N is isostructural to Sr_2NX (X=Cl,Br,I); and Ba_2N is isostructural to Ba_2NX (X=Cl,Br,I). The same is true of the layered rare earth metal carbides. Gd_2C is isostructural to Gd_2CX_2 (X=Cl,Br); Ho_2C is isostructural Gd_2CX_2 (X=Cl,Br,I). Even the electrides with different bonding motifs have isostructural halides or oxides. For example, $[Ca_{24}Al_{28}O_{64}]^{4+}(4e^-)$(ref 18) is isostructural to $[Ca_{24}Al_{28}O_{64}]^{4+}(2O^{2-})$. $[La_8Sr_2(SiO_4)_6]^{4+}(4e^-)$(ref 110) is isostructural $[La_8Sr_2(SiO_4)_6]^{4+}(2O^{2-})$.

From these comparisons, we developed a powerful new concept, electron-anion exchange, which I believe has the potential to shift some of the paradigms of electrochemistry, energy science, and electronics, and suggests a new use for electride's electrons as a means of storing chemical energy.

1.2.2.1 Electrochemical electron-anion exchange

The concept of electron-anion exchange is that we insert an anion into an electride lattice and remove the electron via an electrical circuit, reversibly, and at room-temperature, as shown in equation 1.1. Drawing

from the literature on battery technology, we recognize that this may be accomplished electrochemically by using the lattice as an electrode.

$$[\mathrm{Y_2C}]^{2+}\cdot 2e^- + 2\mathrm{F}^-_{\text{(electrolyte)}} \rightleftharpoons [\mathrm{Y_2C}]^{2+}\cdot 2\mathrm{F}^- + 2e^-_{\text{(circuit)}} \tag{1.1}$$

This exchange allows for the dense storage of electrochemical potential energy. Because of the strong electron affinity by the fluoride atom, the electrochemical potential of the valence electrons in the electride and fluoride are very different. This means that we can store energy at a high electrochemical potential (electride), use that energy (driven by intercalation of fluoride), and repeat the process reversibly. Technologically, this process offers a superior storage of energy per volume and comparable energy per mass to the best known lithium ion batteries.

A fascinating aspect of the proposed electrode/electrolyte system is the intercalation mechanism. In general, when an anion (cation) enters an electrode, the requirement of charge neutrality means that an electron must leave (enter) the electrode. In every electrode yet reported, the loss (gain) of electrons occurs through an oxidation (reduction) of atoms within the electrode. For example, when Li^+ enters graphite, carbon atoms are reduced. But in the electrodes that we study, a fundamentally new mechanism is at play: the insertion of an anion is not accompanied by a redox process. This arises because the electrodes are electrides, which have lattice sites that contain just an electron. An example is $\mathrm{Y_2C}$, formally written as $[\mathrm{Y_2C}]^{2+}\cdot 2\mathrm{e}^-$ (1.1). If an anion such as F^- inserts into $\mathrm{Y_2C}$, F^- simply replaces e^-, occupying the same lattice site. Because F^- replaces an electron, the host lattice, $[\mathrm{Y_2C}]^{2+}$, is not oxidized. To my knowledge, a mechanism of ion-insertion without redox chemistry has never been explored. In chapter 5, I provide theoretical and experimental evidence for this new process, we call "electrochemical electron-anion exchange".

1.2.2.2 Discovery of $\mathbf{Y_2CF_2}$

An outstanding challenge in the field of solid-state chemistry is the identification of new phases, especially those which possess a desired property. The exciting properties of electrides have motivated considerable efforts to identify phases with properties such as improved chemical stability.[111–113]

In the search for layered electrides, high-throughput computational screening has successfully predicted the existence of several electrides, for example $\mathrm{Y_2C}$,[68] which later led to the experimental observation

of Y_2C as an electride.[48] Researchers explored high-throughput screening of binary[114–117] and ternary compounds[118,119] and predicted new stable electride phases.

With the advancements in computational abilities, researchers have also begun re-examining known compositions to reclassify them as electrides. Zhang et al. suggested that some metal monohalides (*e.g.* LaCl[120], YCl[121]) may be layered electrides. In a beautiful work, Hautier and coworkers performed a systematic search of the Inorganic Crystal Database (ICSD) using high-throughput screening to identify crystals that were known but not identified as electrides.[122] They intentified 65 new candidates.

Of these efforts to identify new phases, a few researchers recognized and incorporated the similarity in structure between halides and electrides into their studies. Ming et al. explored the hypothetical electrides CaF, SrF, and BaF by taking the structures from the related halides (CaFCl, SrFCl, and BaFCl).[49] Zhu et al. supported their classification for $[Yb_5Sb_3]^+ \cdot e^-$ as an electride in part by synthesizing the isostructural Yb_5Sb_3F and comparing the lattices.

Building both on our concept of electron-anion exchange and the methods developed to discover new phases, we were driven to identify the halide analogs of known electrides, especially those that had a modest band gap and fast diffusion of fluoride ions. Using the structure of the electride, Y_2C, we predicted and then synthesized a stable Y_2CF_2 compound. Independently, we used high-throughput computational screening to predict the correct crystal structure, suggesting that similar methods can be used to explore the phase diagrams of metal carbide halides, as they have been for electrides. The synthesis and properties of Y_2CF_2 are described in chapter 4.

CHAPTER 2–METHODS FOR PREPARATION AND CHARACTERIZATION OF ELECTRIDES

"The scientist is not a person who gives the right answers, he's one who asks the right questions."

- Claude Lévi-Strauss, *Mythologiques*

2.1 Introduction

Over the last five years, I have developed expertise in the synthesis of electrides and related phases, their characterization by powder X-ray diffraction, and studying their properties using Density Functional Theory (DFT). In this chapter, I present experimental and computational details that do not appear elsewhere in my dissertation. This includes techniques for the synthesis of electrides and related compounds (section 2.2), for understanding the crystal structure via powder X-ray diffraction (section 2.3), and for specific calculations using DFT to study the stability and physical properties of electrides (section 2.4).

2.2 Synthesis of electrides and related phases

For many of the reactions described in this work, the basic synthetic method consists of a high-temperature (>800 °C) solid-state reaction of powdered precursors in an inert atmosphere. Because the temperatures used are below the melting temperatures of the reagents and products, the reactions rely on the diffusion of atoms through solids. Generally, the rate of that diffusion is slow, necessitating long reaction times (days-weeks) to react completely.[123] To assist in driving the reactions to completion, the reagents should have intimate and high-surface area contact, which is accomplished by 1) using powdered reagents with high surface areas, 2) thoroughly mixing the reagents together, and 3) using high pressures to form dense pellets of the mixed powders. These reactions yield powders made up of small, polycrystalline particulates with a range of crystal domain sizes. For a given reaction, depending on the temperature, time, and melting points of the reagents and products, the average crystal size may range from 50 nm to 10 μm. Because of the high temperatures

used, this method is useful for synthesizing thermodynamically stable phases. For a given synthetic target, it is essential to understand the Hull diagram for the entire relevant phase space, which will inform about competing phases and possible off-stoichiometry compounds.

2.2.1 Preparation of reagents

Careful sample preparation for these reactions is key to the success of the synthesis. We purchased the starting reagents in pure ($>$99.9% when available), anhydrous forms and store the reagents in a glovebox (oxygen $<$ 0.01 ppm). Because many of the starting reagents, particularly reducing metals, metal nitrides, and metal halides, oxidize in air or form hydrates in the presence of water, it is necessary to manipulate them in a glovebox to avoid oxidation. As I have learned, it is necessary to check the purity of the reagents when they are purchased; even reputable vendors do not always provide chemicals with the purity that they advertise. For example, we received yttrium metal with significant quantities of yttrium hydride present and yttrium fluoride that was actually a mixture of Y_2O_3 and gagarinite ($YNaCaF_6$). I found that collecting a quick low-quality X-ray diffraction pattern suffices to reveal crystalline impurities.

To accurately prepare the reagents in the desired molar ratio, I weighed all solids by difference using an analytical balance. Because static electricity can limit the accuracy of a balance in a glovebox, I used either an Andwin Zerostat Anti-static gun or Mettler Toledo's Anti-Static U Ionizer to discharge powders before weighing them to improve the accuracy of the measurement. To mix the reagents, I ground the powders together by hand using an agate mortar and pestle for at least five minutes. Recently, I mixed reagents using a Spex 8000M ball mill located inside of a glovebox (oxygen $<$ 0.01 ppm) with stainless steel jars and balls. Milling for several minutes to tens of minutes generally yields mixtures that afford homogenous products after the reaction. The grinding and milling have a second benefit; the processes reduce the particle size and increase the surface area of the reagents.

Then to bring the powders into intimate contact, I pressed the powders into pellets using steel pellet dies and a Carver model C 12-ton hydraulic press, applying 80,000 psi of pressure. Depending on the desired quantity of product, I used either a 13-mm die producing pellets approximately 0.75 cm^3 in volume or a 6-mm die producing pellets approximately 0.15 cm^3 in volume. To form pellets under an Ar atmosphere, I loaded the die with reagents in a glovebox, held the plunger and base-plate in place with tape, and, sealed the assembled die in 6-mil polyethylene tubing, using a Uline heat impulse sealer. Then I removed the plastic

from the glovebox, pressed the reagents into pellets while in the plastic, and pumped the pellets back into the glovebox.

2.2.2 Ampoules, containers, and crucibles for high-temperature reactions

In order to run a reaction, the pellet needs to be placed in a container. For many of my reactions, I sealed the pellet in quartz ampoules because quartz affords high mechanical strength at temperatures as high as 1240 °C. In addition, because of its low thermal expansion coefficient, quartz is easy to heat to high temperatures and cool rapidly without breaking. We purchased fused quartz tubing from Technical Glass, primarily in three sizes: an 8 mm/12 mm inner/diameter (ID/OD), a 9 mm/15 mm, and an 18 mm/20 mm.

To weld quartz ampoules, I used an oxy-hydrogen welding torch, which produces the very high temperatures ($\sim$ 2000 °C) needed to melt quartz. In brief, the torch has two inputs, one connected to a hydrogen gas cylinder (regulated to 14 psi) and one to an oxygen gas cylinder (regulated to 25 psi). The actual flow rate of gas was adjusted manually using valve knobs on the torch. To operate the torch, I first opened the hydrogen line and ignited the flame using a long gas lighter. Then I opened the oxygen line, which produced a clear flame with an inner blue cone. For welding thick (2-3 mm wall thickness) quartz, I set a flow of hydrogen and oxygen to produce a 1 cm blue cone. For thinner (1 mm) quartz, I set the flow to produce a 0.5 cm blue cone. To maximize heat, the ideal ratio of hydrogen to oxygen is 2:1 in accordance with the stoichiometric reaction of hydrogen and oxygen to form water; however control over the ratio is limited and can only roughly be judged by the brightness of the flame and by how much black body radiation the quartz gives off when heated. I found that adjusting the flow rate to achieve the optimal temperature saves time instead of working with a sub-optimal flame. When working with thin-walled quartz, it is imperative to taper welds and work with lower temperatures to avoid forming holes in the tube. If the reaction does reach high pressures, it is possible to adopt an alternative strategy to seal the tube as described below.

To prepare a quartz ampoule, I welded a clean quartz tube closed in a circular fashion, leaving at least 20 cm of tube on each end of the weld. I cut excess lengths of quartz tubing using a Griffin-type glass tube cutter. Then I baked the tube to degas any adsorbed water, brought the tube, now sealed at one end, into the glovebox, and loaded it with the reagents. When loading powders into a tube, I took precautions to avoid coating the walls in powder, which creates challenges later when attempting to seal the ampoule as the powders vaporize and interrupt the quartz-quartz seal and may affect the chemistry inside the ampoule. To avoid coating the walls in powder, I used a clean glass cylinder, for example the large end of a glass pipette, to transfer powder.

First, I filled the cylinder, then slid the ampoule over it and inverted both the cylinder and ampoule together, depositing the reagents at the bottom of the tube. In this way, I loaded the powders into the tube without the powders contacting the walls.

Then, to bring the tube out of the glovebox to the torch without exposing the reagents to oxygen, I attached the quartz to a short piece of gum-rubber tubing with an inner diameter equal to the outer diameter of the quartz and fastened the tube with a hose clamp. To the other end of the rubber, I inserted a hose-barb-to-vacuum-flange adapter secured with a second hose clamp. Finally, to the adapter I attached an Edwards SP speedivalve using a vacuum flange clamp and closed the diaphragm of the speedivalve. I refer to this complete setup as the "speedivalve assembly". Then I removed the assembly from the glovebox and attached it to a dedicated vacuum line without exposing the reagents to oxygen or moisture. The vacuum line consists of a 4-way cross connected via vacuum flanges and flexible bellows hoses to 1) an Edwards RV3 oil sealed rotary vane pump, 2) an active pirani pressure gauge, 3) a valve-controlled line of high-purity argon from a gas cylinder, and 4) a needle valve that connects to the speedivalve assembly, which is oriented vertically. The needle valve is necessary when working with fine powders to prevent bumping and blowing the powder throughout the tube.

By manually controlling the valves and by back-filling with argon, I could seal ampoules at a range of pressures from 10^{-3} to 10^{2} mbar. I sealed the ampoule at the desired pressure by slowly welding the quartz tube shut, leaving about 8 cm between the weld and the rubber and 8 cm between the weld and the sample. Leaving too short of a distance results in burning the rubber or heating the reagents.

To seal quartz with a thinner wall-thickness and large diameter, I used a different technique. With thin-walled quartz, it is easy to pop a hole in the quartz when the tube is already under vacuum, even with a lower temperature flame. Therefore, rather than try to seal the quartz directly, I welded the quartz to a second tube, which is already shut at one end. For example, to seal a 18 mm/20 mm ID/OD tube, I first sealed the one end of the tube, carefully tapering the weld to avoid popping a hole, leaving a length of 20 cm. Then, I sealed a second tube, a 9 mm/15 mm ID/OD tube. To get this second tube to stay in place while sealing the system, I introduced a small angle ($\sim 10^{\circ}$) into the tube by heating about 10 cm from the sealed end. Then I pump both into the glovebox, load the larger tube as usual, and slide the smaller angled tube inside, before attaching the rest of the Speedivalve assembly. Because of the angle, the smaller tube props conveniently against the larger tube, allowing me to remove the assembly and weld the two tubes together while they are oriented vertically and under vacuum.

2.2.2.1 Molybdenum and tantalum as crucibles and ampoules

In many of the reactions, at least one of the reagents is known to attack quartz at high temperature, which can break the ampoule or liberate oxygen from the silica surface. Therefore, to physically separate the reagents from the quartz, I used thin foils (0.025 mm) of inert metals like tantalum or molybdenum ($> 99.9\%$ purity), which I crimped into pockets, as crucibles to hold the reagents. I then sealed these metal pockets inside of the quartz ampoules as described above. This process worked well for reagents that have a low vapor pressure at the maximum temperature of the reaction and for reagents that do not attack quartz.

John Corbett once wrote about the exploratory synthesis of metal halides that "the availability of tantalum containers has more than any other single factor made the present sort of research possible."[124] It is worth a few more words describing why tantalum and to a lesser extent molybdenum are ideal choices for our reactions and why these metals have become a staple in solid-state chemical synthesis. (citations) Active transition metals (Sc, Y, Zr, etc.), rare earth metals (Gd, La, etc.), alkaline earth metals (Mg, Ca, Sr, etc.), alkali metals (Li, Na, and K at elevated temperatures) and some metal halides (YCl_3, GdI_3, NaF, etc.) in the vapor phase react with glass and ceramic containers to form very stable oxidies, silicides, carbides, or nitrides. In my experience, even a small addition (5 mg) of NaF to a quartz ampoule can result in its failure. In contrast, refractory metals like Ta, which can sustain high temperatures exceeding 1500 K without losing mechanical integrity, and, which do not react with reducing metals or metal halides, are ideal candidates. Tantalum is inert to these metal halides because it has a lower ΔH_{form} per equivalent for its halides than other metals. Similarly, it is inert to carbon and nitrogen in our reactions, which is likely due to the greater thermodynamic stability of yttrium (Sc, Gd, etc.) carbides than tantalum carbide.[125] A second advantage of tantalum is that because of its high melting point (2996 °C),[126] eutectic points with other metals lie at very high temperatures. Furthermore, because of its melting point, the mobility of impurities, particularly other metals, is low.[127] Therefore, Ta contributes few impurities and does not alter the stoichiometry of the reaction. A third advantage is that Ta is relatively easy to machine and can be purchased as a tube in high purity. The Ta tubes can be sealed by arc welding in argon and used as the ampoule for a reaction. This is especially useful for running reactions that employ reactive metals (Ca, Sr, Mg, Li, etc.) and metal halides (YCl_3, GdI_3, NaF, etc.), which have a high vapor pressure at the reaction temperatures.

We purchased Ta tubing with a 1 cm diameter at 99.95% purity and cut the tubing to 5 cm lengths. The University of North Carolina's Physics and Astronomy instrument shop fashioned caps, also made out of Ta,

using a die and press. The process of sealing a tantalum ampoule is similar in principle to that of quartz: I loaded the reagents into the Ta tube in the glovebox, hammered in the cap forming an air-tight seal, and then welded the cap shut by arc welding in an argon atmosphere. To protect the Ta from reaction with oxygen at the high temperatures of the reaction, I then sealed the Ta ampoules in quartz jackets under 1 mbar of Ar.

Welding the Ta ampoule shut requires some skill and practice. The arc melting system consists of an arc furnace, a direct current (DC) Miller Goldstar 452 welding power supply, and a set of recirculated ethylene glycol-cooled power cables to bring power and coolant to the furnace. The furnace, a 5SA single arc furnace from Centorr Vacuum Industries, has two sections: an upper and lower section separated by a Pyrex window, which insulates the two sections. Power cables feed power and coolant to each section. In the top section, a brass stinger rod houses a lanthanated tungsten electrode, which serves as the cathode (negative). The rod is mounted into a Teflon swivel ball, which is sealed to the upper section by Viton O-rings and vacuum grease and is clamped into place. The bottom section, the anode (positive), is a solid brass block with two ports—one connected to Gast rotary vane vacuum pump (maximum vacuum $\sim 1.5 \times 10^2$ mbar) and a second connected to a high-purity argon gas cylinder—and a tapered opening, which holds a copper hearth. The type of hearth is interchangeable. For welding Ta ampoules, we designed a custom hearth that consists of a thick pipe clamp, made of copper and held together by threaded stainless steel screws. The clamp serves three purposes: 1) it holds the Ta ampoule vertically during the welding process, 2) it serves as the anode and makes electrical contact to the instrument, and 3) because it makes good thermal contact with the actively cooled instrument, it provides a sink for the massive amounts of heat generated.

Because the wall-thickness of the Ta tubing and the thickness of the caps in our setup is only 0.5 mm, the Ta can quickly melt and form a hole. I welded using minimal amperage (between 10-25 amps) with the arc-force—a tool that helps maintain a more constant amperage as the height of the electrode changes—set to 40%. Even under these low amperage conditions, the welding is best done by welding one side of the ampoule at a time. Because of the active cooling and design of the hearth and clamp, the reagents resting at the bottom of the Ta ampoule do not experience the full temperature of the welding process. In fact, the temperature is likely less than a few hundred degrees. For example, I have successfully welded Li metal, which vaporizes at temperatures as low as 500 °C, into Ta tubes without issue. Others have modeled the heat transfer during the welding process for a similarly designed hearth and found that the reagents reach a temperature from 32-200 °C.[128]

2.2.3 Furnaces and rates of heating

I performed the reactions inside of Lindberg Blue M tube furnaces. For reactions under 1100 °C, I used either a Mini-mite single-zone furnace or a 3-zone furnace with a quartz tube and alumina-silicate refractory ceramic fiber to insulate the furnace. For reactions over 1100 °C, I used a higher temperature tube furnace with silicon carbide heating elements and an alumina tube capped with steel flanges. In the higher temperature reactions, I passed a slow ($\sim$ 0.5 cc/min) stream of argon through the tube. This furnace is not located in a fume hood and the stream of argon served to direct vapors into a fume hood in the event of a failure.

For all reactions in the Mini-mite single-zone and 3-zone furnaces, I ramped the temperature up at 4 °C per minute and held the maximum temperature for 3-5 days. For reactions using the 1500 °C furnace, I ramped up at 10 °C/min because the faster ramp rates actually extend the lifetime of the silicon carbide heating elements. In all syntheses, I cooled the products slowly ($\sim$20 °C/hr) to minimize thermal stresses and favor crystal growth over nucleation. After the reactions, I brought the quartz tubes into the glovebox and cut open the ampoules to retrieve the products.

2.2.4 Synthesis of bulk Ca_2N

I synthesized 3D Ca_2N by the reduction of Ca_3N_2 (Alfa Aesar, 99%) with Ca metal (Alfa Aesar, redistilled granules $\sim$ 16 mesh, 99.5%) as adapted from previous literature.(citations) I ground the Ca_3N_2 into a very fine powder and added Ca granules. The mixture was ground lightly together in a 1.02:1 Ca:Ca_3N_2 molar ratio (total mass of a typical batch: 1.2 g) and pressed into a pellet under $\sim$0.56 GPa of pressure using a hydraulic press. The pellet, along with an additional $\sim$0.600 g of Ca metal, was placed into a pocket of Mo foil (Alfa Aesar 99.95%), which was subsequently crimped closed. I then sealed the Mo pocket inside an evacuated (4×10^{-3} mbar) quartz ampoule (18 mm ID, $\sim$6-7 cm in length). The ampoule was heated in a tube furnace to 1100 K at a ramp rate of 100K/hr. The temperature was held at 1100 K for 2 days and cooled to room temperature over 24 hours. The additional calcium metal that was added inside of the Mo pocket reacted with the quartz ampoule covering the ampoule wall in shiny black/grey material. We found that adding Ca helped prevent the loss of Ca from the pellet. Importantly, the addtional Ca metal does not scale with the quantity of the reaction but with the size of the ampoule. This Ca does attack the quartz at elevated temperature but did not cause the ampoule to fail. The obtained Ca_2N pellet was black. Occasionally, the

pellet was coated in a yellow-orange powder, which could easily be separated by filing off the outer surface. When broken apart, the material was black and shiny with a blue luster.

2.2.5 Synthesis of Y_2CF_2

Y_2CF_2 was synthesized by the solid state reaction of YF_3 (Sigma Aldrich, granules, 0.09% oxygen, <0.02% Cd, Co, Cr, Fe, Hg, Mn, Pb each) with Y metal (Alfa Aesar, ∼40 mesh powder, 99.6% (REO)) and graphite (Sigma Aldrich, ∼100 mesh flakes, 99.9%). The reagents were ground into a very fine powder in a stoichiometric ratio (total mass of a typical batch: 0.5-1.0 g) and pressed into a pellet under ∼0.56 GPa of pressure using a hydraulic press. The pellet was placed into an ampoule made of tantalum (Ta) metal welded closed at one side. A cap, also made of Ta, was hammered into the ampoule and sealed in argon by welding the cap and ampoule together with an electric arc. The Ta tubing, 99.95% Ta seamless tubing, was purchased from Eagle Alloys in a 1 cm diameter and cut to 5 cm lengths. The caps, made of the same Ta, were made by the University of North Carolinas Physics and Astronomy instrument shop. The tubes and caps were cleaned by sonicating in hexanes, isopropyl alcohol (IPA), and acetone. After welding the reagents inside a Ta ampoule, the Ta ampoule was sealed in a fused quartz ampoule under 1 mbar Ar. Then the ampoule was placed in a Lindberg Blue M tube furnace to 1513 K at a ramp rate of 10 K/min. The temperature was held at 1513 K for 3 days, then cooled to 1273 K over 10 hrs, then cooled to 1073 K over 5 hrs, and to room temperature over 5 hours. The ampoule was then brought into the glovebox and opened with a pipe cutter. The pellet remained intact through the reaction. On the pellets surface grew vibrant green crystals and when broken apart revealed homogenous green crystals throughout.

In an attempt to lower the amount of oxygen in the sample, which typically was around 1% by mol as determined the presence of α-YOF by X-ray diffraction, we explored an alternative synthesis. We found that Y_2CF_2 was synthesized by the solid-state reaction of Y_2C (prepared in house as described below), graphite (Sigma Aldrich, ∼100 mesh flakes, 99.9%), and YF_3 (Sigma Aldrich, granules, 0.09% oxygen, <0.02% Cd, Co, Cr, Fe, Hg, Mn, Pb each). Similarly, this reaction yielded bright green crystals and still had around 1% oxygen by mol.

2.2.6 Arc-melting as a synthetic scheme

Arc melting is used to melt metals, primarily in the production of steel, and in a lab-setting in the synthesis of alloys and metallic compounds. The basic principle of operation is to use an electric arc to

generate heat, often in excess of 2000 °C. In this dissertation, I describe our arc-melting setup and its use to synthesize yttrium carbides. As mentioned previously, the arc melting system consists of an arc furnace, a welding power supply, and recirculated cooled power cables to bring power and coolant to the furnace. Unlike the welding setup, for arc melting, the hearth is a copper bowl, which holds the material that will be melted and which serves as the anode during operation.

Preparation of the reagents is again key to the success of the reaction. In my experience, dendritic forms of metals offer far superior products than metal powders, even when those powders are pressed into pellets or remelted in slugs. Essentially, powdered metals, especially active metals like Y and Sc, contain a considerable fraction of oxygen. Yttrium for example has a very strong affinity for oxygen and dissolves oxygen in large concentrations.[129] While the oxygen concentration is not measured or included in the advertised purity of yttrium powders, it can be on the order of 1% by mol.[130] This point, that powdered metals contain oxygen, cannot be emphasized enough. I observed that this small fraction of oxygen lead to the synthesis of different phases than when I used dendritic, pure metals.

The preparation of carbon is also important. I attempted using different forms of carbon, such as glassy carbon beads and powdered graphite, and found that the most facile form is graphite flakes (Sigma Aldrich, $\sim$100 mesh flakes, 99.9%), which I pressed into pellets under $\sim$0.56 GPa of pressure using a hydraulic press. Glassy carbon beads and powdered graphite had a strong tendency to move inside the arc melter in response to the flow of argon gas and moved violently in response to the heat of the arc melter, presumably by asymmetric thermal expansion. The yttrium and graphite were both stored in a glovebox (oxygen $<$ 0.01 ppm).

To begin melting, the chamber was brought under vacuum (500 mbar) and back-filled with argon (25 psi). This was repeated this seven times to exchange the atmosphere for argon. During melting, the atmosphere remained a positive pressure of argon (2 psi). To strike the arc, I initiated the current through a foot-controlled pedal, brought the tungsten electrode into contact with the hearth and away from the sample, and drew apart the electrodes quickly to a small distance (3 mm-1 cm) initiating an electric arc. The arc can be maintained only at a small distance. I found that increasing the arc force to 40% improved the stability of the arc while moving the stinger. To melt yttrium, I applied 100-150 amps. In my experience, the most consistent route to synthesize metal carbides involves first melting the metal around the carbon. The key distinction is that the carbon itself is not melted or put under the electric arc. In the event that carbon does come under the arc, it is more likely to ablate than melts. Therefore, the best route is to melt the metal around the carbon so that

the metal engulfs the entire pellet of carbon. Then, by melting the metal surrounding the carbon, the carbon dissolves into the molten metal.

To synthesize layered Y_2C (trigonal phase, space group No. 166, $R\bar{3}m$), I used dendritic yttrium (Sigma Aldrich, 99.9% trace rare earth metals basis) and graphite flakes pressed into a pellet in a slightly sub-stoichiometric ratio. In my syntheses, the ratio of Y:C was always 2.00:0.93 owing to the wide phase width of layered Y_2C_x centered at a slightly carbon-deficient composition.[131,132] I melted the reagents as described above in 2-minute increments to ensure that the arc-melter did not overheat. Each time the pellet cooled, I flipped the pellet using the stinger. For each synthesis, I remelted the pellet 15-20 times to ensure homogenous distribution of carbon. Through the course of the synthesis, the color changes from the dull silver of yttrium to the deeper grey color of Y_2C. After the reaction finished and the sample cooled to room temperature, I brought the pellet out of the arc melter and into the glovebox. In this step, the sample experienced a small amount of oxygen and developed a gold-colored coating assumed to be a thin oxide layer. Inside the glovebox, I polished the sample using a silicon-carbide sanding pad, which removed the golden oxide coating, leaving a dark silvery button of Y_2C.

We found that we could reproducibly synthesize an alternate phase of Y_2C, the cubic phase (rock-salt structure, space group No. 225 $Fm\bar{3}m$) seen for other transition metal carbides like TiC and ZrC. To synthesize the cubic phase, I used powdered yttrium (Alfa Aesar, $\sim$40 mesh powder, 99.6% (REO)), pressed into pellets and arc-melted into slugs. I then melted the slugs around pellets of graphite as described above, and in the ratio of Y:C of 2.00:0.93. All other steps were identical to the synthesis of layered Y_2C. The synthesized button appeared identical by eye to that of layered Y_2C.

These synthetic procedures yields buttons of Y_2C typically 2-4 g in mass and 1-2 cm in diameter. To use this pellet, I needed to break it apart, but it is much too hard to grind in a mortar and pestle. I used a tungsten-carbide coated chisel and hammer to break the pellet into smaller ($\sim$1 mm) chunks. Then, with considerable difficulty, I ground the chunks into a powder. This afforded a powder with a distribution of particle sizes of 1-100 μm; however, for our desired chemistries, smaller particle sizes with more exposed surface area are required. Therefore, I comminuted powders using a high energy SPEX ball mill located inside of a glovebox as described in section 2.2.1. Because of the relative hardness of the sample, I used tungsten-carbide balls and jars. For our mass of Y_2C, I used a 5 mL-sized jar and loaded Y_2 at a ratio of $\sim$20-40% of the jar by volume. Milling times on the order of hours succeeded in comminuting the powder to an average particle size $<$1 μm. Owing to the small size of particles, the milling jars were wrapped with

tape to catch powder that might escape the seal of the jar during milling. Because of the much higher surface area powder, these finely milled powders of Y_2C can be pyrophoric and explosive in contact with water. Therefore, I handled them in a glovebox.

2.3 X-ray powder diffraction

X-ray powder diffraction (PXRD) is a fast, non-destructive analytical tool that can provide a wealth of information about a sample. I primarily used PXRD for phase identification of polycrystalline solids and refinement of the crystal structure, affording the lattice constants, relative concentrations of phases, and size of crystal domains. In the following sections, I will describe the theory of PXRD (section 2.3.1), the experimental conditions used to collect data (section 2.3.2), and the analysis of data (section 2.3.3).

2.3.1 Theory of diffraction

When an incident wave interacts with a periodic arrangement of objects that scatter the wave, and the wave has a wavelength similar to the length scale of the periodic arrangement, the wave diffracts, or in other words, the scattered wave interferes with itself, constructively and deconstructively. Because typical interatomic distances in crystals are on the order of angstroms and the wavelength of X-rays are also on the order of angstroms, X-rays can diffract from crystals. By collecting the diffracted light, we can observe the constructive interference and therefore probe the atomic structure of crystals.

The formulation for the theory of X-ray diffraction by a crystal was described by W.H. and W.L. Bragg and M. von Laue in the early 1900s. M. von Laue considered the crystal as a periodic arrangement of scatterers (atoms) placed at sites R of a Bravais lattice. Each atom interacts with the incident radiation and re-emits the radiation in all directions. Importantly, when the scattered radiation interferes constructively, intense peaks are observed. Therefore, by understanding the condition for constructive interference, we can relate the observed peaks in intensity to the atomic structure of the crystal.

The condition for constructive interference can be derived easily from a one-dimensional periodic array of scatterers as described in *Solid State Physics* by Ashcroft and Mermin.[133] Essentially, constructive interference occurs when the change in wave vector for the scattered wave is a vector of the reciprocal lattice (2.1).

$$K = k' - k \tag{2.1}$$

We can relate this condition back to the crystal lattice in real space. Because the scattering is elastic, k and k' share the same magnitudes and make the same angle, θ, with the plane perpendicular to K. Therefore,

$$K = 2k \sin\theta \tag{2.2}$$

From the definition of a Bravais lattice, for each reciprocal lattice vector, there is a family of lattice planes normal to K and separated by a distance d, where

$$K = \frac{2\pi n}{d} \tag{2.3}$$

By combining equations 2.2 and 2.3, we observe that d and the scattering angle θ are related.

$$k \sin\theta = \frac{\pi n}{d} \tag{2.4}$$

Because k is a wave vector and thus $k = 2\pi/\lambda$, we can arrive at Braggs Law:

$$n\lambda = 2d \sin\theta \tag{2.5}$$

Thus constructive interference occurs when the change in wave vector is a vector of the reciprocal lattice, which corresponds to an elastic reflection from the family of lattice planes perpendicular to the reciprocal lattice vector.

By using a sharp, fixed wavelength of X-ray, the angle at which we observe constructive interference is only a function of the separation between lattice planes, d,

$$d = \frac{C}{\sin\theta} \tag{2.6}$$

where C = $n\lambda/2$. Powder samples contain millions of crystallites with a distribution of orientations such that there are crystallites oriented to afford constructive interference for each family of planes. Then by scanning through a range of angles, we can collect the diffraction peaks for each set of planes. This gives the

diffraction pattern, the intensity of scattered radiation as a function of angle, which we can use to measure the spacing between lattice planes.

The intensity of peaks in a diffraction pattern also contains a wealth of information. The intensity is determined by conditions in the diffractometer and by the sample. We maintain constant conditions of the diffractometer such as the distance of the sample to the detector and wavelength of radiation, which contribute a constant term, K_e, to the observed intensity. In addition, factors of the sample, K_s, and the underlying crystal structure, K_c, also contribute to the intensity of peaks.

$$I_{hkl} = K_e K_c K s \tag{2.7}$$

The contribution from the sample, K_s, to the intensity of the observed reflection relates directly to the volume fraction of the crystalline phase giving the reflection, ν_α. This is important in patterns acquired from a mixture of multiple crystalline phases.

$$K_{s_\alpha} \propto \nu_\alpha \tag{2.8}$$

In addition, the intensity can be affected by the background, largely caused by the sample holder. This effect is discussed in section 2.3.2.2. The contribution from the crystal, K_c, is determined by four factors: 1) the multiplicity, M_{hkl}, or the number of identically spaced planes cutting a unit cell in a particular hkl family; 2) the square of the structure factor for the reflection, F_{hkl}, which is a description of the amplitude and phase of a wave diffracted from crystal lattice planes that is derived from the geometry of the lattice; 3) the volume of the unit cell, V_α; and 4) the linear attenuation coefficient of the specimen, μ_s.

$$K_c = \frac{M_{hkl} F_{hkl}^2}{V_\alpha^2 \mu_s} \tag{2.9}$$

Combining these contributions, we can understand the intensity of diffracted radiation in the idealized case; however, in real experiments other factors can contribute to peak intensities. The two most pertinent examples are the effect of a preferred orientation and the effect of the crystallite size.

In the description of the X-ray experiment, I stated that many powder samples consist of crystallites with an even distribution of orientations such that for each family of lattice planes there are crystallites oriented in which the scattering vector is perpendicular to planes. However, in samples made of anisotropic

crystals, especially layered crystals, the distribution of orientations is often not random. This is because layered crystals tend to exhibit a platy morphology and the crystals tend to align flat against the substrate. Imagine, for example, tossing a stack of papers into the air. The majority land flat on the ground. The same is true for layered crystals. Their morphology prefers a particular orientation. Consequently, in a powder X-ray diffraction experiment, the intensity of the observed diffraction pattern changes considerably if the distribution of orientations is not random. The intensity of some peaks increase and others decrease. I discuss the analysis of preferred orientation in section 2.3.3.2.

A second common effect on peak intensity is the crystallite size. Because diffraction peaks result from constructive interference of X-rays reflected by crystal planes, the conditions for constructive interference are relaxed in small crystallites where the number of reflection planes is small. Analytically, the relationship of peak width to crystallite size can be derived either by considering the structure factor of the crystal in the condition with a small crystallite[134] or by considering the superposition of waves in a multi-slit approximation.[135] The result, by either derivation, is the Scherrer equation,[136] where t, K, λ, B, and θ are the crystallite size, a constant near unity related to the crystallite shape, the peak width, and the scattering angle, respectively:

$$T = \frac{K\lambda}{B\cos\theta} \tag{2.10}$$

The Scherrer equation considers the width of an individual peak and is highly susceptible to instrumental errors, the background subtraction, broadening from strain, and preferred orientation effects. With modern software, it is possible to handle the peak widths for the whole pattern after whole pattern fitting, which gives much more accurate and reliable results. The Halder-Wagner method[137] builds off of the Scherrer equation, but seeks to isolate effects from crystallite size and strain. The method assumes that the broadening due to crystallite size is observed only in the Lorentzian component of the integral breadth, $\beta^\star$, of the reciprocal lattice point, while strain is observed only in the Gaussian component. This gives a relationship where $d^\star$ is the reciprocal lattice distance, K is a constant near unity related to the crystallite shape, D is the crystallite size, and ϵ is the microstrain.

$$\left(\frac{\beta^\star}{d^\star}\right)^2 = \frac{K\beta^\star}{D(d^\star)^2} + (2\epsilon)^2 \tag{2.11}$$

The equation can be rewritten into real space by using the relations $\beta^\star = \frac{\beta \cos\theta}{\lambda}$ and $d^\star = \frac{2\sin\theta}{\lambda}$. This equation has the form of a straight line ($y = mx + b$) where the slope, m, is related to the crystallite size, and the intercept, b is related to the microstrain.

$$\left(\frac{\beta}{\tan\theta}\right)^2 = \frac{K\lambda}{D} \cdot \frac{\beta}{\tan\theta \sin\theta} + 16\epsilon^2 \tag{2.12}$$

Therefore by plotting $y = \frac{\beta^2}{\tan\theta}$ against $x = \frac{\beta}{\tan\theta \sin\theta}$, as in the Williamson-Hall method,[138] the slope yields $\frac{K\lambda}{D}$, where λ is known and K is a constant near unity assumed to be $\sim \frac{4}{3}$, providing a reliable measure of crystallite size.

This method has several advantages. First, it relies on the integral breadth of the fit from the whole pattern and is therefore less influenced by abnormalities in single peaks. Second, the equation more equally weights data from high and low angles than other methods. Third, the method successfully separates broadening caused by crystallite size from that caused by strain.

Still, in a real experiment, the peak width is given by a convolution of a number of factors. For example, the observed peak width results from diffraction from a number of crystallites and is, in fact, a mass-averaged value that over-represents the larger crystallites. Instrumental broadening usually limits the detection of peak widths for crystals greater than 1 μm in size. In practice, the technique is accurate for smaller crystallites (10-200 nm in size). Finally, because the Halder-Wagner method uses integral breadth, the tails of peaks are more important than in the Scherrer method. Therefore, more care needs to be taken, especially at low angles, to ensure a good background subtraction and proper instrumental setup (e.g. proper length limiting slit) to avoid asymmetric peak shapes that introduce error into the measurement. Because of these limitations, it is best to couple these measurements with high-resolution transmission electron microscopy, which can directly image crystallites.

X-ray diffraction is a powerful technique, which can provide information about the crystal structure and give highly accurate lattice constants. By quantitatively measuring the intensity of peaks, we can learn a lot about the sample, including the relative concentration of phases, the orientation of grains, and the crystallite size.

2.3.2 Experimental conditions for X-ray diffraction

The experimental conditions of the diffractometer and sample affect the quality of data collected. In the first section (2.3.2.1), I describe the diffractometer. In the second section (2.3.2.2), I describe the two useful geometries of the diffractometer and I give a brief description of the components and settings that provide quality data. In the third section (2.3.3), I describe two useful methods of sample preparation for air-sensitive samples that afford quality results.

2.3.2.1 X-ray diffractometer

X-ray powder diffraction experiments were carried out using a Rigaku Smartlab diffractometer with Cu Kα radiation, λ=1.5418 Å, monochromated by a Kβ filter (a 15 μm nickel foil), and an applied voltage and current 44 kV, 40 mA, respectively. The different focusing optics will be discussed in the following section (2.3.2.2). For all experiments, the divergence of the incident beam was reduced by soller slits (5 deg) and an incident slit (2/3 deg). The instrument uses a HyPix-3000 detector, which is a 2D array of individual photon detectors, which operate in a 1D mode. In 1D mode, the divergence of the beam leading to the receiving optics was not reduced (no soller slits) and the receiving slit was left open, allowing X-rays of a small range of scattered angles to reach the detector array. The software on the instrument then integrates the signals spatially along the Debye Scherrer rings into a 1D pattern and resolves the 1D pattern into angles using the positions of the pixels. As a result, the 1D mode outputs intensity as a function of angle, like a normal point detector (0D mode) but at a faster rate.

2.3.2.2 Diffractometer geometry

The most common geometry is the Bragg-Brentano geometry in which the sample is fixed and the scattering vector is maintained normal to the sample. For our diffractometer, I use a θ/θ measurement in which the X-ray tube rotates at negative theta degrees per minute and the X-ray detector rotates at theta degrees per minute so that the incident angle is half of the 2 theta angle throughout the measurement.

Because many of our samples are air-sensitive, I prepare the samples in a glass sample holder in our glovebox and cover the holder with a thin Kapton tape (a 1 mil-thick polyimide film with a 1.5 mil-thick silicone adhesive). The tape shields the sample from air for about 24 hours because of its low permeability to oxygen and water, and it contributes only a very weak background. At angles greater than 25°, the

contribution from the tape is featureless. Alternatively, I found that Kapton film without adhesive provides even less background, but without the adhesive it is less easy to use. Other thin materials can also be used, for example, polyester, polycarbonate, and 15 μm thick aluminum foil; however, the backgrounds for each are higher than that of Kapton.

This geometry and sample preparation provides a fast method for phase identification. Unfortunately, the background from the Kapton obscures the intensity of peaks at low angles substantially, limiting the usefulness of this geometry to phase identification. For more detailed analysis of peak intensities, as in a Reitveld refinement, an alternate geometry (capillary transmission geometry) provides better quantitative data for air-sensitive samples.

The second geometry is the capillary transmission geometry. Again, in this geometry, I used a θ/θ measurement in which the X-ray tube rotates at negative θ degrees per minute and the X-ray detector rotates at θ degrees per minute so that the incident angle is half of the 2θ angle throughout the measurement. The major difference in the instrumentation is that the incident beam is focused by a multilayer mirror to a smaller beam width so that more of the X-rays impinge on the capillary. The optics on the receiving side remain the same; however, I found that operation in the 1D mode and transmission geometry with fully open receiving slits gave broad artifacts in the background at high angles ($\sim$90°). The artifacts did not appear by slightly closing the receiving slits. I kept the incident slit as 1°, the first receiving slit as 20°, and the second as 20.1°.

The largest difference in sample preparation is that the sample is loaded into a capillary tube. The capillary tubes, purchased from Hampton Research, are a borosilicate glass that has a low linear absorption coefficient and wall-thicknesses of only 10 μm. As a result the tubes provide a low, featureless background. The tubes come in a variety of diameters to accommodate samples with a range of linear absorption coefficients. In a transmission X-ray experiment, the diffracted light is scattered forward to the detector. As a result, samples that significantly attenuate the X-ray yield low counts and a poor ratio of signal to noise. Understanding this informs us that thicker tubes, which hold more sample, are not always better. For example, because heavier atoms tend to have higher absorption coefficients, samples with heavier atoms often give better data when loaded into thinner capillaries. As a rule of thumb, the product of the diameter of the capillary (cm) and the linear absorption coefficient (in cm^{-1}) should be about 1. For the same reason, phases made of lighter elements produce stronger signals in a transmission geometry than in a reflection geometry.

To load a powder into a capillary tube requires that the sample be a very fine powder; otherwise the sample will clog the tube. Loading the sample is accomplished by placing the capillary into a glass holder,

such as the fine end of a glass pipette, filling powder into the capillary head with a curved spatula, and rubbing the glass holder with a course metal grating. The grating applies vibrations to the holder that shake the capillary tube and cause the powder to fall and pack densely. Denser packing is preferred. Usually, this density is only 20-50%. For the most careful studies, it is useful to measure the packing density by measuring the mass of the powder loaded into the capillary because later during the refinement, this information can help inform whether a refinement provides a reasonable scale factor.

Importantly, because the powder is not sitting flat on a plate, preferred orientation is greatly reduced. In addition, the capillary tube is rotated (at a speed of 5-10 rpm), which helps ensure random counting of crystallite orientations.

2.3.3 Analysis of PXRD data

2.3.3.1 Phase identification

The simplest and most common analysis of powder X-ray diffraction data is phase identification. The goal of this analysis is the identification of the crystalline phases present in the sample. This analysis depends mostly on the angle of the peaks and less on the intensity. Therefore, this is the easiest and fastest information to acquire. For this type of information, I ran quick scans (10-20°/minute) with the sample under Kapton tape. The limit of detection for a phase is approximately 2%, although phases with light elements (e.g. Li), which show weaker reflections in a reflection geometry, may have a higher limit of detection ($\sim$5%) in that geometry. Essentially, phase identification is a matching exercise, matching the experimental diffraction pattern to patterns in a database. At the University of North Carolina, I had access to the Inorganic Crystal Structure Database (ICSD), which contains over 200,000 crystal structures and is an invaluable tool for phase identification.

I used Rigaku's PDXL integrated powder X-ray diffraction software, version 2.8. In this software, the algorithm for phase identification allows the user to specify which elements are present in the sample to quickly filter unreasonable phases. In my experience, this element-specific search algorithm accelerates the identification process; however, I suggest a certain procedure for this search. First, I limited the search to the elements expected for the sample. If I could assign all peaks in the diffraction pattern to phases with those compositions, then I determined that no further searching was necessary. But if I could not assign some peaks, I broadened the search to include elements that I suspected could have contaminated the sample. Of

these elements, the most common is oxygen, especially when working with rare earth metal, metal halides, alkaline metals, and alkali metals. Carbon, nitrogen, and hydrogen are other likely suspects.

To assign a phase with confidence, I checked that all reflections from that phase were present in the diffraction pattern. For minor impurities, only a single reflection may be present. To assign a phase based on a single reflection requires support from other considerations. First, I confirmed that the reflection was the most intense in its pattern. If only one peak is observed it should be the most intense peak for that phase. Second, I considered whether there was a reason to suspect that the impurity phase may have a strong preferred orientation. For example, graphite, which is occasionally observed as an impurity in the products of metal carbides has a platy morphology and often has a strong preferred orientation. The preferred orientation increases the intensity of the peak at 26.6° from the $\{002\}$ family of planes[139] and diminishes the other peaks. Therefore, I am confidant in the assignment of graphite from a single peak at 26.6°. Third, if possible, I obtained compositional information, which could help narrow the list of potential impurities.

2.3.3.2 Whole pattern fitting by Rietveld refinement

Beyond simple phase identification, further analysis—quantification of relative concentrations of phases, the lattice constants, the occupancies of atomic sites, the crystallite size, etc.—depends on the intensity of signal in the diffraction pattern, which is a convolution of a number of factors described in equation 2.7. As a result, to gain further information about the sample requires deconvolution of factors that contribute to the intensity by fitting the whole diffraction pattern.

The most common method of whole pattern fitting is the Rietveld refinement.[140] The Rietveld refinement is a multiparameter fitting procedure. It aims to minimize the sum of the weighted squared differences between observed and calculated intensities at each angle in a diffraction pattern. The model includes contributions from sharp Bragg reflections from crystalline phases often described by pseudo-Voigt functions, from a smooth background fit with a spline function, and from parameterized descriptions of various systematic effects (e.g. X-ray absorption) that modify the intensity of the pattern—essentially all components described in equation 2.7. Because the method compares an observed pattern to a calculated pattern, the method requires knowledge of the crystal structure of all phases in the sample before a refinement can be attempted. Therefore, the first step in a refinement is comprehensive phase identification.

It is worth reiterating that no amount of fitting can refine poorly collected data. For an accurate refinement, the pattern needs to be of very high quality. I refer the curious reader to "Rietveld refinement guidelines" by

L. B. McCusker and coworkers,[141] which provides detailed instruction for how to collect quality data for a variety of different samples. In my experience, the best experiment for refining air-sensitive samples is the θ/θ experiment in transmission capillary mode making use of as high of an angle as possible (154° in our instrument). The capillary tube affords a smooth featureless background that is easy to fit—in contrast to Kapton film—and reduces preferred orientation effects both by rotating the sample and by the nature of the curved capillary walls. Scan speeds on the order of 0.1-0.25° per minute with the detector in 1D mode afforded very high quality data.

To begin the Rietveld refinement, I first refined the structure using an alternative whole pattern fitting algorithm, the decomposition method proposed by Pawley[142] and implemented in PDXL.[143] The method decomposes the pattern into individual Bragg components without reference to a structural model. It was designed to refine unit cell parameters with less computational effort and with lower quality data. I used the decomposition method to fit the baseline of my pattern using a spline function. Because the decomposition method considers each peak separately without the context of a structural model, it fits the baseline with fewer correlated errors, which is especially useful at high angles. After fitting the baseline using the decomposition method, I switched to the Rietveld refinement and did not refine the baseline again.

In the first cycle of refinement, I refined the scale factor, which is a constant that scales the calculated intensities of all reflections in a phase. The scale factor directly relates the volume fraction of a phase, ν_α, in equation 2.8. This refinement roughly scales the intensity of the phases in the calculated pattern to those in the observed pattern. Other parameters were fixed. The first values to refine are the unit-cell parameters and the 2θ correction. In my experience on the Rigaku Smartlab diffractometer, the automated height alignment procedure works well enough that 2θ corrections have been small to negligible; however, I still checked the 2θ value by re-running the sample with an internal standard, usually silicon mixed into the powder, to correct the angle to that known for silicon.

Once I refined the unit cell parameters and 2θ correction, which together refines the positions of the peaks, and roughly refined the height through the scale factor, I refined the width of the peaks. The angle-dependence of the peak width is described by the Caglioti[144] and Cauchy[145] equations, which accounts for both the Gaussian (eq. 2.13) and Lorentzian (eq. 2.14) components respectively that make up the pseudo-voigt shape.[146] The parameters U, V, W, X, and Y are refined.

$$\left(\mathrm{FWHM}_{\mathrm{Gaussian}}\right)^2 = U\tan^2\theta + V\tan\theta + W \tag{2.13}$$

$$\text{FWHM}_{\text{Lorentzian}} = X \tan\theta + Y/\cos\theta \tag{2.14}$$

Next, I considered the effect of preferred orientation. For layered crystals, some preferred orientation always occurs. I modeled preferred orientation using the March-Dollase approach,[147,148] which introduces a single parameter weight function, $W(\alpha)$, to describe the fraction of crystallites oriented such that the vectors of the reciprocal lattice are normal to the sample surface.

$$W(\alpha) = \left(r^2 \cos^2\alpha + \frac{\sin^2\alpha}{r}\right)^{-3/2} \tag{2.15}$$

For layered crystals, I always input the (001) plane as the plane of preferred orientation. The angle between the surface normal and that of the preferred orientation, α, encompasses slightly tilted samples. In the refinement, the March-Dollase parameter, r, is refined. At $r = 1$, $W(\alpha) = 1$ and the weight does not depend on the angle, which describes a randomly oriented powder. As $r \to 0$, the equation transforms into a delta function, which describes a perfectly oriented powder. Typically, I found a value of r roughly around 0.75 for layered crystals. At this stage, I re-refined the widths of peaks, and re-refined the preferred orientation. In this way, the refinement process is cyclical.

Last, I refined the atomic positions, the occupancies, and the thermal parameters—the finer details of the structure. These are the most difficult to refine because they are highly correlated to each other. A good practice described by Post and Bish[149] involves fixing the occupancies to values known by quantitative analysis and fixing the thermal parameters to reasonable values taken from trustworthy literature sources of the identical element in a related compounds with similar a coordination environment. In the first step, I refined the atomic positions. Note that some atomic positions, restricted by the symmetry of Wyckoff position, are not refined. Then, I refined the occupancies of the heaviest elements and subsequently the occupancies of the lighter elements. Finally, I refined the thermal parameters. Thermal parameters acquired through powder X-ray diffraction are often less accurate than those acquired by single crystal X-ray diffraction or powder neutron diffraction. The accurate refinement of thermal parameters from PXRD data requires data that span a wide range of angles (10-154°) and particularly data collected at high angles, where the thermal parameters have relatively more weight in observed intensities. After the refinement, I checked the thermal parameters against literature sources, ideally neutron diffraction or single crystal experiments, when possible or otherwise left the parameters unrefined.

Throughout the refinement, the difference between the observed pattern and the calculated pattern should decrease. The best tool for observing this is by plotting the residual, which can reveal errors in peak shape, background fitting, and other common errors.[141] The agreement of the fitting is also reported numerically through several metrics. The weight-profile R value, R_{wp}, relates the observed intensity, $y_i\,(\text{obs})$, to the calculated intensity, $y_i\,(\text{calc})$ at each step in angle, i, and weight, w_i.

$$R_{wp} = \left(\sum_i w_i [y_i\,(\text{obs}) - y_i\,(\text{calc})]^2 / \sum_i w_i [y_i\,(\text{obs})]^2 \right)^{1/2} \tag{2.16}$$

The numerator is the value that is minimized during the refinement. This value should be small; however, it can be misleading. If the signal to noise is poor and the background counts are relatively high, much of the data is accounted for in the background fit, which lowers the R_{wp}. Therefore, a second metric, R_{exp}, which attempts to describe the quality of the data—whether the counts are high enough—is also reported. This expected R value relates the number of observations, N, the number of parameters, P, to the observed intensity as

$$R_{exp} = \left((N - P) \,/ \sum_i^N w_i y_i\,(\text{obs})^2 \right)^{1/2} \tag{2.17}$$

Lastly, the goodness of fit, χ^2, is the ratio of the weight-profile R value and the expected R value and ideally should be close to 1. A $\chi^2 \gg 1$ indicates that the data is under-collected and a slower scan rate or better conditions are required.

$$\chi^2 = \frac{R_{wp}}{R_{exp}} \tag{2.18}$$

A complete refinement provides valuable information about the lattice constants, the relative concentration of phases, the lattice constants, the atomic positions, the occupancies of atomic sites, and the crystallite size; however this method is also limited by the quality of the data. For example, a sample with grain sizes of only 10 Å that has overlapping peaks will afford a low quality diffraction pattern with broad peaks and shoulders. Similarly, data that has been undercollected provides low quality data with low counts. A third possibility is that a sample contains multiple (three or more) phases with overlapping peaks. In these cases, the data cannot be refined to give the most detailed structural information—atomic positions, occupancies of atomic sites, and thermal parameters, but may be provide information about the lattice constants and crystallite size. In

the second case with undercollected data, a Pawley decomposition refinement may provide more accurate refinement of lattice constants than the Rietveld refinement. Effort in collecting quality data goes a long way to accessing the wealth of information obtained by PXRD.

2.4 Density functional theory

Density functional theory (DFT) is a powerful approach to study the electronic structure of condensed matter. It provides a fast method to determine the properties of a crystalline phase just from limited structural and compositional information. It allows a researcher to make predictions of experimentally observable phenomena in known materials and make predictions about materials that have not even been synthesized experimentally. In my opinion, in the field of solid-state chemistry, the new model of scientific discovery begins with calculating properties by DFT, which enables scientists to test hypotheses quickly before investing the time and resources into implementing experiments. In the follow subsections, I describe the basic principles of DFT, that it might serve as a useful introduction to future students and reinforce my understanding of the subject. Then I describe how I used DFT to determine properties about crystalline compounds, including the work function and ionization potential, binding energy, potential energy surfaces for sliding, and geometry optimizations of 2D heterostructures.

2.4.1 Basic principles of DFT

Density functional theory began in the 1960s when Hohenburg and Kohn theorized that, in a many-electron system, the ground-state electron density can determine all ground-state properties.[150] Their seminal theory leads to the conclusion that the ground-state electron density determines the Hamiltonian and, via the Schrodinger equation, the Hamiltonian determines the wavefunction. Therefore, the expectation value of any operator is a unique functional of the ground-state electron density. Building off of this theorem, Hohenburg and Kohn also showed that the correct electron density of the ground-state minimizes the total energy of the system.

To solve for the ground-state electron density, Kohn and Sham theorized that the exact ground state density can be rewritten as the ground state density of a fictitious system of noninteracting electrons.[151] Then, solving a set of independent, one-electron equations that describe the fictitious system and self-consistently minimizing the total energy obtains the exact ground-state electron density. The single particle equations take

a Schrodinger-like form for the independent Kohn-Sham orbitals, ψ_i, (eq. 2.19) and the orbitals relate back to the electron density, ρ, (eq. 2.20). While the Kohn-Sham orbitals are "fictitious" in that that they describe a fictitious system of noninteracting particles, they do in fact have physical significance. Their number, symmetry properties, and shape are just like those of the expected one electron orbitals.[152] Therefore, just like extended Hückel orbitals, Kohn-Sham orbitals, especially those that make up the valence band, can be used to rationalize chemical phenomena.[153]

$$H_{\text{KS}}\psi_i(r) = \epsilon_i\psi_i(r) \tag{2.19}$$

$$\rho(r) = \sum_{i}^{N} |\psi_i(r)|^2 \tag{2.20}$$

The Hamiltonian takes the form shown in eq. 2.21 where the first term is the kinetic energy and the second is the Kohn-Sham potential, $\upsilon_{\text{KS}}(r)$:

$$H_{\text{KS}}(r) = -\frac{1}{2}\nabla^2 + \upsilon_{\text{KS}}(r) \tag{2.21}$$

The Kohn-Sham potential contains three terms: the external potential introduced in the DFT formalism, the classical Coulomb interaction called the Hartree potential, and the exchange correlation.

$$\upsilon_{\text{KS}}(r) = \upsilon_{\text{ext}}(r) + \upsilon_{\text{H}}(r) + \upsilon_{\text{XC}}(r) \tag{2.22}$$

The Hartree potential only considers the electron interacting with the average electron density and neglects many-body Coulomb interactions. The exchange correlation energy is simply defined as the sum of the difference between the exact kinetic energy, $T(\rho)$, and the Kohn-Sham kinetic energy for a one-particle equation, $T_{\text{KS}}(\rho)$ and the difference between the exact energy of the many electron system, $E_{\text{ee}}(\rho)$, and the Hartree energy (eq. 2.23).

$$E_{\text{XC}}(\rho) = T(\rho) - T_{\text{KS}}(\rho) + E_{\text{ee}}(\rho) - E_{\text{H}}(\rho) \tag{2.23}$$

As a result, while this functional is exact, the form of the exchange correlation is not known. Therefore to solve the DFT functional, we need to appoximate the exchange correlation. Physically, the exchange energy

arises from Pauli repulsion described in the Pauli exclusion principle while the correlation energy result from collective behavior that screen the Coulombic interaction. Neither of these effects are easily described in a mean-field-like theory such as DFT.

2.4.1.1 Approximations to the exchange correlation functional

The simplest approximation is the local density approximation (LDA),[154] which assumes that the functional of exchange correlation only depends on the local electron density (eq. 2.24). In the LDA approach, the correlation energy for a given volume of space is assumed to be the same as that of a homogenous electron gas with the same electron density, which is known analytically. The correlation energy is calculated at each volume in space independently. Naturally, this approximation succeeds reasonably well in describing systems that have minimal variation of electron density.[155] In general, LDA overestimates the correlation energy and underestimates exchange energy. Importantly to the chemist, this results in a tendency for the LDA functional to overbind atoms. Calculations using LDA predict atomic distances that are 4-8% too short, Bader charges (an analysis to measure oxidation states) that suggest the compound is more ionic, and a significant underestimation of the band gap.

$$E_{XC}^{LDA}[\rho(r)] = \int \rho(r)\, \epsilon_{XC}^{LDA}[\rho(r)] d^3r \tag{2.24}$$

To better account for the variation in electron density in most solids, we can expand the LDA to include the local density gradient (eq. 2.25). This is called the generalized gradient approximation, GGA. GGA essentially adds a correction to the approximation of the homogenous electron gas, which better describes the tails of the valence orbitals. For the chemist, this results in a tendency for GGA to slightly underbind atoms. Calculations using GGA predict atomic distances that are often 2-4% too long, lower Bader charges than predicted using LDA, and a significant but smaller underestimation of the band gap. The most common form of GGA is that devised by Perdew, Burke and Ernzerhof (PBE), which was chosen to satisfy some of the conditions of the exact exchange correlation functional and to contain no empirical parameters.

$$E_{XC}^{GGA}[\rho(r)] = \int \rho(r)\, \epsilon_{XC}^{GGA}[\rho(r)\,, \nabla(r)] d^3r \tag{2.25}$$

Perdew and coworkers have since introduced an additional revised form of the functional to better describe solids and surfaces, called PBE-sol.[156] The difference between the two is actually only in two parameters

that modify the gradient. The analytical forms are the same. GGA-PBE augments the exchange energy, $E_X^{GGA-PBE}[\rho(r)]$ given by LDA (eq. 2.26) with two physically determined parameters. One parameter, μ, comes from the second term in the expansion of the gradient. In GGA-PBE the value of μ was chosen to be approximately twice that of a slowly varying electron gas, which accurately represents the exchange energy for neutral atoms. In PBE-sol, the value of μ is chosen to be that of a slowly varying electron gas, which better represents solids, but at the cost of yielding less accurate atomization energies. Secondly, GGA-PBE describes the correlation energy, $E_C^{GGA-PBE}[\rho(r)]$, as the correlation energy per particle of uniform electron gas like LDA modified by the reduced density gradient, t, which is scaled by a coefficient, β_C (eq. 2.27). For GGA-PBE, β_C was chosen to reproduce the correlation energy of a uniform electron gas, whereas for PBE-sol β_C was chosen to reproduce the *surface* exchange-correlation energy of uniform electron gas, which is decreased by $\sim 2/3$. This has the effect of increasing the exchange energy and decreasing the correlation energy, which GGA-PBE underestimates and overestimates, respectively. For the chemist, this results in a functional that predicts lattice constants very accurately, Bader charges close to those predicted by GGA-PBE but slightly more ionic, and more accurate values of surface energies and work functions.

$$E_X^{GGA-PBE}[\rho(r)] = \int \rho(r)\, \epsilon_X^{LDA}[\rho(r)] \left\{ 1 + \kappa \left(1 - \frac{1}{1 + \frac{\mu s^2}{\kappa}} \right) \right\} d^3r \tag{2.26}$$

$$E_C^{GGA-PBE}[\rho(r)] = \int \rho(r)\, \{\epsilon_C^{LDA}[\rho(r)] + \beta_C t^2 + ...\} d^3r \tag{2.27}$$

The LDA and GGA functionals inaccurately describe the long-range intramolecular forces found in van der Waals (vdw) materials. To account for these forces, I used the Tkatchenko and Scheffler (TS-vdw) approach. Like other approaches to describe long range forces such as DFT-D, the TS-vdw approach adds a potential to the atomic positions that decays with R^{-6}. The potential is damped at short-ranges, which, in the TS-vdw approach, is described by a single empirical parameter determined for the functional. Unlike DFT-D, which includes additional empirical parameters for each atom, the TS-vdw approach uses the effective charge calculated using Hirshfeld partitioning to handle the ionic volumes of the atoms.

Heyd–Scuseria–Ernzerhof introduced the idea of a hybrid functional that mixes the PBE exchange correlation energy with the Hartree Fock exchange energy in a ratio empirically chosen to provide remarkably better values for band gaps and optical properties. The band gaps calculated by PBE are under-estimated because of the self-interaction error, which erroneously raises the energy of states at the valence band edge.

By introducing the Hatree Fock exchange energy, the HSE06 functional lowers the energy of the states at the valence band edge and widens the band gap. I refer the curious reader to my colleague, Dr. Adam Woomer's thesis, *From van der Waals to coulombic heterostructures: understanding charge transfer in 2D materials* for a description of hybrid functionals like HSE06 and PBE0.

2.4.1.2 Approximations made in implementing DFT

To run calculations that use DFT, we use a code, like CASTEP or VASP. In the implementation of the codes, we make additional approximations that accelerate the calculations and reduce the computation to a finite size. These approximations introduce error and uncertainty. Therefore, it is worth laying out the approximations to understand how to minimize these errors.

To calculate the orbitals in an infinitely large crystal, we can use Bloch's theorem to simplify the problem. Bloch's theorem states that the wavefunction of an electron in a periodic potential, like that of a crystal lattice, can be written as the product of a periodic function and plane wave. Consequently, instead of considering the infinitely large crystal, we only need to consider the electrons in the smallest repeating unit. Mathematically, the periodic function, $u_i(r)$ can be expanded into an infinite sum of plane-waves, with coefficients ($c_{i,G}$), where k is a wavevector of the first Brillouin zone, and G is a wavevector of the reciprocal lattice, shown in eq 2.28. Therefore, plane-waves with periodic boundary conditions are a natural choice for a basis set to describe the wavefunction in crystals.

$$\psi_{i,k} = u_i(r)\, e^{ikr} = \sum_G c_{i,G} e^{i(k+G)r} \tag{2.28}$$

To reduce the basis set to a finite size, we truncate the expansion of the plane wave basis at an energy, the plane-wave cutoff energy. The choice for the plane-wave cutoff energy for a given calculation relates to the atoms involved. More specifically, it relates to the valence orbitals of the atoms involved and their proximity to the nucleus. Atoms, like carbon and fluorine whose valence orbitals are close to the nucleus require a higher plane-wave cutoff energy. Many computational codes make recommendations of a minimum energy for the atoms in the unit cell. These recommendations make a good starting point. The choice for a plane-wave cutoff energy also needs to account for vacuum space. The value of plane-wave cutoff energy should roughly scale with the volume fraction of vacuum space in the unit cell. For example, if vacuum space

takes up half of the volume, the plane-wave cutoff energy should be doubled. The best method for choosing a plane-wave cutoff energy is through a convergence test described in section 2.4.2.

Even with the simplification using Bloch's theorem to consider only the unit cell, the electron density and other quantities of interest involve an integral over k-space. To compute the integral exactly requires the computation of the wavefunction at infinite points in k-space. In practice, we can only calculate the wavefunction at a finite number of points in k-space. Therefore, we approximate the wavefunction for a small volume of k-space by calculating the wavefunction at only one point in that volume, because we assume that the wavefunction varies slowly with k. Then, the quantity of interest, $f(r)$, is approximated by a weighted sum evaluated at discrete k-points as shown in eq 2.29. There are a number of schemes for choosing which k-points to use. The most common method for dividing k-space into smaller volumes is the Monkhorst-Pack sampling scheme,[59] which I used in my calculations.

$$f(r) = \int_{BZ} F(k,r)\, dk \approx \frac{\Omega_{BZ}}{N_k} \sum_{i}^{N_k} F(k_i, r) \tag{2.29}$$

Still with these assumptions, the computational time is prohibitive simply because the systems contain too many electrons. To reduce the number of electrons, Hellmann introduced the idea of a pseudopotential.[157] The concept of a pseudopotential draws on the realization that only the electronic structure of the valence electrons changes in different chemical environments. The core electrons are essentially frozen regardless of the structure, composition, and bonding. Furthermore, because of their nodal structure, the wavefunction of core electrons vary in k space sharply and require higher energy plane waves to accurately capture their structure. Instead, the potential of the core electrons can be approximated by a smoothly varying pseudopotential, which requires fewer plane waves to compute. The pseudopotential is chosen such that, after a given radius from the center of an atom, the pseudopotential is identical to the potential of the all-electron system so that it does not alter the potential of the valence electrons. This approximation greatly reduces the number of electrons in the calculation and conserves computational effort. In my calculations I used Vanderbilt ultrasoft pseudopotentials[56] unless using a hybrid functional, in which case I used norm-conserving pseudopotentials.[158]

To calculate a property, first the electron density must be found. Hohenburg and Kohn theorized that the correct electron density of the ground-state minimizes the total energy of the system. Therefore to find the electron density, we need to minimize the total energy. In practice, the absolute minimum energy is not found.

Instead, we set a converge tolerance and minimize the energy through a self-consistent field (SCF) loop until the change in energy from the previous iteration to the current iteration is less than the tolerance. In this way we calculate an electron density, one that we hope approximates the real electron density. In many codes, the "window" is the number of iterations that are compared for the convergence tolerance. For example, a window of 3 means that the current iterations of the SCF loop and the two iterations prior to it are compared to test if they are within the convergence tolerance. In most of my calculations, I used a convergence tolerance of 5.0 $\times 10^{-7}$ eV/atom and a window of 3.

Importantly, two external tests for convergence should always be performed to ensure that the density is near the minimum. First, in a series of increasingly stringent calculations the plane-wave cutoff energy should be increased in multiples of 25 eV and the energy minimized for each calculation until the change in the minimum energy vs. the change in natural log of plane wave cutoff is less than 0.01 eV/atom. Second, in another series of increasingly stringent calculations, the number of k-points should be increased and the energy minimized for each calculation until the change in energy/change in k-point is less than 0.01 eV/atom. The convergence of energy with the number of k-points does not necessarily decrease monotonously, as changing the number of k-points results in sampling different regions of the Brillouin zone. Consequently, it is better to use a stricter convergence tolerance (dE/dk$_{\#} < 0.005$ eV/atom) when comparing the total energy between systems that have different symmetries, which do not benefit from any cancellation of errors one might get by sampling the same Brillouin zone. This second test, checking the convergence of the calculations with respect to the number of k-points, is very important. In my experience, an unconverged system can yield errors exceeding 300 meV, which in some calculations is an error of over 100%, and lead to qualitatively incorrect results.

2.4.2 Calculating properties using DFT

With these approximations, we can run DFT calculations efficiently. In my studies, I used the CASTEP code implemented in the Materials Studio software. I ran the calculations on the University of North Carolina at Chapel Hill's *dogwood* and *longleaf* partitions.

Prior to calculating any properties, we need to optimize the geometry of the crystal structure. Essentially, we want to find the geometry of atoms that minimizes strain, the forces on the nuclei, and the energy. Importantly, because the geometry optimization uses a minimization algorithm, the strategy identifies a structure with a *local* minimum in energy, not necessarily a global minimum of energy. This can be beneficial

in circumstances where the structure of interest is meta-stable; however, consequently the initial structure in the search significantly determines the result.

To find an initial structure, I used the experimentally known crystal structure with its lattice constants and atomic positions when available. I pulled structure files (.cif) from the Crystallography Open Database (COD) and the Inorganic Crystal Structure Database (ICSD) to which we have access through CHANL's subscription on the X-ray diffractometer. If the crystal structure was not known experimentally, I also checked the Materials Project database, a database of structures computed by DFT. For unknown structures, identifying a good initial structure is far more difficult. I used one of two methods to find the initial structure: 1) I researched the elements of interest and known crystals structures and identified elements that bond similarly (for example, yttrium and holmium). Importantly, the crystallographic ionic radius, electronegativity, and oxidation states of the elements should match. Then I searched for related phases where I could substitute one atom for another (for example, Y for Ho in Ho_2CF_2), which provides a structure for the initial geometry optimization. 2) My colleagues used the Universal Structure Predictor: Evolutionary Xtallography (USPEX) algorithm, an evolutionary search algorithm that explores the phase space computationally. The algorithm computes the enthalpy of thousands of candidate crystal structures and uses similarities in bond distances, coordination, symmetry, and a number of other identifiers to find the most stable phase for a given composition.

To optimize the initial geometry, I used the BFGS algorithm with a convergence tolerance of 5.0×10^{-7} eV/atom for energy, 0.01 eV/Å for maximum force, 0.02 GPa for maximum stress, and 5.0×10^{-4} Å for maximum displacement, allowing the full cell to optimize. I used the PBE-sol functional, which accurately calculates lattice constants at relatively little computational effort, and the TS-vdw approach to account for long range intramolecular forces. With the optimized structure, we can compute properties. In DFT, the expectation value of any operator is a unique functional of the ground-state electron density, therefore, for many properties, the first step involves calculating the ground-state electron density even more accurately than was done in the geometry optimization. In the following subsections, I describe some of the calculations that I performed and make recommendation that I hope will help future students. I refer the curious reader to my colleague, Dr. Adam Woomer's thesis, *From van der Waals to coulombic heterostructures: understanding charge transfer in 2D materials* for an excellent discussion of the calculation of band structure and densities of states using the hybrid HSE06 functional.

2.4.2.1 Work function and ionization potential

One of the important characteristics of a metal or any solid is its work function, (WF), the energy required to remove an electron from its surface. As many have shown, DFT can reliably calculate WF for a metal;[156,159] however DFT erroneously places the Fermi level for a semiconductor as the top of the valence band. This is because DFT considers the Fermi level as the lowest energy filled state. Therefore, DFT can only predict directly an ionization potential (IP) for a semiconductor, not a work function. Here I outline a procedure, the "the thin-slab approach,"[160] to accurately calculate the WF of metals and the IP of semiconductors.

Calculating the WF or IP of a monolayer is simpler than that of a bulk system. The calculation of a monolayer is simply a series of convergence tests that result in a single energy calculation using strict tolerances. I used the PBE-sol functional, which more accurately calculates WF and IP than the GGA-PBE, LDA, or HSE06 functionals. First, I calculated the work function with a relatively high plane-wave cutoff energy (e.g. 500 eV), a relatively dense set of k-points (0.01 Å^{-1}), and a precise FFT grid. In the CASTEP code, the results for the calculation are found in the analysis of the potentials. The potential of the vacuum is taken as the average of the potential of the flat region away from the crystal. It is imperative to have a slab of vacuum at least 12 Å thick to ensure that the electron density and therefore the exchange correlation potential decays to its minimum. Then in a series of calculations, I increased the plane-wave cutoff energy in intervals of 25 eV until the value of the WF or IP varied by less than 0.1 eV. Finally I increased the k-point density until the value of the WF or IP varied by less than 0.05 eV with a window of three calculations. This ensures that the system is very well converged and that the value is trustworthy.

The calculation of a WF or IP of a bulk system is more intensive. First I calculate the WF or IP for a series of increasingly thick slabs of the material separated by 12 Å of vacuum until the value converges to within 0.05 eV. This is intensive because it requires the slab at each thickness to be optimized and converged. Unoptimized surfaces can cause errors of up to 0.5 eV. Though intensive, this series yields an interesting result for layered and 2D materials because it provides the WF or IP as a function of thickness, i.e. for the monolayer, bilayer, trilayer, etc. If this is not important for the system, only the calculation of a thick slab is necessary. From these calculations, I obtain the potential of the vacuum, $E_{\text{vac}}^{\text{slab}}$, and the potential of the atomic cores at the center of the slab, $E_{\text{core}}^{\text{slab}}$. Then, I calculate the potentials of the bulk crystal, which provides the Fermi level of the bulk material, E_F^{bulk}, and the potential of the atomic cores in the bulk, $E_{\text{core}}^{\text{bulk}}$. To obtain the

WF or IP for the bulk material, I correct the Fermi level of the thick slab that of the bulk crystal by using the potentials of the atoms as a reference (eq. 2.30). The correction assumes that the potentials near the center of the thick slab should be equal to the potentials in the bulk material, which for a thick slab is a good approximation.

$$\phi_{\text{bulk}} = \left(E_{\text{vac}}^{\text{slab}} - E_{\text{core}}^{\text{slab}}\right) - \left(E_{F}^{\text{bulk}} - E_{\text{core}}^{\text{bulk}}\right) \tag{2.30}$$

For non-symmetric crystals, dipole corrections are necessary. The best correction is the self-consistent dipole correction,[161] which considers an external electric field to cancel the field generated by the dipole. Unfortunately, the addition of this dipole-correction nearly doubles the computational time.

2.4.2.2 Binding energy

For a layered crystal, the binding energy is the difference between the energy of the optimized structure, E_{ild}, and energy of the structure where the layers are separated by infinite distance, E_{∞}. This quantitative metric describes the nature of the interlayer interactions and can be used to predict whether a crystal can be exfoliated.[61,98] The value is best reported as an energy per unit area, either meV/Å^2 or J/m^2, or as an energy per mole. Older literature, which examined single element compositions like graphite or phosphorene, may report the value as meV/atom. This unit obfuscates comparison between systems as the value depends inadvertently on the density of the lattice. When using the description as an energy per unit area, the concept of a binding energy is very similar to that of a surface energy; however, the concept of a binding energy extends easily to heterogeneous systems, like the donor–acceptor heterostructures[162] described in chapter 4. Therefore, I define the binding energy per area as:

$$E_{BE} = \frac{E_{ild} - E_{\infty}}{A} \tag{2.31}$$

where A is the area of the unit cell and equal to the quantity, V/c, where V is the volume of the cell and c is the height of the cell in the out-of-plane direction.

To calculate a binding energy, we perform at least two calculations, one of the energy of the optimized structure and one of the structure at an "infinite" distance, which we approximate by calculating a structure with the layers separated by 12 Å of vacuum. I found that 12 Å of vacuum provided sufficient distance for the two layers to become non-interacting and therefore reasonably approximate the structure at an infinite

distance. Often, I calculated the binding energy as a function of distance, producing a curve in the spirit of a Leonard-Jones or Morse potential. This curve also allows the calculation of the cleavage strength, which is the first derivative of binding energy with respect to distance. Because cleavage strength is a derivative of binding energy, the changes in distance used in the calculation need to be small, especially when the change in energy is steep.

For a binding energy calculation, I used identical parameters, including structural parameters like the volume of the unit cell, for the individual calculations of energy. This is a good practice. When using identical parameters, the binding energy converges at lower tolerances (e.g. k-point density) due to cancellation of errors. Another good practice is to check that the calculation is converged with respect to both the plane-wave cutoff energy and the number of k-points because binding energy calculations require large volumes of vacuum and therefore higher plane-wave cutoff energies than that of a 3D lattice. As described in section 2.4.1, the PBE-sol functional calculates energies related to surfaces, including the binding energy, more accurately than GGA-PBE, LDA, or HSE06. Therefore, I used the PBE-sol functional to calculate the binding energy. As a suggestion to future students, I generated the structure files for these calculations using a perl script in Materials Studio and submitted the calculations to the cluster using a linux script, which saves significant time.

2.4.2.3 The potential energy surfaces for sliding

The potential energy surface for sliding a layered crystal against itself or another 2D material may be of interest in studies that try to explore exfoliation or friction at the atomic scale. The calculation of the potential energy surface for sliding consists of a series of individual energy calculations in which one lattice is translated in two-dimensions, x and y, with respect to the other lattice. In certain situations, where the crystals are commensurate and "corrugated" as in the ZrS_2-Ca_2N heterostructure, the potential energy surface could also consider translation in the third dimension, z. Then to reduce the dimensionality of the problem, the minimum energy at each z is projected onto the 2D, xy, plane of translation. The results are then smeared or interpolated into a continuous potential energy surface.

In some instances, the potential energy surface varies sharply, especially when atoms approach one another at distances dominated by nuclear repulsive forces. In these situations, the density of translation needs to be small in order to accurately capture the smooth potential energy surface. I used a regular spacing of 0.1-0.2 Å in my calculations. It is reasonable to suspect that if given a rough sense of the potential

energy surface, a non-regular spacing could be chosen that greatly conserves computational effort. For my purposes, I did not find it practical to do so; however, given that computing the potential energy surfaces can require thousands of individual energy calculations, I did seek to reduce the number of calculations using the symmetry of the potential energy surface. Importantly, I learned that the symmetry of the potential energy surface for sliding shares all of the rotational, translational, and mirror-plane symmetry elements of the smaller lattice that are restricted to the plane of translation. For example, in these calculations the overall structure often consists of supercells of two crystals, for example a 3x3 cell of graphene and 2x2 cell of 2D Sr_2N. In this case, because of the symmetry of graphene, I calculated the potential energy at points for only $1/16^{th}$ of one unit cell of graphene or $1/144^{th}$ of the entire area of the structure.

As a suggestion to future students, I generated the structure files for these calculations using a perl script in Materials Studio and submitted the calculations to the cluster using a linux script, which saves significant time.

2.4.2.4 Geometry optimization of 2D heterostructures

The geometry optimization of 2D heterostructures is a non-trivial calculation. In addition to the normal optimization of the atoms, we need to consider the distance and translation of the lattices with respect to one another, because, as described above in section 2.4.2, the minimization algorithms only identify local energy minima. To optimize the geometry of a 2D heterostructure, we first perform a geometry optimization at a set interlayer distance of 3.3 Å chosen as a typical van der Waals distance. This calculation roughly determines the interlayer distance for the heterostructure. Then we calculated the potential energy surface for sliding the lattices with respect to one another, including small translations in the third dimension. We identify the local minima of the potential energy surface from these calculations and use the structures at the minimum potential energies as initial structures in further geometry optimization. We assume that these minimums provide reasonable initial structures for BFGS minimizations, because, especially for layered crystals, the in-plane bonding is as strong or stronger than the interlayer interactions and thus the 2D lattices resist significant deviation. Even for donor-acceptor heterostructures like the h-BN-Sr_2N heterostructure with strong interlayer interactions, the optimization of the structure that gave the minimum potential energy in the calculation of the potential surface lead to the lowest energy structure identified.

CHAPTER 3–EXPERIMENTAL DEMONSTRATION OF AN ELECTRIDE AS A 2D MATERIAL

"All my life through, the new sights of Nature made me rejoice like a child."

- Marie Curie,1923

3.1 Introduction

Nearly every ionic solid consists of positively and negatively charged atoms, but in exotic materials called electrides, the negative ion is just an electron with no nucleus. The electrons wave function occupies the space typically filled by anions like Cl^-.[4,22,163,164] Materials with anionic electrons can serve as strong reducing agents[73,83] or catalysts for chemical syntheses,[165,166] and have been predicted to serve as low-temperature electron emitters,[167] transparent conductors,[168,169] and battery electrodes.[88] With so much to be discovered about electrides, their exotic physical properties may open avenues to different kinds of energy storage,[88] optoelectronic,[170] and magnetic devices.

Electrides have two known structures: cage structures[18,23,171] in which anionic electrons are located within zero-dimensional cages, and layered structures,[26,32] in which anionic electrons are found in two-dimensional (2D) planes. In layered electrides, the proximity of the anionic electrons causes them to partially delocalize[35] as a 2D electron gas.[26] The electron gas enables high electrical mobility (160 $cm^2V^{-1}s^{-1}$ at room temperature),[26] high carrier concentrations (1.4×10^{22} cm^{-3}),[26] and rapid electrical transport to the materials surfaces.

The exciting properties of layered electrides have prompted theoretical studies into their lower dimensional forms. For example, a recent report[172] presented density functional theory (DFT) calculations of 2D Ca_2N, which suggest that the 2D form could be thermally and mechanically stable and possesses an

Portions of this chapter reproduced with permission from Druffel, D. L.; Kuntz, K. L.; Woomer, A. H.; Alcorn, F. A.; Hu, J.; Donley, C. L.; Warren, S. C. Experimental Demonstration of an Electride as a 2D Material. *Journal of the American Chemical Society* **2016**, 138, 1608916094. Copyright 2016 American Chemical Society.

electron gas on its surface. That result suggests that 2D Ca_2N might be synthesized by exfoliation of 3D Ca_2N. Despite the growing interest, to our knowledge, no electride has been synthesized or experimentally studied as a 2D material or nanomaterial.

Here we demonstrate that electride nanomaterials can be produced by exfoliating a layered electride, Ca_2N. We have applied the liquid exfoliation methodology, previously used to break apart van der Waals solids,[99] to exfoliate the layered Ca_2N crystal into 2D nanosheets. As we show, the 2D flakes are crystalline, have a stoichiometry of $Ca_2N_{0.99\pm0.01}$, and are stable in a nitrogen atmosphere or in several organic solvents for at least one month. In addition, our photoemission and optical measurements, which are consistent with the electronic band structure calculated by density functional theory (DFT), suggest that the anionic electrons are retained in the 2D flakes

3.2 Results and Discussion

3.2.1 The synthesis of 2D Ca_2N by liquid exfoliation

We synthesized bulk Ca_2N by a high-temperature reaction between Ca_3N_2 and calcium metal as reported previously,[26,173] with details described in section 2.2. Powder X-ray diffraction patterns of our bulk Ca_2N confirm that the samples have the layered anti-$CdCl_2$-type crystal structure (Figure A.1) with lattice parameters matching those in the literature.[32] Figure 3.1a depicts the crystal structure of Ca_2N, in which planes of Ca_6N octahedra are separated by a 3.9 Å interlayer gap.[25,26,32] Because of the formal oxidation states of Ca^{2+} and N^{3-}, the formula unit has a positive charge and is best represented as $[Ca_2N]^+$. Anionic electrons balance the positive charge of the $[Ca_2N]^+$ layers by occupying the interlayer gap. Using DFT,[150,151] we calculated projections of electron density for the highest occupied band (1.49 eV to E_F, the Fermi level) shown in Figure 3.1b (see A.2 for details). We provide an electron density profile with respect to the z-axis of the hexagonal unit cell for this band Figure (3.1c) and find that the interlayer electron gas consists of *ca.* 0.7 electrons per formula unit. The bands below the highest occupied band do not contribute additional electron density to the interlayer electron gas.

To understand the energetics of exfoliating Ca_2N into nanosheets, we calculated the binding energy between layers as a function of interlayer distance. We found that our binding energy between Ca_2N layers was 396 meV per calcium atom or 1.11 J/m^2. These calculations match those performed by others who report a cleavage strength of 1.09 J/m^2 for Ca_2N.[172] In addition, we find that the binding energy of Ca_2N is only

about four times that of graphite (0.31 J/m^2), as shown in Figure 3.1d. Electrostatic interactions between the $[Ca_2N]^+$ and electron gas likely account for the greater binding energy of Ca_2N compared to graphite, a van der Waals solid. These calculations suggest that it may be possible to exfoliate Ca_2N into 2D flakes, although with somewhat greater difficulty than graphite.

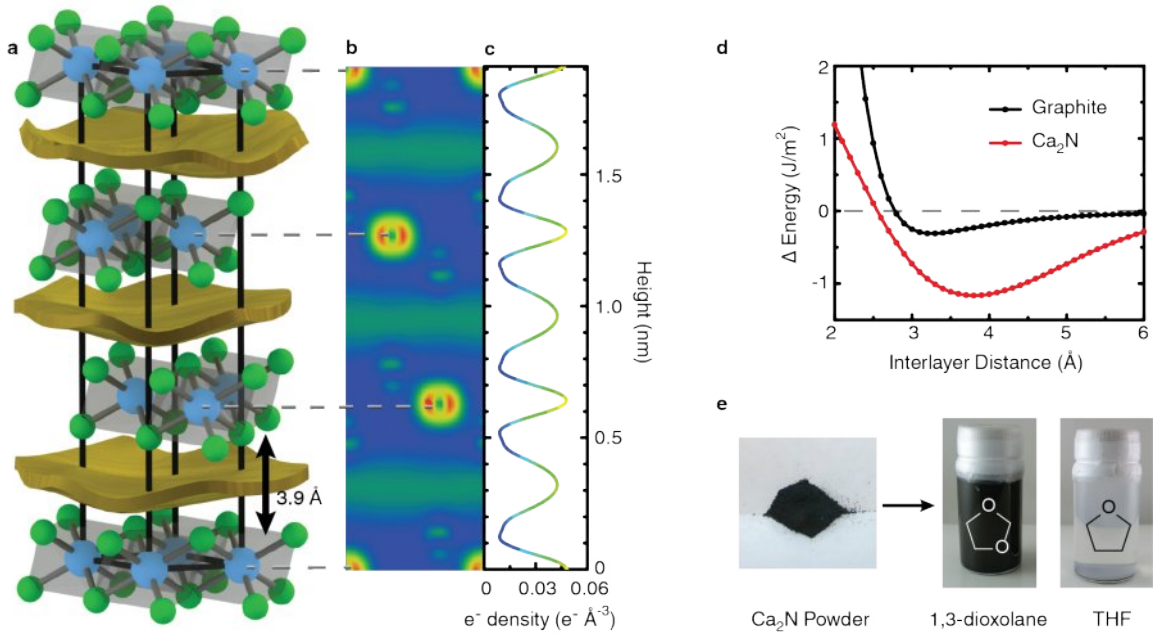


Figure 3.1: Liquid exfoliation of Ca_2N. (a) The unit cell of Ca_2N depicting layers of $[Ca_2N]^+$ (Ca^{2+} is green, N^{3-} is blue) that alternate with layers of delocalized electrons (gold). (b) Projection of the integrated electron density in the unit cell as calculated by density functional theory (DFT). The integration is over occupied states in the highest occupied band. (c) The electron density profile integrated along the z-axis of the unit cell for the occupied band shown in b. (d) Interlayer binding energy versus interlayer distance, as calculated by DFT. (e) Photos of Ca_2N bulk powder and 2D Ca_2N suspensions in 1,3-dioxolane and tetrahydrofuran (THF).

Scotch-tape methods used to exfoliate layered van der Waals solids may not be appropriate for Ca_2N. Ca_2N is chemically reactive and can decompose in contact with many adhesives. For such a reactive material, the conditions of liquid exfoliation are more suitable because the solvents functional groups can be chosen to avoid reaction. Liquid exfoliation offers additional advantages such as a much higher yield, scalability, facile material transfer, and easy thin-film preparation.[99]

To identify solvents that are stable in the presence of Ca_2N, we screened 30 solvents (Table S1) with different functional groups. Working under anhydrous and oxygen-free conditions, we suspended bulk Ca_2N powder in each solvent and sonicated the suspensions for 100 min in a water bath sonicator (see A.3 for details).

Reactions between many of the solvents and the bulk Ca_2N were easy to identify by eye. As expected, protic solvents like isopropyl alcohol and *N*-methylformamide reacted vigorously with Ca_2N to form $Ca(OH)_2$. In other solvents—chloroalkanes, ketones, aldehydes, nitriles, and even some ethers—the dark blue Ca_2N powder decomposed to a white powder in less than 24 h. Therefore, these solvents are not appropriate for liquid exfoliation. Nonpolar hydrocarbons including benzene and hexanes did not react with Ca_2N, but the dispersions precipitated within minutes. While nonpolar hydrocarbons may not be appropriate for liquid exfoliation, this finding suggests that they could be used to protect Ca_2N from air or water environments. Finally, exfoliation in aprotic amides like *N*-methyl-2-pyrrolidone showed only modest stability: the materials precipitated rapidly and partially oxidized to $Ca(OH)_2$ over a period of 5 to 10 days.

Through the screening process we identified several promising solvents that did not visibly react with Ca_2N, including 1,3-dioxolane, dimethyl carbonate, and dimethoxyethane. These solvents have been successfully employed in lithium-ion batteries[174,175] and are stable against reduction. Although each of these three solvents merits further study, we pursued 1,3-dioxolane because it produced the darkest, most concentrated dispersions and because of its volatility (boiling point = 75 °C).

Although the chemical structures of 1,3-dioxolane, tetrahydrofuran (THF), and 1,4-dioxane are similar, the reactivity of these solvents toward Ca_2N is markedly different. Ca_2N is stable in 1,3-dioxolane for at least a month and remains as a dark suspension, whereas in THF and 1,4-dioxane, it decomposes into white $Ca(OH)_2$ in less than 1 day (Figure 3.1e, A.2). Further studies are underway to better understand the greater stability of Ca_2N in 1,3-dioxolane.

3.2.2 Characterizing electride nanosheets by electron microscopy

After identifying 1,3-dioxolane as a promising solvent, we sought to characterize the exfoliated material. Figure 3.3a shows an image of a nanosheet of Ca_2N acquired using a high-resolution transmission electron microscope (HR-TEM). The material is a single crystal and crystalline out to the edges of the flake, which suggests minimal degradation of the sample during the exfoliation process or while loading into the TEM. The nanosheet is flat and transparent to electrons. Although the predominant morphology is sheet-like, our liquid-exfoliation method does yield some material that is nonsheet-like or that appears to be an aggregate of sheets (Figure A.4), despite our attempt to isolate the thinnest materials by centrifugation. We also note that like other liquid exfoliated materials,[98,99,176] our 2D Ca_2N flakes have a distribution of lateral dimensions (approximately 0.2–10 μm) and thicknesses.

We analyzed selected area diffraction patterns to understand the crystal structure of the nanomaterials. The diffraction patterns showed a hexagonal crystal structure with a d-spacing of 1.80 ± 0.01 Å, which matches the simulated d-spacing (1.80 Å) for the $\{1,1,0\}$ family of planes. In addition, we observed a second set of hexagonal diffraction spots with a larger d-spacing (3.12 ± 0.02 Å) not present in the simulated patterns of bulk Ca_2N.

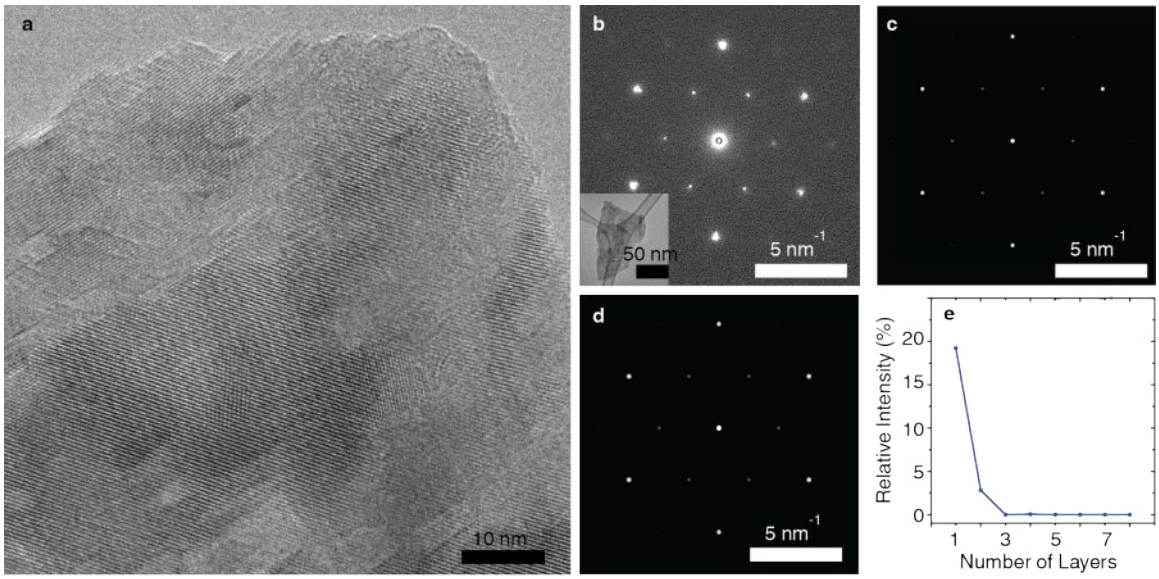


Figure 3.2: Morphology and crystallinity of exfoliated Ca_2N. (a) High resolution TEM image of 2D Ca_2N showing the sheet-like morphology and crystallinity. (b) Diffraction pattern of 2D Ca_2N with the low resolution TEM image of the corresponding 2D flake. Simulated diffraction pattern of (c) bilayer Ca_2N and (d) Ca_2N with translational disorder looking down the [001] zone axis. (e) Comparison of the relative intensity of the spots at 3.21 nm^{-1} to the spots at 5.56 nm^{-1} in the simulated diffraction patterns for different thicknesses of 2D Ca_2N.

To understand the origin of the spots with a larger d-spacing, we used multislice calculations (JEMS)[177] to simulate diffraction patterns for crystals of differing thicknesses and translational disorder. We found that these spots are present in the diffraction pattern of Ca_2N structures that break the unit cells symmetry in the z-direction. For example, the spots are present in simulated diffraction patterns for monolayer and bilayer structures (Figure 3.3c,e) as well as structures with translational disorder (Figure 3.3d, A.5, see section A.4 for details).

One possible explanation for the presence of translational disorder is turbostratic disorder either present in the 3D parent crystal or introduced in the exfoliation process by grinding the crystal into a powder or by sonicating the powder into 2D flakes. This possibility fits with recent DFT calculations that show that the energy barrier to laterally slide planes of $[Ca_2N]^+$ in a crystal is remarkably low, only $\sim$17 meV.[64] Though

we have shown that the layer thickness or translational disorder can explain this data, we note that partial oxidation of the sample surface or a surface reconstruction are also possible explanations. Therefore, we conclude that the crystal structure of our 2D Ca_2N is hexagonal with lattice parameters matching the bulk crystal and that there is aperiodicity in the z-direction.

3.2.3 Understanding the composition of 2D Ca_2N

To understand the composition of our 2D material, we measured the calcium and nitrogen content of samples of bulk (3D) Ca_2N and exfoliated (2D) Ca_2N. Details of the assays and an experimental confirmation of the applicability of these assays are given in the SI. We measured the stoichiometry of the 3D crystal as $Ca_2N_{1.00\pm0.01}$ and of the 2D material as $Ca_2N_{0.99\pm0.01}$ with the error reported as twice the standard deviation. A two-sample *t* test with a significance level of 0.05 suggests that the compositions of the 3D and 2D material are not different; however, a one-sample t test with a significance level of 0.05 suggests that the stoichiometry of the 2D material is nitrogen-deficient or calcium-rich compared to the expected ratio of Ca_2N. This result can be explained by a small amount of oxidation on the surface of the 2D material that resulted in the loss of nitrogen as ammonia gas. Therefore, it is likely that the exfoliated material has slightly oxidized during the exfoliation process or subsequent handling.

X-ray photoelectron spectroscopy (XPS) provides insight into the chemical environment of the surface of our exfoliated Ca_2N. The calcium 2p core electron spectra (Figure 3.2a, Table 3.1) of 2D Ca_2N have a Ca 2p doublet with a spinorbit splitting of 3.5 eV. The Ca $2p_{3/2}$ peak is centered at 347.5 $\pm$ 0.2 eV (Table 3.1) with a full-width-half-max (FWHM) of 1.9 eV. In addition, the Ca 2p spectra show plasmon loss peaks shifted by 7.9 and 11.4 eV relative to the Ca $2p_{3/2}$ center. These values are in agreement with our 3D Ca_2N (Table 3.1) and with previous literature.[34] After the measurement, we exposed the 2D Ca_2N samples to ambient conditions, which caused oxidation and a corresponding color change from black to white. The XPS spectra of these deliberately oxidized samples match that of $Ca(OH)_2$ (Figure 3.2a, A.6, and Table 3.1). We conclude that the surface of our as-synthesized 2D Ca_2N has not oxidized to $Ca(OH)_2$. However, because the Ca 2p binding energy is relatively insensitive to the local chemical environment,[178] we do not draw further conclusions about the surface of our 2D Ca_2N from the Ca 2p peak positions.

To further understand the chemical environment of the surface of our 2D Ca_2N, we examined the nitrogen 1s core electron binding energy (Figure 3.2b). We attribute the peak, centered at 399.2 $\pm$ 0.1 eV with a fwhm of 2.2 eV, to the N 1s core electrons in 2D Ca_2N, in agreement with our 3D Ca_2N (399.3 $\pm$ 0.1 eV). We note

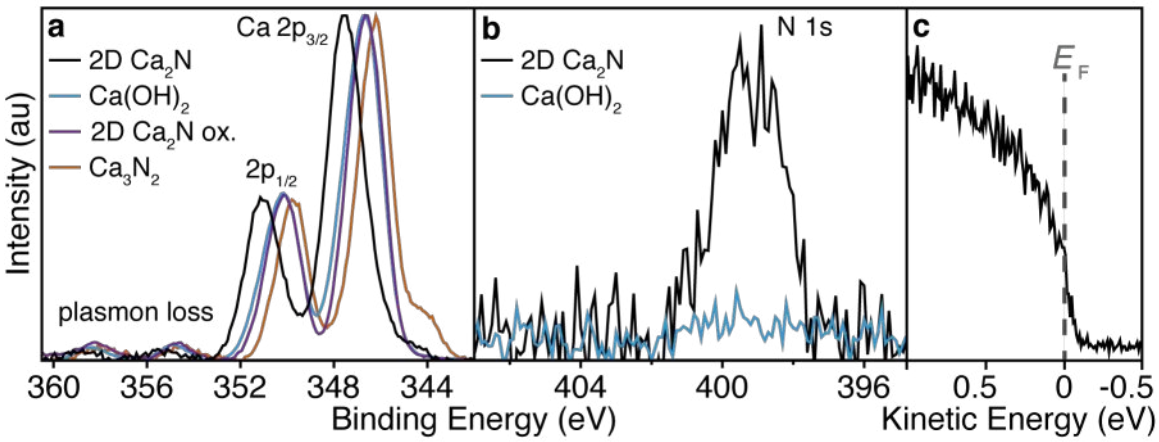


Figure 3.3: Photoemission spectra of calcium nitride species and related oxidized species. (a) XPS spectra of core Ca 2p electrons for 2D Ca_2N, deliberately oxidized 2D Ca_2N, Ca_3N_2, and $Ca(OH)_2$. (b) XPS spectra of core N 1s electrons for 2D Ca_2N and $Ca(OH)_2$. (c) Ultraviolet photoemission spectroscopy Fermi edge of the metallic 2D Ca_2N.

the N 1s peak is positioned at a different binding energy than previously reported, but we cannot compare absolute positions because a carbon reference was not provided.[34]

Table 3.1: XPS Binding Energies (eV) of Ca 2p Electrons from Ca_2N

Material	$2p_{3/2}$	$2p_{1/2}$	plasm. A	plasm. B
2D Ca_2N	347.5	351.0	355.4	358.9
3D Ca_2N	347.5	351.0	355.5	359.0
Ca_3N_2	346.2	349.7	354.3	358.0
$Ca(OH)_2$	346.7	350.3	354.8	358.3
2D Ca_2N ox.	346.6	350.2	354.7	358.3

The C 1s core electron spectra (Figure A.6) show that adventitious carbon species such as adsorbates from 1,3-dioxolane are present on the surface of our 2D Ca_2N. While our measurements are representative of the surface of our liquid exfoliated 2D Ca_2N, future XPS measurements on clean 2D Ca_2N cleaved in vacuum are needed to provide more insight into the intrinsic bonding and local environment of 2D Ca_2N.

3.2.4 Analyzing the electronic structure of 2D Ca_2N

Ultraviolet photoelectron spectroscopy (UPS) offers information about the electronic structure of our 2D flakes. The density of states at the Fermi energy, E_F, (Figure 3.2c) demonstrates that the electronic structure of our 2D Ca_2N is metallic (Figure A.7). The work function of our material could not be quantified because

all samples of bulk and 2D Ca_2N showed evidence of differential charging (Figure A.8 and section A.5 for details), in agreement with previous reports.[34]

In order to better understand the electronic structure of our 2D Ca_2N solutions, we measured the optical response of our 2D flakes with UV–visible–near IR (λ = 280–2200 nm) transmission spectroscopy. Dilute solutions of 2D Ca_2N in 1,3- dioxolane were light brown in color and transparent (Figure 3.4a), with an optical extinction that depended linearly on sample concentration (Figure A.9), which allows us to estimate an attenuation coefficient and molar extinction coefficient (Figure 3.4b). Concentrated solutions (1.05 mg/mL) appear opaque (inset 3.4b) and transmit less than 1% of light at certain wavelengths.

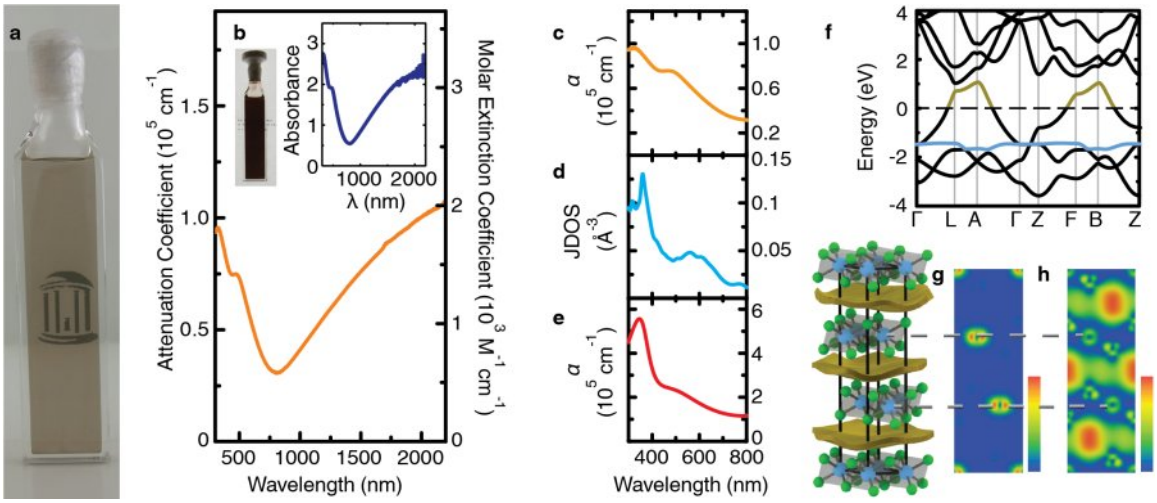


Figure 3.4: Optical properties of 2D Ca_2N. (a) Photo of a cuvette containing 2D Ca_2N suspended in 1,3-dioxolane. (b) The attenuation coefficient and molar extinction coefficient of 2D Ca_2N vs the wavelength of light. The inset of (b) shows a photo of a cuvette containing concentrated 2D Ca_2N and its absorbance spectrum. The short-wavelength response (300–800 nm) comparing (c) the attenuation coefficient α of 2D Ca_2N, (d) the joint density of states calculated by density functional theory for 2D Ca_2N, (e) the attenuation coefficient α of 3D Ca_2N calculated from literature data.[26] (f) The band structure of Ca_2N. Projection of the integrated electron density in the unit cell integrated over (g) states in the flat band (shown in blue in f) and over states in the band (shown in gold) above the Fermi level. The scale bars for g and h are 0.00 to 1.49 $\times$ 10^{-3} e^- $Å^{-3}$ and 0.00 to 0.12 $\times$ 10^{-3} e^- $Å^{-3}$, respectively.

UV–visible–near IR spectra of 2D Ca_2N suspensions show absorbance peaks at 330 and 480 nm (Figure 3.4c). To understand the origin of these peaks, we compare our measurements both to our calculated joint density of states (JDOS), for which we used the OptaDOS code,[179–181] and to previously reported[26] experimental data on 3D Ca_2N. The JDOS shown in Figure 3.4d (see section A.6 for details), has local maxima at wavelengths of 360 and 560 nm, in agreement with our experimental results. In addition, we extended a previously reported[26] Drude-Lorentz fit of a reflectivity spectrum for 3D Ca_2N to calculate the

attenuation coefficient of the 3D material (Figure 4e, see section A.6 for details). We calculated that the 3D material has local maxima at 360 and 520 nm, in agreement with the JDOS and our experimental data of 2D Ca_2N. Therefore, we assign the peaks in the UV–vis spectra of 2D Ca_2N to interband transitions.

We can learn more about the nature of the interband transitions by examining the calculated band structure of 2D Ca_2N (Figure 3.4f). Projections of the electron density integrated over states with energies -1.50 to -1.72 eV (highlighted in blue in Figure 3.4f) show that the electron density resides in the N p orbitals (Figure 3.4g), in agreement with previous findings.[35,66] Projections of the electron density integrated over states with energies 0 to +1.00 eV (highlighted in gold in Figure 3.4f) show that when these states are populated, the electron density occupies the interlayer gap (Figure 3.4h). Interestingly, direct transitions from the flat band (blue) to the unoccupied conduction band (gold) constitute nearly 100% of the lowest energy transitions, which begin at 900 nm (1.38 eV) to about 700 nm (1.77 eV) (Figure A.10). In addition, about 50% of the direct transitions that make up the peak at 560 nm in the JDOS result from transitions from these bands. This suggests that interband absorption events may add electron density to the interstitial electron gas, which could impact the materials work function and electrical conductivity under high intensity illumination.

The near IR data show a response at wavelengths longer than 800 nm (Figure 3.4b). To qualitatively understand whether the long-wavelength response is dominated by scattering or absorbance, we measured the transmittance with the cuvette inside or outside an integrating sphere (Figure A.11). The difference between the spectra, which should be due primarily to light scattering, does not have the same wavelength-dependence as the long-wavelength signal itself. In addition, the attenuation for the two geometries differs by only 20%. This suggests that the near IR response is largely due to the absorbance of light and not scattering. The long-wavelength response is most likely the result of an intraband absorbance of the 2D electron gas, although understanding the nature of the response will require samples that are more uniform in size than are produced in this work (see A.4 for details).

3.3 Conclusions

We have demonstrated that layered electrides can be exfoliated into 2D nanosheets despite the electrostatic interactions that hold the layers together. We have shown that the exfoliated 2D flakes are crystalline and metallic, which suggests that the delocalized anionic electrons are preserved in the 2D system. This work provides the first demonstration of a conceptually new class of high surface-area, electride nanomaterials.

These materials combine the high surface area of 2D materials with the exotic properties of anionic electrons. For example, monolayer Ca_2N has a theoretical specific surface area of 1460 m^2/g, which far exceeds the highest reported specific surface area ($\sim$20 m^2/g) of other electrides.[182] At the same time, Ca_2N has a high electrical conductivity (3.57×10^5 S/cm),[26] comparable to Al metal,[183] and a low work function (2.4 to 3.5 eV),[32,184] comparable to alkaline earth metals.[185] The material has high transparency for a metal: our experiments show that a 10-nm thick film would transmit 97% of light, while also having a sheet resistance of just 4 Ω/□. The properties of these electride nanomaterials suggest a number of applications, such as reagents or catalysts in chemical synthesis,[73,83,165,166] as transparent conductors,[168,169] or as battery electrodes.[88]

CHAPTER 4–BONDING IN 2D DONOR–ACCEPTOR HETEROSTRUCTURES

"The electron is not as simple as it looks."

- Sir Lawrence Bragg, 1924

4.1 Introduction

Nearly every material property, from color to conductivity to chemical reactivity, is influenced by the distance between atoms. As atoms approach and orbitals overlap, bonds form and wave functions delocalize. Even for materials in which interatomic distances are difficult to change, many theoretical approaches, such as Pauling's bond orders and resonance,[106] Mulliken's overlap populations,[107] or Hückel and Hoffmann's linear combination of atomic orbitals,[108,109] guide understanding and motivate the search for improved control. One such material system for which control of interatomic distances has been elusive is stacks of 2D materials, often called van der Waals heterostructures.[101] These heterostructures have attracted intense study because 2D materials with unique electrical, optical, and magnetic properties can be assembled in virtually any sequence, thereby encoding complex functions into the final material. Because of the weak van der Waals forces between adjacent layers, they are usually separated by 3 to 4 Å (Figure 4.1a), which is 1 to 2 Å more than covalent or ionic bonds. As such, 2D heterostructures with strong interlayer interactions, which could give rise to reduced interlayer distances and radically different properties, have been rarely explored.

Here we explore the creation of 2D donor–acceptor heterostructures to create strong bond-like interactions between layers. This strategy is analogous to NaCl salt formation, where the electron transfer from Na metal to Cl_2 gas yields a short Na–Cl distance due to the Coulombic attraction between positive and negative ions. A similar effect might be achieved in layered heterostructures if electrons were transferred from a 2D donor to a 2D acceptor. Well-established rules for electron transfer[186–188] provide two criteria for transferring a large amount of charge: the two materials must have (1) a difference in Fermi levels and (2) a large density of states

Portions of this chapter reproduced with permission from Woomer, A. H., Druffel, D. L.; Sundberg, J. D.; Pawlik, J. T.; Warren, S. C. Bonding in 2D Donor–Acceptor Heterostructures. *Journal of the American Chemical Society* **2019**, article ASAP. Copyright 2019 American Chemical Society.

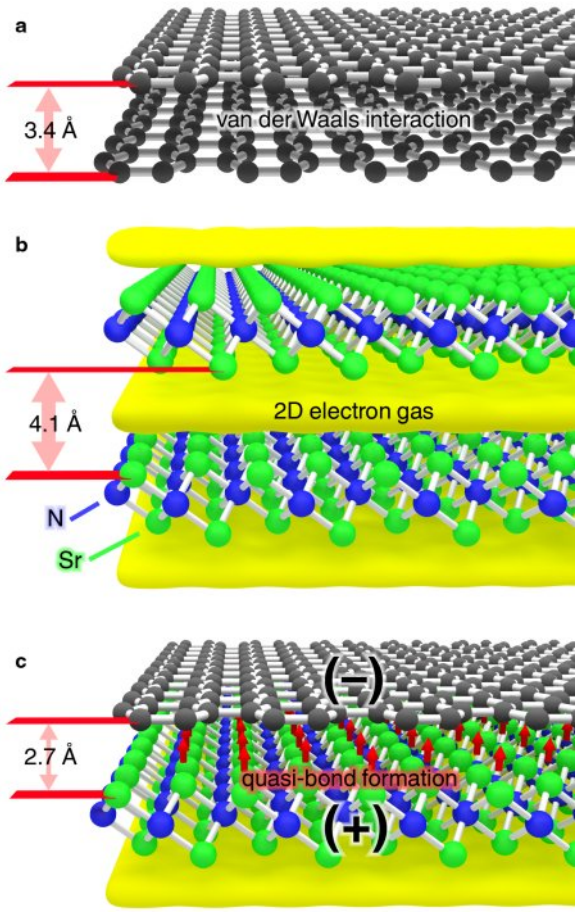


Figure 4.1: Illustration of a donor–acceptor heterostructure constructed from graphene and an electrene. (a) Bilayer of graphene. (b) Bilayer of Sr_2N, an electride in which layers of atoms (Sr: green, N: blue) alternate with layers of delocalized electrons (yellow), a 2D electron gas. Common layered electrides have the composition M_2N (M = Ca, Sr, or Ba) or M_2C (M = Y, Gd). (c) Electrene–graphene (e-C) heterostructure. Red arrows indicate quasi-bond formation between the electrene donor and graphene acceptor. The interlayer distance is shown for each material.

between the two Fermi levels.[162] In heterostructures such as MoS_2–WSe_2[189] or graphene–MoO_3,[190,191] only the first criterion is fulfilled so that fewer than 0.01 electron transfers per atom. The resulting attraction is insufficient to reduce the interlayer distance.[103,192] Therefore, if interlayer bonding is to be realized via electron transfer, a different type of 2D material that better meets these criteria is needed.

Recently, we synthesized a new class of 2D materials, called electrenes,[61,65] that are poised to act as exceptional electron donors. Electrenes are exfoliated from layered electrides,[26,61,65,87] an unusual class of materials of which typical examples are Sr_2N, Ca_2N, and Y_2C. In Sr_2N, for example, positively charged layers of $[Sr_2N]^+$ alternate with negatively charged layers of delocalized electrons, called a 2D electron gas (Figure 4.1b). When exfoliated, these electrons become exposed on the materials surface.[172] Electrenes are

an ideal candidate for meeting the first criterion of electron transfer because they can have an ultralow work function, *ca.* 2.4 to 3.3 eV,[26,48,49] that is comparable to lithium metal, and therefore have a large driving force for donating electrons. In addition, the carrier concentration is nearly 10^{15} cm^{-2},$^{(ref.\ 172)}$ 1000 times higher than undoped graphene,[90] thereby fulfilling the second criterion. Density functional theory (DFT) calculations show that electrons extend a considerable distance beyond the surface, suggesting that they can be readily donated.[172,193] Indeed, experiments have confirmed that surface-exposed electrons can be donated to adjacent materials. For example, in the case of a 30 nm thick electride flake next to $MoTe_2$, 0.11 e^- per atom was transferred.[87] This massive electron transfer sets the stage for an investigation of bond formation between 2D materials, which we report here.

4.2 Results and Discussion

4.2.1 Creating heterostructures with donor–acceptor interactions

We calculate from first-principles the heterostructures of electrenes with other 2D materials. DFT calculations were performed with CASTEP[54] using ultrasoft pseudopotentials[56] and a 600 eV plane wave cutoff energy. A GGA PBE functional[57] and Grimme's DFT-D correction[58] were used for exchange–correlation interactions and long-range dispersion forces, respectively. A Monkhorst–Pack grid[59] of 16 × 16 × 4 k-points was used for geometry optimization and increased to 32 × 32 × 6 for electronic structure calculations. Supercells were constructed to keep strain below 2% for each material.[162] A 12 Å vacuum space was introduced to prevent the interaction of periodic images. We calculated electron transfer using Bader charge analysis[194–197] for several functionals, including PBE, PBE0,[198] HSE06,[199] and sX.[200] A full description of methods is provided in the manuscript.[162]

Because of graphene's importance in the field of 2D materials,[90] we first considered an electrene–graphene heterostructure, which we label hereafter as e-C. Our calculations reveal a profound change in the heterostructure: graphite, with an interlayer distance of 3.4 Å (Figure 4.1a), and the electride Sr_2N, with an interlayer distance of 4.1 Å (Figure 4.1b), yield a heterostructure with an interlayer distance of just 2.7 Å (Figure 4.1c). A similar decrease has been calculated in a Ca_2N–graphene heterostructure.[172,193] To see if this unusual change also occurs with insulating and semiconducting 2D materials, we performed calculations on Sr_2N–boron nitride (e-BN), Ca_2N–phosphorene (e-P), and Ca_2N–ZrS_2 (e-ZrS_2). In all cases, we find a remarkable decrease in interlayer spacing, with distances from 2.0 Å (e-ZrS_2) to 2.8 Å (e-BN).

To investigate whether the reduced interlayer distance were related to electron transfer, we performed Bader charge analyses. For the e-C heterostructure, we found that 0.12 e^- were transferred to each carbon atom, in agreement with reports of a Ca_2N–graphene heterostructure.[172,193] In the e-BN heterostructure, 0.09 e^- were transferred per atom. However, we found that B accepts nearly all of the transferred electrons, so that 0.18 e^- were transferred per B. For a monolayer of phosphorene or ZrS_2, which are several atoms thick, electrons transferred principally to the atoms in direct contact with the electrene. In e-P and e-ZrS_2, 0.27 e^- and 0.53 e^- were transferred per contacting atom, respectively. We repeated these calculations with PBE0, HSE06, and sX because hybrid functionals mitigate PBE's self-interaction error,[201] which can overestimate electron transfer.[202] The electron transfer obtained with hybrid functionals fell within 15% of the PBE value, supporting the idea that electron transfer led to an electrostatic attraction between layers. The observations of electron transfer and shortened interlayer distance raise questions about the nature of interlayer bonding in these materials.

Historically, the nature of bonding in molecules and solids has been described using a bonding tetrahedron[203] (Figure 4.2a). Here we use a bonding triangle to quantify covalent vs ionic vs van der Waals interactions, as estimated by our calculations of electron transfer and bond length (Figure 4.2b). The horizontal axis of the bonding triangle is the average electrons transferred per acceptor atom. The electrene heterostructures show interactions that range from low polarity (similar to Cl-F) to intermediate polarity (similar to $TiCl_4$). The vertical axis of the bonding triangle is the interatomic distance, reported as a percentage of the van der Waals distance. For example, the e-C heterostructure has a Sr–C distance of 2.7 Å, which is 68% of the van der Waals distance for Sr + C (4.0 Å). We found that values of 65–70% are typical of all electrene heterostructures. For comparison, we quantified the interatomic distances in all compounds from the Materials Project[204] (Figure 4.2c) and found that covalent or ionic interactions were 45–70%. The region between 70% and 95% has been called the van der Waals gap,[205] a range of interatomic distances where bonding is rarely observed. The observation of bond distances between 65% and 71% in electrene heterostructures (Figure 4.2b) is atypical of covalent, ionic, and van der Waals interactions, and we therefore label this interaction a quasi-bond (Figure 4.1c). In addition, on the basis of the charge transfer between layers, we use the name donor–acceptor heterostructure (Figure 4.2b), in contrast to van der Waals heterostructure, to describe an assembly made of an electrene and another 2D material.

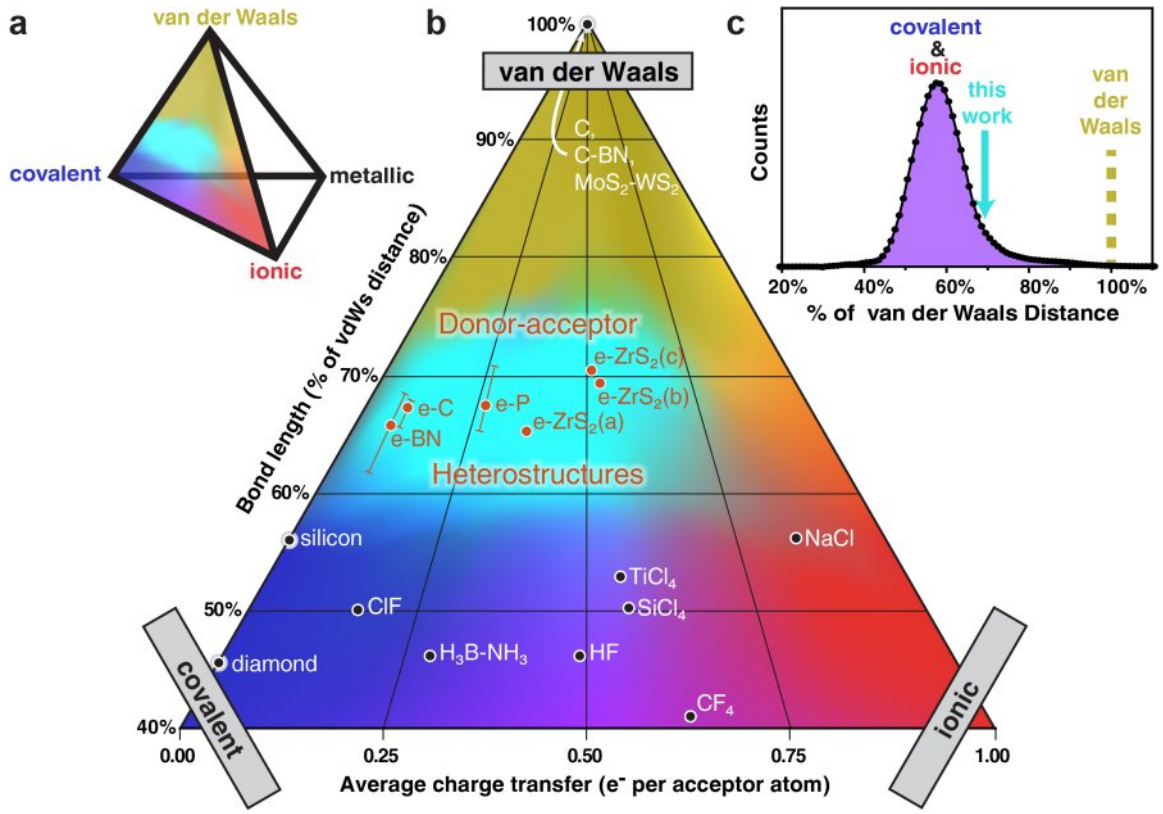


Figure 4.2: Bonding and electron transfer in molecular compounds, van der Waals materials, and donor–acceptor heterostructures. (a) Traditional representation of bonding types including van der Waals, ionic, covalent, and metallic. (b) Bonding interactions between van der Waals, covalent, and ionic compounds as described by bond length (% of van der Waals distance) and average electron transfer per acceptor atom. For example, the C–C bond of diamond has no net electron transfer, so the compound lies within the covalent region, while in NaCl, 0.83 e^- are transferred from Na to Cl, so it appears within the ionic region. (c) Examination of the prevalence of bond length in all crystals from the Materials Project. The peak represents covalent and ionic bonds.

4.2.2 Understanding sterics and energetics of donor–acceptor heterostructures

The unusual placement of the donor–acceptor heterostructures within the bonding triangle warrants a deeper understanding of how and why they form. To visualize electron transfer, we plotted the electronic structure of isolated graphene (Figure 4.3a), Sr_2N (Figure 4.3b), and the e-C heterostructure (Figure 4.3c). Upon formation of the heterostructure, we observe an increase in the electron density in the π^* orbitals of graphene and a decrease in the electron density of the 2D electron gas of Sr_2N. Additionally, we illustrate this electron transfer in Figure 4.3d as Δn:

$$\Delta n = n_{HS} - (n_e + n_g) \tag{4.1}$$

where n_{HS}, n_g, and n_e are the electron densities of the e-C heterostructure, graphene, and monolayer Sr_2N, respectively. These calculations show that electrons are primarily transferred from the electron gas at the interfacial surface of Sr_2N into the π^* orbitals of graphene, with almost no change in the electron gas on the exposed surface of Sr_2N. The apparent weakening of in-plane (σ) interactions in graphene is similar to that observed in donor-doped graphite.[206] This visual depiction of electron transfer confirms that the electron gas is readily donated to adjacent 2D materials and suggests there is a strong Coulombic attraction between layers.

We sought to characterize this attraction and therefore considered the interaction energy, ΔE, between adjacent layers:

$$\Delta E = \frac{(E_d - E_\infty)}{A} \tag{4.2}$$

where E_d is the energy of the heterostructure at a separation d in Å, E_∞ is the energy of a noninteracting heterostructure, and A is the interfacial area in square meters. We calculated the interaction energy for the donor-acceptor heterostructures, including three orientations of e-ZrS_2 (Figure 4.3e–g), and plot the results in Figure 4.3h. We find for each heterostructure that ΔE is negative as d approaches the interlayer distance of the optimized structure, which confirms that electron transfer is energetically favorable. To quantify and compare the strength of the interaction in each system, we report the binding energies as the minimum of ΔE. In general, we found that the binding energy of donor-acceptor heterostructures can range from 1.0 to 3.0 J/m^2. For comparison, the surface energy of diamond on (111) is 5.1 J/m^2 $^{(ref.\ 207)}$, and we calculated that the binding energy of bilayer graphene is 0.28 J/m^2, similar to reported values.[208] The binding energy in donor–acceptor heterostructures is over an order of magnitude larger and suggests that a strong attractive force, comparable to ionic or covalent bonding, exists between layers. Although the choice of functional and interpretation of long-range dispersion forces can affect binding energy, this does not obscure the marked contrast between donor–acceptor heterostructures and van der Waals materials.

To better understand these results and elucidate structure–property relationships for the binding energy of donor-acceptor heterostructures, we turn to two familiar concepts that govern bond formation and electron transfer: steric hindrance and reorganization energy.

Steric hindrance occurs when a bulky substituent blocks an active site with repulsive interactions. In chemistry and biology, the control of sterics has a profound effect on reaction selectivity, catalytic activity, and

interaction energy. In e-ZrS_2(a) (Figure 4.3e), interfacial Ca and S are directly aligned, thus exhibiting strong steric hindrance. Indeed, we found an interlayer distance of 2.75 Å and a binding energy of 1.96 J/m^2. But when we translate the layers by a fraction of a unit cell (Figure 4.3f,g), steric hindrance is minimized. This led to the smallest interlayer distances, 2.0 Å, and largest binding energies, 3.0 J/m^2, of any donor–acceptor heterostructure we investigated. These heterostructures also had the largest electron transfer (*ca.* 0.51 e$^-$ per acceptor atom). Our results show that the strongest interlayer interactions will occur when the two materials have matching lattice constants (the crystals are commensurate) and are positioned so that a protruding atom in one layer fits into a cavity in the adjacent layer (the crystals interdigitate). This finding has a direct parallel in molecular and solid-state systems, where the removal of steric hindrance leads to stronger and shorter bonds.[209] By selecting 2D materials with varying degrees of lattice matching and steric hindrance, we predict that it is possible to control electron transfer and binding energy and, therefore, the resulting properties of the heterostructure.

Reorganization energy is the energy penalty for nuclear reorganization that accompanies electron transfer.[188] Understanding this energy has been of central importance in the development of Marcus theory[188] and polaron theory.[210] The e-C and e-BN heterostructures illustrate the importance of reorganization energy. Both heterostructures have similar amounts of electron transfer and interlayer distances, which suggests that they should have comparable binding energies. However, we observe different energies: 1.15 J/m^2 for e-C but just 0.21 J/m^2 for e-BN (Figure 4.3h). In the e-BN structure, we observe that some B distorts out of plane toward the electrene, and we calculate that this distortion costs 0.5 J/m^2, which explains a significant portion of the difference between e-C and e-BN. The reorganization energy is so large that the nuclear rearrangement is preceded by the physisorption of planar BN on the electron gas at a separation of 4.0 Å (Figure 4.3h). This example illustrates that heterostructure composition can be used to vary reorganization energy, and thus binding energy and potentially other heterostructure properties.

4.2.3 Donor–acceptor analogy

Of the donor–acceptor heterostructures, e-BN is perhaps most surprising. Our calculations show that the BN is highly doped (Figure 4.2b), with a carrier concentration of 2×10^{14} cm^{-2}, even though the conduction band of planar BN is 2.0 eV above the Fermi level of the electrene. This electron transfer is even more surprising given that prior efforts to dope BN with alkali metals have not succeeded.[211]

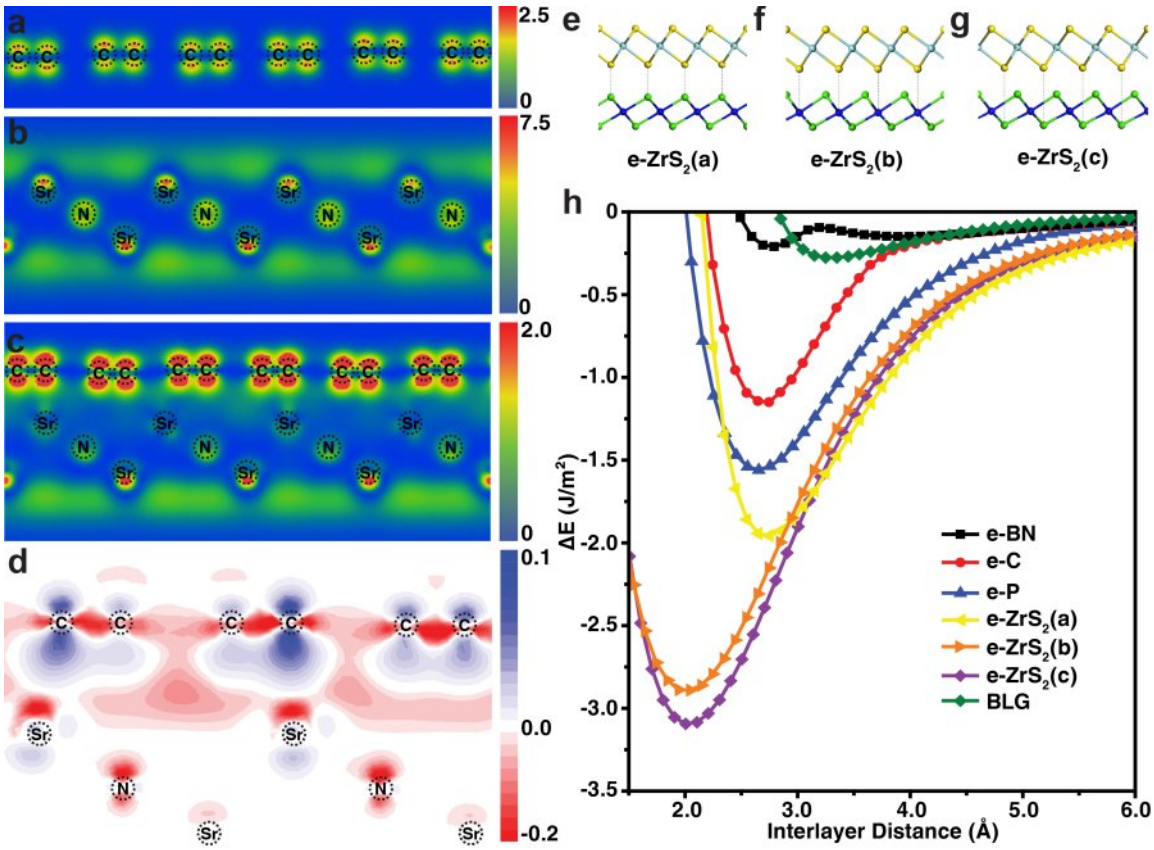


Figure 4.3: Orbital projections, electron density, and interlayer interaction energies in donor–acceptor heterostructures. The orbital projection of electronic states near the Fermi level ($\pm$25 meV) for (a) monolayer graphene, scale bar: $e^{-}Å^{3} \times 10^{-4}$; (b) monolayer Sr_2N, scale bar: $e^{-}Å^{3} \times 10^{-4}$; and (c) the e-C heterostructure, scale bar: $e^{-}Å^{3} \times 10^{-3}$. (d) Change in electron density, Δn, upon assembly of the e-C heterostructure. The gain (loss) of electron density is shown in blue (red). For calculating Δn, graphene and Sr_2N in the heterostructure have the same coordinates as isolated graphene and monolayer Sr_2N. (e–g) Three structural orientations for e-ZrS_2. Dashed lines between atoms indicate their alignment along the z axis. (h) Interlayer interaction energies, ΔE, for donor–acceptor heterostructures and bilayer graphene (green). The binding energies in (h) are converged with respect to the choice of supercell: larger supercells with less strain afford the same binding energy.

To understand the electron transfer in e-BN, we examine an analogous system: the donor–acceptor molecule ammonia-borane, H_3N–BH_3 (Figure 4.4a). Although the B–N bond forms in a seemingly simple way—by donation of ammonia's lone pair electrons to the empty p_z orbital of B—the molecular orbital diagram shows this explanation cannot be correct because the B p_z orbital is higher in energy than ammonia's lone pair. Instead, the bond forms when the wave functions of the two molecules mix, creating a stabilized bonding state into which electrons from ammonia are transferred (Figure 4.4a). The partial transfer of electron density from ammonia to borane through a polar covalent bond is a classic example of a donor-acceptor interaction.

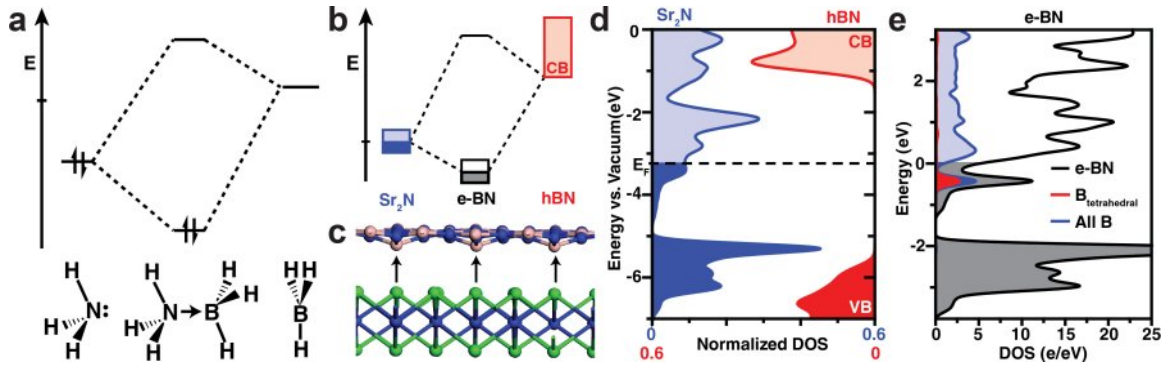


Figure 4.4: Donor–acceptor analogy to rationalize electron transfer in e-BN. (a) Molecular orbital diagram of NH_3–BH_3. (b) Molecular orbital diagram of Sr_2N (blue), hBN (red), and e-BN (black), suggesting the creation of a quasi-bond. (c) Supercell of e-BN, showing the displacement of boron atoms into the interlayer space. Arrows depict transfer of the electron gas to the displaced B and formation of a donor–acceptor interaction. (d) Density of states (DOS) of Sr_2N (blue) and hBN (red) relative to one another. (e) DOS of e-BN (black) and partial DOS for displaced B atoms (red) and all B atoms (blue). e-BN is metallic, but mobility is low.

We hypothesize that the quasi-bond in e-BN forms via a similar mechanism. Although the conduction band in BN is too high in energy to accept electrons from the electrene (Figure 4.4b), bonding between the electrene and BN could create an analogous donor-acceptor interaction at the interface between materials. In fact, the conduction band of BN is made largely of empty B p_z orbitals, thereby providing the optimal orientation to create a hybrid state with the electron gas. To assess bonding in e-BN, we performed a geometry optimization (Figure 4.4c) and examined the resulting electronic structure (Figure 4.4d,e). Structurally, we find that one in nine B distorts out-of-plane (Figure 4.4c), providing these B with a tetrahedral geometry. We note that the proportion that distort depends on the choice of supercell, but, in all cases, distortion is observed. The same distortion occurs in H_3N–BH_3, where borane undergoes a planar-to-tetrahedral rearrangement to increase the wave function overlap that is needed for bonding. Stronger evidence for bonding in e-BN is seen in a comparison of the density of states before (Figure 4.4d) and after (Figure 4.4e) assembling e-BN. Upon forming e-BN, new states emerge -0.5 eV below the Fermi level (Figure 4.4e). These states partially derive from tetrahedral B (Figure 4.4e, red), demonstrating its important role in bonding. From a Bader charge analysis, we calculate that each tetrahedral B receives 0.75 e^- from the electrene, which is even more than the *ca.* 0.3 e^- that borane accepts from ammonia.[212] These remarkable similarities demonstrate the utility of the donor-acceptor concept in understanding these 2D heterostructures. Donor-acceptor interactions have not been observed in van der Waals heterostructures, suggesting that the heterostructures presented here can have unique electronic structures and properties. For example, the ability to produce donor-acceptor interactions

by stacking 2D materials could be useful in rectifying current for new classes of diodes, separating electrons and holes in solar cells or photodetectors, or generating power in piezoelectrics.

4.2.4 Understanding the polarity of quasi-bonds

The discovery of donor–acceptor interactions in 2D heterostructures suggests that classical descriptors of bonding, e.g., covalent or ionic, can be applied to quasi-bonds. To test this idea, we used atomic density deformation (Δn_{add}), an important indicator of bonding,[213] to visualize the changes that occur when donor-acceptor heterostructures form. We calculate Δn_{add}, as

$$\Delta n_{add} = n_{HS} - n_{AO} \tag{4.3}$$

where n_HS is the electron density of the final, optimized heterostructure and n_AO is the electron density of noninteracting atomic orbitals that are placed at identical atomic coordinates. In short, Δn_{add} shows where electrons move when bonds form. For reference, we begin by plotting Δn_{add} of three well-known systems: H_2, H_3N–BH_3, and NaCl (Figure 4.5a-c). In H_2, an increase in electron density (blue) is seen in the area between H atoms, which arises from strong covalent bonding. In NaCl, electron density decreases (red) on Na and increases on Cl, which results from a strong ionic interaction. Between these extremes is ammonia-borane, in which Δn_add shows characteristics of both covalent and ionic bonding. We first calculate the Δn_{add} for e-BN and observe a pronounced increase in electron density between tetrahedral B and the electron gas (Figure 4.5d, black arrows). This change resembles Δn_{add} of H_2 and H_3N–BH_3, suggesting that the interlayer interaction has polar covalent character. In the e-C heterostructure, the decrease in electron density within the interlayer gap is not consistent with a covalent interaction (Figure 4.5e) and implies that the interaction is primarily ionic. The e-P heterostructure is intermediate between these extremes, with only a small increase in electron density in the interfacial region (Figure 4.5f, black arrows). This suggests that the bond is best described as polar covalent.

To better understand these bond-like interactions in donor-acceptor heterostructures, we examine a guiding principle of molecular orbital theory: the energy difference between two interacting orbitals or states will influence bond polarity. As this energy difference, called the Coulomb integral, becomes larger, the resulting bond is less covalent and more ionic.[214] To see if the trends in bonding from ionic e-C to nearly covalent e-BN could be explained by the Coulomb integral, we inspected the energy difference between

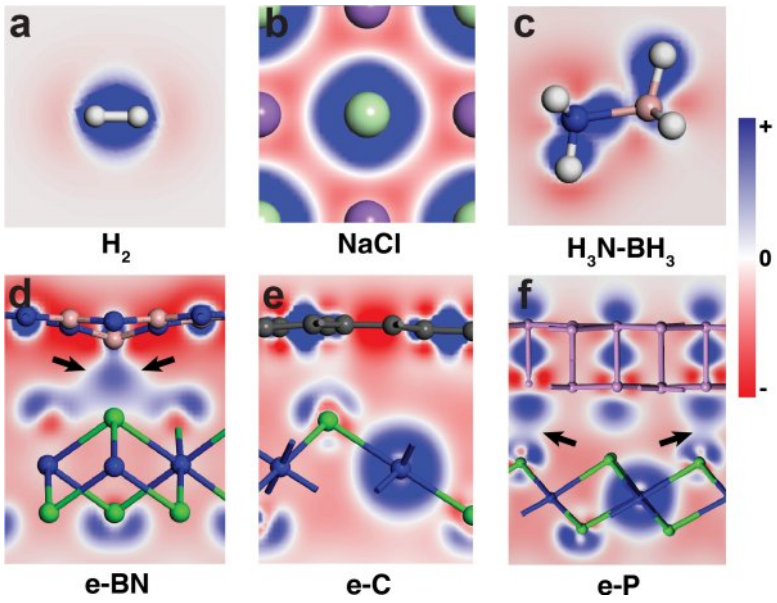


Figure 4.5: Atomic density deformation of donor–acceptor heterostructures and common materials. The Δn_{add} for (a) H_2, scale bar: ± 0.2 $e^- Å^3$; (b) NaCl, scale bar: ± 0.05 $e^- Å^3$; (c) NH_3–BH_3, scale bar: ± 0.2 $e^- Å^3$; (d) e-BN, scale bar: ± 0.1 $e^- Å^3$; (e) e-C, scale bar: ± 0.1 $e^- Å^3$; (f) e-P, scale bar: ± 0.1 $e^- Å^3$. Blue and red regions show increases and decreases in electron density, respectively, and are calculated versus noninteracting atomic orbitals.

interacting states. In e-C, we found an energy difference of 1.2 eV between the Fermi levels of electrene and graphene. This decreased to 0.7 eV in e-P, as calculated from the difference between the electrene's Fermi level and the bottom of phosphorene's conduction band. In e-BN, the energy difference between the electron gas and BN's conduction band is large, as discussed above, but the distortion from planar to tetrahedral B lowers the conduction band[214] and decreases the Coulomb integral while also maximizing wave function overlap. This results in interfacial bonds with the lowest polarity of the three heterostructures. These findings confirm the predictive role of the Coulomb integral in determining bond polarity in donor–acceptor heterostructures. We describe below potential applications that emerge from the control over the nature of quasi-bonding.

4.2.5 Applications of donor–acceptor heterostructures

The introduction of quasi-bonding interactions in stacked 2D materials enables a new approach to designing materials for catalytic, mechanical, optoelectronic, and energy applications. Here we highlight how quasi-bonding in donor–acceptor heterostructures can be used to reduce sliding friction, control work functions, and engineer the voltages in lithium-ion batteries.

Historically, layered materials such as graphite and MoS_2 have been attractive additives in solid lubricants to minimize friction. The lubricity is assessed from sliding energy, which is the activation energy for one layer to translate past the other. The short interlayer distances and large binding energies of donor–acceptor heterostructures might suggest that translation is unfavorable. However, we calculated the potential energy surface for sliding in e-ZrS_2, e-BN, and e-C (Figure 4.6a–c) and found that the sliding energy can span 4 orders of magnitude, from 181 meV/atom for e-ZrS_2 to 0.26 meV/atom for e-C. Surprisingly, the sliding energy of e-C is significantly lower than those of MoS_2[214] (9 meV/atom) and graphene[215] (6.5 meV/atom) and suggests that donor-acceptor heterostructures can exhibit lower friction than common lubricants—called superlubricity—despite shorter interlayer distances (Figure 4.2b) and stronger interlayer interactions (Figure 4.3h). To understand this unexpected outcome, we examine the roles of reorganization energy and steric hindrance on sliding energy. Reorganization energy, as discussed above for e-BN, results in an energy penalty for translation due to changing bond lengths at the interface. Steric hindrance results in atomic repulsion as materials slide, often leading to changes in interlayer distance. This is illustrated by the large sliding energy of e-ZrS_2, for which translation causes repulsion between S and Ca. Similarly, the low sliding energy of e-C results from even less steric hindrance than bilayer graphene, as e-C has an incommensurate interface[216] for which a periodic interdigitation of atoms cannot occur. The surprising combination of strong interlayer interactions and superlubricity could result in a new class of lubricants with distinctive rheology and wetting characteristics.[217]

The work function, or the energy required to remove an electron from the surface of a material to vacuum, is an important property for the design of electronic materials and catalysts. Work functions depend on surface dipoles and, therefore, can be tailored using dangling bonds, surface reconstruction, and adsorbates. We calculate that a freestanding electrene monolayer of Ca_2N has a work function of 3.5 eV, which is consistent with experimental measurements of the bulk Ca_2N surface.[26] When we assemble a donor–acceptor heterostructure, we find that the work function on the electrene side of the heterostructure always decreases, usually by 0.1 to 0.5 eV (Figure 4.6d). In general, in donor–acceptor heterostructures with greater electron transfer, such as e-ZrS_2(c), there is a larger decrease in the work function. We attribute this decrease to electron transfer, which sets up a surface dipole that facilitates electron emission in the opposite direction (Figure 4.6e). The possibility of achieving exceptionally low work functions in a highly conductive material suggests potential applications in, for example, electron emission.[218]

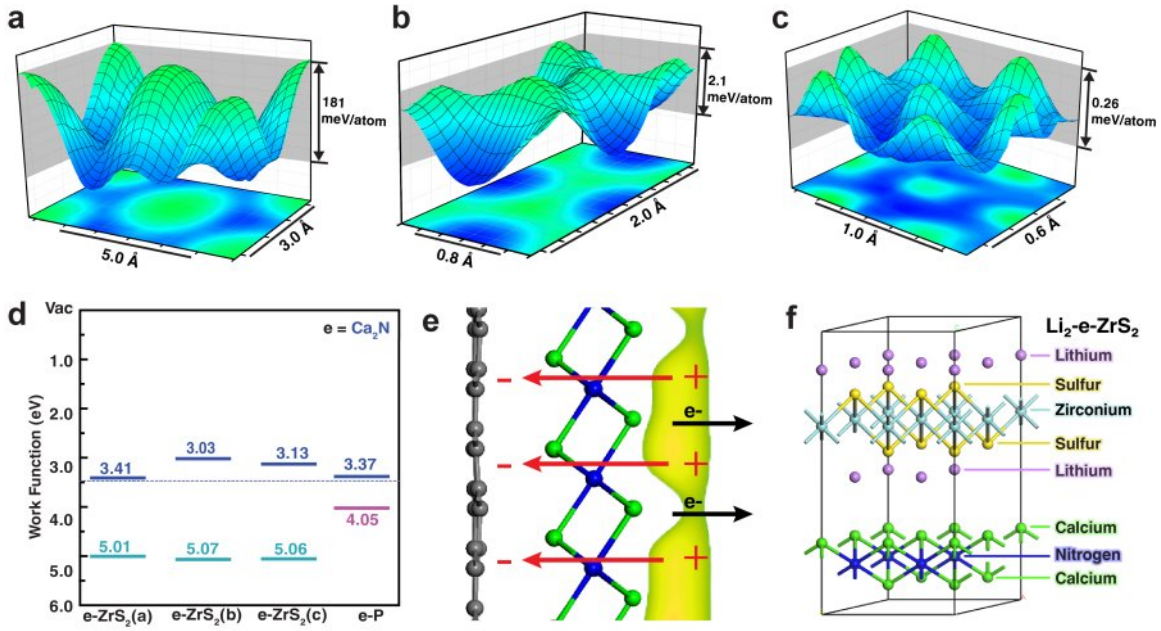


Figure 4.6: Applications of donor–acceptor heterostructures. The potential energy surfaces for sliding in (a) e-ZrS_2, (b) e-BN, and (c) e-C. (d) Work functions of the electrene surface (dark blue, lower work function) and adjacent 2D material surface (higher work function) in four donor–acceptor heterostructures. For reference, the work function of an electrene monolayer is shown as a dashed line. (e) Depiction of the electric field (red arrows) in e-C that will lower the work function from the electron gas (black arrows). (f) Structure of a repeating e-ZrS_2 heterostructure that has been intercalated with lithium ions.

Graphite is an ideal battery anode because of its high capacity, fast ion transport, and negative potential for lithium-ion insertion. Transition metal dichalcogenides (TMDCs) also have high capacities and fast transport, but the potentials for lithium insertion are neither very negative nor very positive, making them unsuitable as an anode or cathode. We hypothesized that integrating TMDCs in donor-acceptor heterostructures could alter their potentials for ion insertion. To test this idea, we calculated the voltage for intercalation, V_{int}, of Li into e^- ZrS_2 to be

$$V_{int} = \frac{E_{Li_2-e-ZrS_2} - (E_{e-ZrS_2} + E_{Li})}{2e} \tag{4.4}$$

where E_{Li}, E_{e-ZrS_2}, and $E_{Li-e-ZrS_2}$ are the energies of Li (two atoms in unit cell), e-ZrS_2, and e-ZrS_2 with two Li per formula unit (Figure 4.6f), respectively, and e is the charge of an electron. We found that V_{int} shifts from +1.9 V vs Li/Li^+ $^{(ref.\,219)}$ to -0.08 V vs Li/Li^+. Although calculations for Li insertion are often imprecise, the large effect seen here indicates the likelihood of using donor-acceptor heterostructures to provide many new electrode compositions for insertion batteries. Just as in van der Waals heterostructures,[220]

we expect that features such as stacking sequence, 2D material selection, and other structural modifications could afford greater control over electrode potential.

4.3 Conclusions

In this work, we have described a class of materials in which electrons are transferred from a 2D donor to a 2D acceptor, which creates bond-like interactions between layers with unusual properties. Because of the Lego-like modularity of 2D materials,[101] our findings provide innumerable opportunities to explore 2D donor-acceptor heterostructures with distinctive structures, compositions, and stacking sequences. Multilayer $MoTe_2$ has been successfully transferred onto thick Ca_2N $^{(ref.\ 87)}$, suggesting that mechanical assembly of 2D donor-acceptor heterostructures may be possible. Alternative routes may yield interfaces with less contamination, however, such as chemical vapor deposition. More broadly, our findings extend the donor-acceptor concept from small molecules and polymers to 2D materials. The donor-acceptor concept provides many structure-property relationships that can predict useful properties in 2D heterostructures. For example, donor-acceptor systems have a built-in electric field that is commonly used to rectify current or separate excitons. This could make 2D donor-acceptor heterostructures particularly helpful in minimizing recombination at the metal-semiconductor junction in photovoltaics, since 2D materials have clean interfaces and are thin enough to permit rapid charge transport. Moreover, because electrenes can be combined with many other 2D materials, it should be possible to build diodes with complex functions. For example, if combined with a 2D ferromagnet, the resulting heterostructure could rectify spin-polarized current. Lastly, although this work focuses on the electron-donating properties of electrenes, it is possible that other 2D materials with low work functions and high carrier concentrations may be used in place of electrenes, further expanding the opportunities for materials discovery.

CHAPTER 5–THE SYNTHESIS AND ELCTRONIC STRUCTURE OF Y_2CF_2: A CRYSTALLINE STACK OF MXENE SHEETS

"A scientific research is a search after truth, and it is only after discovery that the question of applicability can be usefully considered."

- Henri Moissan, 1897

5.1 Introduction

Research into layered and 2D metal carbides such as MXenes has rapidly grown[221] due to their remarkable properties and applications in electronic,[222,223] sensing,[224,225] and energy storage devices.[226–228] Despite the interest in MXenes in the last decade, all of the MXenes reported have a random mixture of surface terminations (-O, -OH, -F), which complicates their study and use. The presence of multiple surface terminations on MXene sheets owes to their synthesis, which involves etching a MAX (M = metal; A = Al, Ga, Si, In; and X = C, N) phase with aqueous HF.[229] Further complicating their study, restacked 3D films of MXenes have turbostratic disorder[230,231] and often contain ions, solvent, and other species in between their layers.[232,233]

Given the general interest in MXenes, it is remarkable that no pure (i.e. no -O, -OH), crystalline transition metal carbide fluoride has been reported. Of the transition metals, only Y,[125,234–242] Sc,[125,243–247] Zr,[125,248,249] and W[250] have been studied as pure metal carbide halides, and none as fluorides, leaving a large void in our knowledge of ternary phase diagrams. Our efforts in this work are to synthesize the first transition metal carbide fluoride, and to highlight a largely unexplored class of compositions that may find utility in optoelectronics.

Here we report Y_2CF_2, a layered crystal with a unit cell isostructural to a 2D MXene, in which layers are capped only by fluoride anions. Relatively strong electrostatic interactions bind the layers together into a 3D crystal. Therefore, we consider Y_2CF_2 as a pure 3D crystalline stack of MXene-like sheets. Instead of the etching approach, we introduce a new synthetic method. We directly synthesize the 3D crystal through a

high-temperature solid-state reaction in the absence of air and water. The synthesis affords the 3D crystal in high yield and purity and ensures that only fluoride ions terminate the layers.

5.2 Results and discussion

5.2.1 Synthesis and crystal structure

We accomplish the synthesis of Y_2CF_2 by reacting stoichiometric amounts of yttrium, carbon, and fluorine at 1240 °C in sealed tantalum ampoules according to the following reaction:

$$4Y + 3C + 2YF_3 \rightarrow 3Y_2CF_2 \tag{5.1}$$

The product is a pellet of beautiful green crystals (Figure 5.1a) that easily grinds into a powder (Figure 5.1b). Unfortunately, the synthesized crystals were too small and inter-grown to perform single crystal X-ray diffraction measurements. Therefore, we combined two independent approaches to determine the crystal structure.

First, we performed powder X-ray diffraction experiments of the product and obtained a diffraction pattern (Figure 5.1c), which indexed as a trigonal crystal structure with space group $P\bar{3}m1$-D_3d. Then, we refined the pattern by the Rietveld method[251] (Table 5.1). The analysis concludes that the trigonal space group $P\bar{3}m1$ is a good fit, with lattice constants a=3.6651 (3) Å and c = 6.29697 (7) Å at room temperature (Figure 5.1c, Table 5.1).

Independently, we used an evolutionary search algorithm, USPEX,[252] to explore the phase space for Y_2CF_2 crystal structures computationally. The algorithm computes the enthalpy of hundreds of candidate crystal structures and uses similarities in bond distances, coordination, symmetry, and a number of other identifiers to find the most stable phase for a given composition. Using the algorithm, we found that the $P\bar{3}m1$ structure is the most enthalpically favorable phase for the composition Y_2CF_2, in agreement with our diffraction experiments. We then performed a geometry optimization calculation using the PBEsol[156] functional to calculate the lattice constants. We calculated constants very close to the experimental value (1.6% shorter in a and 0.8% shorter in c, Figure 5.2b).

We also note that many yttrium compounds are isostructural to gadolinium and holmium compounds (e.g. YOCl[253], YCl_3[254], YF_3[255]) because of the similarity in the crystallographic ionic radius of Y (104 pm)[256] to that of Gd and Y (108 and 104 pm respectively).[256] In support of our indexing, we found known

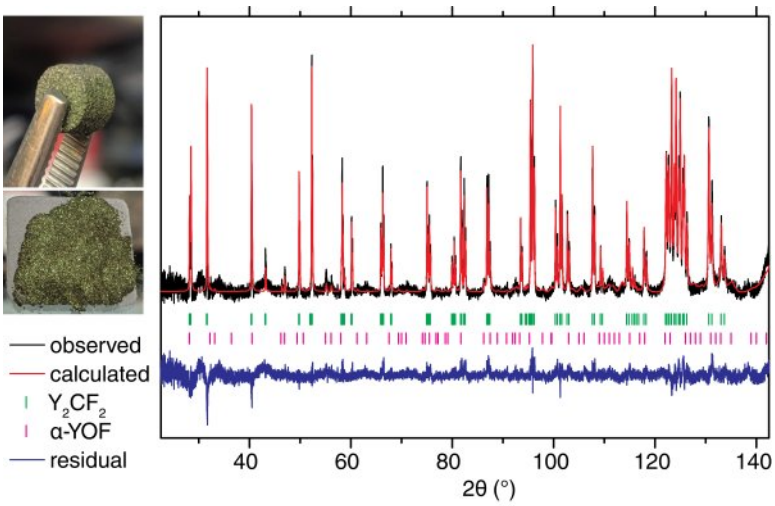


Figure 5.1: Observed, calculated and difference profiles for Y_2CF_2 at 300 K measured on a Rigaku Smartlab diffractometer with a Cu Kα source, λ = 1.5406 Å. The pattern was refined to two phases, a Y_2CF_2 phase and a α-YOF phase (Space group P4/nmm, a = 3.922 (2) Å, c = 5.409 (4) Å), which made up less than 4% by mole of the sample. Vertical tick marks indicate calculated reflection positions. The broad maxima in the background are due to diffuse scattering from the quartz ampoule.

Table 5.1: Final parameters, R factors and interionic distances for Y_2CF_2 at 300 K. Space group $P\bar{3}m1$. a = 3.6651 (3) Å, c = 6.29697 (7) Å. Volume = 73.2536 Å^3, density = 4.394 g cm^{-3} Rietveld analysis standard agreement indices are the residual factor Rp = 2.5%, the weighted residual factor Rwp = 4.97% and the goodness of fit factor S = 1.96. U, V, W (deg^2): 0.000, -0.021, 0.000

Atom	Site	symmetry	X	Y	Z	B (Å^2)	N	Occupancy
Y	2d	3m	$\frac{1}{3}$	$\frac{2}{3}$	0.21450 (10)	0.526 (12)	2	1.00 (1)
C	1a	$\bar{3}$m	0	0	0	0.1 (4)	1	0.93 (3)
F	2d	3m	$\frac{1}{3}$	$\frac{2}{3}$	0.0.6031 (5)	0.555 (11)	2	1.00 (6)

gadolinium and holmium compounds (Gd_2CF_2 [257] and Ho_2CF_2 [258]) isostructural to Y_2CF_2 with very similar lattice constants.

The crystal structure of Y_2CF_2 (Figure 5.2a) is similar that of MXenes. Six Y cations octahedrally coordinate each carbon atom and the Y_6C octahedra (Figure 5.2c) bond into a two-dimensional layer—just like the 2D Ti_2C(-O, -OH, -F) MXene.[259] However, in the Y_2CF_2 structure, each Y cation also coordinates to four F^-, forming face-capped octahedrons (Figure 5.2b). Thus, in Y_2CF_2, double layers of fluoride ions bind adjacent metal-carbide layers forming a crystalline 3D stack of MXene-like sheets.

Naturally, we became interested in the interlayer bonding of Y_2CF_2, which is distinct from the 2D nature of MXenes. The F coordinate to 4 Y with four nearly symmetric distances (Figure 5.3c), three to the Y in the adjacent layer (2.408 Å) and one to the Y in the opposite layer at an only slightly elongated distance (2.447

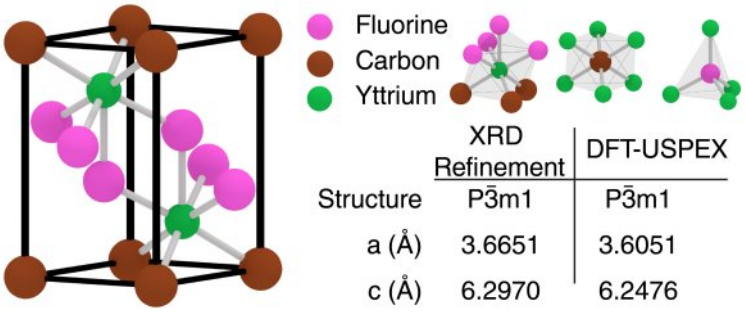


Figure 5.2: Crystal structure, bonding polyhedral, and lattice constants for Y_2CF_2. The crystal structure and lattice constants obtained independently from two methods: 1) experimental synthesis and Rietveld refinement of X-ray diffraction data and 2) USPEX, a DFT-based search algorithm to find the most stable crystal structure for a given composition.

Table 5.2: Atomic distances in the crystal structure of Y_2CF_2, determined by the refinement of powder X-ray diffraction data. All distances are reported in Å.

Atoms	Atomic distances Å
Y–Y	3.4315 (2), 3.6651 (3), 4.1720 (1)
Y–F	2.4077 (3), 2.4470 (1)
F–F	2.4827 (7)
Y–C	2.5104 (6)
F–C	3.2747 (6)

Å)(Table 5.2). This suggests that the interlayer bonding is relatively strong (as strong as the Y–F bonds) and electrostatic in nature.

This electrostatic interlayer bonding contrasts with that of other known layered metal carbide halides. For example, in Y_2CCl_2,[125] which shares the same crystal structure (Figure 5.3b, Cl coordinates only to 3 Y, all in the adjacent layer (2.755 Å). The distance to the Y in the opposite layer is nearly double (4.770 Å), far too long for any Y–Cl electrostatic bonding interaction (Figure 5.3d). Instead, the primary interlayer interactions in Y_2CCl_2 are weak van der Waals forces.

Using DFT we calculated the binding energy—the energy difference between the equilibrium bulk separation and the state in which the planes are separated by an infinite distance as approximated by a 15 Å-thick vacuum-gap (Figure 5.3e). The binding energy for Y_2CF_2 is 0.90 J/m^2, over 6$\times$ that of Y_2CCl_2 (0.14 J/m^2) and 3$\times$ that of graphite (0.31 J/m^2). Electrostatic interactions between the F anion and Y cation likely account for the greater binding energy. This leads us to conclude that Y_2CF_2 is an ionic crystal in the out-of-plane direction. Still, the binding energy of Y_2CF_2 is less than that of other layered crystals that have been exfoliated successfully into 2D materials.[61] These calculations suggest that it may be possible to

exfoliate Y_2CF_2 into 2D flakes, although with somewhat greater difficulty than van der Waals crystals like Y_2CCl_2 or graphite.

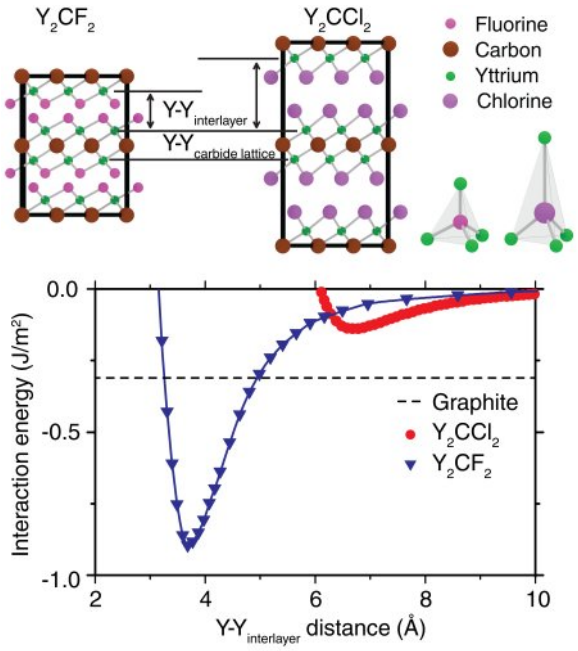


Figure 5.3: Comparison of the crystal structure of Y_2CF_2 to Y_2CCl_2 showing a) the unit cells along the [100] axis, b) the tetrahedral bonding polyhedron for yttrium and fluorine in Y_2CF_2 and the same polyhedron drawn for Y_2CCl_2 with the elongated Y–Cl distance in the z-direction, and c) the interlayer binding energy for Y_2CF_2 (blue) and Y_2CCl_2 (red) calculated using DFT.

5.2.2 Composition and purity

We sought to confirm the composition of our sample, as some metal carbides can sustain a variety of sub-stoichiometric compositions. We used energy-dispersive X-ray spectroscopy (EDS) to quantify the amount of yttrium and fluorine (Figure C.2) and measured a ratio of 1:0.98 $\pm$ 0.05 Y:F in agreement with the stoichiometry of Y_2CF_2. These results also agree with the refinement from powder X-ray measurements, which yielded an occupancy of 1 for both yttrium and fluorine in each of their 2d sites. Unfortunately, our EDS instrument does not quantify carbon reliably because the signal is obscured by electronic noise. Therefore, we quantified carbon by refining the occupancy of the 1a (carbon) site during the Rietveld refinement, which revealed that only 93 $\pm$ 3 % of carbon sites are occupied. We conclude that the composition Y_2CF_2 represents the synthesized phase, though the real structure has a small fraction of carbon vacancies, $Y_2C_{0.93}F_2$.

5.2.3 Electronic structure of Y_2CF_2

To investigate the effect of interlayer ionic bonding on the electronic structure of stacked MXene sheets, we performed optical measurements experimentally and modeled the materials optoelectronic properties using DFT. For all of the DFT calculations of the electronic structure, we used the HSE06 hybrid functional,[260] which we selected because of its suitability for estimating band gaps.

First, we performed transmission measurements (described in section C.3) to measure the absorption coefficient (Figure 5.4a). We observe a gradual increase in absorption beginning at ∼775 nm (1.6 eV), which we attribute to the band gap. The absorption increases and plateaus from 400-550 nm at a magnitude of 3.4×10 cm^{-1}. The absorption coefficient peaks at 342 nm and again at 244 nm, though the peak at 244 is obscured by the onset of attenuation of our quartz substrate. As shown in figure 5.4b, our model calculates a gradual increase in absorption beginning at 700 nm (1.7 eV), in excellent agreement with our experimental measurements. The absorption coefficient plateaus from 375-450 nm at a magnitude of 3.4×10 cm^{-1}, nearly identical to our experiment. Finally, the model predicts peaks at 300 nm and 210 nm, redshifted only 40 nm from our experimental data.

Next, we performed specular-reflectance measurements on single facets of Y_2CF_2 crystals (Figure C.4) using a microspectrophotometer. To obtain a representative spectrum, we averaged the spectra from individual crystallites together (Figure 5.4c). The representative spectrum has a peak at ∼540 nm, corresponding to yellow-green light. To compare with our model of the electronic structure, we calculated the reflectivity for the bulk Y_2CF_2 (Figure 5.4d), which shows a single broad peak at ∼500 nm, again redshifted only 40 nm from experiment. We do note that the intensity of the reflection in the experiment is almost double that of the calculated value. While the calculation provides qualitative information, the calculation does not consider all of the complexity of the real system—chemical differences at the surface, an interface with a changing dielectric, or the convolution of reflection and absorption events. Therefore, we attribute the difference in magnitude to these factors. Despite this difference, the model reproduces the major feature of the experiment very well.

We calculated the electronic band structure for the first Brillouin zone of Y_2CF_2 shown in Figure 5.4e,f. In agreement with our experimental measurements, we calculate that Y_2CF_2 is a semiconductor with a 1.7 eV indirect gap (from Γ–M) and a 2.0 eV direct gap (M–M)(Figure 5.4f). From the band structure, we can understand that the low absorption coefficient at 700 nm (Figure 5.4a,b) is due to the indirect nature of the

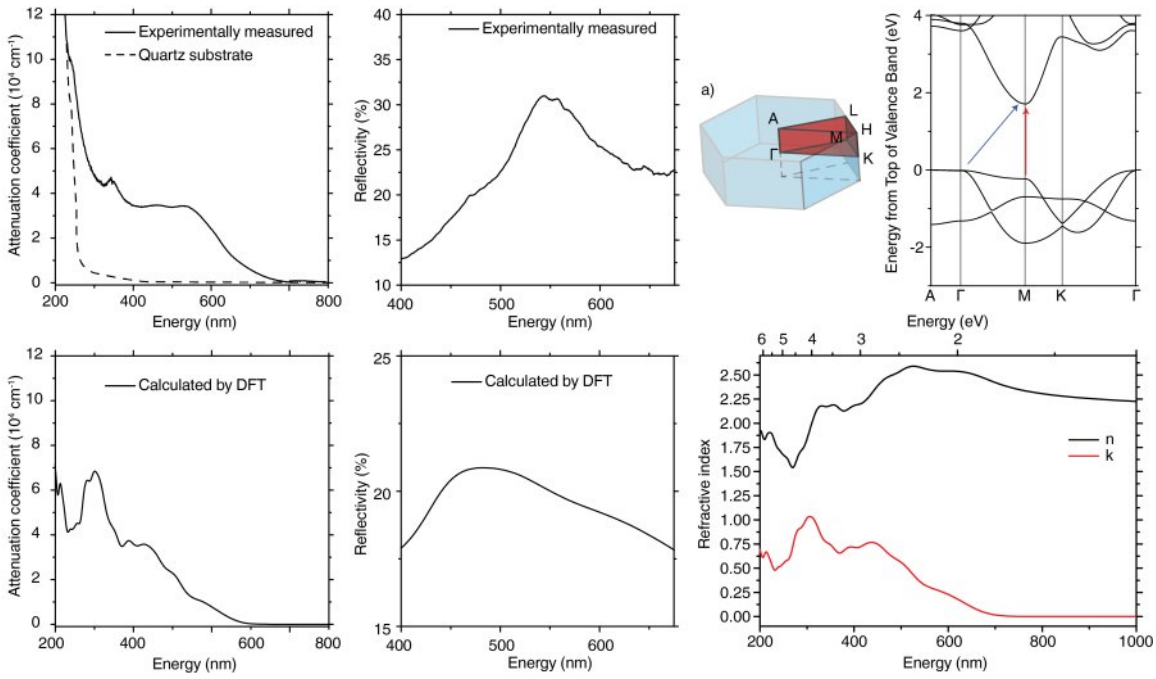


Figure 5.4: Optical properties of Y_2CF_2. The attenuation coefficient a) measured experimentally and b) calculated by DFT, the reflectivity c) measured experimentally and d) calculated by DFT. e) The first Brillouin zone for Y_2CF_2 with the irreducible Brillouin zone highlighted in red and f) the electronic band structure where the M–Γ vector runs along (010), while the Γ–A vector runs along (001). g) The optical constants, n and k, calculated by DFT.

transitions and the low density of states in the conduction band. Moreover, we gain information about the band dispersion. The bottom of the conduction band has a parabolic band dispersion, which should correspond to a relatively light effective mass for electrons in the conduction band. In contrast, the valence band is relatively flat. Interestingly, the band has almost no dispersion along the path Γ–A (Figure 5.4f) indicating very limited overlap of orbitals in the z-direction. This is likely due to the strong localization of electrons around the nucleus of the fluorine atoms, which separate layers of yttrium and carbon atoms.[261] Therefore, the ionic bonding between MXene sheets effectively insulate the sheets from one another electronically, which we anticipate gives rise to interesting, anisotropic behavior.

Because of the excellent agreement between theory and experiment, we present the optical constants (Figure 5.4g), n and k, calculated by DFT with confidence that the energy-dependence of the optical constants and that the magnitude of k represent the synthesized Y_2CF_2. Due to the difference in magnitude between experiment and theory we are less confident in the magnitude of n.

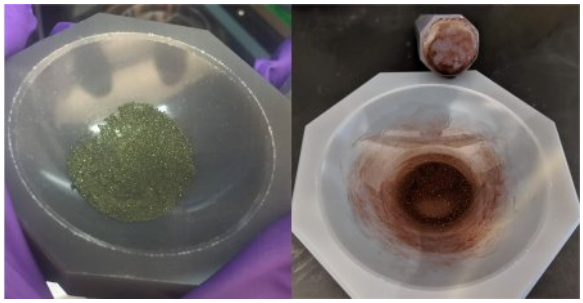


Figure 5.5: Photograph of a) green Y_2CF_2 before grinding and b) red Y_2CF_2 after grinding.

This electronic structure also explains beautifully an observation about the perceived color of Y_2CF_2. When we ground the green crystals (Figure 5.5a) in a glovebox in the absence of air or water, the material transforms into a red powder shown in Figure 5.5b. By examining the electronic structure, we conclude that the initially perceived green color is due to specular reflection of green light from flat crystalline surfaces, as evidenced by the peak in reflection at 540 nm in Figure 5.4c. By grinding the crystals into small particles, we destroy the flat surfaces and the specular reflection of green light. Once ground, absorption, originating from the band gap at 775 nm, dominates the apparent color of the material. To test this hypothesis, we ball milled the crystals to a fine powder with a particle size qualitatively determined as less than 5 μm (Figure C.6). We confirmed, via pXRD, that the crystal structure is preserved after ball milling (Figure C.7). Then we measured the reflectance of the finely ground sample using a microspectrophotometer (Figure C.8). We found that the peak at 540 nm, observed for the green crystals, was not present in the ball-milled sample.

5.2.4 Sensitivity to oxygen

This understanding of its electronic structure also led us to understand its sensitivity to oxygen and water. We removed samples of crystalline, green Y_2CF_2 from the glovebox, exposing the crystals to air and water for one month. After two weeks, the once-green crystals appeared red (Figure C.9). Examining the crystals in the microspectrophotometer in reflectance mode, we found that the peak in reflectance at 540 nm corresponding to the green color was not present. Instead, we observe clear evidence for thin-film optical effects including rainbow-striping (Figure C.11) and periodic oscillating signals in the reflectance spectra (Figure C.11). The formation of a thin-film on the surface of many semiconductors is commonly caused by a slow reaction with air or water, which forms a thin oxide coating.[262–264] Therefore, we suspected that Y_2CF_2 in air develops a thin film of an oxide or related species.

Table 5.3: X-ray photoemission spectra from Y_2CF_2 exposed to air for 1 week, after sputtering, and from Y_2CF_2 kept in an Ar-filled glovebox (oxygen < 0.01 ppm) for 1 week. All binding energies and full-width half-max values given in eV. [a]All binding energies were referenced to adventitious carbon (284.6 eV) after determination that no carbidic carbon species was detectable.

Sample	Atom	Core	Binding Energy[a]	FWHM	Atomic %
Air-exposed	Y	$3d_{\frac{5}{2}}$	157.6	1.56	21.3
	C_{adv}	1s	284.6[a], 286.3	1.33, 2.24	17.1
	$C_{carbonate}$	1s	289.4	1.63	7.9
	F	1s	684.8	1.81	10.5
	O	1s	531.2	1.88	43.2
Air-exposed sputtered	Y	$3d_{\frac{5}{2}}$	157.6	4.06	33.8
	C_{adv}	1s	284.6[a], 286.0	1.67, 1.76	5.3
	$C_{carbonate}$	1s	289.9	1.57	1.9
	F	1s	685.0	2.11	16.9
	O	1s	531.3	3.91	42.1
Glovebox	Y	$3d_{\frac{5}{2}}$	155.0	1.26	4.1
	Y	$3d_{\frac{5}{2}}$	157.5	2.47	21.7
	Y	$3d_{\frac{5}{2}}$	159.9	2.00	4.5
	C_{adv}	1s	284.6[a], 286.0	1.25, 1.76	22.2
	F	1s	684.8	2.78	20.4
	O	1s	531.4	3.89	27.1

To test whether the Y_2CF_2 crystals react with oxygen or water, we performed X-ray photoemission spectroscopy (XPS) on crystals exposed to air for 1 week and on crystals kept in the glovebox. We examined the yttrium *3d*, carbon *1s*, fluorine *1s*, and carbon *1s* core electron binding energies (Table 5.3). For the sample exposed to air for 1 week, we observed a single peak at a binding energy of 684.8 eV (Figure 5.6a) corresponding to the F *1s* core binding energy, in agreement with the binding energy of fluoride.[265] However, the Y:F ratio measured through XPS quantitative analysis is 2.0:1, suggesting a deficiency of fluorine at the surface. In the Y *3d* spectrum we observe a doublet with a binding energy of 157.7 eV (Figure 5.6c). The position of this peak matches that of yttrium carbonate ($Y_2C_3O_9$)[266,267] and is too high to be the expected Y^{2+} oxidation state ($\sim$156.2 eV).[268,269] In addition, the spectrum of the carbon *1s* core (Figure 5.6b) reveals two distinct peaks, one centered at 284.6 eV, which is adventitious carbon and one centered at 289.4 eV, which matches that of a carbonate(Figure 5.6b).[267,270] Moreover, through quantitative XPS analysis, we measure the ratio of Y:O to be 1.0:2.1, which can only be explained by a carbonate, not Y_2O_3 or YOF. Therefore, we conclude the surface of the sample exposed to air has oxidized, at least partially, to $Y_2C_30_9$.

We attempted to clean the surface of the air-exposed sample by argon ion sputtering. Both the oxygen *1s* and carbon *1s* (Figure 5.6d) signals decrease in intensity relative to the yttrium. The Y:O ratio decreases to 1:1.2. This suggests that the oxidation is a surface effect. For additional support of that hypothesis, we

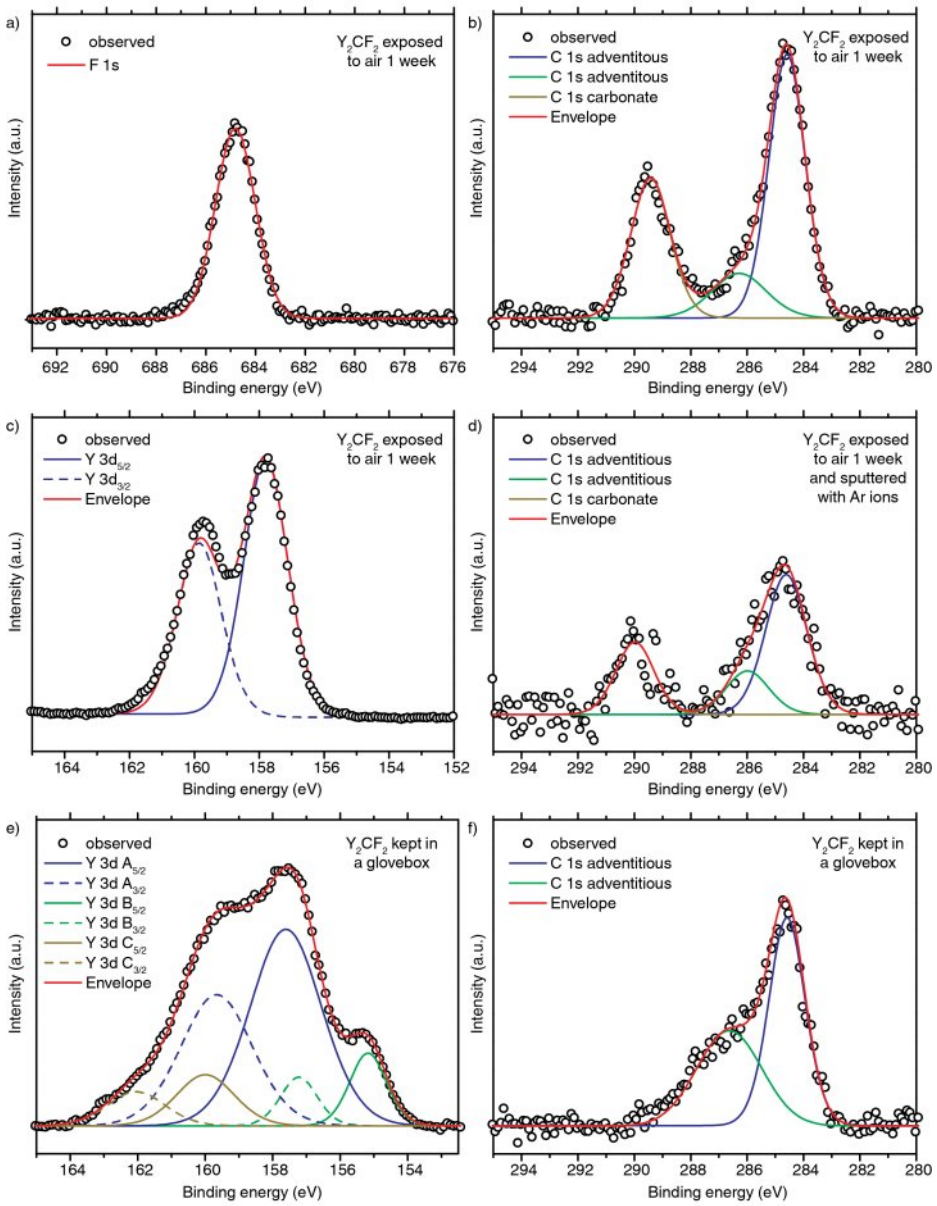


Figure 5.6: X-ray photoemission spectra from Y_2CF_2 exposed to air for 1 week for the a) fluorine *1s*, b) carbon *1s*, c) yttrium *3d* core electron binding energies. d) The spectrum for carbon *1s* core electrons from air-exposed Y_2CF_2 after sputtering. Spectra from Y_2CF_2 kept in a glovebox for the e) yttrium *3d* and carbon *1s* core electron binding energies.

performed XRD measurements on the samples exposed to air (Figure C.10). We found the crystal structure remained intact after exposure to air for 1-4 weeks, which supports the conclusion that the oxidation affects the surface and not the bulk of the sample.

For the sample kept in a glovebox, we note that we briefly exposed the sample to air during the transfer into the XPS instrument. In the Y *3d* spectrum, we observed a convoluted yttrium signal with an asymmetric lineshape (Figure 5.6e). One contribution is from a reduced form of yttrium with a binding energy of 155.5 $\pm$ 0.3 eV, and a second contribution matches that of the air-exposed sample at 157.8 eV. To account for the tail at higher binding energies, a third contribution was also added to the fit, though others have observed asymmetric tails at high binding energies from the reduced forms of Y.[268,269] The carbon *1s* spectrum (Figure 5.6f) shows a single peak, attributed to adventitious carbon. We do not see evidence for a carbonate species. Surprisingly, we did not observe a peak from a carbide species, expected at a lower binding energy ($\sim$282 eV) for similar metal carbides.[125] Therefore, we conclude that the surface oxidizes quickly during the brief transfer of the sample into the instrument and that the oxidation affects the carbidic carbon at the surface. Unfortunately, sputtering the surface seemed to damage the sample and resulted in charging and broadened peaks.

Together these XPS results suggest that the surface of Y_2CF_2 oxidizes after only a brief exposure to air and forms a layer that slows further oxidation. After exposure to air for extended periods (days-weeks), a thin film of oxidized material grows on the surface, which gives rise to optical thin-film effects. In the samples exposed for extended periods, we observe carbonate species on the surface, consistent with observations of other yttrium oxides in the presence of carbon dioxide.[267,270] XPS and XRD experiments suggest that the oxidation is a surface feature and does not significantly affect the bulk structure.

We return to the electronic structure to understand why Y_2CF_2 oxidizes in air. In order to understand this, we place the band edges of Y_2CF_2 on an absolute scale along with the reduction potentials of oxygen and water, which are likely redox couples. We combined several measurements and calculations to place the band edges: ultraviolet photoelectron spectroscopy (UPS) gave the bulk materials work function, ϕ, (Figure5.7a) and valence band edge (Figure 5.7b), our spectroscopic measurements (Figure 5.4a) provided band gaps, and DFT calculations support the band gaps (Figure 5.4b,e) and valence band edge (Figure 5.7c). Surprisingly, UPS reveals that the work function of Y_2CF_2 is only 2.6 $\pm$ 0.1 eV, a low work function for a semiconductor. The Fermi level (E_F) is positioned 1.3 eV above the valence band edge, indicating that the sample is *n*-doped. This doping could be due to the small deficiency of carbon, as anion vacancies are consistent with *n*-type doping.

We gain further understanding of its reactivity through analysis of the partial density of states (PDOS), deconstructed into the elemental compositions and angular momentum (Figure 5.7d-f). The valence band

consists of Y *4d* and C *2p* states. The C *2p* states lie at a relatively high potential, or in the vernacular of chemists, the C *2p* states have reducing character. According to our placement of the band edges, electrons in the valence band may transfer to O_2 and H_2O producing a hydroxide anion. Subsequently, we expect that the oxidized Y_2CF_2 may continue to oxidize to even more oxidized forms like $Y_2C_3O_9$. This mechanism is consistent with the XPS observations of fast partial oxidation to an oxide or hydroxide after a brief exposure to air and a subsequent slow oxidation to a more oxidized form.

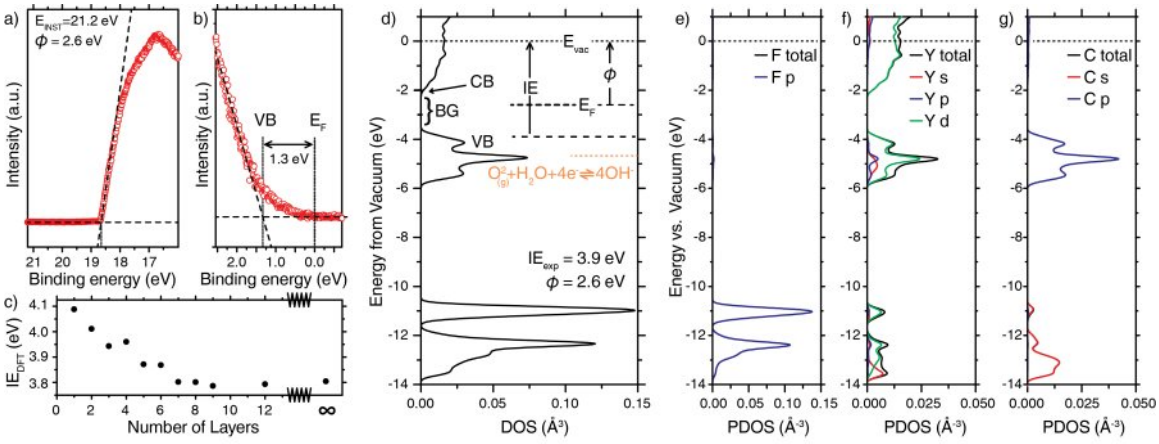


Figure 5.7: The band positions of Y_2CF_2 on an absolute scale. a,b) Results from ultraviolet photoemission spectroscopy, which measure the work function, ϕ, and the valence band edge (VE) relative to the Fermi level, E_F. c) Calculations of the IE by DFT for increasingly thick slabs of Y_2CF_2, which plateau at a value of $\sim$3.8 eV for a 12-slab and for a bulk crystal. d) The density of states (DOS) calculated by DFT on the left referenced to vacuum energy, showing the valence band (VB), conduction band (CB), and band gap (BG). The right side of the plot shows the experimentally determined values for the IE, position of E_F, and ϕ. The partial density of states for e) fluorine, f) yttrium, and g) carbon in Y_2CF_2.

In general, MXenes have been considered stable in air and water; however, growing evidence reveals that MXenes actually decompose over the course of a few days to a few weeks.[113,271–277] For example, Ti_3C_2 (-O, -OH, -F) decomposes to form TiO_2 in the presence of oxygen[271,276] and water.[273,275] In fact, the etching synthetic method, which uses strong oxidants like HF,[229] H_2O_2,[278] or HCl/LiF,[279] contributes to the oxidation, as evidenced by the formation of -O terminating moieties. The oxidation has real consequences on the electronic structure.[280] For example, the work function of Ti_3C_2X (X = -O, -OH, -F) was predicted to vary from 1.9 to 6.2 eV depending on the surface terminations.[281] Moreover, the work function of MXenes with random surface moieties depends on the complex interplay between the different surface moieties and their local dipoles.[282]

In this context, Y_2CF_2 and crystalline stacked MXenes provide an opportunity. The uniform, single F- moiety of crystalline stacked MXenes could facilitate experiments to understand and control its surface oxidation.

Although we have observed that Y_2CF_2 oxidizes in air, the direct synthesis does not oxidize the material, in contrast to the etching synthesis of 2D MXenes, which inherently causes oxidation. We expect that simple air-free handling of crystalline stacked MXenes will yield un-oxidized samples. In this way, Y_2CF_2 and crystalline stacked MXenes offer a material without oxidation or disorder, which should afford control over surface properties and chemistries.

5.3 Conclusion

We have synthesized Y_2CF_2, a crystalline, 3D stack of MXene-like sheets capped exclusively by fluorine. Instead of the etching approach, we introduce a new synthetic method to directly synthesize the 3D crystal through a high-temperature solid-state reaction that ensures that only fluoride ions terminate the layers. Unlike MXenes, ionic bonds hold the 3D crystal together. Interestingly, the lack of orbital overlap between planes gives rise to a description of Y_2CF_2 as slabs of MXene-like sheets electrically insulated from one another. The valence band edge, made of Y *4d* and C *2p* states, sits at a high potential, affording a low work function and reducing character, which makes the crystal sensitive to air, but also suggests that the crystal could be useful as low work function electron emitters[283] and catalysts,[284,285] in addition to applications in electronic,[222,223] sensing,[224,225] and energy storage.[226–228]

The success of this new, direct synthetic approach motivates the exploration of the ternary phase diagrams for other transition metals-carbon-fluorine systems. While experimental exploration of phase diagrams is taxing, we have shown that a DFT-based high-throughput method correctly predicts the structure of a metal-carbide fluoride and that DFT calculations of the electronic structure remarkably match our experimental data. Therefore, we suggest that a high-throughput DFT-based method has the ability to fully uncover other ternary phase diagrams and predict other new crystalline, 3D stacks of MXene-like materials.

CHAPTER 6–ELECTROCHEMICAL ELECTRON-ANION EXCHANGE: A NEW MECHANISM OF ION-INSERTION AND ITS APPLICATION IN FLUORIDE-ION BATTERIES

"I was captured for life by chemistry and by crystals."

- Dorothy Hodgkin, 1964

6.1 Introduction

Rapid progress in batteries that shuttle cations between electrodes has led to their widespread use.[286] Although lithium-ion batteries dominate the market for high-energy density batteries, there are considerable efforts to develop alternate cation shuttles, including magnesium, sodium, and zinc.[287–290] Anion shuttle batteries have received little attention due to a lack of suitable electrodes.

In general, when an anion (cation) enters an electrode, the requirement of charge neutrality means that an electron must leave (enter) the electrode.[291] In every electrode yet reported, the loss (gain) of electrons occurs through an oxidation (reduction) of atoms within the electrode. For example, when Li^+ enters graphite, carbon atoms are reduced.[292–294]

However, there is a class of material, called "electrides", in which nearly free electrons are decoupled from the atomic orbitals of the lattice. In these exotic ionic solids, the negative "ion" is just an electron with no nucleus. The electrons wave function occupies the space typically filled by anions like Cl^- or O^{2-}.$^{(ref.\ 4,14,25,295)}$

The syntheses of many electrides involves the chemical reduction of an iso-structural oxide at extremely high temperatures (e.g. 800 °C):[18,22]

$$Ca_{24}Al_{28}O_{66} + 2\,Ca \xrightarrow{800°C} [Ca_{24}Al_{28}O_{64}]^{4+} \cdot 4e^- + 2\,CaO \tag{6.1}$$

The crystal structure of the resulting electride is nearly identical to that of the oxide. Analysis of the crystal structure and electronic structure shows that the electrides electrons fill the lattice sites previously

occupied by O^{2-}.[ref. 18,22] Therefore, these chemical reduction reactions are analogous to de-insertion reactions in cation shuttles.

Unlike cation shuttles, high temperatures are used in the chemical reduction reactions to compensate for sluggish anion diffusion. Prior studies on solid-state anion transport show that the rate-limiting step is the hopping of an anion between lattice sites.[296] In common oxides (e.g., TiO_2 or $SrTiO_3$), the large activation energy (1.1 eV) to move O^{2-} into a vacant site means that the materials must be heated above 400 °C to have mobile O^{2-}.[ref. 297]

Building off of these concepts, here we explore a fundamentally new mechanism for the storage of ions, one in which the insertion of an anion in not accompanied by a redox process. We show that when an anion such as F^- inserts into an electride such as Y_2C, F^- simply replaces e^-, occupying the same site. The half reaction is:

$$[Y_2C]^{2+} \cdot 2e^- + 2F^-_{\text{(electrolyte)}} \rightarrow [Y_2C]^{2+}(F^-)_2 + 2e^-_{\text{circuit}} \tag{6.2}$$

Because F^- replaces an electron, the Y_2C lattice is not oxidized. Furthermore, we provide calculations, which suggest it can occur at room temperature, and demonstrate experimentally that this exchange can occur at lower temperatures ($<$ 500 °C). We introduce the name "electrochemical electron-anion exchange" to describe this mechanism and lay the intellectual framework for what is likely to be a large and important field of materials for electrochemistry, energy science, and electronics.

6.2 Results and Discussion

6.2.1 Electron analog pair

Y_2C is a layered crystal,[43,131,132] with space group #166, $R\bar{3}m$, the same as excellent materials for storing Li-ions, like CoO_2.[298,299] Six Y atoms coordinate to each carbon atom and the edge-sharing Y_6C octahedra bond into two-dimensional layers. However, in Y_2C, nearly free electrons occupy the space between layers of Y_2C slabs (Figure 6.1a).[48,70]

Recently, we synthesized Y_2CF_2, the analog of Y_2C but fully inserted with F^-. The crystal structures are remarkably similar. Comparison of the structures informs about the structural changes that might occur during insertion/deinsertion of F^-. Complete fluorination (Y_2CF_2) results in the expansion of the crystal lattice in the *a* parameter by only 1.1% (Table 6.1), suggesting very little distortion of the lattice. The *c*

Table 6.1: Atomic distances in the crystal structure of Y_2C taken from literature[80] and Y_2CF_2 taken from powder X-ray diffraction experiments presented in chapter 4. All distances are reported in Å. The volume, V, is reported in Å^3

	Y_2C	Y_2CF_2	Difference (%)
a	3.62483	3.6651	1.1
c	17.964	18.8907	5.2
Y–Y	3.2.493	2.510	0.7
Y–C	3.423	3.431	0.2
Y–C–C	180°	180°	–
V	204.413	219.761	7.5

parameter expands only by 5.2% (Table 6.1). The total volume expands only 7.5% upon complete fluorination. Minimal changes in volume with ion-insertion are desired for ion-storing materials, so that the materials avoid swelling or damaging electrical contacts.[300,301] For comparison, lithium insertion into graphite, the champion anode for lithium-ion batteries, results in a 13.2% expansion in volume.[302]

Close inspection of the structures reveals that all of the Y–C atomic distances and Y–Y atomic distances within a layer change by less than 1.1% (Table 6.1). This indicates that the exchange of an electron with F^- does not perturb the individual Y_2C layers or the Y–C bonding. Using density functional theory (DFT), we calculated Bader charge densities to understand the oxidation states of Y and C atoms in both Y_2C and Y_2CF_2 (Table 6.2). The oxidation states of Y (1.9+) and C (2.1-) in Y_2CF_2 are nearly identical to those in Y_2C (1.9+ and 2.0- respectively)(Table 6.2). This supports our claim that the lattice is not oxidized by the exchange.

Table 6.2: Charges on the constituent atoms in Y_2C taken from literature[48] and Y_2CF_2 calculated using DFT and the Bader charge analysis. The DFT calculations were performed using the CASTEP code[54] with plane-wave basis set approximations[55] and a 500 eV cut-off energy. Ultrasoft pseudopotentials[56] were used to describe core electrons. A GGA PBEsol functional[57] was used for the exchange-correlation contribution to total energy. A Monkhorst-Pack grid[59] of 32×32×6 and FFT grid of 30×30×150 was used.

Atoms	Charges	
	$[Y_2C]^{2+}\cdot 2e^-$	Y_2CF_2
Y	+1.94	+1.91
C	-2.04	-2.14
e/F	-0.91	-0.85

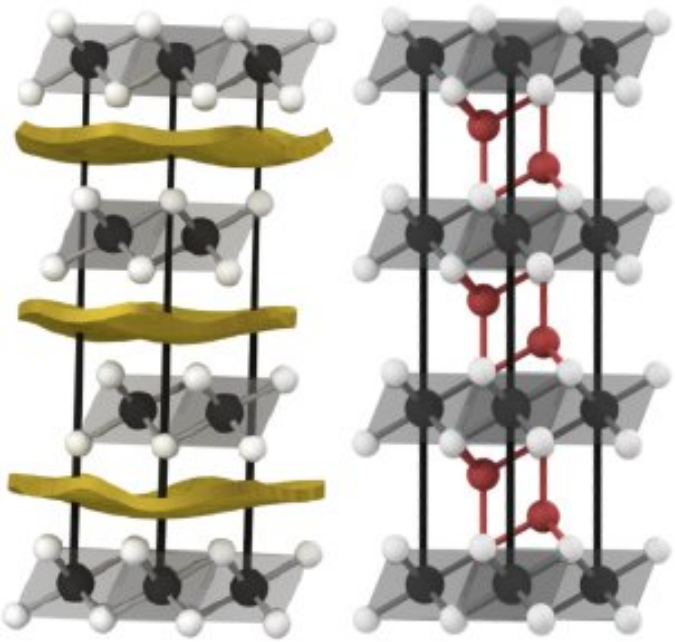


Figure 6.1: The crystal structures of a) Y_2C in its layered phase, space group #166 $R\bar{3}m$, and b) Y_2CF_2, space group #164 $P\bar{3}m1$. Yttrium atoms are represented as white spheres, carbon as black spheres, fluorine as red spheres, and the electron gas in gold. The Y_6C octahedra are shown in grey.

6.2.2 Activation barrier for F^- diffusion

We hypothesized that the electron-filled interlayer space could provide a channel through which anions could hop from site to site. We calculated the activation barrier for F^- diffusion using DFT by moving a F^- through a rigid lattice in steps of 0.1 Å and extracting the lowest-energy path, which has accurately reproduced the activation barriers for Li^+ hopping in hosts.[303,304] We calculate an astonishingly low energy barrier for F^- diffusion of only 110 ± 10 meV (Figure 6.2a). We performed additional calculations using a second method, the image-dependent pair potential method,[305] to consider some of the local disorder induced by anion hopping. These calculations similarly find a low energy barrier for F^- diffusion of 100 ± 10 meV. An energy barrier of only 100 meV for F^- diffusion suggests that F^- can diffuse at room temperature. For comparison, the barrier for Li^+ diffusion is $\sim$300 meV[306] in $LiCoO_2$ and $\sim$260 meV[307] in graphite. We note that in recent years, a more rigorous method, the nudged elastic band (NEB) method,[308] has been used to calculate activation barriers of ion diffusion. We are currently performing the time-intensive NEB calculations to calculate the diffusion of F^- in Y_2CF_2.

The lowest energy pathway for F^- diffusion in Y_2CF_2 is the F^- moving directly from tetrahedral site to tetrahedral site. The distance between sites is only 2.438 Å. The energy barriers for other pathways

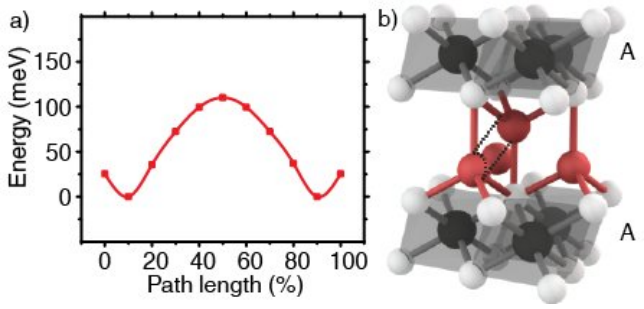


Figure 6.2: a) The activation barrier for the diffusion of F^- in Y_2CF_2 along the linear path from one tetrahedral site to a vacant tetrahedral site. The energy was calculated through DFT calculations by moving a F^- through a rigid lattice in steps of 0.1 Å and extracting the lowest-energy path. b) The crystal structure of Y_2CF_2 with yttrium, carbon, and fluoride ions represented by white, black, and red spheres respectively. The path from tetrahedral site to tetrahedral site is marked by a dashed line.

are considerably higher ($\sim$1 eV); however, the entire 2D network of sites is accessible by hopping from tetrahedral site to tetrahedral site. Therefore, we expect this is the dominant mechanism.

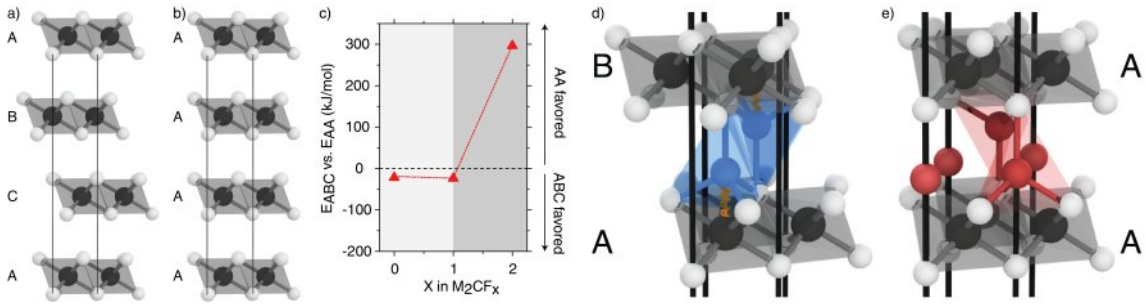


Figure 6.3: The two stacking sequences of a) R$\bar{3}$m Y_2C (ABC) and b) P$\bar{3}$m1 Y_2CF_2 (AA). c) The relative stability of the stacking sequences as a function of x in Y_2CF_x. d) A representation of two-layers of the ABC-stacked structure where the two tetrahedral sites are occupied by F^- represented in blue. The proximity of the F^- to the carbon anions (black) is highlighted by yellow springs. e) A representation of the AA-stacked structure where the two tetrahedral sites are occupied by F^- represented in red.

In other ion-storing materials, the phase can change upon insertion of ions.[309–311] We expect that a phase change is possible upon F^- insertion into Y_2C. This is apparent from the crystal structures. Y_2C (R$\bar{3}$m) is ABC-stacked (6.3a); whereas Y_2CF_2 (P$\bar{3}$m1) is AA-stacked (Figure 6.3b). We calculated the enthalpy of the two phases as a function of fluorination (Figure 6.3c). After insertion beyond 1 F^- per formula unit, the AA-stacked structure is thermodynamically favorable. The ABC-stacking sequence offers a stable octahedral site, which can accommodate up to 1 F^-. Insertion of additional F^- forces the F^- into a tetrahedral site proximal to the carbon (C^{2-}) anion (Figure 6.3d), which is less favorable. In contrast, the AA-stacking sequence affords two tetrahedral sites with relatively long F–C distances (Figure 6.3e).

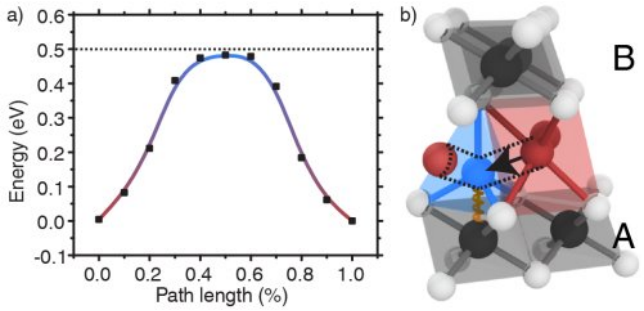


Figure 6.4: a) The activation barrier for the diffusion of F^- in ABC-stacked Y_2CF along the linear path from one octahedral site through an intermediate tetrahedral site to a vacant octahedral site. The energy was calculated through DFT calculations by moving a F^- through a rigid lattice in steps of 0.1 Å and extracting the lowest-energy path. The color (red-to-blue-to-red) corresponds to the movement between sites in b). b) A representation of two-layers of the ABC-stacked Y_2CF crystal with yttrium, carbon, and fluoride ions represented by white, black, and red spheres respectively. The path from the octahedral site (shown in red) through a tetrahedral site (shown in blue) to an octahedral site is marked by a dashed line. A yellow spring highlights the proximity of the intermediate tetrahedral site to a carbon anion.

Because the phase change may affect the energy barrier for F^- diffusion, we calculated the barrier for F^- diffusion in the ABC-stacked structure with a stoichiometry of Y_2CF (Figure 6.4a). We found that the energy barrier is 480 $\pm$ 10 meV, low enough for room-temperature F^- diffusion. The lowest energy path involves F^- hopping from one octahedral site to another by passing through an intermediate tetrahedral site (Figure 6.4b). This is believed to be the mechanism of Li^+ diffusion in the iso-structural $LiCoO_2$ as well.[312] We recognize that the activation energy for F^- diffusion likely depends on the concentration of F^-, as has been observed for Li^+ diffusion in Li^+-hosts.[312,313] Therefore, with such a large phase-space (multiple pathways, phase changes, dependence on F^- concentration, and local structural disorder), experimental measurements are necessary to narrow the computational exploration.

6.2.3 Experimental evidence for electron-anion exchange

We are in the process of developing an electrochemical model to test electron-anion exchange experimentally. In the interim, I turned to a chemical system to test the hypotheses. The closest model of electrochemical reduction is chemical reduction, though certainly the differences are considerable, such as the absence of a solid-electrolyte interphase and the presence of an interface of molten lithium, LiF, and Y_2CF_2. In my first attempt, I reacted Y_2CF_2 with Li metal in welded tantalum ampoules at 500 °C. After the reaction, I washed away the excess Li by dissolving the Li in a solution of naphthalene and diglyme and separated the products by serial washing and centrifugation. The product is a grey powder, in contrast to the green Y_2CF_2.

X-ray diffraction experiments reveal that the product is a mixture of three phases: layered Y_2C, a cubic phase of Y_2CF_x, and LiF (Figure 6.6a). This initial result is extremely promising and informative. This experiment yielded Y_2C and LiF confirming that Y_2CF_2 can be dehalogenated and at least at a temperature as low as 500 °C. To put this into context, this synthesis of Y_2C was accomplished at the lowest temperature of any inorganic electride reported. Attempts at lower temperatures are currently underway.

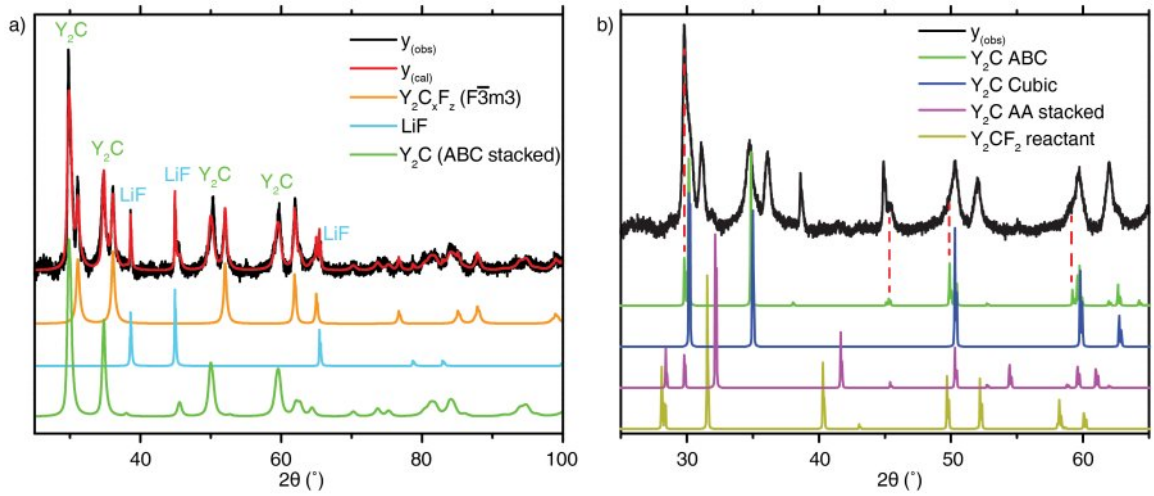


Figure 6.5: a) A powder X-ray diffraction pattern of Y_2CF_2 dehalogenated by chemical reduction using lithium metal at 500 °C. The observed data shown in black is well fit by three phases, layered ABC-stacked Y_2C ($R\bar{3}m$) shown in green, LiF shown in blue, and a cubic phase of Y_2CF_x ($F\bar{3}m3$) shown in orange. b) The same powder X-ray diffraction pattern of Y_2CF_2 dehalogenated by chemical reduction using lithium metal at 500 °C showing different hypothetical phases that could account for the peaks in the spectra. The reactant Y_2CF_2 (gold), layered AA-stacked Y_2C (purple), cubic Y_2C (blue), and layered ABC-stacked Y_2C (green). Lattice constants were chosen to match the most intense peak at 30° and best fit the data as attempted by a Pawley decomposition method.

In addition, the reaction provides information about the structural changes that occur during defluorination, at least at 500 °C. The XRD provides strong evidence that the Y_2C product is the layered structure (space group #166, $R\bar{3}m$, a = 3.620 Å, c = 17.85 Å)(Figure 6.6a). The position of the peak at 45.3°, which is from both the (107) and (009) planes, is consistent only with layered Y_2C, not cubic Y_2C (Figure 6.6b). Moreover, we observe shoulders of peaks at 29.8°, 49.9°, and 59.1°, which are only present in the layered phase (Figure 6.6b). Therefore, we conclude that during the defluorination reaction, the Y_2C lattice reorganizes from the AA-stacking sequence to the ABC-stacking sequence as predicted by our model; however, the structural reorganization could be significantly different at room temperature.

The cubic phase ($Fm\bar{3}m$) produced during the experiment is also interesting. The lattice constants for this phase (a = 4.962 Å) are smaller than what is observed for the cubic phase of Y_2C (a = 5.115 Å). Interestingly,

the Y–Y atomic distances (3.51 Å) are shorter than those in yttrium metal (3.56 Å),[37] but similar to those in $YC_{0.3}O_{0.7}$.[ref. 314] We have no reason to suspect contamination of oxygen. More likely the compound consists of Y, C, and F, which crystallize in a disordered phase. A similar disordering to a cubic phase has been observed during the lithiation and de-lithiation of layered $LiTiO_2$.[315]

Y_2C adopts the cubic phase under a number of circumstances, which we have come to understand. Cubic Y_2C forms if even a small amount of oxygen is present during its synthesis; it forms for Y_2CO[ref. 316]; and it forms for Y-rich yttrium carbides (e.g. $YC_{0.33}$,[ref. 317] YC[ref. 318]). In all of these instances, the phase forms when the ratio of Y:anions deviates too far from the 2:1 ratio. With this knowledge, we suggest that the observed cubic structure may be an intermediate in the defluorination of Y_2CF_2; as the reaction proceeds and the lattice reorganizes to accommodate the change in stacking sequence, the structure disorders to a cubic phase, and then reorders to a layered phase as the F^- are nearly completely replaced by electrons. We need to perform further experimentation to understand the structural complexity in this F^- host system.

6.2.4 Storage of electrochemical energy

In this final section, we discuss a natural application of this new mechanism— electrochemical energy storage. In a typical device, energy is stored by raising the electrochemical potential of a system, for example by reducing a transition metal to a lower oxidation state.[291,319] In the present system, the electron is decoupled from atomic orbitals. Instead, the energy stored is the difference in electrochemical potential energy between the fluoride and electride systems. Intuitively, one would expect this energy is related to the electron affinity of the nucleus of the fluorine atom; however, we have yet to work out a complete theoretical model that explicitly defines the relationship. Instead, we can consider the differences in the density of states and partial density of states of F^- in Y_2CF_2 and of e^- in Y_2C (Figure 6.6a).

The system stores considerable energy in this difference between the fluoride and electride state. As a visual demonstration of its stored electrochemical energy, we show an image from a video that we captured of an unexpectedly violent reaction of Y_2C with ZnF_2 simply by grinding the powders in a mortar and pestle (Figure 6.6b). According to our calculations, this reaction gives of -336 kJ/mol of energy causing it to self-heat and become a run-away reaction.

To understand roughly how Y_2CF_2 might perform in a fluoride-ion battery, we estimate the reduction potential of Y_2CF_2 versus Li/Li^+. In equation 6.3, we write a series of chemical equations that combine to give the reduction potential of Y_2CF_2 versus Li^+/Li.

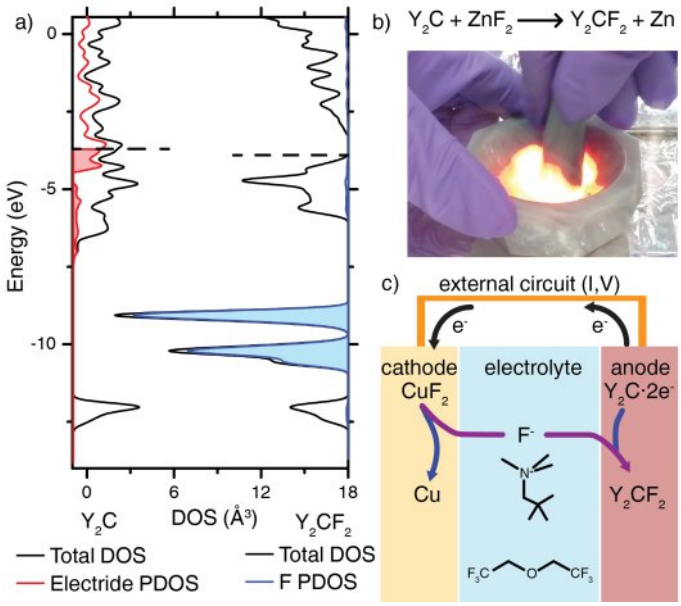


Figure 6.6: a) The density of states (DOS) for Y_2C taken from literature[48] and Y_2CF_2 calculated using the CASTEP code[54] with plane-wave basis set approximations[55] and a 500 eV cut-off energy. Ultrasoft pseudopotentials[56] were used to describe core electrons. A GGA PBEsol functional[57] was used for the exchange-correlation contribution to total energy. A Monkhorst-Pack grid[59] of $32\times32\times16$ and FFT grid of $27\times27\times48$ was used. The energy was placed on an absolute scale by taking the known ionization potentials and aligning the Fermi level appropriately with respect to the vacuum potential. The partial density of states (PDOS) for the electride in Y_2C, taken from literature[48], are shown in red. The partial density of states for the fluoride in Y_2CF_2 are shown in blue. b) A still frame taken from a video of a runaway reaction of Y_2C and ZnF_2 accidentally initiated by grinding in a mortar and pestle. c) Schematic of a fluoride-ion battery during discharge using Y_2C as an anode.

$$\begin{aligned}
&Y_2CF_{2(s)} + 2Li_{(s)} \rightarrow Y_2C_{(s)} + 2LiF_{(s)} && \Delta G_{rxn}\\
&2LiF_{(s)} \rightarrow 2Li^+_{(solvated)} + 2F^-_{(solvated)} && \Delta G_{solv}\\
+\quad &2Li^+_{(solvated)} + 2e^- \rightarrow 2Li_{(s)} && E^{Li^+}_{red}\\
\hline
&Y_2CF_{2(s)} + 2e^- \rightarrow Y_2C_{(s)} + 2F^-_{(solvated)} && E^{Y_2CF_2}_{red}
\end{aligned} \tag{6.3}$$

In a hypothetical cell with lithium, the voltage of the cell, ΔE, is the sum of reduction potential of Y_2CF_2, $E^{Y_2CF_2}_{red}$, and the oxidation potential of lithium metal, E^{Li}_{ox} (eq. 6.4). We can instead write the equation in terms of the reduction potential of Li^+ (eq. 6.6). Through the Nernst equation (eq.6.7), we can relate the Gibbs free energy, ΔG, of the reduction reaction, to the voltage of the cell (eq. 6.11). The Gibbs fee energy of the reduction reaction is the sum of the Gibbs free energy of a solid-state reaction of Y_2CF_2 and lithium metal,

ΔG_{rxn}, and the Gibbs free energy of the solvation of solid LiF, ΔG_{solv}. Substituting terms and rearranging the equation yields an equality (eq. 6.12) that allows us to estimate the reduction potential of Y_2CF_2 vs. Li/Li^+ from values of ΔG_{rxn}, ΔG_{rxn}.

$$\Delta E = E_{red}^{Y_2CF_2} + E_{ox}^{Li} \tag{6.4}$$

$$E_{ox}^{Li} = -E_{red}^{Li^+} \tag{6.5}$$

$$\Delta E = E_{red}^{Y_2CF_2} - E_{red}^{Li^+} \tag{6.6}$$

$$\Delta G = -nF(\Delta E) \tag{6.7}$$

$$\Delta G = \Delta G_{rxn} + \Delta G_{solv} \tag{6.8}$$

$$-nF(\Delta E) = \Delta G_{rxn} + \Delta G_{solv} \tag{6.9}$$

$$-nF(E_{red}^{Y_2CF_2} - E_{red}^{Li^+}) = \Delta G_{rxn} + \Delta G_{solv} \tag{6.10}$$

$$E_{red}^{Y_2CF_2} = \frac{\Delta G_{rxn}}{-nF} + \frac{\Delta G_{solv}}{-nF} + E_{red}^{Li^+} \tag{6.11}$$

$$E_{red_{vs.\ Li/Li^+}}^{Y_2CF_2} = \frac{\Delta G_{rxn}}{-nF} + \frac{\Delta G_{solv}}{-nF} \tag{6.12}$$

We approximated ΔG_{rxn} by neglecting the change in entropy of the solid reaction and calculating the enthalpy using DFT, affording a value of -209.3 kJ/mol. To estimate the ΔG_{solv}, we used an experimental value of the the energy of solvation of LiF (21.13 kJ/mol) in the ionic liquid, 1-butyl-3-methylimidazolium trifluoromethanesulfonate ([C_4C_1im][OTf]).[320] It is worthwhile to understand the sources of error and relative

accuracy of this estimate. We performed four DFT calculations, each of which may contain an error of 1-2 kJ/mol, contributing an error of $\sim$4 kJ/mol. We neglected the change in the entropy of the solids. The sum of these terms at 300 K, each with a value of around 10 kJ/mol, likely gives an error of $\sim$2 kJ/mol. Rather than [C_4C_1im][OTf], our experiments will employ a different solvent, an ionic liquid consisting of *N,N,N*-dimethyl-*N,N*-dineopentylammonium fluoride and bis(2,2,2-trifluoroethyl) ether, which has a very high conductivity (3.5 mS/cm) for a F^- electrolyte and a higher free energy of solvation for F^-.[321] The error associated with this term could be as large as $\sim$20 kJ/mol. Together these errors, $\sim$26 kJ/mol, suggest a liberal estimate of 14% error. The reduction potential of Y_2CF_2 is +0.97 $\pm$ 0.13 V vs. Li/Li^+. With such a negative reduction potential of Y_2CF_2, we anticipate that Y_2C could serve as an anode in a F^--ion battery (Figure 6.6c).

Finally, we comment on the density of F^- that can be stored in Y_2CF_2. Because two F^- can insert into each unit of Y_2C, the density of ion-storage is impressive, reaching volumetric densities of 2.73-2.94$\times10^4$ ions/cm^3 and gravimetric densities of 6.21-6.35$\times10^3$ ions/g. These values are comparable to the density of lithium ions stored in $LiCoO_2$ (3.11$\times10^4$ ions/cm^3 or 6.15$\times10^3$ ions/g).[322] We suspect that the gravimetric capacity for F^- storage can be improved easily. By alloying Y with Sc as has been reported,[323] for example $Y_{0.8}Sc_{1.2}C$, the density can be improved to 8.30$\times10^3$ ions/g. By replacing Y with entirely with Sc, the density can reach 11.37$\times10^3$ ions/g, nearly double that of $LiCoO_2$.

6.3 Conclusions

Here we have demonstrated a fundamentally new mechanism for the storage of ions, "electrochemical electron-anion" exchange, in which the insertion of an anion in not accompanied by a redox process. We show that when an anion such as F^- inserts into an electride such as Y_2C, F^- simply replaces e^-, occupying the same site, without oxidizing the Y_2C lattice.

In addition, we provided calculations, which suggest that the exchange process can occur at room temperature, and demonstrated that this exchange can occur at the lowest temperatures ($<$ 500 °C) reported by chemical reduction with lithium metal.

Finally, we proposed that Y_2C could store energy, not by changing the oxidation state of a transition metal, but through the difference in electrochemical potential energy between the fluoride and electride systems. With a reduction potential of +0.97 V vs. Li/Li^+, we expect that Y_2CF_2/Y_2C could serve as an

anode in a reversible F^- ion battery and with a volumetric density of F^- storage in Y_2C double that Li^+ storage in $LiCoO_2$.

APPENDIX A–SUPPORTING INFORMATION FOR CHAPTER 3.

A.1 3D Ca_2N synthesis and characterization

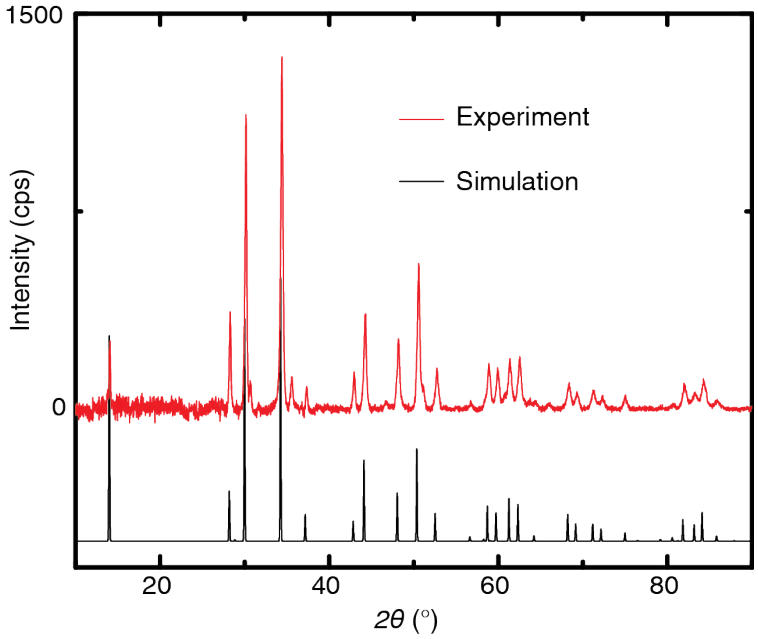


Figure A.1: Powder X-ray diffraction pattern of synthesized Ca_2N compared to a simulation of the diffraction pattern using reported crystal parameters.

A.2 DFT calculations of Ca_2N and graphite

Density functional theory (DFT) calculations were performed using the CASTEP[54] code with plane-wave basis set5 approximations. Ultrasoft[56] pseudopotentials were used to describe core electrons, and a 400 eV cut-off energy was used. For this cut-off energy, calculations were convergent with dE/dE_{cut} less than 0.01 meV/atom. A GGA PBE functional[57] was used for the exchange-correlation contribution to total energy and Grimmes DFT-D[58] correction was used to account for long-range dispersion forces. Both graphite and bulk Ca_2N were structurally relaxed prior to further calculations. A Monkhorst-Pack[59] grid of $8\times8\times2$ k-points was used for the geometry optimization and interlayer binding energy study. Each crystal structure relaxed to within 2% of experimentally determined parameters.

Portions of this chapter reproduced with permission from Druffel, D. L.; Kuntz, K. L.; Woomer, A. H.; Alcorn, F. A.; Hu, J.; Donley, C. L.; Warren, S. C. Experimental Demonstration of an Electride as a 2D Material. *Journal of the American Chemical Society* **2016**, 138, 1608916094. Copyright 2016 American Chemical Society.

To determine binding energy for both graphite and Ca_2N, we varied the interlayer distance between layers in each crystal structure and then calculated the total energy. An infinite structure was built with an interlayer distance of 12 Å, such that there were no interactions between sheets. We then calculated the interlayer binding energy as either (E-E_∞)/(# of atoms at interface) or (E-E_∞)/(# of interfaces $\times$ area). For electronic structure calculations, we used a denser MK grid, of $64\times64\times10$ and $64\times64\times64$ for the hexagonal and rhombedral orientations of Ca_2N. The bandstructure of rhombohedral Ca_2N shown in Figure 3.4e agrees with previously reported calculations[26] and experimentally determined band structures.[66] The integrated electron density was within 0.0001 e- of the total electron count, and thus we assume all electrons were accounted for and our mesh was sufficient to accurately describe electron density. The joint density of states (JDOS) was calculated from the CASTEP output with OptaDOS code[179–181] using a Gaussian broadening scheme with a 0.05 eV smearing width. To image the orbital projections of valence and conduction band states, we used the STM profile module of CASTEP for a given negative or positive bias, respectively. Specifically, an applied bias of -1.49 eV was used to image the interlayer electron gas of bulk Ca_2N. To obtain the electron density profile, we used Perl scripting to extract and integrate total electron count across the z-axis of the hexagonal unit cell. The band structure of Ca_2N changes subtly with thickness (Figure A.22a,f) in agreement with other reports[170] and does not change with lateral interlayer translation.[64] Therefore, we expect the band structure of our few-layer flakes to be similar to that of the 3D solid, which was recently shown by angle-resolved photoemission spectroscopy to match the DFT predictions.[66] Images of the orbital projections for monolayer Ca_2N show that both of the bands that cross the Fermi level contribute to the electron density covering the monolayers surface (Figure A.2b,c,d) in agreement with previous findings.[170,172] The electron gas extends as far as 2.0 Å from the calcium atoms of the monolayer. Images of the orbital projections for bilayer Ca_2N show that the electron gas sandwiched between layers is at a slightly lower energy than the electron gas at the surface (Figure A.2g,j) and that the electron gas at the surface consists largely of filled states in the energy range -0.56 eV to E_F (Figure A.2i,j).

The JDOS for the bilayer has a distinct peak at 1500 nm (Figure A.2), which arises from direct transitions from the lowest of the three bands crossing the Fermi level to either of the top two bands crossing the Fermi level. These bands are split by $\sim$0.83 eV because of the coupling between the electron layers.[170] The top two bands are primarily composed of states in which the electron density resides on the outer-most electron layer, while the lowest of the three bands is composed of states in which the electron density is sandwiched in between planes of $[Ca_2N]^+$.

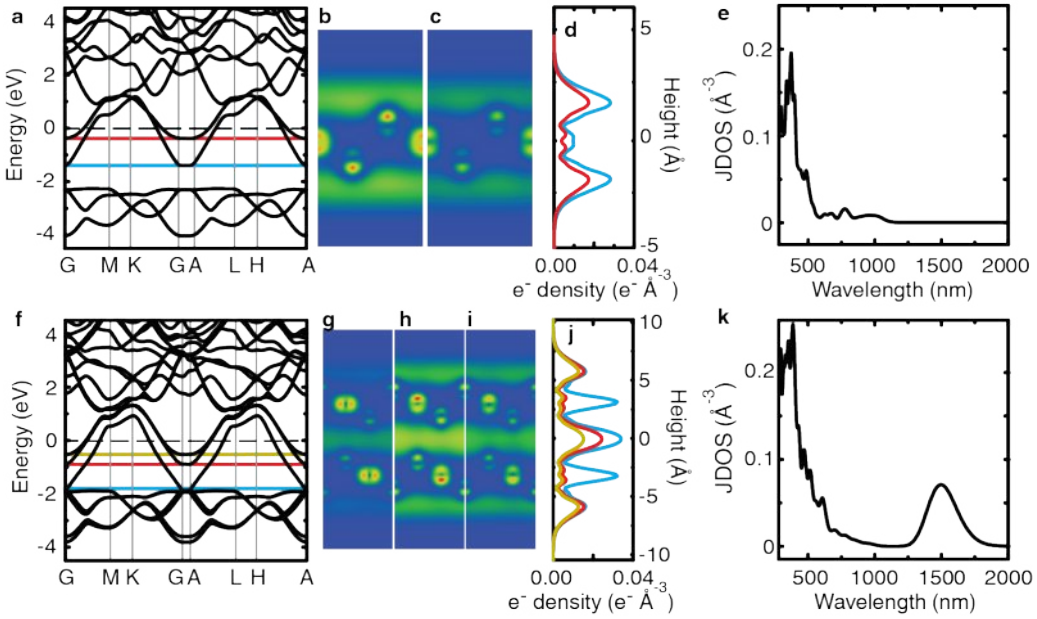


Figure A.2: Electronic structure of mono- and bilayer Ca_2N. a) Band structure of monolayer Ca_2N calculated from the hexagonal unit cell. Projections of the integrated electron density of monolayer Ca_2N within the unit cell as calculated by density functional theory (DFT). The integration is over states in the energy range b) -1.41 eV (blue line) to E_F and c) -0.39 eV (red line) to E_F. The color gradient in b and c ranges from an electron density of 0.00 (blue) to 0.10×10^{-3} e^- $Å^{-3}$ (red). d) The electron density profile integrated along the z-axis of the unit cell for the states in b and c. e) The joint density of states (JDOS) for monolayer Ca_2N. f) Band structure of bilayer Ca_2N calculated from the hexagonal unit cell. Projections of the electron density of bilayer Ca_2N integrated over states in the energy range g) -1.88 eV (blue line) to E_F, h) -0.90 eV (red line) to E_F, and i) -0.56 eV (yellow line) to E_F. The color gradient (blue to red) in g, h, and i varies from 0.00 to 0.41×10^{-3} e^- $Å^{-3}$, 0.00 to 0.14×10^{-3} e^- $Å^{-3}$, and 0.00 to 0.14×10^{-3} e^- $Å^{-3}$, respectively. j) The electron density profile integrated along the z-axis of the unit cell for the states in g, h and i. k) The JDOS for bilayer Ca_2N.

A.3 Screening solvents for liquid exfoliation of Ca_2N

After identifying 1,3-dioxolane as the most promising solvent, we repeated the screening with 1,3-dioxolane, tetrahydrofuran (THF), and 1,4-dioxane, which have similar structures. Ca_2N (10 mg) decomposed to a white powder after 24-72 hours of exposure to THF or 1,4-dioxane. To ensure that the solvents had very minimal water content and to remove stabilizers, we dried each solvent over sodium metal and distilled the dry solvent over a Schlenk line with N_2 environment. The repeated screening yielded the same results; Ca_2N (10 mg) decomposed to a white powder after 24-72 hours of exposure to THF or 1,4-dioxane. The X-ray diffraction pattern of the white powder matches that of $Ca(OH)_2$ (Figure A.3). In all subsequent experiments, 1,3-dioxolane was dried over sodium and distilled just before use.

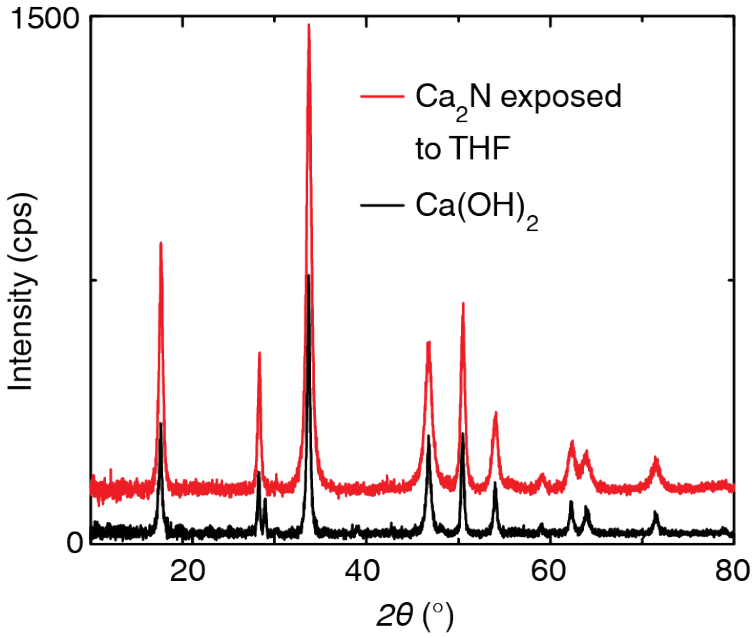


Figure A.3: Powder X-ray diffraction pattern of $Ca(OH)_2$ and Ca_2N exposed to THF for 24 hours.

A.4 Transmission electron microscopy experiments and simulations

In a typical experiment, Ca_2N powder was suspended in 1,3-dioxolane (2.5 mg/mL) as described above and was sonicated for 800 minutes under anhydrous and oxygen-free conditions. The suspension was centrifuged at 300 rpm for 15 min to isolate the exfoliated material. Several microliters of the suspension were drop-cast onto a lacey carbon grid and dried in a vacuum chamber for 30 minutes. The samples were loaded into a high-resolution transmission electron microscope (HR-TEM) using a nitrogen-filled glovebag to minimize exposure to air and water. To obtain selected area diffraction patterns, the samples were loaded into a low resolution TEM following the same procedure as above. TEM images show that the materials are thin and flat though there is a distribution of flake thicknesses and sizes (Figure A.4). Some material is nonsheet-like or appears to be an aggregate of sheets despite our attempt to isolate the thinnest materials.

We simulated the selected area diffraction pattern by multislice calculations (JEMS).[177] To understand the effect of flake thickness on the diffraction pattern, we modeled crystal structures of Ca_2N with thicknesses of 1-8 layers. The monolayer (Figure A.5a) shows two sets of hexagonal diffraction spots with *d*-spacing 1.80 and 3.12 Å, in agreement with our experimental measurements. For flakes thicker than a bilayer, the intensity of the spot corresponding to the larger *d*-spacing is negligible. The effect of translational disorder was examined by modeling various stacking configurations of Ca_2N. The material is expected to have an

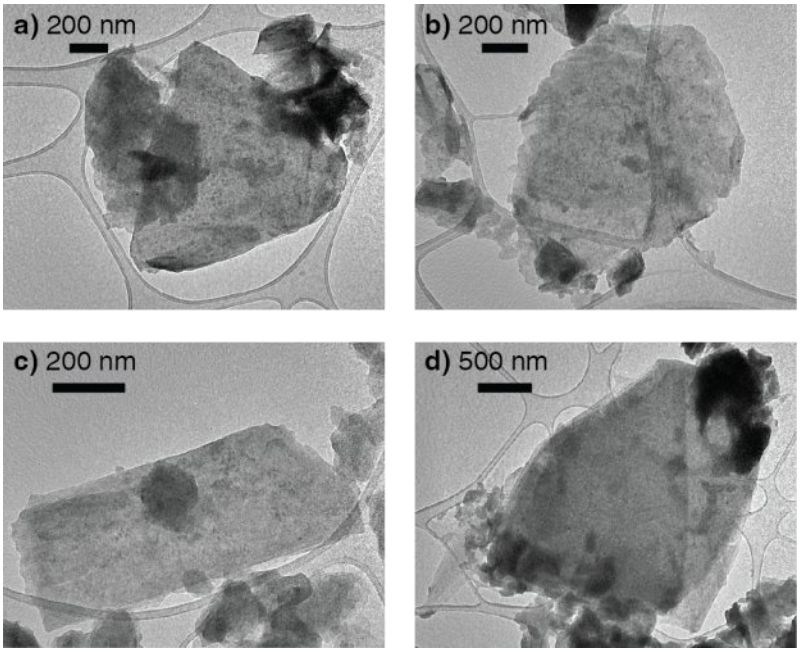


Figure A.4: Low-resolution transmission electron microscopy images of flakes of 2D Ca_2N.

ABC stacking sequence in the three layers in the unit cell, but the energetic cost of translating layers is low. We modeled alternate stacking sequences, including ABAC, ABAB, ACAC, ABC-ABC-ABA-ABC-ABC, ACC-ACC-ABACBB-BAB. For example, in the sequence ABC-ABC-ABA-ABC-ABC the ninth C plane has been replaced with an A plane, which is equivalent to translating that C plane by 2.09 Å in the direction perpendicular to the *x*-axis. In the translated structures, like the ABC-ABC-ABA-ABCABC stacking sequence (Figure A.5c), both sets of diffraction spots are present. The intensity of the spots varies significantly with the stacking sequence. For example, in the highly disordered sequence ACC-ACC-ABA-CBB-BAB (Figure A.5d), the diffraction spots of the larger *d*-spacing (3.12 Å) are more intense than the spots at the smaller *d*-spacing (1.80 Å).

A.5 Photoemission experiments of 2D and 3D electrides

X-ray photoemission spectroscopy (XPS) was used to investigate the surface of 2D Ca_2N, 3D Ca_2N, Ca_3N_2, oxidized Ca_2N, and $Ca(OH)_2$. Suspensions of 2D Ca_2N in 1,3-dioxolane were dropcast onto a *p*-doped silicon wafer with a thick thermal oxide (300nm) under inert atmosphere (N_2, $<$0.01 ppm O_2, $<$0.01 ppm H_2O). The wafer was heated to 75 °C for 15 min and subsequently dried under low vacuum for 15 min to drive off 1,3-dioxolane. Ca_3N_2, $Ca(OH)_2$, and oxidized Ca_2N (exposed to ambient conditions for two

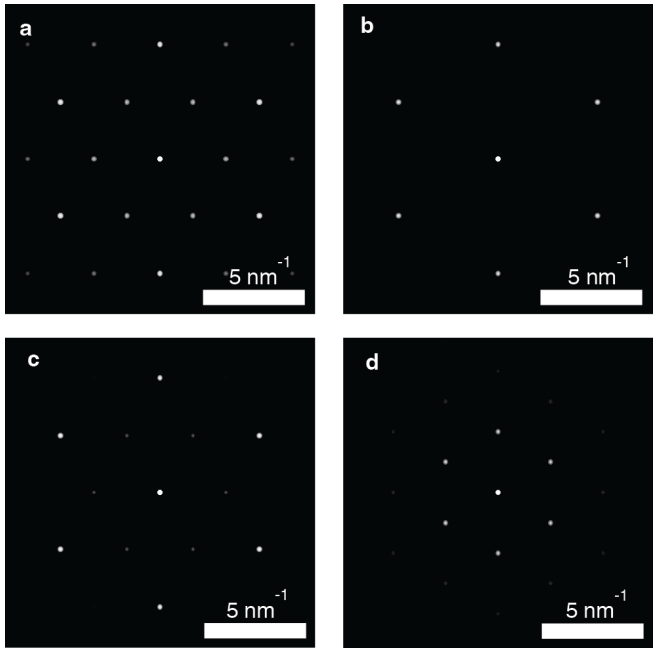


Figure A.5: Simulated diffraction pattern of a) monolayer Ca_2N, b) trilayer Ca_2N, Ca_2N with a stacking sequence ABC–ABC–ABA–ABC–ABC, c) Ca_2N with stacking sequenc ACC–ACC–ABA–CBB–BAB looking down the [001] zone axis.

weeks) were each imbedded into indium foil under inert atmosphere. The samples were then loaded into a Kratos Axis Ultra Delay-Line Detector (DLD) spectrometer under dry N_2 conditions and held under a high vacuum ($<10^{-9}$ torr) for analysis. The oxide species were loaded into the XPS instrument separately from air-sensitive samples. The X-ray source was a monochromatic Al Kα source (1487.7 eV). A charge neutralizer (1.8 A filament current, 2.8 V charge balance, 0.8 V filament bias) was used with all oxide species; air-sensitive species were investigated with and without the charge neutralizer. The spectra were corrected to the carbon 1s peak for adventitious carbon (284.6 eV).[324] By comparing the area of the peaks of the Ca 2p core electrons to N 1s core electrons and accounting for the atomic sensitivity factors, we measured the ratio of Ca:N for 2D Ca_2N (5.3:1), Ca_3N_2 (4.6:1), and oxidized Ca_2N (18:1). We found that the ratio is significantly calcium-rich in all measurements and the intensity of the nitrogen peak is low in all samples. We noticed a trend in the C 1s spectra that the area of the peak at 289.5 eV increases relative to the area of the peak at 284.6 eV for oxidized 2D Ca_2N relative to unoxidized Ca_2N (Figure A.6). This was observed in all samples and may be indicative of $CaCO_3$ or other C=O bond formation.

Ultraviolet photoemission spectroscopy (UPS) provides information about the valence band of the material and the density of states near the Fermi energy edge. For UPS studies, 2D Ca_2N samples were

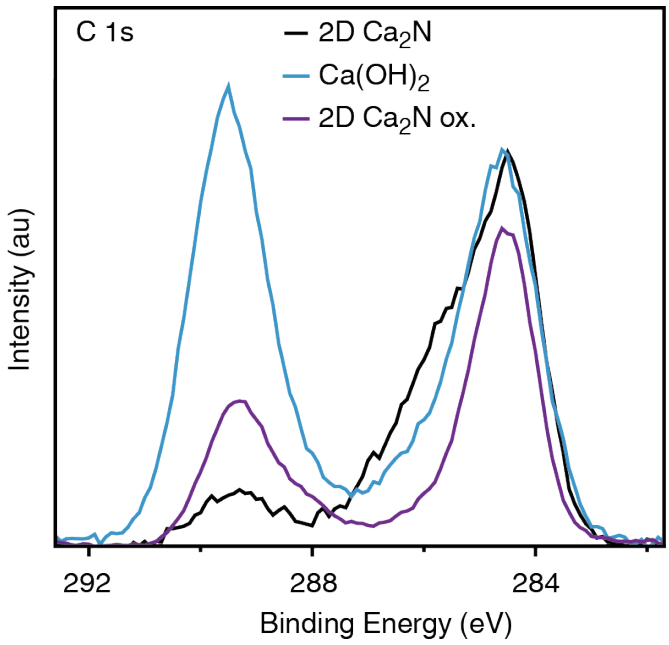


Figure A.6: XPS spectra of core C 1s electrons for 2D Ca_2N, deliberately oxidized 2D Ca_2N, and $Ca(OH)_2$.

drop-cast onto metal-plated silicon wafers (5 nm adhesive metal, either Cr or Ti, and 50 nm of conductive metal, either Au or Pt). Samples were prepared in the same manner as for XPS analysis described above. A He I source (21.2 eV) was used for UPS measurements. In order to measure the metallic character of Ca_2N and not the substrate, we cast films much thicker than the escape depth of electrons. We characterized the films by XPS and then cleaned the surface of the films by argon ion sputtering. The quality of substrate coverage by Ca_2N was assessed by measuring the area of peaks from Pt or Au. We performed sputtering twice for 15 minutes, each time with an accelerating voltage of 1 kV and an emission current of 10 mA. The resulting spectra are shown in the Figure A.7. After sputtering the surface of 2D Ca_2N, we used XPS to determine the relative content of carbon (Figure A.7a), platinum (Figure A.7b), calcium (Figure A.7c), and nitrogen (Figure A.7d). We found that the carbon content decreased as sputtering time increased and that the calcium and nitrogen content increased. This is consistent with the removal of hydrocarbons from the surface of 2D Ca_2N. Furthermore, the unchanged position and shape of the calcium and nitrogen peaks after the sputtering indicated that we are not changing or damaging our material during the sputtering process. Additionally, this verifies that the film is generally thicker than the escape depth of the electrons since peaks from the Pt substrate (Figure A.7d) are barely detectable. Furthermore, the density of states up to the Fermi edge (Figure A.7e) becomes more prominent as hydrocarbons are removed from the surface of our thick film.

Because XPS probes even deeper into the sample than UPS, we are confident that the density of states at the Fermi edge probed in our UPS measurements are exclusively attributable to the film of 2D Ca_2N and not the substrate.

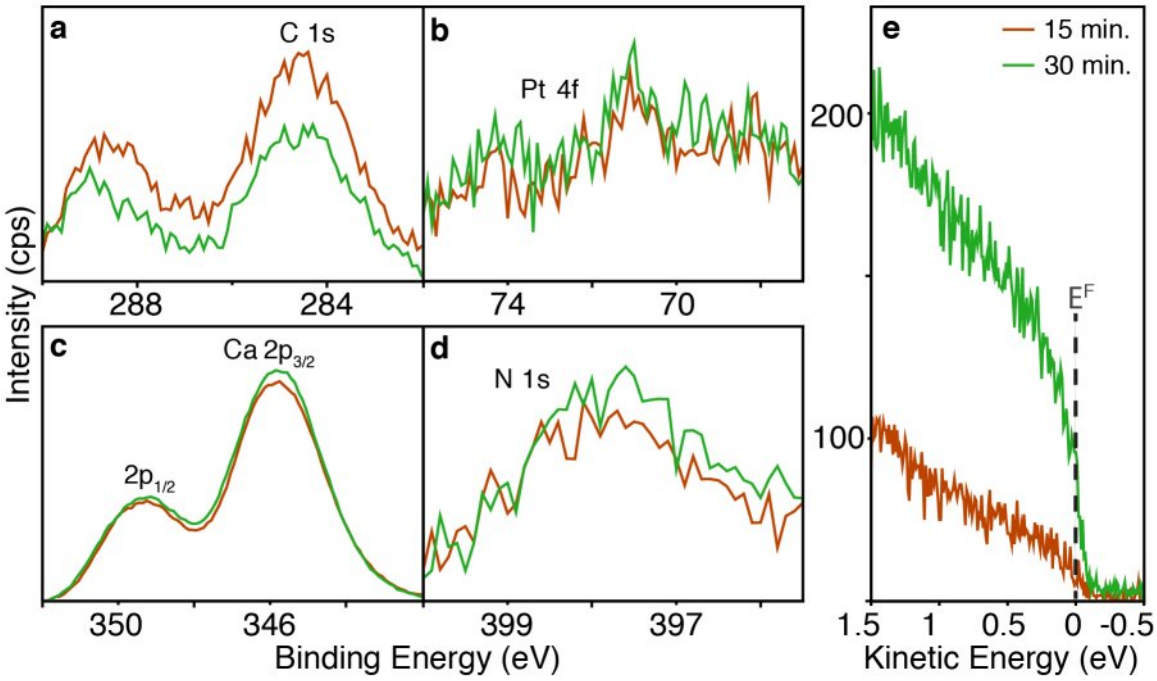


Figure A.7: Photoemission spectroscopy of a thick film of 2D Ca_2N on a platinum-coated silicon wafer. After sputtering the film with argon ions to remove surface contamination, the film was characterized. In XPS, (a) the carbon content on the surface of 2D Ca_2N decreased as sputtering time increased from 15 minutes (orange) to 30 minutes (green). (b) The Pt film is almost entirely covered by Ca_2N, as shown by the extremely small peaks at 71.1 and 74.4 eV. The dashed line shows the positions of a bare Pt substrate; the intensities of the dashed line were reduced by a factor of 30. The inset shows a magnified version of the intensities for the Pt core electron binding energies on the film with 2D Ca_2N, showing that the Pt signal does not increase with sputtering time. (c) The calcium and (d) nitrogen peaks increase in area as hydrocarbons are removed by sputtering. (e) In UPS measurements, as hydrocarbons are removed, the density of states at the Fermi edge become more prominent and provides evidence for the metallic character of 2D Ca_2N.

Generally, UPS allows for calculation of the work function Φ of a material. The work function is related to the Fermi energy of the instrument E_F, the energy of the incident photon h, and the lowest kinetic energy at which electrons are emitted, E_{SECO}:

$$E_{SECO} = h\nu - (E_F - E_{SECO}) \tag{A.1}$$

For conductive homogenous samples in electrical contact with the sample holder, the kinetic energy shifts exactly with the biasing potential; however, if different areas of the sample have different electrical

conductivity or photoionization cross sections, then the areas of the sample have different steady-state potentials and some features only shift by a fraction of the biasing potential.[325] We find that the surface of Ca_2N experiences this effect, which is called differential charging. As shown in Figure A.8a, the XPS spectra of Ca 2p core electrons with the charge neutralizer active shows an additional feature that is not present in the spectra when the charge neutralizer is off; this is evidence of differential charging. Similarly in UPS, differential charging affects the secondary electrons emitted and prevents an accurate work function from being measured. The secondary cutoff electron edge E_{SECO} of 2D Ca_2N corrected by the applied bias, shown in Figure A.8b, have a secondary feature that is induced with increasing applied biases. In Figure A.8c, the work functions extracted from Figure A.8b are plotted against the applied bias. The slope of the line ($\Delta\ \Phi$ / Δ bias) varies between samples, but in all cases is much less than 1, which suggests that the sample exhibits differential charging. Unfortunately, this also indicates that we cannot extract a reliable work function from the surface of the material because the energy of the secondary electrons are dependent on the applied bias and the degree of differential charging each sample experiences. We tested other metals (eg. Au, Pt) with known work functions and did not observe differential charging. Therefore, we believe that this response is from the Ca_2N sample and not an artefact of the instrument.

While this response could be caused by poor electrical contact between the sample holder and the drop-cast film, we think that this explanation is unlikely because our observation is consistent over many samples and the same observation was made on 3D Ca_2N in two other studies.[26,34] As suggested by others,[34] the response may be related to the highly anisotropic character of the samples that have areas of markedly different work functions.

A.6 Optical response of 2D Ca_2N

We measured the optical response of 2D Ca_2N with UV–visible–near IR (λ = 280-2200 nm) transmission spectroscopy using a Cary 5000 double-beam spectrometer with an external integrating sphere attachment. Quartz cuvettes (Starna 1 mm path length) were filled with suspensions of 2D Ca_2N in 1,3-dioxolane in a glovebox and sealed with parafilm to maintain the N_2 atmosphere during the measurement. The attenuation of light through the sample depended linearly on sample concentration across all measured wavelengths (Figure A.9).

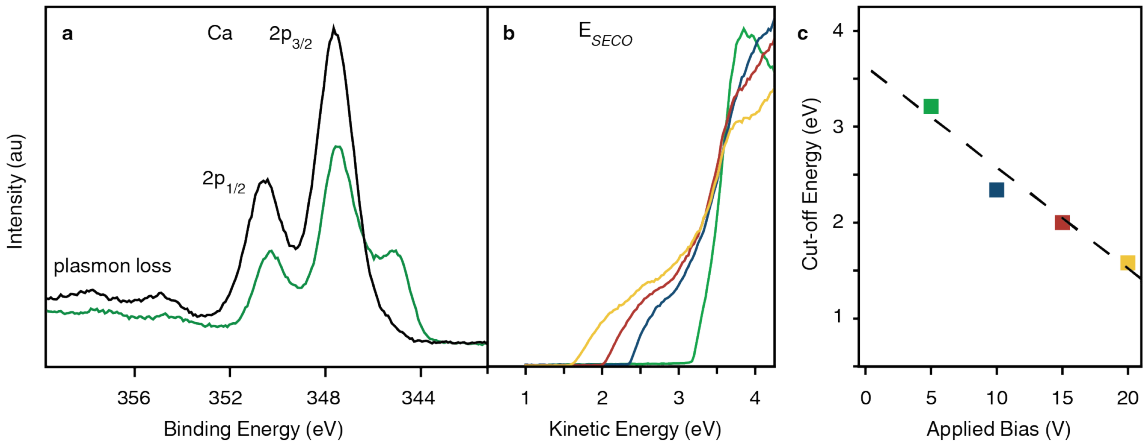


Figure A.8: Differential charging of samples of 2D Ca_2N. a) XPS spectra of bulk Ca_2N Ca 2p electrons with the charge neutralizer on (green) and with the charge neutralizer off (black). b) UPS spectra of bulk Ca_2N with 5V (green), 10V (blue), 15V (red), and 20V (yellow) applied biases at the secondary cut-off energy, E_{SECO}. The spectra are corrected to account for the different applied biases. (c) Work function, Φ, plotted against the applied bias for one sample of 2D Ca_2N.

Previously reported reflectivity data for 3D Ca_2N[26] yielded a fit to the Drude-Lorentz model, which resolved one Drude component, described by a plasma frequency, ω_p, of 2.78 eV and mean scattering time, τ, of 0.64 ps, and two Lorentz components at 2.39 and 3.37 eV.

$$\omega_p^2 = \frac{Ne^2}{m_o \epsilon_o} \tag{A.2}$$

The Drude susceptibility χ_D, described by ω_p and a damping factor $\gamma = 1/\tau$ (Equation A.3), primarily accounts for intra-band absorbance of free-carriers.

$$\chi_D(\omega) = \frac{-\omega_p^2}{\omega^2 + i\gamma\omega} \tag{A.3}$$

The Lorentz contribution χ_{Lj}, described by an oscillator frequency ω_j and damping factor γ (Equation A.4), accounts for inter-band transitions.

$$\chi_{Lj}(\omega) = \frac{\omega_p^2}{\omega_j^2 - \omega^2 + i\gamma\omega} \tag{A.4}$$

The fit can be used to calculate the dielectric function $\epsilon(\omega)$ (Equation A.5), which is related to the imaginary part of the refractive index, k.

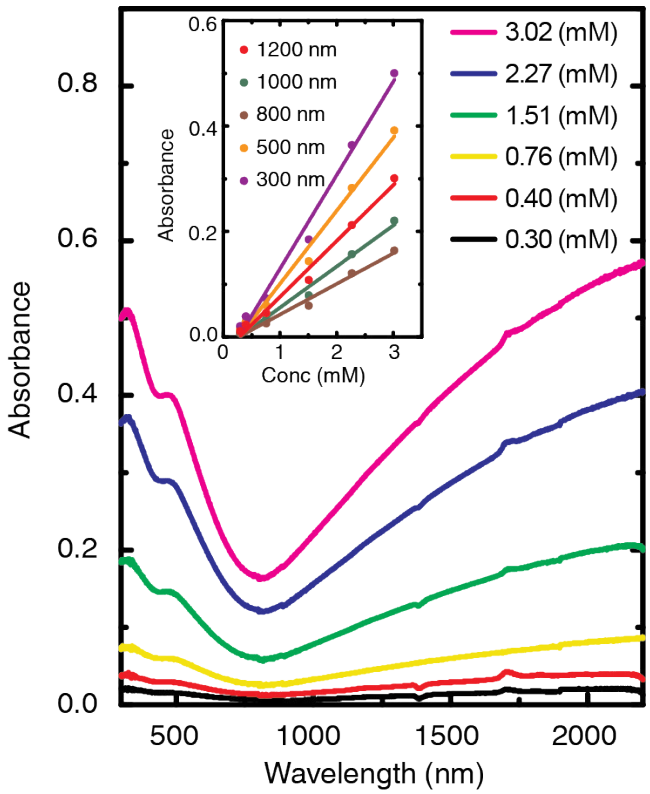


Figure A.9: The absorbance of suspensions of 2D Ca_2N vs wavelength. The solvent has been background subtracted. The inset shows that the absorbance depends linearly on the concentration across the UV–Vis–IR range.

$$\epsilon(\omega) = 1 + \chi_D(\omega) + \sum_{j=1}^{n} \chi_{Lj}(\omega) \tag{A.5}$$

$$\epsilon(\omega) = \epsilon_1(\omega) + i\epsilon_2(\omega) \tag{A.6}$$

$$k(\omega) = \frac{1}{\sqrt{2}}(-\epsilon_1(\omega) + \sqrt{\epsilon_1(\omega)^2 + \epsilon_2(\omega)^2})^{\frac{1}{2}} \tag{A.7}$$

$$a = \frac{2k\omega}{c} \tag{A.8}$$

The attenuation coefficient α (Equation A.8), which is reported in Figure 4b, can be calculated by from k, the frequency of light ω, and the speed of light, c.[326] The fit shows local maxima in attenuation at 360 nm and 520 nm in agreement with the JDOS and our experimental data. The magnitude of the attenuation coefficient

predicted by the Drude-Lorentz model only differs from that of our 2D flakes by a factor of three. We note that because the reflectivity data used to make the fit to the Drude-Lorentz model only measured to 350 nm as a high energy bound, the damping term that describes the higher energy Lorentz component is subject to error; as a result, we believe that the attenuation coefficient calculated from this fit is likely overstated at 360 nm. In addition, we compared our data to the JDOS of Ca_2N calculated from the band structure (Figure A.10a). The JDOS accounts for direct transitions from unfilled states to filled states as illustrated by dark blue arrows. Interestingly, transitions from the flat band around -1.7 eV to the unfilled states in the conduction band constitute a large portion of the total JDOS (Figure A.10b).

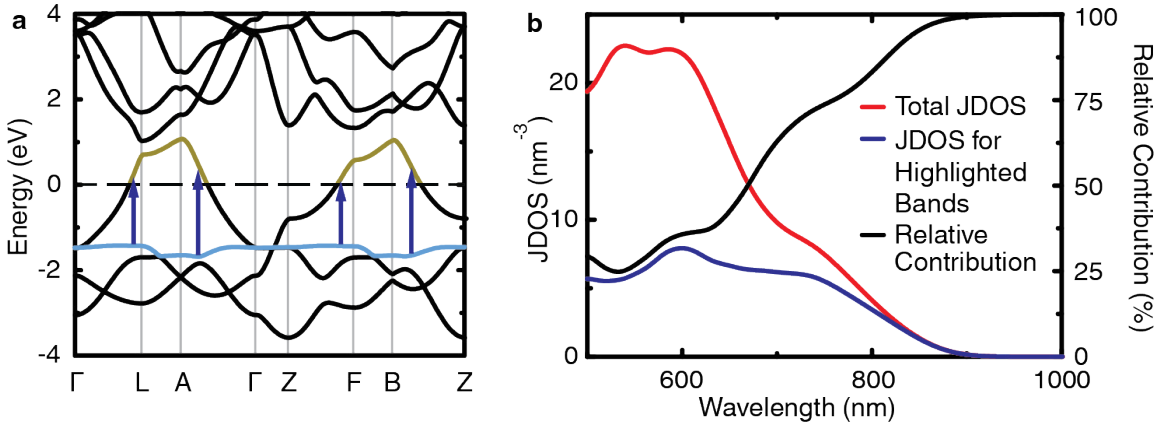


Figure A.10: a) The band structure of Ca_2N highlighting the flat band of states with energies of -1.72 eV to -1.5 eV (blue) and the unfilled states in the conduction band with energies 0 eV to 1.00 eV (gold). Dark blue arrows depict direct transitions from the flat band to the conduction band. b) The joint density of states (JDOS) for the entire band structure (red) and for only the transitions from the flat band to the conduction band (dark blue). The relative contribution of those transitions to the total JDOS is given in black.

The experimental near IR data shows attenuation at wavelengths longer than 800 nm (Figure 3.4b). Because our experiment measures the transmittance of light, the attenuation is a combination of light scattering and absorbance despite our attempts to minimize the scattering component by using an integrating sphere. To try to qualitatively understand whether the long-wavelength response is dominated by scattering or absorbance, we measured the transmittance with 1-cm quartz cuvette inside the integrating sphere and at the front of the integrating sphere (Figure A.11). The wavelength was only measured to 1600 nm because the solvent, 1,3-dioxolane, absorbs too strongly in the NIR with a 1-cm cuvette to yield measurable signals.

The Drude-Lorentz model predicts a minimum in effective attenuation around 800 nm in excellent agreement with our data. In the Drude-Lorentz model, the impinging light is either scattered from the surface

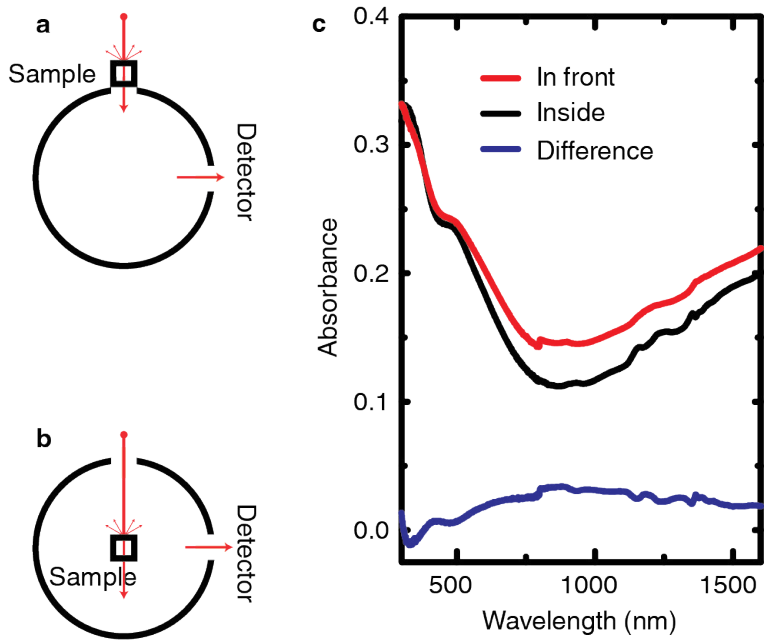


Figure A.11: Schematic of the measurement with the sample a) in front of the integrating sphere and b) inside of the integrating sphere. The UV–Vis–NIR absorbance spectra of Ca_2N vs wavelength with the sample in different geometries. The solvent has been background subtracted.

or attenuated by electron scattering events inside of the particle. Because our particles have a high surface area to volume ratio, we expect electron surface scattering to decrease the mean scattering time, τ relative to bulk samples (0.64 ps).[26] Therefore we expect greater attenuation in our 2D Ca_2N. Still, a much smaller τ on the order of 1 fs or smaller would be needed to fit our data to the observed shape and we think that such a small relaxation time is unphysical. The long-wavelength response could be due to overlapping plasmonic signals from the broad distribution of particle shapes and sizes. However, our measurements seem insensitive to the distribution of particle shapes and sizes. Without controlling for the size and shape of the particle and even with centrifuging at different speeds the long-wavelength response is consistent in all measurements. Therefore, the near IR response could have contributions from Drude absorbance and plasmonic signals. Further studies are needed to understand the long-wavelength response.

APPENDIX B–SUPPORTING INFORMATION FOR CHAPTER 4

B.1 Requirements for electron transfer between materials

A rigorous understanding of electrons and electron transfer has been one of the central principles of chemistry, physics, and material science for over a century.[107,186,187,327–330] In 1950, D.A. Dowden[187] formulated guidelines for the transfer of electrons between two materials, which we have condensed here into two criteria:

(i) **Driving force**: There must be a difference in the electrochemical potential of electrons (i.e., the Fermi level) between the two materials. This may be induced by differences in electron affinity (A), ionization energy (I), or work function (ϕ). The Fermi level approaches equilibrium through the transfer of electrons if the change in free energy of electron transfer is negative.

(ii) **States are available**: Electron transfer will occur from filled states of one material to unfilled states of the other material. Alternatively, the hybridization of states between the two materials may provide new states into which electrons are shared between materials.

In Figure B.1, we present familiar systems in which electron transfer, or the lack thereof, can be understood via the criteria outlined above. We begin with a simple interpretation of bonding between two elements (Figure B.1a). As two elements are brought together, orbital mixing of the highest energy electronic states will create new, hybridized bonding and antibonding states (red). Differences in A and/or I will determine the extent to which electron transfer occurs, but this difference is often simplified as the difference in electronegativity (χ) between species. An illustrative case is the formation of ionic interactions in NaCl, a system with a large difference between A_{Cl} and I_{Na}. Electrons in Na *3s* orbitals (I_{Na}: *ca.* 5.2 eV) are donated to unfilled Cl *3p* orbitals (A_{Cl}: *ca.* 13.8 eV) to form states that are almost entirely Cl *3p* in character with relatively little hybridization (Figure B.1b).

We can expand this model for electron transfer between discrete atomic orbitals to include a continuous density of states. In Figure B.1c,d, we present three models for electron transfer between metals and adsorbates. Positive ions can be formed on the surface of a metal when $I < \phi$, such that an electron is transferred from the adsorbate to the metal (Figure B.1c). With a continuous density of unfilled states above the Fermi level (E_F) multiple adsorbates can transfer electrons to the metal until all adsorbates have been oxidized or until ϕ is equal to I. Negative ions can be formed on the surface of a metal when $A >$, such that an electron is transferred to the adsorbate from the metal (Figure B.1c). Electrons are transferred from the

metal to a density of adsorbates on the surface until all adsorbates have been reduced or until ϕ is equal to A. Electron transfer between metals and adsorbates can also form covalent bonds (Figure B.1d), in which electrons occupy a hybridized M-A state. Common examples of this type of electron transfer are the poisoning of metal catalysts with carbon monoxide, thiols, cyanides, nitriles, etc.

To further illustrate the influence of point (ii), we present the interactions of a metal-metal junction and a semiconductor-semiconductor junction. First, consider two metals in close proximity with work functions ϕ_I and ϕ_{II} such that $\phi_I < \phi_{II}$ (Figure B.1e). The continuous density of states around E_F of each metal enables the transfer of electrons from metal I to metal II until E_F is equilibrated at the interface. We now consider the case for two pristine, intrinsic semiconductors, such that there is no surface or defect states within the forbidden region (or the band gap) between the minimum unoccupied conduction band states (E_C) and highest occupied valence band states (E_V) (Figure B.1f). While this system will meet criterion (i) due to the difference in ϕ_I and ϕ_{II}, there are no states in which an electron can be donated or accepted, thus failing criterion (ii) and there is limited electron transfer.

While the discussion of pristine semiconductors is interesting from the perspective of systems with limited electron transfer, it is far from a realistic condition. In fact, it is often the case that there is a large amount of electron transfer between two semiconductors (Figure B.1g). In realistic systems, criteria (ii) is met because of the presence of defect and surface states within the band gap at concentrations *ca.* 10^{-3}/atom, such that electron transfer can proceed. As a final example, we discuss the interface of two semiconducting two-dimensional materials, MoS_2 and WSe_2 (Figure B.1h). Because of the large interlayer distance due to van der Waals forces, as well as the naturally low concentration of defect and surface states in 2D materials in general, it is intuitive that despite meeting criteria (i), there is negligible electron transfer. This finding can be generalized to all van der Waals layered materials and van der Waals heterostructures and establishes the context in which donor-acceptor heterostructures are a fundamentally new architecture for two dimensional materials in which electron transfer is favorable.

B.2 Overview of density functional theory methods using CASTEP

Density functional theory (DFT) calculations were performed using the CASTEP[54] code with plane-wave basis set approximations.[55] To describe core electrons, ultrasoft pseudopotentials[56] was used with a 600 eV cut-off energy. For this cut-off energy, calculations were convergent with $dE_{tot}/dlnE_{cut}$ less than

0.01 meV/atom. A GGA PBE functional[57] was used for the exchange-correlation contribution to total energy and Grimme's DFT-D correction[58] was used to account for long-range dispersion forces. To prevent self-interactions between periodic images, a 12 Å vacuum space was included in the z-direction.

Geometry optimizations of all structures were first performed. A Monkhorst-Pack grid[59] of 16×16×4 k-points were used and structures were optimized using a BFGS algorithm[331] with a convergence tolerance of 5.0×10^{-7} eV/atom for energy, 0.01 eV/Å for max force, 0.02 GPa for max stress, and 5.0×10^{-4} Å for max displacement. Further discussion on the optimized geometries of donor–acceptor heterostructures, as well as lattice constants and strain can be found in Section B.3. Electronic structure calculations were performed at a finer k-point mesh of 32×32×6. In particular, we performed the following analyses using the finer mesh: Bader charge analysis[194–197] (Section B.4), band structures (Section B.6), binding energies (Section B.7), sliding energies (Section B.8), and work functions (Section B.9). Additional computational details can be found within the corresponding section.

B.3 Structural optimization of electrene and 2DM heterostructures

Donor–acceptor heterostructures were constructed from monolayer slabs of electrenes (Ca_2N, Sr_2N) and other 2D materials (graphene, phosphorene, ZrS_2, and hexagonal boron nitride), and geometry optimized according to the method described in Section B.3. We minimized strain in our donor–acceptor heterostructures using supercells (Figure B.3). For example, an e-C heterostructure consists of a 3×3 slab of graphene adjacent to a 2×2 slab of Sr_2N. In general, we found that supercell geometries can keep the strain for each layer below 2% (Table B.1). One exception to the need for a supercell is e-ZrS_2. Because of the matching lattice constants (i.e., the lattices are commensurate), strain is minimized without a supercell. As stated previously, we introduced a 12 Å vacuum space in the z-direction to prevent self-interactions between periodic images. We calculate the interlayer distance of donor–acceptor heterostructures by taking the difference between the average z-coordinate of atoms at the interface (Figure B.2, dashed red lines) and report this value in Table B.1 and Figure 4.2b.

B.4 Bader charge analysis and hybrid functionals

We calculate electron transfer using Bader charge analysis,[194–197] as implemented by Henkelman and colleagues. Bader charge analysis will partition the electron density using zero-flux boundaries and integrates

Table B.1: Lattice matching, interlayer distances, and strain on the 2DM and electrene components after structural optimizations

Structure	Supercell of 2DM	Supercell of Electrene	Lattice Constants (Å)	Strain	ILD (Å)
Sr_2N/Graphene (e-C)	3×3	2×2	a=b=7.448264	e: +0.7% C: -1.0%	2.754
Ca_2N/BP (e-P)	2×2	5 unit cells	a=6.382972 b=9.604992	e: +1.0% C: -2.0%	2.624
Sr_2N/BN (e-BN)	3×3	2×2	a=b=7.56458	e: +1.8% BN: -0.1%	2.861
Ca_2N/ZrS_2 – A (e-ZrS_2A)	1×1	1×1	a=b=3.611331	e: ∼0.0%	2.750
Ca_2N/ZrS_2 – B (e-ZrS_2B)	1×1	1×1	a=b=3.594225	e: ∼0.0%	2.044
Ca_2N/ZrS_2 – C (e-ZrS_2C)	1×1	1×1	a=b=3.601243	e: ∼0.0%	2.105

the resulting Bader volumes for a total charge. Compared to the Mulliken populations calculated from CASTEP, Bader charge analysis has significantly improved results. For example, we calculate a formal charge of ±0.5 e- for Na and Cl ions in NaCl using Mulliken population, while Bader charge analysis is *ca.* ±0.8 e^- and is much closer to experimental values.

For each heterostructure we first perform electronic structure calculations. The resulting .den_fmt file was converted to a .cube file. The new .cube file and .castep file were then used to calculate the bader volumes and bader charges for a structure. The amount of charge transferred (q_t) was calculated then as a difference between the electrenes (or paired 2DM) integrated electron density within the heterostructure versus the total electron count of the isolated electrene (or paired 2DM). With the exception of e-C, we found that electrons will be predominantly transferred to particular atoms: e-P and e-ZrS_2 has electron transfer to the atoms closest to the electrene, while e-BN shows electron transfer primarily to B atoms. We therefore calculate the charge transfer per acceptor atom and report these values in Table B.2.

Table B.2: Electron transfer in donor-acceptor heterostructures calculated from bader charge analysis

Structure (e-X)	q_t/supercell (e^-)	q_t/electride formula unit (e^-)	q_t/atom of X (e^-)	q_t/acceptor atom (e^-)
C	1.51	0.38	0.08	0.08
BP	2.13	0.43	0.13	0.26
BN	1.17	0.29	0.07	0.13
ZrS_2(a)	0.37	0.37	0.12	0.37
ZrS_2(b)	0.53	0.53	0.18	0.53
ZrS_2(c)	0.51	0.51	0.17	0.51

It is well known that spurious self-interactions in DFT will often undervalue the band gap,[332] activation energy,[333] and charge transfer.[334] The interaction of an electron with itself will increase the energy of the highest occupied states, thereby lowering the Kohn-Sham band gap. To mitigate the effects of self-interaction, an exact approach to the exchange energy can be included in the functional. In particular, the Hartree-Fock method[335–337] will perfectly cancel self-interactions for occupied states but is computationally expensive. The hybrid functionals, such as PBE0,[198] HSE06,[199] were thus empirically designed to balance a portion of the exact Hartree-Fock exchange energy with the PBE exchange-correlation energy and have shown improved results for band gap, activation energy, and charge transfer values.

We calculate the electron transfer in donor-acceptor heterostructures using the hybrid functionals PBE0, HSE06, and sX.[200] These calculations require norm-conserving pseudopotentials,[338] a plane wave cut-off energy of 900 eV, and an EDFT electron minimization scheme.[339] Given the computational costs and size of the donor-acceptor heterostructures, we focused on the electron transfer in e-ZrS_2 and e-C using hybrid functionals. We started with gamma point calculations and increased the number of k-points in the x and y directions until the energy converged. We report our results in Table B.3:

Table B.3: Electron transfer for two donor-acceptor heterostructures using hybrid functionals. Charge transfer (qt) is reported per supercell.

Structure	k-point mesh	q_t with PBE0 (e^-)	$q_t$with HSE06 (e^-)	q_t with SX atom (e^-)
e-C	3×3×1	1.56	1.56	1.32
e-C	8×8×1	0.55	0.55	0.4915

B.5 Bond length assessment from the Materials Project

Our goal was to build a histogram of bond distances between atoms in crystalline materials. We are interested specifically in examining atom-atom distances in the first coordination sphere around a given atom—i.e., atoms that are in direct contact and that are not sterically hindered. For example, in diamond, we would want to include the bond distances to the four nearest neighbors of each carbon atom, but we would not want to include atoms that are farther away (e.g., second or third nearest neighbors).

We created an algorithm in the Python language to examine bond lengths in each crystal structure. We built a 3×3×3 supercell from each unit cell. The algorithm compiled a list of interatomic distances between each atom in the central unit cell and every other atom within the supercell. The list of interatomic distances

for each atom was sorted based on length. The closest neighbor (N_1) to each atom (A) in the central unit cell was automatically included as being within the coordination sphere, and the bond distance for A-N_1 was stored for use in the histogram. The algorithm then examined the next closest atom to in the sorted list (N_2), which often had the same length as the first bond. The algorithm included this atom within the coordination sphere if the angle N_1-A-N_2 was greater than a threshold value (e.g., 55 degrees). The algorithm repeated this process for each atom (N_x) in the sorted list, and the bond length A N_x was stored for the histogram only if the angle between A-N_x and every shorter bond was greater than the threshold value. The purpose of a threshold angle is to ensure that an atom is not sterically restricted. For example, if the A-N_1 bond is 1.8 Å, the A-N_3 bond is 2.5 Å, and the angle between N_3-A-N_1, is 25°, then the distance 2.5 Å would not be included in the histogram since N_3 is sterically restricted by N_1. We explored threshold values between 50° and 70°, because, based on our manual inspection of several important structure types (e.g., FCC, BCC, HCP, AlB_2, etc.), we found that angles less than 54° we always considered sterically restricted and than angles greater than 65° we always considered to be not sterically restricted. The histograms that we built between 50° and 70° were quite similar to each other, and we therefore selected a threshold of 60° to build our histogram.

We applied our algorithm to the full database of 69,640 geometry-optimized .cif files from the Materials Project, downloaded on November 28, 2017. The resulting histogram is shown in Figure 4.2c.

B.6 Electronic structure of donor–acceptor heterostructures

We calculated the electronic structure using the methods described in Section B.2. In Figures B.3, B.4, B.5, B.6, we plot the band structure and density of states for the four donor–acceptor heterostructures. The Fermi level is positioned at 0 eV for both band structure and density of states plots. To plot the density of states and partial density of states, a Gaussian type broadening was applied (0.1 eV width, 100 interpolation points per eV).

B.7 Binding energy

We calculate the interlayer binding energy by varying the interlayer distance between the electrene and 2D materials and then calculating the total energy. An ‘infinite’ structure was built with an interlayer distance of 12 Å, such that there were no interactions between sheets. We then calculated the energy difference as:

$$E_{BE} = E_{ild} - E_{\infty} \tag{B.1}$$

where E_{∞} is the energy of the infinite structure and E_{ild} is the energy of heterostructure held at a particular interlayer distance d. The interlayer binding energy, E_{BE} is calculated when d is equal to the interlayer distance of the optimized structure. In Table B.4, we report the binding energy in three different forms: per unit cell of the acceptor (non-electrene material), per atom of the acceptor in closest contact, and per square meter of interfacial area.

Because the BN layer will pucker upon the assembly of e-BN, we use a modified procedure to calculate the interlayer interaction energy. We calculated the interaction energy for both planar BN (Figure B.3a, black) and puckered BN (Figure B.3a, red). It is clear from this plot that at distances $>$ 3.57 Å, the planar phase of BN is more favorable. However at distances $<$ 3.38 Å, the puckered conformation of BN is more favorable due to the interaction between BN and the electrene. To resolve this discrepancy for the region between $ca.$ 3.4 Å and 3.6 Å, we linearly interpolated the the atomic positions between puckered BN (at an interlayer distance of 2.85 Å) and planar BN (at an interlayer distance of 3.64 Å) to generate 14 intermediate structures (Figure B.3a, blue). We found that these interpolated structures more accurately accounted for the transition from puckered BN to planar BN structure. We compiled our results into a single interaction energy curve (Figure B.3b) that is colored according to the derived structure (red: puckered e-BN, black: planar BN, blue: interpolated BN). This curve is presented in Figure 4.3e.

Table B.4: Binding energies for the donor-acceptor heterostructures

Structure	Optimized distance (Å)	E_{BE} (eV/unit cell of acceptor)	E_{BE} (eV/ acceptor atom)	E_{BE} (J/m^2)
e-C	2.754	0.231	0.115	1.150
e-P	2.624	0.701	0.701	1.560
e-BN	2.861	0.149	0.149	0.210
e-ZrS_2(a)	2.750	1.372	1.372	1.956
e-ZrS_2(a)	2.044	2.018	2.018	2.890
e-ZrS_2(a)	2.105	2.17	2.17	3.094
Bilayer graphite	3.258	n/a	n/a	0.276

B.8 Sliding energy in donor-acceptor heterostructures

We calculate the sliding energy of donor-acceptor heterostructures from the following equation:

$$\Delta E = E_{(x,y,z)} - E_{\text{opt}} \tag{B.2}$$

where E_{opt} is the energy of the geometry optimized structure and $E_{(x,y,z)}$ is the energy of the structure with the non-electrene layer translated along Cartesian coordinates. The position of the non-electrene layer in the geometry optimized structures were taken as the origin [(x, y, z) = (0 Å, 0 Å, 0 Å)]. For donor–acceptor heterostructures constructed with planar 2D materials, BN and graphene layers were displaced in 0.2 Å steps in both the x and y directions, while the z-coordinate was held constant.

For the non-planar ZrS_2, we also considered translations in the z-direction to account for the repulsion of atomic nuclei during sliding. Specifically, we calculated 2527 total structures for e-ZrS_2, which corresponds to a grid 19×19×7 structures with a 0.2 Å step for x- and y-translations and a 0.1 Å step for z-translations. Given the extra dimensionality of the e-ZrS_2 sliding energy calculations, we consider only the lowest energy structure among varying z-heights for each (x, y) coordinate. In this manner we calculate the minimum energy pathway for sliding the corrugated structures of ZrS_2 and Ca_2N past each other.

In Figure B.11, we plot the potential energy surface for sliding in the e-C, e-BN, and e-ZrS_2 heterostructures, respectively. We interpolate this raw data using MatLab (Version R2013a; function: interp2; method: spline; two interpolations) to create the potential energy surfaces seen in Figure 4.6c-e.

B.9 Work functions and potential energy

To calculate the work function of the donor-acceptor heterostructures, we included self-consistent dipole corrections, which are implemented in CASTEP as defined by Neugebauer and Scheffler.[340] This correction is necessary when there are different work functions for each surface of the donor-acceptor heterostructure. To correctly apply the dipole correction, we increased the vacuum space between periodic images from 12 Å to 20 Å in each donor–acceptor heterostructure. Here we show the potential energy diagrams and work functions for donor–acceptor heterostructures (Figure B.12, B.13, B.14, B.15, B.16, B.17,). The work function for each side of the heterostructure is taken as the difference between the Fermi level (red dashed line) and the vacuum potential.

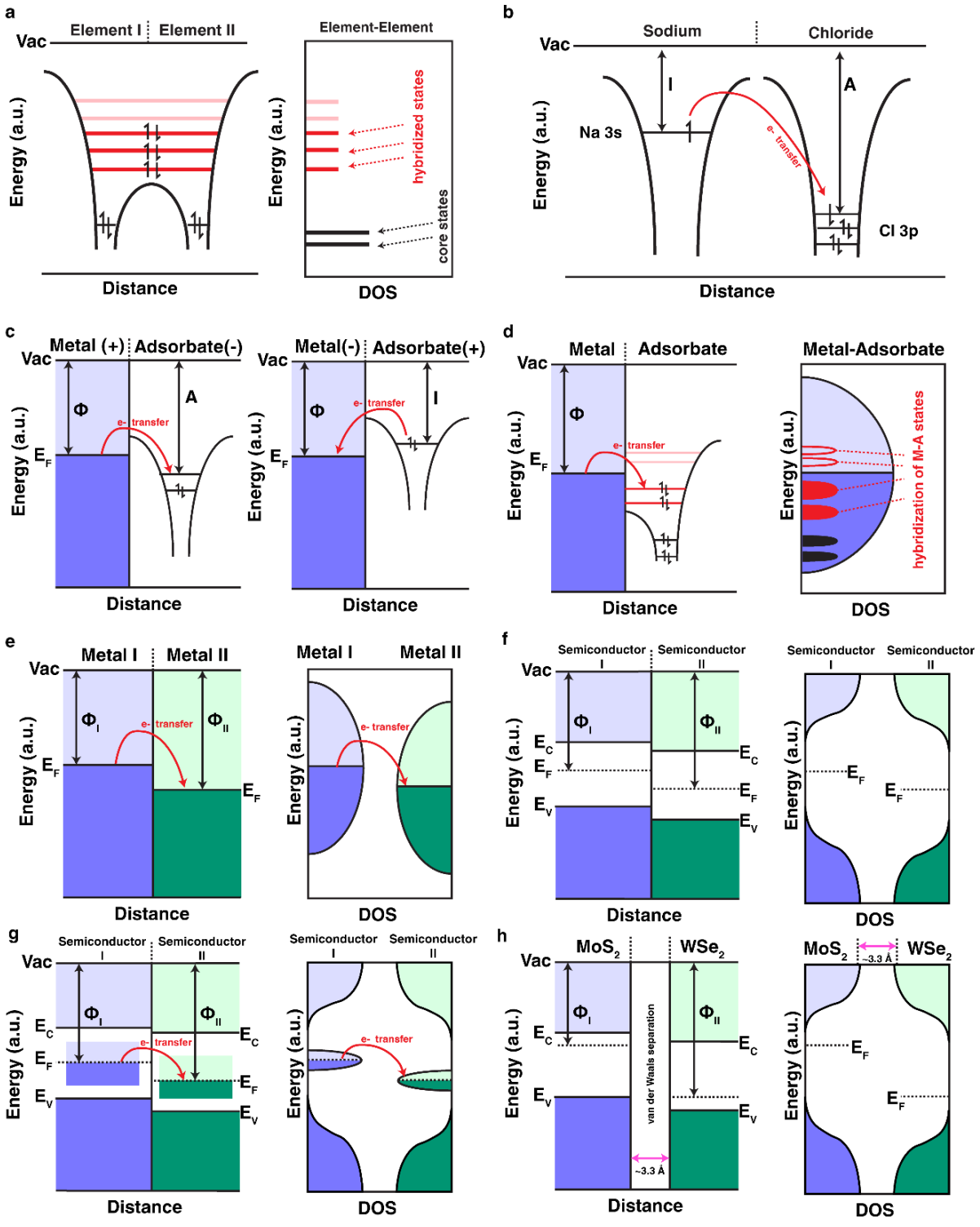


Figure B.1: Electron transfer models in molecular systems and solids using band alignment and density of states. a, Formation of hybridized bonding states (red) in molecular systems. b, Formation of ionic bonding in NaCl due to electron transfer. Metal-Adsorbate electron transfer to form (c, left) a negative ion, (c, right) a positive ion, and (d) a covalent bond. e, Electron transfer between two metals. f, Band alignment in a type II semiconductor junction. g, Electron transfer in semiconducting systems, as mediated by surface and defect states within the band gap. h, MoS_2-WSe_2 heterostructure showing minimal electron transfer.

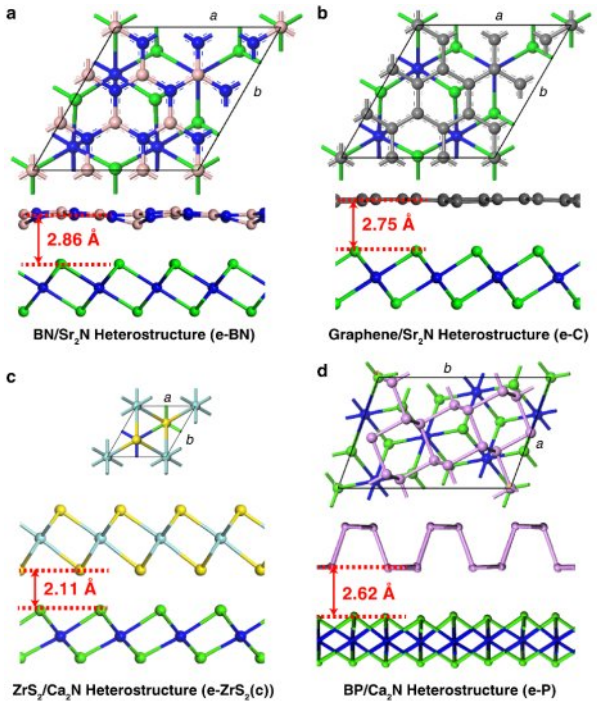


Figure B.2: Optimized structure of the donor-acceptor heterostructures. a, e-BN (blue: nitrogen, pink: boron, green: strontium). b, e-C (blue: nitrogen, green: strontium, gray: carbon), c, e-ZrS_2(c), the most energetically favorable orientation of e-ZrS_2 (blue: nitrogen, green: calcium, teal: zirconium, yellow: sulfur). d, e-P (blue: nitrogen, green: calcium, pink: phosphorus).

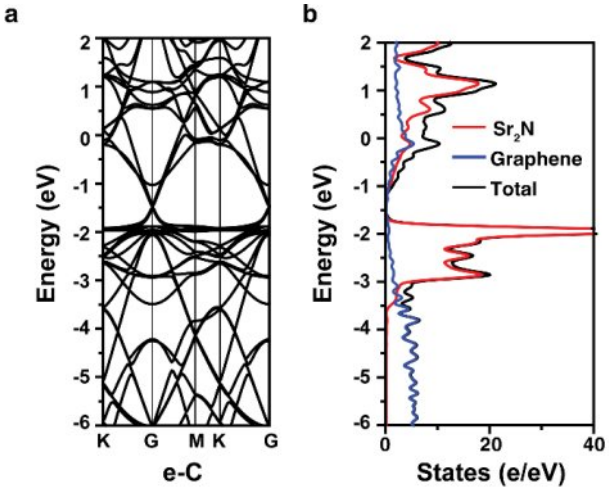


Figure B.3: Electronic structure of the e-C donor-acceptor heterostructure. a, Band structure. b, Total density of states (black) and partial density of states for Sr_2N (red) and graphene (blue).

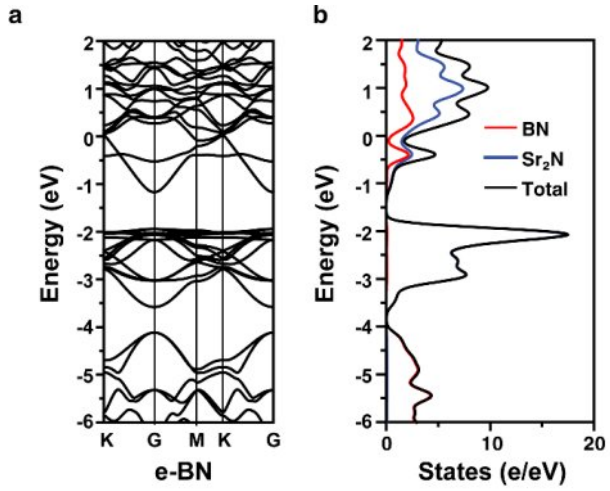


Figure B.4: Electronic structure of the e-BN donor-acceptor heterostructure. a, Band structure. b, Total density of states (black) and partial density of states for Sr_2N (blue) and BN (red).

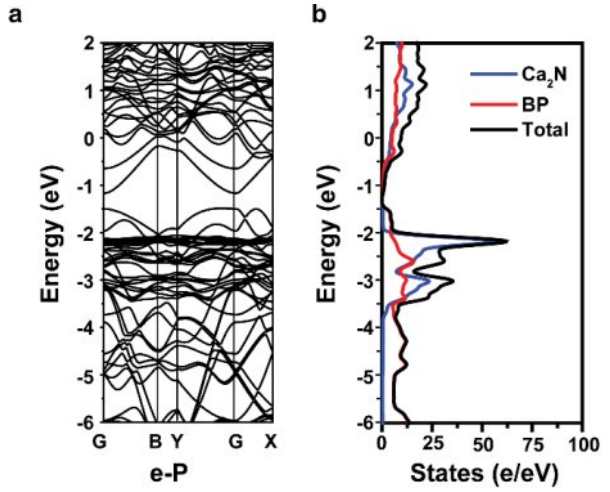


Figure B.5: Electronic structure of the e-P donor-acceptor heterostructure. a, Band structure. b, Total density of states (black) and partial density of states for Ca2N (blue) and phosphorene (red).

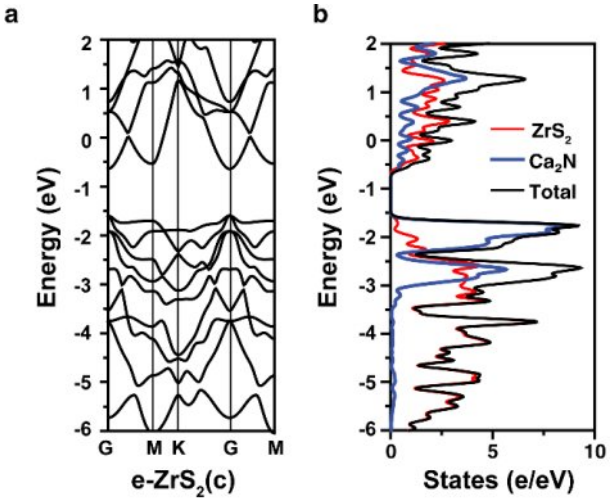


Figure B.6: Electronic structure of the e-ZrS_2(c) donor-acceptor heterostructure. a, Band structure. b, Total density of states (black) and partial density of states for Ca_2N (blue) and ZrS_2 (red).

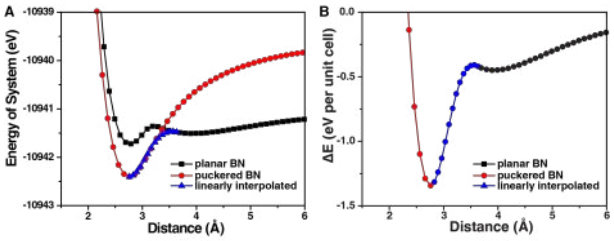


Figure B.7: Determining the binding energy of e-BN. a, Plot of binding energy using planar BN (black), puckered BN (red) and a linearly interpolated structure of e-BN (blue). We compile the results to generate a single interaction energy curve (b). The energy is compared to the infinite structure (12 Å) using planar BN.

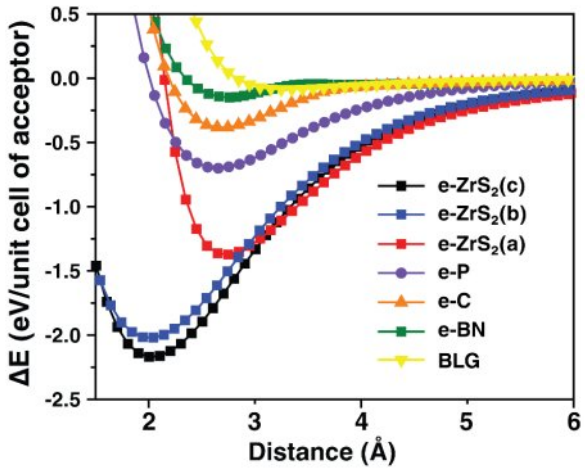


Figure B.8: Binding energy of donor-acceptor heterostructures per unit cell of acceptor.

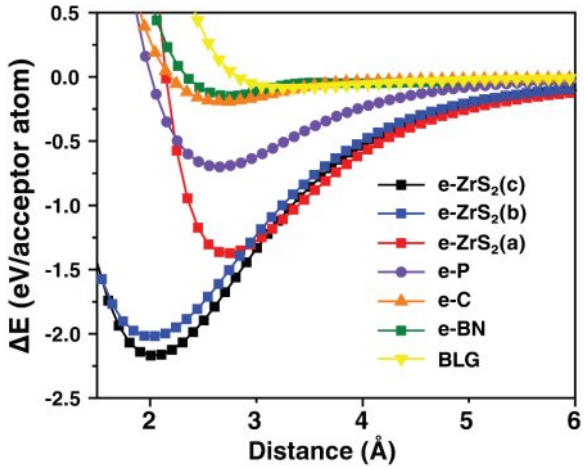


Figure B.9: Binding energy of donor-acceptor heterostructures per acceptor atom nearest the electrene.

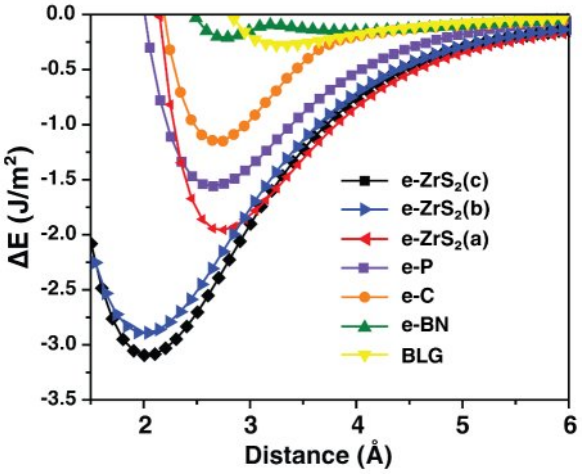


Figure B.10: Binding energy of donor-acceptor heterostructures in Joules per square meter.

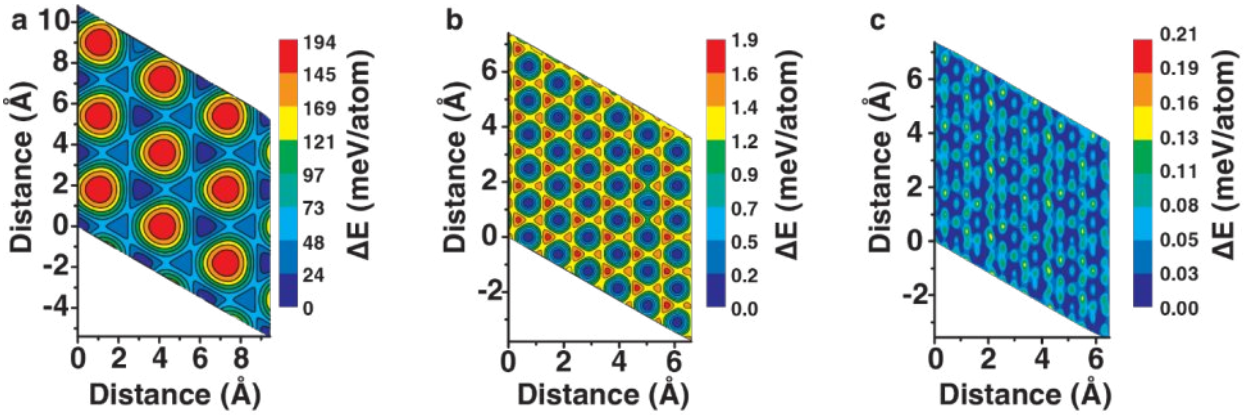


Figure B.11: Potential energy surface for sliding in donor-acceptor heterostructures. a, e-ZrS2. b, e-BN. c, e-C.

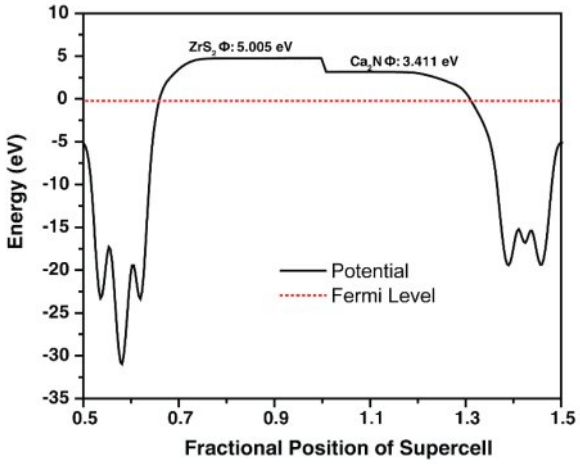


Figure B.12: Potential energy diagram and work function of e-ZrS_2(a)

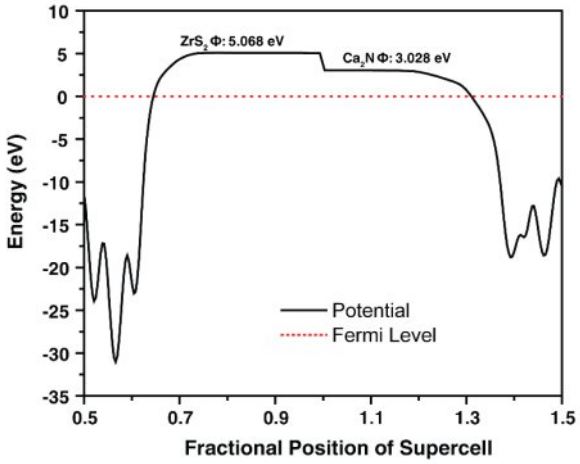


Figure B.13: Potential energy diagram and work function of e-ZrS_2(b)

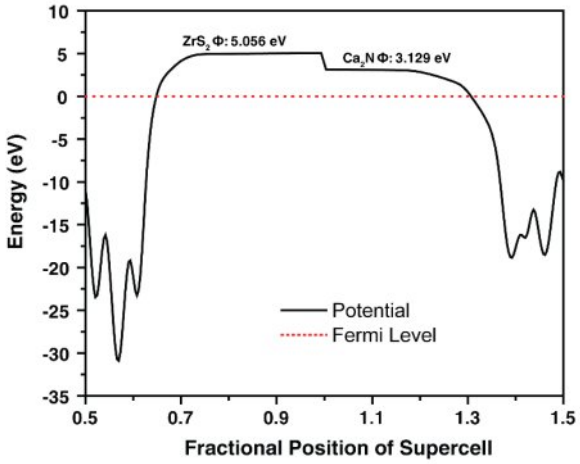


Figure B.14: Potential energy diagram and work function of e-ZrS_2(c)

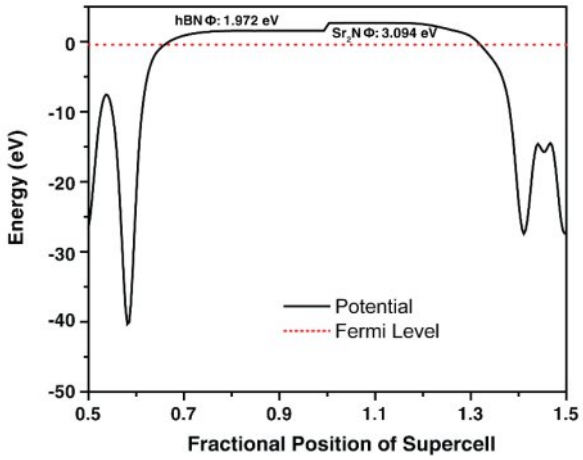


Figure B.15: Potential energy diagram and work function of e-BN

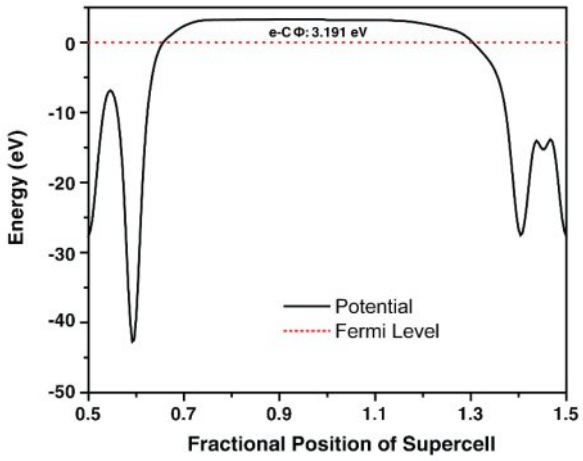


Figure B.16: Potential energy diagram and work function of e-C

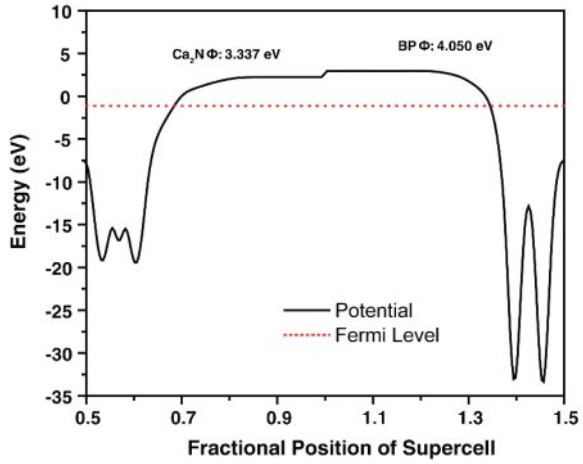


Figure B.17: Potential energy diagram and work function of e-P

APPENDIX C–SUPPORTING INFORMATION FOR CHAPTER 5

C.1 The synthesis of Y_2CF_2

Y_2CF_2 was synthesized by the solid state reaction of YF_3 (Sigma Aldrich, granules, 0.09% oxygen, <0.02% Cd, Co, Cr, Fe, Hg, Mn, Pb each) with Y metal (Alfa Aesar, ∼40 mesh powder, 99.6% (REO)) and graphite (Sigma Aldrich, ∼100 mesh flakes, 99.9%). The reagents were ground into a very fine powder in a stoichiometric ratio (total mass of a typical batch: 0.5–1.0 g) and pressed into a pellet under ∼0.56 GPa of pressure using a hydraulic press. The pellet was placed into an ampoule made of tantalum (Ta) metal welded closed at one side. A cap, also made of Ta, was hammered into the ampoule and sealed in argon by welding the cap and ampoule together with an electric arc. The Ta tubing, 99.95% Ta seamless tubing, was purchased from Eagle Alloys in a 1 cm diameter and cut to 5 cm lengths. The caps, made of the same Ta, were made by the University of North Carolina's Physics and Astronomy instrument shop. After welding the reagents inside a Ta ampoule, the Ta ampoule was sealed in a fused quartz ampoule under 1 mbar Ar. Then the ampoule was placed in a Lindberg Blue M tube furnace to 1513 K at a ramp rate of 10 k/min. The temperature was held at 1513 K for 3 days, then cooled to 1273 K over 10 hrs, then cooled to 1073 K over 5 hrs, and to room temperature over 5 hours. The ampoule was then brought into the glovebox and opened with a pipe cutter. The pellet remained intact through the reaction. Vibrant green crystals grew on the surface of the pellet. The pellet revealed homogenous green crystals throughout when broken apart. All materials were stored in a glovebox with an argon atmosphere (oxygen $<$ 0.01 ppm) and all synthetic steps were carried out under argon atmosphere.

We chose 1240 °C for two reasons: first, we recognized that Y metal, graphite, and YF_3 all have high melting points (1526, ∼4800, and 1387 °C respectively).[341–343] Therefore, the reaction is likely a solid-state reaction with the kinetics governed by diffusion of atoms through the solids. Higher temperatures, like 1240 °C, greatly accelerate the kinetics of solid-state reactions. Secondly, this temperature is at the highest end of temperatures where fused quartz maintains its mechanical strength. We use sealed quartz jackets to prevent oxidation of the tantalum ampoules at high temperature. In our experiments, lower reaction temperatures (1100 °C) yielded poor products with significant amounts of unreacted reagents. The reaction at 1240 °C yields beautiful reflective green crystals, typically tens to hundreds of μm in size.

C.2 X-ray diffraction experiments of Y_2CF_2

Powdered samples of Y_2CF_2 were characterized at room temperature in a capillary transmission geometry across a range of 20-150°. A reference scan was run with silicon (a = 5.430 Å) as an internal standard using Cu Kα (λ = 1.54056 Å). The peaks were not corrected as the height of the sample was exactly correct. I indexed the patterns using Treor[344] implemented in the Match! software.[345] I refined the patterns using the PDXL software from Rigaku.[346]

We can understand the purity of the product through powder X-ray diffraction. The experiment reveals the presence of an impurity phase, which could be indexed to a yttrium oxide fluoride. Because many phases of yttrium oxide fluorides share very related crystal structures, the exact phase could not be identified at such a low fraction of the sample. The sample could be α-YOF, $Y_5O_4F_7$, or $Y_6O_5F_8$. In any case, the presence of the phase by weight is less than 5%. While this impurity does complicate the analysis of the stoichiometry, it does not impede our analysis of the structure or properties. The origin of the oxygen in the sample proved a mystery. We believe that the oxygen in the impurity phase originates from oxygen already present in the yttrium metal reactant when purchased for a few reasons: 1) powdered yttrium metal is notoriously difficult to purify of oxygen and in our experience almost always contains oxygen up to 1-5% by wt; 2) we attempted reactions with added Zr-foil to scavenge oxygen and this did not change the concentration of the impurity phase. For this reason, we attempted to synthesize an alternative source of yttrium, reacting dendritic Y, which has far less oxygen than powdered sources, with carbon to form a brittle yttrium-carbide phase, which we could mill into a powder. We attempted reacting this yttrium carbide with additional graphite and yttrium fluoride in the following reaction:

$$2Y_2C + C + 2YF_3 \rightarrow 3Y_2CF_2 \tag{C.1}$$

This reaction also yielded beautiful green crystals of Y_2CF_2 (Figure C.1), but still had a few percent by weight yttrium oxide fluoride. It is possible that the yttrium carbide reacted with a small amount of oxygen during synthesis and handling or that the oxygen comes from the yttrium fluoride that we purchased.

The crystal structure of Y_2CF_2 is similar to the layered Ta_2CS_2 and many other ternary carbides with the form M_2CX_2 (M=metal and X = F, H, Cl, S, Br, I, etc.) such as Nb_2CS_2, Gd_2CCl_2, and Y_2CH_2 for example in which the second anion has a different ionic radius than carbon (132 pm in carbides). In general,

the presence of two anions (carbon and fluorine in this case) with different ionic radii (132 pm and 119 pm respectively) seems to favor the formation of a layered crystal with this symmetry or a very related symmetry (e.g. R$\bar{3}$m).

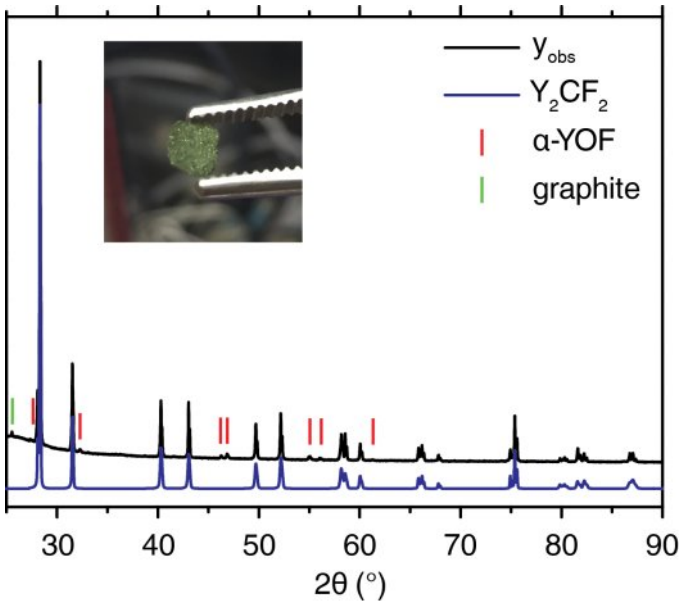


Figure C.1: Powder X-ray diffraction pattern of Y_2CF_2 synthesized from Y_2C as described in equation C.1. The sample was loaded under onto a flat glass substrate and sealed beneath Kapton tape. The intensities of the peak $\sim 28°$ is increased by strong preferred orientation.

C.3 Microscopy and spectroscopy of Y_2CF_2

During these experiments, the samples were briefly exposed to air. In the case of the SEM, samples were loaded onto the stage in the glovebox, sealed in plastic, and brought to the instrument. The total exposure to oxygen was less than 5 seconds. In the case of the microscopy, the optical microscopy was performed in air within the span of one hour. No oxidation was apparent during that time. For the transmission measurements, the discs were encased within glass wells and and sealed between two pieces of optical-grade quartz using a two-part epoxy inside of the glovebox.

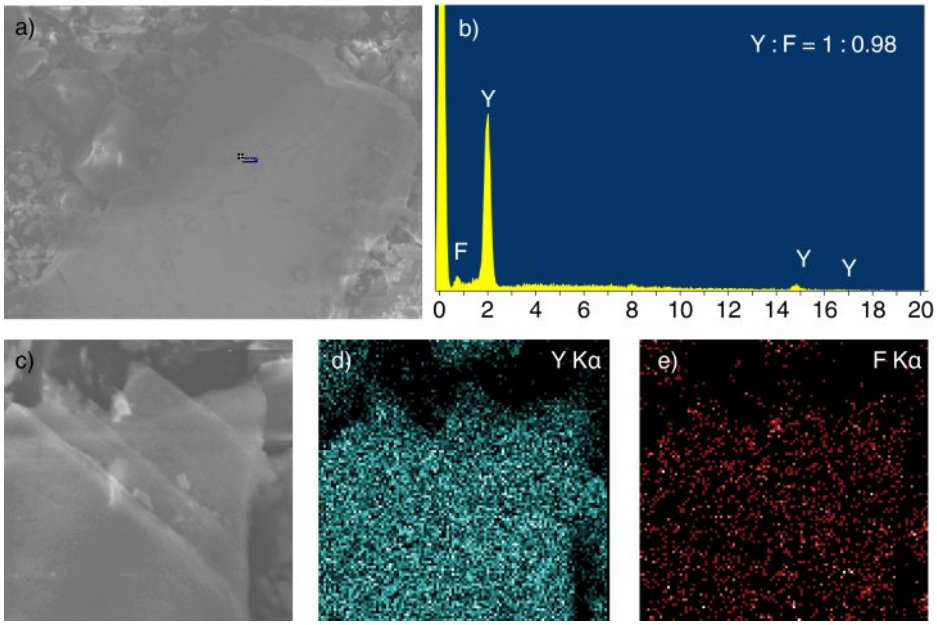


Figure C.2: a) Scanning electron image of a Y_2CF_2 surface corresponding to an b) energy dispersive X-ray spectroscopy (EDS) spectrum, which reveals the ratio of Y:F is 1:0.98 $\pm$ 0.05. c) Another scanning electron image of a flaky crystal of Y_2CF_2 and corresponding EDS maps, which reveal that yttrium and fluorine are homogenous throughout the crystal and spatially correlated, as expected.

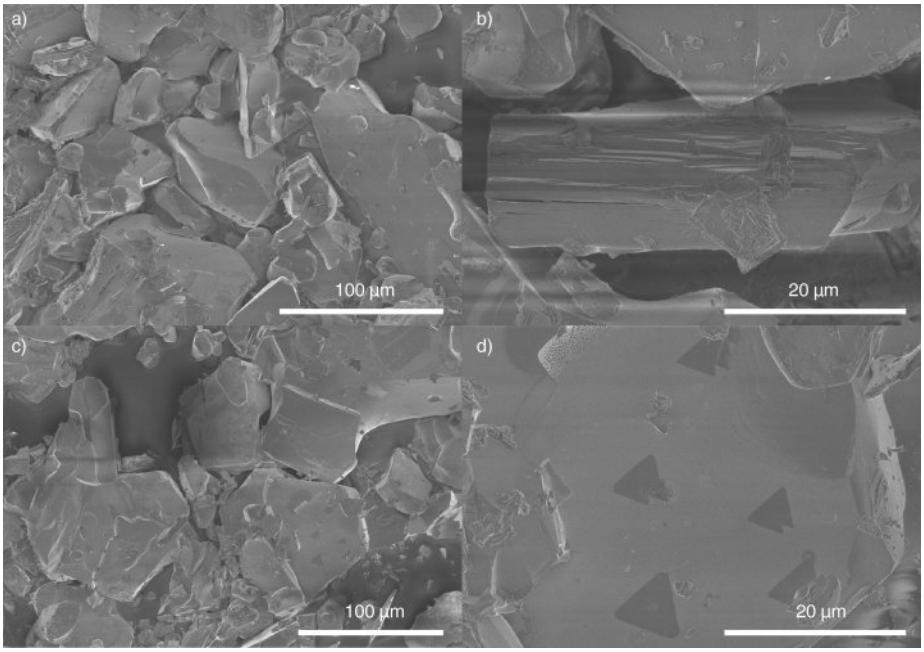


Figure C.3: Scanning electron images showing a,c) the faceted morphology of Y_2CF_2 only lightly ground in a mortar and pestle, b) the layered crystal morphology, and d) triangular growth pits aligned on the surface of a crystal that highlight the crystalline and hexagonal structure of Y_2CF_2.

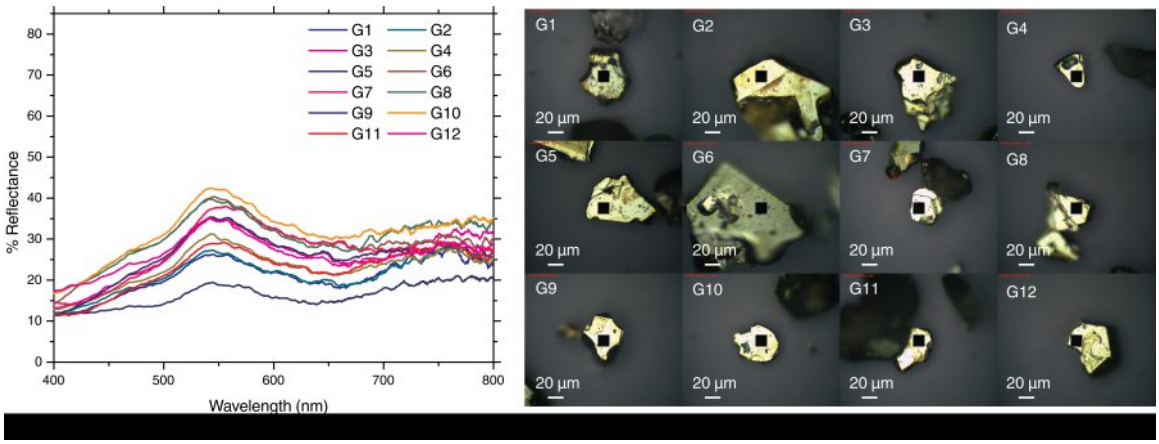


Figure C.4: Spectra collected from clean facets of Y_2CF_2 in a microspectrophotometer and their corresponding images.

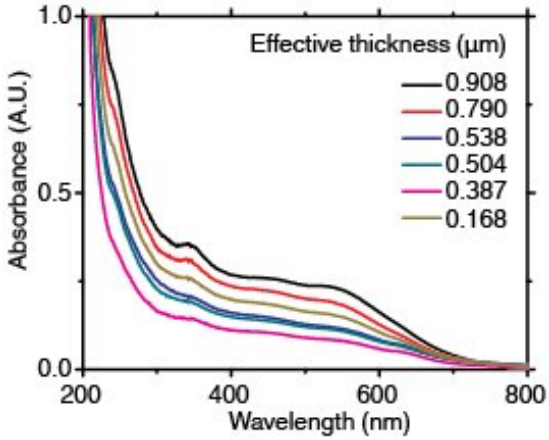


Figure C.5: Absorbance spectra of Y_2CF_2. The Y_2CF_2 powder was ground very finely and diluted with spectroscopic grade KBr. The mixture was ground until homogenous, then pressed into discs using the pellet press. The thickness of the discs was approximately 1 mm. The background due to scattering from KBr was subtracted by pressing a number of films of KBr of varying thickness to estimate its effective attenuation as a function of thickness and subtracting a weighted fraction from the acquired spectra. Some films had to be re-run and others re-made to avoid specks of inhomogeneity. All discs appeared red, not green. The spectra were collected by measuring the transmission of light through the thin discs.

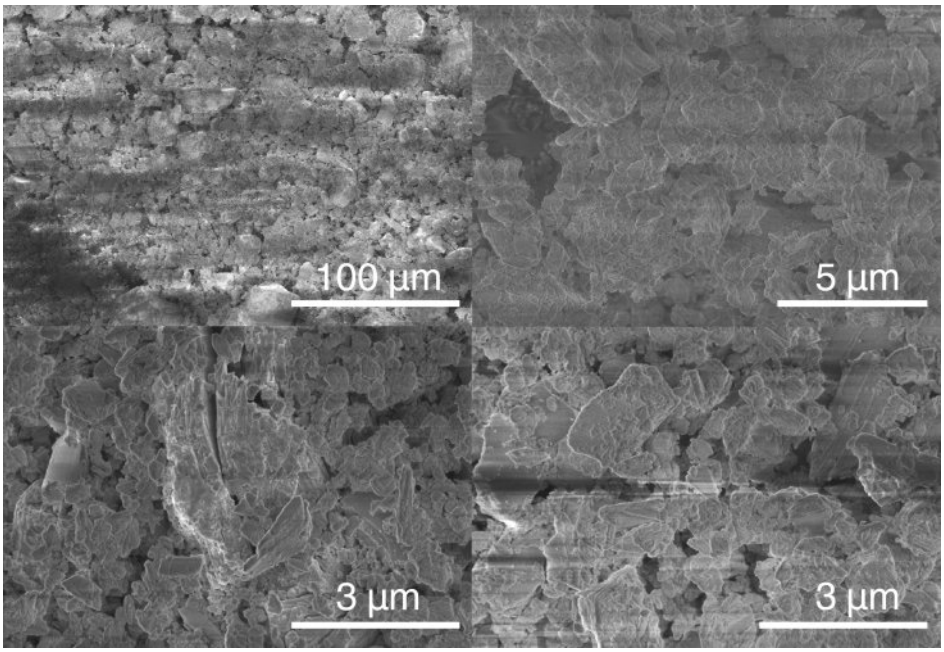


Figure C.6: Micrographs of Y_2CF_2 ball-milled to < 5 µm particles.

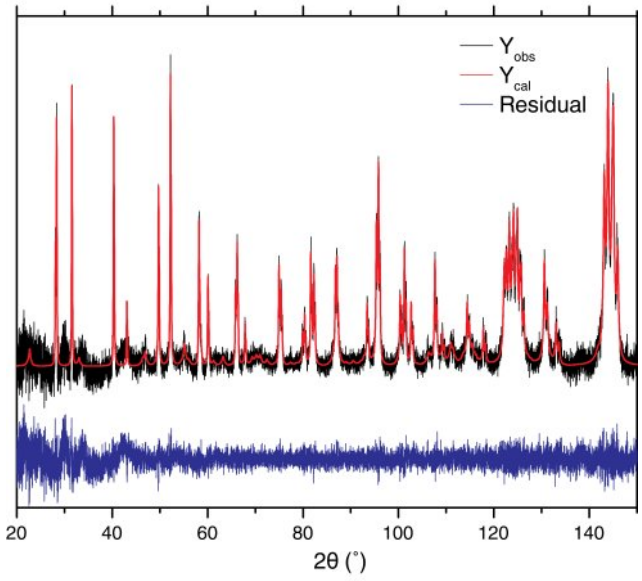


Figure C.7: Powder X-ray diffraction pattern of Y_2CF_2 ball milled in a Spex high energy mill for 30 minutes in steel jars, acquired using a Rigaku Smartlab diffractometer with a Cu Kα source. The red powder was loaded into a capillary tube and measured. The crystal structure, including the lattice constants, remain unchanged through the milling process. As in the un-milled sample, a minor impurity phases, α-YOF, was detected.

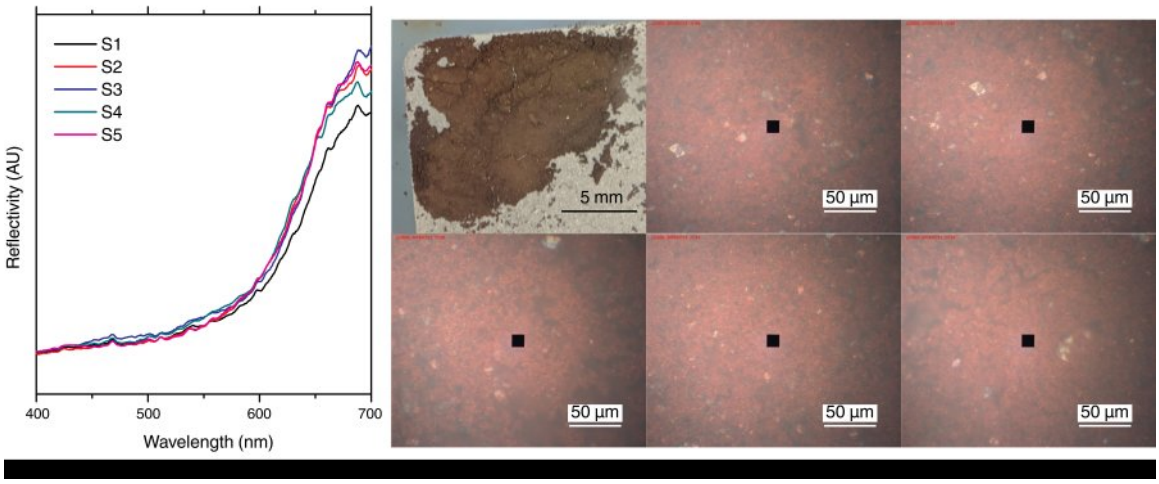


Figure C.8: Reflectivity of ball-milled Y_2CF_2, which has no peak at 540 nm. Instead the reflectivity decreases at higher energy wavelengths as a fraction of that light is absorbed by the sample. The red powder is shown in the images on the right.

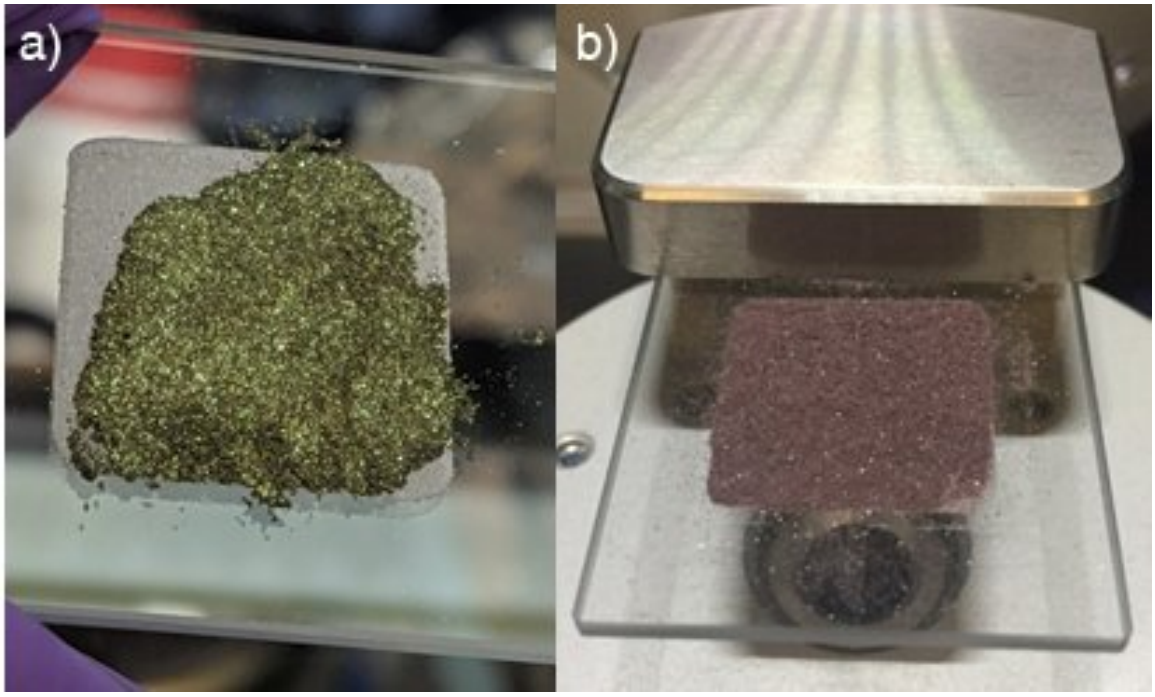


Figure C.9: Photographs of a) unoxidized Y_2CF_2 kept in a glovebox and b) oxidized Y_2CF_2 let sit in air for 1 week.

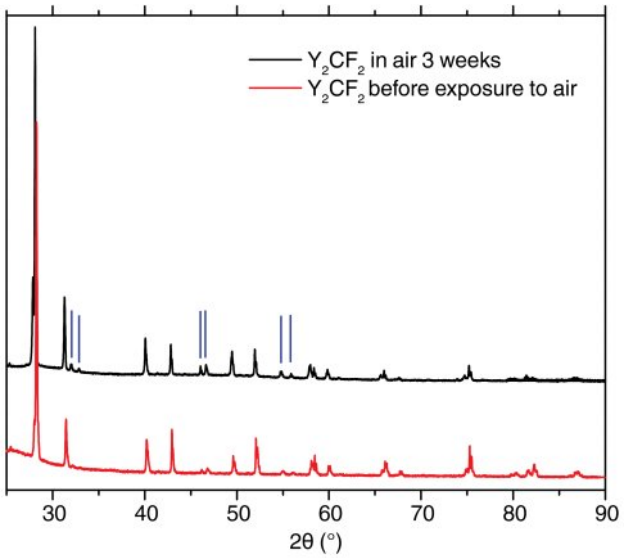


Figure C.10: X-ray diffraction patterns of Y_2CF_2 exposed to air for 3 weeks (black) and the pattern acquired before exposure to air (red). The pattern changes only slightly suggesting that the oxidation process is exceedingly slow or limited to the surface. Marked in blue are peaks from the crystalline phase α-YOF. The intensity of these peaks seems to increase with prolonged exposure to air.

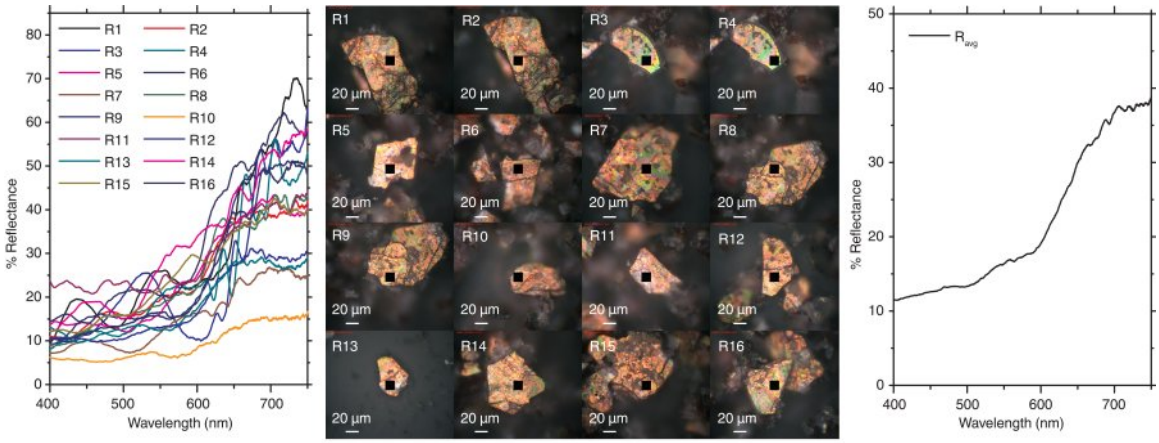


Figure C.11: Reflectivity of Y_2CF_2 exposed to air for 1 month and images of the corresponding crystals from which the spectra were acquired. Wavelength-dependent oscillations in the reflectivity spectra and the rainbow-like coloration visible in the images intimates of thin-film effects altering the reflection at the surface. No peak is visible at 540 nm. Instead, on average, shown on the right, the reflectivity decreases at higher energy wavelengths as a fraction of that light is absorbed by the sample. The red powder is shown in the images on the right.

REFERENCES

"If I have seen further, it is by standing on the shoulders of Giants."

- Isaac Newton

[1] Kraus, C. A. Solutions of metals in non-metallic solvents; IV. Material effects accompanying the passage of an electrical current through solutions of metals in liquid ammonia. Migration experiments. *Journal of the American Chemical Society* **1908**, *30*, 1323–1344.

[2] Dawes, S. B.; Ward, D. L.; Fussa-Rydel, O.; Huang, R. H.; Dye, J. L. Crystal structures and properties of two sodides and an electride. *Inorganic Chemistry* **1988**, *28*, 2132–2136.

[3] Toda, Y.; Hirayama, H.; Kuganathan, N.; Torrisi, A.; Sushko, P. V.; Hosono, H. Activation and splitting of carbon dioxide on the surface of an inorganic electride material. *Nature Communications* **2013**, *4*, 2378.

[4] Dye, J. L. Electrides: ionic salts with electrons as the anions. *Science* **1990**, *247*, 663–668.

[5] Kraus, C. A. Solutions of metals in non-metallic solvents; I. General properties of metals in liquid ammonia. *Journal of the American Chemical Society* **1907**, *29*, 1557–1571.

[6] Kraus, C. A. Solutions of metals in non-metallic solvents; II on the formation of compounds between metals and ammonia. *Journal of the American Chemical Society* **1908**, *30*, 653–668.

[7] Kraus, C. A. Solutions of metals in non-metallic solvents; III the apparent molecular weight of sodium dissolved in liquid ammonia. *Journal of the American Chemical Society* **1908**, *30*, 1197–1219.

[8] Kraus, C. A. Solutions of metals in non-metallic solvents. V. The electromotive force of concentration cells of solutions of sodium in liquid ammonia and the relative speed of the ions in these solutions. *Journal of the American Chemical Society* **1914**, *36*, 864–877.

[9] Kraus, C. A. Solutions of metals in non-metallic solvents. VI. The conductance of alkali metals in liquid ammonia. *Journal of the American Chemical Society* **1921**, *43*, 749–770.

[10] Thompson, J. C. *Electrons in Liquid Ammonia*, 1st ed.; Oxford University Press: Walton Street, Oxford, 1976.

[11] de Boer, J. H.; Verwey, E. J. W. Semi-conductors with partially and with completely filled 3d-lattice bands. *Proceedings of the Physical Society of London* **1937**, *49*, 59.

[12] Mott, N. F.; Peierls, R. Discussion of the paper by de Boer and Verwey. *Proceedings of the Physical Society of London* **1937**, *49*, 72.

[13] Landau, L. On the motion of electrons in a crystal lattice. *Physikalische Zeitschrift der Sowjetunion* **1933**, *3*, 664–665.

[14] Dye, J. L. Recent developments in the synthesis of alkalides and electrides. *Journal of Physical Chemistry* **1984**, *88*, 3842–3846.

[15] Issa, D.; Ellaboudy, A.; Janakiraman, R.; Dye, J. L. Magnetic susceptibilities and electron paramagnetic resonance spectra of a ceside and an electride. *Journal of Physical Chemistry* **1984**, *88*, 3847–3851.

[16] Dye, J. L.; Yemen, M. R.; DaGue, M. G.; Lehn, J. Optical spectra of alkali metal anion and electride films. *Journal of Chemical Physics* **1978**, *68*, 1665–1670.

[17] Le, L. D.; Issa, D.; Eck, B. V.; Dye, J. L. Preparation of alkalide and electride films by direct vapor deposition. *Journal of Physical Chemistry* **1982**, *86*, 7–9.

[18] Matsuishi, S.; Toda, Y.; Miyakawa, M.; Hayashi, K.; Kamiya, T.; Hirano, M.; Tanaka, I.; Hosono, H. High-density electron anions in a nanoporous single crystal: $[Ca_{24}Al_{28}O_{64}]\cdot 4(e^-)$. *Science* **2003**, *301*, 626–629.

[19] Miyakawa, M.; Kim, S. W.; Hirano, M.; Kohama, Y.; Kawaji, H.; Atake, T.; Ikegami, H.; Kono, K.; Hosono, H. Superconductivity in an inorganic electride $12CaO \cdot 7Al_2O_3{:}e^-$. *Journal of the American Chemical Society* **2007**, *129*, 7270–7271.

[20] Toda, Y.; Yanagi, H.; Ikenaga, E.; Kim, J. J.; Kobata, M.; Ueda, S.; Kamiya, T.; Hirano, M.; Kobayashi, K.; Hosono, H. Work Function of a room-temperature stable electride $[Ca_{24}Al_{28}O_{64}]\cdot 4(e^-)$. *Advanced Materials* **2007**, *19*, 3564–3569.

[21] Sushko, P. V.; Shluger, A. L.; Hayashi, K.; Hirano, M.; Hosono, H. Hopping and optical absorption of electrons in nano-porous crystal $12\ CaO \cdot 7Al_2O_3{:}e^-$. *Thin Film Solids* **2003**, *445*, 161–167.

[22] Kim, S. W.; Shimoyama, T.; Hosono, H. Solvated electrons in high-temperature melts and glasses of the room-temperature stable electride $[Ca_{24}Al_{28}O_{64}]\cdot 4(e^-)$. *Science* **2011**, *333*, 71–74.

[23] Dye, J. L.; Wagner, M. J.; Overney, G.; Huang, R. H.; Nagy, T. F.; Tománek, D. Cavities and channels in electrides. *Journal of the American Chemical Society* **1996**, *118*, 7329–7336.

[24] Zhang, Y.; Xiao, Z.; Kamiya, T.; Hosono, H. Electron confinement in channel spaces for one-dimensional electride. *Journal of Physical Chemistry Letters* **2015**, *6*, 4966–4971.

[25] Keve, E. T.; Skapski, A. C. Ca_2N: a nitride with a layer structure. *Chemical Communications (London)* **1966**, 829–830.

[26] Lee, K.; Kim, S. W.; Toda, Y.; Matsuishi, S.; Hosono, H. Dicalcium nitride as a two-dimensional electride with an anionic electron layer. *Nature* **2013**, *494*, 336–340.

[27] Ariya, S.; Prokofyeva, E. *Journal of General Chemistry of the U.S.S.R. in English* **1955**, *25*, 813.

[28] Ahmad, I. *Ph.D. Thesis* **1963**,

[29] Gaudé, J.; L'Haridon, P.; Laurent, Y.; Lang, J. Le système strontium–azote. III. *É*tude structurale de Sr_2N. *Bulletin de la Socit Franaise de Minralogie et de Cristallographie* **1972**, *95*, 56–60.

[30] Brice, J. F.; Motte, J. P.; Aubry, J. J. Aubry Sur les nitrures anormaux des métaux alcalino-terreux: 'Ca_2N, Sr_2N et SrN'. *Revue de Chimie Minrale* **1975**, *12*, 105–112.

[31] Brese, N. E.; O'Keeffe, M. Synthesis, crystal structure, and physical properties of Sr_2N. *Journal of Solid State Chemistry* **1990**, *87*, 134–140.

[32] Gregory, D. H.; Bowman, A.; Baker, C. F.; Weston, D. P. Dicalcium nitride, Ca_2N–a 2D 'excess electron' compound; synthetic routes and crystal chemistry. *Journal of Materials Chemistry* **2000**, *10*, 1635–1641.

[33] Fang, C.; de Wijs, G.; de Groot, R.; Hintzen, H.; de With, G. Bulk and surface electronic structure of the layered sub-nitrides Ca_2N and Sr_2N. *Chemistry of Materials* **2000**, *12*, 1847–1852.

[34] Steinbrenner, U.; Adler, P.; Hölle, W.; Simon, A. Electronic structure and chemical bonding in alkaline earth metal subnitrides: photoemission studies and band structure calculations. *Journal of Physics and Chemistry of Solids* **1998**, *59*, 1527–1536.

[35] Walsh, A.; Scanlon, D. O. Electron excess in alkaline earth sub-nitrides: 2D electron gas or 3D electride? *Journal of Materials Chemistry C* **2013**, *1*, 3525–3528.

[36] Batsanov, S. S. Van der Waals radii of elements. *Inorganic Materials* **2001**, *37*, 871–885.

[37] Wyckoff, R. W. G. *Crystal Structures*, 2nd ed.; Interscience Publishers: New York, New York, 1963.

[38] Shannon, R. D. Revised effective ionic radii and systematic studies of interatomic distances in halides and chalcogenides. *Acta Crystallographica* **1976**, *A32*, 751–767.

[39] von Schnering, H. G.; Wittmann, M.; Sommer, D. Zur chemie und strukturchemie der phosphide und polyphosphide. *Zeitschrift fr Anorganische und Allgemeine Chemie* **1984**, *510*, 61–71.

[40] Iandelli, A.; Franceschi, E. On the crystal structure of the compounds CaP, SrP, CaAs, SrAs, and EuAs. *Journal of Less Common Metals* **1973**, *30*, 211–216.

[41] Schmettow, W.; von Schnering, H. G. Ba_3As_14, die erste verbindung mit dem cluster-anion As. *Angewandte Chemie (German edition)* **1977**, *89*, 895.

[42] Li, B.; Mudring, A. V.; Corbett, J. D. Valence compounds versus metals. Synthesis, characterization, and electronic structures of cubic Ae_4Pn_3 phases in the systems Ae = Ca, Sr, Ba, Eu; Pn = As, Sb, Bi. *Inorganic Chemistry* **2003**, *42*, 6940–6945.

[43] Otani, S.; Hirata, K.; Adachi, Y.; Ohashi, N. Floating zone growth and magnetic properties of Y_2C two-dimensional electride. *Journal of Crystal Growth* **2016**, *454*, 15–18.

[44] Mudryk, Y.; Paudyal, D.; Pecharsky, V.; Gschneidner, K. Magnetic properties of Gd_2C: Experiment and first principles calculations. *Journal of Applied Physics* **2011**, *109*, 07A924.

[45] Atoji, M. Magnetic and crystal structures of the trigonal Tb_2C. *Journal of Chemical Physics* **1981**, *51*, 3872–3876.

[46] Atoji, M. Neutron-diffraction studies of Tb_2C and Dy_2C in the temperature range 4-296 K. *Journal of Chemical Physics* **1981**, *75*, 1434–1441.

[47] Atoji, M. Neutron-diffraction study of Ho_2C at 4-296 K. *Journal of Chemical Physics* **1981**, *74*, 1893–1897.

[48] Zhang, X.; Xiao, Z.; Lei, H.; Toda, Y.; Matsuishi, S.; Kamiya, T.; Ueda, S.; Hosono, H. Two-dimensional transition-metal electride Y_2C. *Chemistry of Materials* **2016**, *26*, 6638–6643.

[49] Ming, W.; Yoon, M.; Du, M. H.; Lee, K.; Kim, S. W. First-principles prediction of thermodynamically stable two-dimensional electrides. *Journal of the American Chemical Society* **2016**, *138*, 15336–16344.

[50] Pauling, L. The principles determining the structure of complex ionic crystals. *Journal of the American Chemical Society* **1929**, *51*, 1010–1026.

[51] Bowman, A.; Mason, P. V.; Gregory, D. H. Heteroanionic Intercalation into Positively Charged Inorganic Hosts: the First Nitride Mixed Halides. *Chemical Communications* **2001**, 1650–1657.

[52] Bowman, A.; Smith, R. I.; Gregory, D. H. Ternary and quaternary layered nitride halides, $Ca_2N(X,X')$ (X,X'=Cl,Br,I: evolution of structure with composition. *Journal of Solid State Chemistry* **2005**, *178*, 1807–1817.

[53] Brogan, M. A.; Hughes, R. W.; Smith, R. I.; Gregory, D. H. Structural and composition tuning of layered subnitrides: new complex nitride halides. *Dalton Transactions* **2010**, *39*, 7153–7158.

[54] Clark, S. J.; Segall, M. D.; Pickard, C. J.; Hasnip, P. J.; Probert, M. I. J.; Refson, K.; Payne, M. C. First principles methods using CASTEP. *Zeitschrift fr Kristallographie–New Crystal Structures* **2005**, *220*, 567–570.

[55] Kresse, G.; Furthmüller, J. Efficient iterative schemes for ab initio total-energy calculations using a plane-wave basis set. *Physical Review B* **1996**, *54*, 11169.

[56] Vanderbilt, D. Soft self-consistent pseudopotentials in a generalized eigenvalue formalism. *Phys. Rev. B* **1990**, *41*, 7892.

[57] Perdew, J. P.; Yue, W. Accurate and simple density functional for the electronic exchange energy: Generalized gradient approximation. *Physical Review B* **1986**, *33*, 8800.

[58] Grimme, S. Semiempirical GGA-type density functional constructed with a long-range dispersion correction. *Journal of Computational Chemistry* **2006**, *27*, 1787–1799.

[59] Monkhorst, H. J.; Pack, J. D. Special points for Brillouin-zone integrations. *Physical Review B* **1976**, *13*, 5188.

[60] Jesche, A.; Canfield, P. C. Single crystal growth from light, volatile and reactive materials using lithium and calcium flux. *Philosophical Magazine* **2014**, *94*, 2372–2402.

[61] Druffel, D. L.; Kuntz, K. L.; Woomer, A. H.; Alcorn, F. M.; Hu, J.; Donley, C. L.; Warren, S. C. Experimental demonstration of an electride as a 2D material. *Journal of the American Chemical Society* **2016**, *138*, 16089–16094.

[62] Vajenine, G. V.; Grzechnik, A.; Syassen, K.; Loa, I.; Hanfland, M.; Simon, A. Interplay of metallic and ionic bonding in layered subnitrides AE_2N (AE=Ca, Sr, or Ba) under high pressure. *Comptes Rendus Chimie* **2005**, *8*, 1897–1905.

[63] He, Y. The structural, electronic, elastic and thermodynamics properties of 2D transition-metal electride Y_2C via first-principles calculations. *Journal of Alloys and Compounds* **2016**, *654*, 180–184.

[64] Yi, S.; Choi, J. H.; Lee, K.; Kim, S. W.; Park, C. H.; Cho, J. H. Stacking-sequence-independent band structure and shear exfoliation of two-dimensional electride materials. *Physical Review B* **2016**, *94*, 235428.

[65] Druffel, D. L.; Woomer, A. H.; Kuntz, K. L.; Pawlik, J. T.; Warren, S. C. Electrons on the surface of 2D materials: from layered electrides to 2D electrenes. *Journal of Materials Chemistry C* **2017**, *5*, 11196–11213.

[66] Oh, J. S.; Kang, C. J.; Kim, Y. J.; Sinn, S.; Han, M.; Chang, Y. J.; Park, B. G.; Kim, S. W.; Min, B. I.; Kim, H. D.; Noh, T. W. Evidence for anionic excess electrons in a quasi-two-dimensional Ca_2N electride by angle-resolved photoemission spectroscopy. *Journal of the American Chemical Society* **2016**, *138*, 2496–2499.

[67] Guan, S.; Huang, S. Y.; Yao, Y.; Yang, S. A. 2D electrides as promising anode materials for Na-ion batteries from first-principles study. *Physical Review B* **2017**, *95*, 165436.

[68] Inoshita, T.; Jeong, S.; Hamada, N.; Hosono, H. Exploration for two-dimensional electrides via database screening and ab initio calculation. *Physical Review X* **2014**, *4*, 031023.

[69] Inoshita, T.; Hamada, N.; Hosono, H. Ferromagnetic instability of interlayer floating electrons in the quasi-two-dimensional electride. *Physical Review B* **2015**, *92*, 201109(R).

[70] Horiba, K.; Yukawa, R.; Mitsuhashi, T.; Kitamura, M.; Inoshita, T.; Hamada, N.; Otani, S.; Ohashi, N.; Maki, S.; Yamaura, J. I.; Hosono, H.; Murakami, Y.; Kumigashira, H. Semimetallic electride band derived from interlayer electrons in quasi-two-dimesnional electride Y_2C. *Physical Review B* **2017**, *96*, 045101.

[71] Park, J.; Lee, K.; Lee, S. Y.; Nandadasa, C. N.; Kim, S.; Lee, K. H.; Lee, Y. H.; Hosono, H.; Kim, S.-G.; Kim, S. W. Strong localization of anionic electrons at the interlayer for electrical and magnetic anisotropy of two-dimensional Y_2C electride. *Journal of the American Chemical Society* **2016**, *139*, 615–618.

[72] Schindewolf, U. Formation and properties of solvated electrons. *Angewandte Chemie International Edition* **1968**, *7*, 190–203.

[73] Choi, S.; Kim, Y. J.; Kim, S. M.; Yang, J. W.; Kim, S. W.; Cho, E. J. Hydrotrifluoromethylation and iodotrifluoromethylation of alkenes and alkynes using an inorganic electride as a radical generator. *Nature Communications* **2014**, *5*, 4881.

[74] Kim, Y. J.; Kim, S. M.; Cho, E. J.; Hosono, H.; Yang, J. W.; Kim, S. W. Two dimensional inorganic electride-promoted electron transfer efficiency in transfer hydrogenation of alkynes and alkenes. *Chemical Science* **2015**, *6*, 3577–3581.

[75] Kim, Y. J.; Kim, S. M.; Yu, C.; Yoo, Y.; Cho, E. J.; Yang, J. W.; Kim, S. W. Chemoselective hydrodehalogenation of organic halides utilizing two-dimensional anionic electrons of inorganic electride $[Ca_2N]^+ \cdot e^-$. *Langmuir* **2017**, *33*, 954–958.

[76] Kitano, M.; Inoue, Y.; Ishikawa, H.; Yamagata, K.; Nakao, T.; Tada, T.; Matsuishi, S.; Yokoyama, T.; Hara, M.; Hosono, H. Essential role of hydride ion in ruthenium-based ammonia synthesis catalysts. *Chemical Sciences* **2016**, *7*, 4036–4043.

[77] Brese, N. E.; O'Keeffe, M.; Von Dreele, R. B. Synthesis and crystal structure of SrD_2 and SrND and bond valence parameters for hydrides. *Journal of Solid State Chemistry* **1990**, *88*, 571–576.

[78] Sichla, T.; Altorfer, F.; Hohlwein, D.; Reimann, K.; Steube, M.; Wrzesinski, J.; Jacobs, H. Crystal structure determination of a strontium hydride imide nitride Sr_2(H)N/SrNH resp. Sr_2(D)N/SrND by X-ray, neutron, and synchrotron radiation. *Zeitschrift fr Anorganische und Allgemeine Chemie* **1997**, *623*, 414–422.

[79] Chemnitzer, R.; Auffermann, G.; Többens, D. M.; Kniep, R. (Sr_2N)H: on the redox-intercalation of hydrogen into Sr_2N. *Zeitschrift fr Anorganische und Allgemeine Chemie* **2005**, *631*, 1813–1817.

[80] Maehlen, J. P.; Yartys, V. A.; Hauback, B. C. Structural studies of deuterides of yttrium carbide. *Journal of Alloys and Compounds* **2003**, *351*, 151–157.

[81] Höhn, P.; Hoffmann, S.; Hunger, J.; Leoni, S.; Nitsche, F.; Schnelle, W.; Kniep, R. β-Ca_3N_2, a metastable nitride in the system Ca–N. *Chemistry–A European Journal* **2009**, *15*, 3419–3425.

[82] Prots, Y.; Auffermann, G.; Tovar, M.; Kniep, R. Sr_4N_3: a hitherto missing member in the nitrogen pressure reaction series $Sr_2N \rightarrow Sr_4N_3 \rightarrow SrN \rightarrow SrN_2$. *Angewandte Chemie International Edition* **2002**, *41*, 2288–2290.

[83] Kitano, M.; Inoue, Y.; Yamazaki, Y.; Hayashi, F.; Kanbara, S.; Matsuishi, S.; Yokoyama, T.; Kim, S. W.; Hara, M.; Hosono, H. Ammonia synthesis using a stable electride as an electron donor and reversible hydrogen store. *Nature Chemistry* **2012**, *4*, 934–940.

[84] Kobayashi, Y.; Kitano, M.; Kawamura, S.; Yokoyama, T.; Hosono, H. Kinetic evidence: the rate-determining step for ammonia synthesis over electride-supported Ru catalysts is no longer the nitrogen dissociation step. *Catalysis Science & Technology* **2017**, *7*, 47–50.

[85] Ye, T. N.; Li, J.; Kitano, M.; Sasase, M.; Hosono, H. Electronic interactions between a stable electride and a nano-alloy contnroly the chemoselective reduction reaction. *Chemical Science* **2016**, *7*, 5969–5975.

[86] Menamparambath, M. M.; Park, J. H.; Yoo, H. S.; Patole, S. P.; Yoo, J. B.; Kim, S. W.; Baik, S. Large work function difference driven electron transfer from electrides to single-walled carbon nanotubes. *Nanoscale* **2014**, *6*, 8844–8851.

[87] Kim, S.; Song, S.; Park, J.; Yu, H. S.; Cho, S.; Kim, D.; Baik, J.; Choe, D. H.; Chang, K. J.; Lee, Y. H.; Kim, S. W.; Yang, H. Long-range lattice engineering of $MoTe_2$ by a 2D electride. *Nano Letters* **2017**, *17*, 3363–3368.

[88] Hu, J.; Xu, B.; Yang, S. A.; Guan, S.; Ouyang, C.; Yao, Y. 2D Electrides as Promising Anode Materials for Na-Ion Batteries from First-Principles Study. *ACS Applied Materials & Interfaces* **2015**, *7*, 24016–24022.

[89] Hou, J.; Tu, K.; Chen, Z. Two-dimensional Y_2C Electride: a promising anode material for Na-ion batteries. *Journal of Physical Chemistry C* **2016**, *120*, 18473–18478.

[90] Novoselov, K. S.; Geim, A. K.; Morozov, S. V.; Jiang, D.; Zhang, Y.; Dubonos, S. V.; Grigorieva, I. V.; Firsov, A. A. Electric field effect in atomically thin carbon films. *Science* **2004**, *306*, 666–669.

[91] Zhang, Y.; Tan, Y. W.; Stormer, H. L.; Kim, P. Experimental observation of the quantum Hall effect and Berry's phase in graphene. *Nature* **2005**, *438*, 201–204.

[92] Lin, Y. M.; Jenkins, K. A.; Valdes-Garcia, A.; Small, J. P.; Farmer, D. B.; Avouris, P. Operation of graphene transistors at gigahertz frequencies. *Nano Letters* **2009**, *9*, 422–426.

[93] Dean, C. R.; Young, A. F.; Meric, I.; Lee, C.; Wang, L.; Sorgenfrei, S.; Watanabe, K.; Taniguchi, T.; Kim, P.; Shepard, K. L.; Hone, J. Boron nitride substrates for high-quality graphene electronics. *Nature Nanotechnology* **2010**, *5*, 722–726.

[94] Radisavljevic, B.; Radenovic, A.; Brivio, J.; Giacometti, V.; Kis, A. Single-layer MoS_2 Transistors. *Nature Nanotechnology* **2011**, *6*, 147–150.

[95] Splendiani, A.; Sun, L.; Zhang, Y.; Li, T.; Kim, J.; Chim, C. Y.; Galli, G.; Wang, F. Emerging photoluminescence in monolayer MoS_2. *Nano Letters* **2010**, *10*, 1271–1275.

[96] Mak, K. F.; Lee, C.; Hone, J.; Shan, J.; Heinz, T. F. Atomically thin MoS_2: a new direct-gap semiconductor. *Physical Review Letters* **2010**, *105*, 136805.

[97] Coleman, J. N. Liquid exfoliation of defect-free graphene. *Accounts of Chemical Research* **2012**, *46*, 14–22.

[98] Woomer, A. H.; Farnsworth, T. W.; Hu, J.; Wells, R. A.; Donley, C. L.; Warren, S. C. Phosphorene: synthesis, scale-up, and quantitative optical spectroscopy. *ACS Nano* **2015**, *9*, 8869–8884.

[99] Coleman, J. N. et al. Two-dimensional nanosheets produced by liquid exfoliation of layered materials. *Science* **2011**, *331*, 568–571, JID: 0404511; ppublish.

[100] Nicolosi, V.; Chhowalla, M.; Kanatzidis, M. G.; Strano, M. S.; Coleman, J. N. Liquid exfoliation of layered materials. *Science* **2013**, *340*, 1226419.

[101] Geim, A. K.; Grigorieva, I. V. Van der Waals heterostructures. *Nature* **2013**, *499*, 419.

[102] Massicotte, M.; Schmidt, P.; Vialla, F.; Schädler, K. G.; Reserbat-Plantey, A.; Watanabe, K.; Taniguchi, T.; Tielrooij, K.-J.; Koppens, F. H. Picosecond photoresponse in van der Waals heterostructures. *Nature Nanotechnology* **2016**, *11*, 42.

[103] Withers, F.; Del Pozo-Zamudio, O.; Mishchenko, A.; Rooney, A.; Gholinia, A.; Watanabe, K.; Taniguchi, T.; Haigh, S.; Geim, A.; Tartakovskii, A., et al. Light-emitting diodes by band-structure engineering in van der Waals heterostructures. *Nature Materials* **2015**, *14*, 301.

[104] Klein, D. R.; MacNeill, D.; Lado, J. L.; Soriano, D.; Navarro-Moratalla, E.; Watanabe, K.; Taniguchi, T.; Manni, S.; Canfield, P.; Fernández-Rossier, J.; Jarillo-Herrero, P. Probing magnetism in 2D van der Waals crystalline insulators via electron tunneling. *Science* **2018**, *360*, 1218–1222.

[105] Song, T.; Cai, X.; Tu, M. W.-Y.; Zhang, X.; Huang, B.; Wilson, N. P.; Seyler, K. L.; Zhu, L.; Taniguchi, T.; Watanabe, K.; McGuire, M. A.; Cobden, D. H.; Xiao, D.; Yao, W.; Xu, X. Giant tunneling magnetoresistance in spin-filter van der Waals heterostructures. *Science* **2018**, *360*, 1214–1218.

[106] Pauling, L. *The Nature of the Chemical Bond...*; Cornell university press Ithaca, NY, 1960; Vol. 260.

[107] Mulliken, R. S. Electronic population analysis on LCAO–MO molecular wave functions. *The Journal of Chemical Physics* **1955**, *23*, 1833–1840.

[108] Hückel, E. Zur quantentheorie der doppelbindung. *Zeitschrift für Physik* **1930**, *60*, 423–456.

[109] Hoffmann, R. An extended Hückel theory. I. hydrocarbons. *The Journal of Chemical Physics* **1963**, *39*, 1397–1412.

[110] Zhang, Y.; Xiao, Z.; Kamiya, T.; Hosono, H. Electron confinement in channel spaces for one-dimensional electride. *The Journal of Physical Chemistry Letters* **2015**, *6*, 4966–4971.

[111] Lu, Y.; Li, J.; Tada, T.; Toda, Y.; Ueda, S.; Yokoyama, T.; Kitano, M.; Hosono, H. Water durable electride Y_5Si_3: electronic structure and catalytic activity for ammonia synthesis. *Journal of the American Chemical Society* **2016**, *138*, 3970–3973.

[112] Ye, T.-N.; Lu, Y.; Li, J.; Nakao, T.; Yang, H.; Tada, T.; Kitano, M.; Hosono, H. Copper-based intermetallic electride catalyst for chemoselective hydrogenation reactions. *Journal of the American Chemical Society* **2017**, *139*, 17089–17097.

[113] Li, J.; Wu, J.; Wang, H.; Lu, Y.; Ye, T.; Sasase, M.; Wu, X.; Kitano, M.; Inoshita, T.; Hosono, H. Acid-durable electride with layered ruthenium for ammonia synthesis: boosting the activity via selective etching. *Chemical Science* **2019**, *10*, 5712–5718.

[114] Lu, Y.; Wang, J.; Li, J.; Wu, J.; Kanno, S.; Tada, T.; Hosono, H. Realization of Mott-insulating electrides in dimorphic Yb_5Sb_3. *Physical Review B* **2018**, *98*, 125128.

[115] Wang, J.; Hanzawa, K.; Hiramatsu, H.; Kim, J.; Umezawa, N.; Iwanaka, K.; Tada, T.; Hosono, H. Exploration of stable strontium phosphide-based electrides: theoretical structure prediction and experimental validation. *Journal of the American Chemical Society* **2017**, *139*, 15668–15680.

[116] Zhu, S.-C.; Wang, L.; Qu, J.-Y.; Wang, J.-J.; Frolov, T.; Chen, X.-Q.; Zhu, Q. Computational design of flexible electrides with nontrivial band topology. *Physical Review Materials* **2019**, *3*, 024205.

[117] Wan, B.; Lu, Y.; Xiao, Z.; Muraba, Y.; Kim, J.; Huang, D.; Wu, L.; Gou, H.; Zhang, J.; Gao, F.; Mao, H.-k.; Hosono, H. Identifying quasi-2D and 1D electrides in yttrium and scandium chlorides via geometrical identification. *npj Computational Materials* **2018**, *4*, 1–9.

[118] Tada, T.; Takemoto, S.; Matsuishi, S.; Hosono, H. High-throughput ab initio screening for two-dimensional electride materials. *Inorganic Chemistry* **2014**, *53*, 10347–10358.

[119] Wang, J.; Zhu, Q.; Wang, Z.; Hosono, H. Ternary inorganic electrides with mixed bonding. *Physical Review B* **2019**, *99*, 064104.

[120] Araujo, R. E.; Corbett, J. D. Lanthanum monochloride and lanthanum sesquichloride. *Inorganic Chemistry* **1981**, *20*, 3082–3086.

[121] Mattausch, H.; Hendricks, J. B.; R, E.; Corbett, J. D.; Simon, A. Reduced halides of yttrium with strong metal-metal bonding: yttrium monochloride, monobromide, sesquichloride, and sesquibromide. *Inorganic Chemistry* **1980**, *19*, 2128.

[122] Burton, L. A.; Ricci, F.; Chen, W.; Rignanese, G.-M.; Hautier, G. High-throughput identification of electrides from all known inorganic materials. *Chemistry of Materials* **2018**, *30*, 7521–7526.

[123] Brown, M. E.; Dollimore, D.; Galwey, A. K. *Reactions in the solid state*; Elsevier, 1980; Vol. 22.

[124] Corbett, J. D. Extended metal-metal bonding in halides of the early transition metals. *Accounts of Chemical Research* **1981**, *14*, 239–246.

[125] Hwu, S.-J.; Ziebarth, R. P.; von Winbush, S.; Ford, J. E.; Corbett, J. D. Synthesis and structure of double-metal-layered scandium, yttrium, and zirconium chloride carbides and nitrides, M_2Cl_2C and M_2Cl_2N. *Inorganic Chemistry* **1986**, *25*, 283–287.

[126] Esposito, R., Ed. *Lange's handbook of chemistry*, 15th ed.; McGraw-Hill, Inc.: New York, 1999.

[127] Corbett, J. D.; Simon, A. *Inorganic Syntheses*; John Wiley & Sons, Ltd, 2007; Chapter 3, pp 15–22.

[128] Kalkan, B.; Ozdas, E. Staging phenomena in lithium-intercalated boron–carbon. *ACS Applied Materials & Interfaces* **2019**, *11*, 4111–4122.

[129] Solid solubilities of oxygen, carbon and nitrogen in yttrium. *Journal of the Less Common Metals* **1974**, *35*, 275–284.

[130] Electrochemical deoxidation of yttrium-oxygen solid solutions. *Journal of Alloys and Compounds* **1996**, *237*, 150–154.

[131] Predel, B. In *B - Ba . . . Cu - Zr: Supplement to Subvolumes IV/5B, IV/5C and IV/5D*; Predel, B., Ed.; Springer Berlin Heidelberg: Berlin, Heidelberg, 2012; pp 153–154.

[132] Kosolapova, T. Y. *Carbides*; John Wiley & Sons, Ltd, 1971; Chapter 5, p 76.

[133] Ashcroft, N. W.; Mermin, N. D. *Solid state physics [by] Neil W. Ashcroft [and] N. David Mermin.*; New York: Holt, Rinehart and Winston,, 1976.

[134] Scherrer, P. Nachr Ges wiss goettingen. *Math. Phys.* **1918**, *2*, 98–100.

[135] Abdullah, M.; Khairurrijal, K. Derivation of Scherrer relation using an approach in basic physics course. *Jurnal Nanosains & Nanoteknologi* **2009**, *1*, 28–32.

[136] Patterson, A. L. The Scherrer formula for X-ray particle size determination. *Physical Review* **1939**, *56*, 978–982.

[137] Halder, N.; Wagner, C. Separation of particle size and lattice strain in integral breadth measurements. *Acta Crystallographica* **1966**, *20*, 312–313.

[138] Williamson, G.; Hall, W. X-ray line broadening from filed aluminium and wolfram. *Acta Metallurgica* **1953**, *1*, 22–31.

[139] Alcorn, F. M.; Kuntz, K. L.; Druffel, D. L.; Warren, S. C. Aqueous Intercalation of Graphite at a Near-Neutral pH. *ACS Applied Energy Materials* **2018**, *1*, 5062–5067.

[140] Rietveld, H. A profile refinement method for nuclear and magnetic structures. *Journal of Applied Crystallography* **1969**, *2*, 65–71.

[141] McCusker, L. B.; Von Dreele, R. B.; Cox, D. E.; Louër, D.; Scardi, P. Rietveld refinement guidelines. *Journal of Applied Crystallography* **1999**, *32*, 36–50.

[142] Pawley, G. Unit-cell refinement from powder diffraction scans. *Journal of Applied Crystallography* **1981**, *14*, 357–361.

[143] Toraya, H. Whole-powder-pattern decomposition method. *The Rigaku Journal* **1989**, *6*, 28–34.

[144] Caglioti, G.; Paoletti, A. t.; Ricci, F. Choice of collimators for a crystal spectrometer for neutron diffraction. *Nuclear Instruments* **1958**, *3*, 223–228.

[145] Balzar, D. Profile fitting of X-ray diffraction lines and Fourier analysis of broadening. *Journal of Applied Crystallography* **1992**, *25*, 559–570.

[146] Enzo, S.; Fagherazzi, G.; Benedetti, A.; Polizzi, S. A profile-fitting procedure for analysis of broadened X-ray diffraction peaks. I. Methodology. *Journal of Applied Crystallography* **1988**, *21*, 536–542.

[147] March, A. Mathematische Theorie der Regelung nach der Korngestah bei affiner Deformation. *Zeitschrift für Kristallographie-Crystalline Materials* **1932**, *81*, 285–297.

[148] Dollase, W. Correction of intensities for preferred orientation in powder diffractometry: application of the March model. *Journal of Applied Crystallography* **1986**, *19*, 267–272.

[149] Post, J.; Bish, D. Rietveld refinement of crystal structures using powder X-ray diffraction data. *Modern Powder Diffraction* **1989**, *20*, 277–308.

[150] Hohenberg, P.; Kohn, W. Inhomogeneous electron gas. *Physical Review* **1964**, *136*, B864.

[151] Kohn, W.; Sham, L. J. Self-consistent equations including exchange and correlation effects. *Physical Review* **1965**, *140*, A1133.

[152] Stowasser, R.; Hoffmann, R. What do the KohnSham orbitals and eigenvalues mean? *Journal of the American Chemical Society* **1999**, *121*, 3414–3420.

[153] Perdew, J. P.; Levy, M. Physical content of the exact Kohn-Sham orbital energies: Band gaps and derivative discontinuities. *Physical Review Lett.* **1983**, *51*, 1884–1887.

[154] Negele, J. W. Structure of finite nuclei in the local-density approximation. *Physical Review C* **1970**, *1*, 1260.

[155] Hedin, L.; Lundqvist, B. I. Explicit local exchange-correlation potentials. *Journal of Physics C: Solid State Physics* **1971**, *4*, 2064.

[156] Perdew, J. P.; Ruzsinszky, A.; Csonka, G. I.; Vydrov, O. A.; Scuseria, G. E.; Constantin, L. A.; Zhou, X.; Burke, K. Restoring the density-gradient expansion for exchange in solids and surfaces. *Physical Review Letters* **2008**, *100*, 136406.

[157] Hellmann, H. A new approximation method in the problem of many electrons. *The Journal of Chemical Physics* **1935**, *3*, 61–61.

[158] Hamann, D.; Schlüter, M.; Chiang, C. Norm-conserving pseudopotentials. *Physical Review Letters* **1979**, *43*, 1494.

[159] Ekardt, W. Work function of small metal particles: Self-consistent spherical jellium-background model. *Physical Review B* **1984**, *29*, 1558.

[160] Fall, C.; Binggeli, N.; Baldereschi, A. Deriving accurate work functions from thin-slab calculations. *Journal of Physics: Condensed Matter* **1999**, *11*, 2689.

[161] Bengtsson, L. Dipole correction for surface supercell calculations. *Physical Review B* **1999**, *59*, 12301.

[162] Woomer, A. H.; Druffel, D. L.; Sundberg, J. D.; Pawlik, J. T.; Warren, S. C. Bonding in 2D donor–acceptor heterostructures. *Journal of the American Chemical Society* **2019**,

[163] Singh, D. J.; Krakauer, H.; Haas, C.; Pickett, W. E. Theoretical determination that electrons act as anions in the electride Cs^+ (15-crown-5)$_2$·e^-. *Nature* **1993**, *365*, 39–42.

[164] Dye, J. L. Electrons as anions. *Science* **2003**, *301*, 607–608.

[165] Lu, Y.; Li, J.; Tada, T.; Toda, Y.; Ueda, S.; Yokoyama, T.; Kitano, M.; Hosono, H. Water durable electride Y_5Si_3: electronic structure and catalytic activity for ammonia synthesis. *Journal of the American Chemical Society* **2016**, *138*, 3970–3973.

[166] Kuganathan, N.; Hosono, H.; Shluger, A. L.; Sushko, P. V. Enhanced N_2 dissociation on Ru-loaded inorganic electride. *Journal of the American Chemical Society* **2014**, *136*, 2216–2219.

[167] Kim, S. W.; Toda, Y.; Hayashi, K.; Hirano, M.; Hosono, H. Synthesis of a room temperature stable $12CaO \cdot 7Al_2O_3$ electride from the melt and its application as an electron field emitter. *Chemistry of Materieals* **2006**, *18*, 1938–1944.

[168] Son, Y. C.; Ryu, B.; Lee, S. M. Electrically conductive thin films. US Patent 14,567,900, December 11, 2014.

[169] Tai, P.; Jung, C.; Kang, Y.; Yoon, D. Electrical and optical properties of 12 $CaO \cdot 7Al_2O_3$ electride doped indium tin oxide thin film deposited by RF magnetron co-sputtering. *Thin Film Solids* **2009**, *517*, 6294.

[170] Guan, S.; Yang, S. A.; Zhu, L.; Hu, J.; Yao, Y. Electronic, dielectric, and plasmonic properties of two-dimensional electride materials X_2N (X=Ca, Sr): a first-principles study. *Scientific Reports* **2015**, *5*, 12285.

[171] Redko, M. Y.; Jackson, J. E.; Huang, R. H.; Dye, J. L. Design and synthesis of a thermally stable organic electride. *Journal of the American Chemical Society* **2005**, *127*, 12416–12422.

[172] Zhao, S.; Li, Z.; Yang, J. Obtaining two-dimensional electron gas in free space without resorting to electron doping: an electride based design. *Journal of the American Chemical Society* **2014**, *136*, 13313.

[173] Reckeweg, O.; DiSalvo, F. J. Alkaline earth metal nitride compounds with the composition M_2NX (M=Ca, Sr, Ba; X=□, H, Cl or Br). *Solid State Sciences* **2002**, *4*, 575–584.

[174] Whittingham, M. S. Chalcogenide battery. US Patent 4009052, February 22, 1977.

[175] Aurbach, D. J. Review of selected electrode–solution interactions which determine the performance of Li and Li ion batteries. *Journal of Power Sources* **2000**, *89*, 206–218.

[176] Lotya, M.; Hernandez, Y.; King, P. J.; Smith, R. J.; Nicolosi, V.; Karlsson, L. S.; Blighe, F. M.; De, S.; Wang, Z.; McGovern, I. Liquid phase production of graphene by exfoliation of graphite in surfactant/water solutions. *Journal of the American Chemical Society* **2009**, *131*, 3611–3620.

[177] Stadelmann, P.; JEMS-EMS,; Java version, `http://www.jems-saas.ch/`.

[178] Demri, B.; Muster, D. XPS study of some calcium compounds. *Journal of Materials Processing Technology* **1995**, *55*, 311–314.

[179] Morris, A. J.; Nichools, R.; Pickard, C. J.; Yates, J. R. OptaDOS: A tool for obtaining density of states, core-level and optical spectra from electronic structure codes. *Computer Physics Communications* **2014**, *185*, 1477–1485.

[180] Pickard, C. J.; Payne, M. C. Extrapolative approaches to Brillouin-zone integration. *Physical Review B–Condensed Matter and Materials Physics* **1999**, *59*, 4685.

[181] Pickard, C. J.; Payne, M. C. Second-order k · p perturbation theory with Vanderbilt pseudopotentials and plane waves. *Physical Review B* **2000**, *62*, 4383.

[182] Inoue, Y.; Kitano, M.; Kim, S.-W.; Yokoyama, T.; Hara, M.; Hosono, H. Highly dispersed Ru on electride $[Ca_{24}Al_{28}O_{64}]\cdot 4(e^-)$ as a catalyst for ammonia synthesis. *ACS Catalysis* **2014**, *4*, 674–680.

[183] Rossiter, P. L. *The Electrical Resistivitiy of Metals and Alloys*; Cambridge University Press: Cambridge, U.K., 1991.

[184] Uijttewaal, M.; Wijs, G. D.; Groot, R. D. Low work function of the (1000) Ca_2N surface. *Journal of Applied Physics* **2004**, *96*, 1751–1753.

[185] Michaelson, H. B. Work functions of the elements. *Journal of Applied Physics* **1950**, *21*, 536.

[186] Bardeen, J. Surface states and rectification at a metal semi-conductor contact. *Physical Review* **1947**, *71*, 717.

[187] Dowden, D. 56. Heterogeneous catalysis. Part I. Theoretical basis. *Journal of the Chemical Society (Resumed)* **1950**, 242–265.

[188] Marcus, R. A. Chemical and electrochemical electron-transfer theory. *Annual Review of Physical Chemistry* **1964**, *15*, 155–196.

[189] Fang, H.; Battaglia, C.; Carraro, C.; Nemsak, S.; Ozdol, B.; Kang, J. S.; Bechtel, H. A.; Desai, S. B.; Kronast, F.; Unal, A. A., et al. Strong interlayer coupling in van der Waals heterostructures built from single-layer chalcogenides. *Proceedings of the National Academy of Sciences* **2014**, *111*, 6198–6202.

[190] Chen, Z.; Santoso, I.; Wang, R.; Xie, L. F.; Mao, H. Y.; Huang, H.; Wang, Y. Z.; Gao, X. Y.; Chen, Z. K.; Ma, D., et al. Surface transfer hole doping of epitaxial graphene using MoO_3 thin film. *Applied Physics Letters* **2010**, *96*, 213104.

[191] Xie, L.; Wang, X.; Mao, H.; Wang, R.; Ding, M.; Wang, Y.; Özyilmaz, B.; Ping Loh, K.; Wee, A. T.; Ariando,, et al. Electrical measurement of non-destructively p-type doped graphene using molybdenum trioxide. *Applied Physics Letters* **2011**, *99*, 012112.

[192] Kang, K.; Lee, K.-H.; Han, Y.; Gao, H.; Xie, S.; Muller, D. A.; Park, J. Layer-by-layer assembly of two-dimensional materials into wafer-scale heterostructures. *Nature* **2017**, *550*, 229.

[193] Inoshita, T.; Tsukada, M.; Saito, S.; Hosono, H. Probing a divergent van Hove singularity of graphene with a Ca_2N support: A layered electride as a solid-state dopant. *Physical Review B* **2017**, *96*, 245303.

[194] Henkelman, G.; Arnaldsson, A.; Jónsson, H. A fast and robust algorithm for Bader decomposition of charge density. *Computational Materials Science* **2006**, *36*, 354–360.

[195] Sanville, E.; Kenny, S. D.; Smith, R.; Henkelman, G. Improved grid-based algorithm for Bader charge allocation. *Journal of Computational Chemistry* **2007**, *28*, 899–908.

[196] Tang, W.; Sanville, E.; Henkelman, G. A grid-based Bader analysis algorithm without lattice bias. *Journal of Physics: Condensed Matter* **2009**, *21*, 084204.

[197] Yu, M.; Trinkle, D. R. Accurate and efficient algorithm for Bader charge integration. *The Journal of Chemical Physics* **2011**, *134*, 064111.

[198] Adamo, C.; Barone, V. Toward reliable density functional methods without adjustable parameters: The PBE0 model. *The Journal of Chemical Physics* **1999**, *110*, 6158–6170.

[199] Krukau, A. V.; Vydrov, O. A.; Izmaylov, A. F.; Scuseria, G. E. Influence of the exchange screening parameter on the performance of screened hybrid functionals. *The Journal of Chemical Physics* **2006**, *125*, 224106.

[200] Seidl, A.; Görling, A.; Vogl, P.; Majewski, J.; Levy, M. Generalized Kohn-Sham schemes and the band-gap problem. *Physical Review B* **1996**, *53*, 3764.

[201] Zhang, Y.; Yang, W. A challenge for density functionals: Self-interaction error increases for systems with a noninteger number of electrons. *The Journal of Chemical Physics* **1998**, *109*, 2604–2608.

[202] Sini, G.; Sears, J. S.; Brèdas, J.-L. Evaluating the performance of DFT functionals in assessing the interaction energy and ground-state charge transfer of donor/acceptor complexes: tetrathiafulvalene-tetracyanoquinodimethane (TTF- TCNQ) as a model case. *Journal of Chemical Theory and Computation* **2011**, *7*, 602–609.

[203] U, D. Character of metallic solid solutions and compounds. *Zeitschrift fuer Metallkunde* **1934**, *26*, 227–230.

[204] Jain, A.; Ong, S. P.; Hautier, G.; Chen, W.; Richards, W. D.; Dacek, S.; Cholia, S.; Gunter, D.; Skinner, D.; Ceder, G.; Persson, K. A. Commentary: The Materials Project: A materials genome approach to accelerating materials innovation. *Applied Materials* **2013**, *1*, 011002.

[205] Alvarez, S. A cartography of the van der Waals territories. *Dalton Transactions* **2013**, *42*, 8617–8636.

[206] Pietronero, L.; Strässler, S. Bond-length change as a tool to determine charge transfer and electron-phonon coupling in graphite intercalation compounds. *Physical Review Letters* **1981**, *47*, 593.

[207] Zhang, J.-M.; Ma, F.; Xu, K.-W.; Xin, X.-T. Anisotropy analysis of the surface energy of diamond cubic crystals. *Surface and Interface Analysis* **2003**, *35*, 805–809.

[208] Benedict, L. X.; Chopra, N. G.; Cohen, M. L.; Zettl, A.; Louie, S. G.; Crespi, V. H. Microscopic determination of the interlayer binding energy in graphite. *Chemical Physics Letters* **1998**, *286*, 490–496.

[209] Fredrickson, D. C. DFT-chemical pressure analysis: Visualizing the role of atomic size in shaping the structures of inorganic materials. *Journal of the American Chemical Society* **2012**, *134*, 5991–5999.

[210] Brédas, J.-L.; Beljonne, D.; Coropceanu, V.; Cornil, J. Charge-transfer and energy-transfer processes in π-conjugated oligomers and polymers: a molecular picture. *Chemical Reviews* **2004**, *104*, 4971–5004.

[211] Sakamoto, M.; Speck, J.; Dresselhaus, M. Cesium and bromine doping into hexagonal boron nitride. *Journal of Materials Research* **1986**, *1*, 685–692.

[212] Skancke, A.; Skancke, P. Density functional theory and perturbation calculations on some lewis acid-base complexes. A systematic study of substitution effects. *The Journal of Physical Chemistry* **1996**, *100*, 15079–15082.

[213] Hirshfield, F. L. Bonded atom-fragments for describing molecular charge densities. *Theoretical Chemistry Accounts* **2017**, *9*, 10846–10853.

[214] Albright, T. A.; Burdett, J. K.; Whangbo, M.-H. *Orbital interactions in chemistry*; John Wiley & Sons, 2013.

[215] Wang, L.-F.; Ma, T.-B.; Hu, Y.-Z.; Wang, H.; Shao, T.-M. Ab initio study of the friction mechanism of fluorographene and graphane. *The Journal of Physical Chemistry C* **2013**, *117*, 12520–12525.

[216] Wang, L.; Zhou, X.; Ma, T.; Liu, D.; Gao, L.; Li, X.; Zhang, J.; Hu, Y.; Wang, H.; Dai, Y., et al. Super-lubricity of a graphene/MoS_2 heterostructure: a combined experimental and DFT study. *Nanoscale* **2017**, *9*, 10846–10853.

[217] Scharf, T. W.; Prasad, S. V. Solid lubricants: a review. *Journal of Materials Science* **2013**, 511–531.

[218] Toda, Y.; Matsuishi, S.; Hayashi, K.; Ueda, K.; Kamiya, T.; Hirano, M.; Hosono, H. Field emission of electron anions clathrated in subnanometer-sized cages in $[Ca_{24}Al_{28}O_{64}]\cdot 4(e^-)$. *Advanced Materials* **2004**, *16*, 685–689.

[219] McKinnon, W.; Dahn, J.; Levy-Clement, C. Lithium intercalation in Li_xZrS_2. *Solid State Communications* **1984**, *50*, 101–104.

[220] Bediako, D. K.; Rezaee, M.; Yoo, H.; Larson, D. T.; Zhao, S. F.; Taniguchi, T.; Watanabe, K.; Brower-Thomas, T. L.; Kaxiras, E.; Kim, P. Heterointerface effects in the electrointercalation of van der Waals heterostructures. *Nature* **2018**, *558*, 425.

[221] Naguib, M.; Mochalin, V. N.; Barsoum, M. W.; Gogotsi, Y. 25th anniversary article: MXenes: a new family of two-dimensional materials. *Advanced Materials* **2014**, *26*, 992–1005.

[222] Zhao, M.-Q.; Ren, C. E.; Ling, Z.; Lukatskaya, M. R.; Zhang, C.; Van Aken, K. L.; Barsoum, M. W.; Gogotsi, Y. Flexible MXene/carbon nanotube composite paper with high volumetric capacitance. *Advanced Materials* **2015**, *27*, 339–345.

[223] Li, R.; Zhang, L.; Shi, L.; Wang, P. MXene Ti_3C_2: an effective 2D light-to-heat conversion material. *ACS nano* **2017**, *11*, 3752–3759.

[224] Kim, S. J.; Koh, H.-J.; Ren, C. E.; Kwon, O.; Maleski, K.; Cho, S.-Y.; Anasori, B.; Kim, C.-K.; Choi, Y.-K.; Kim, J., et al. Metallic $Ti_3C_2T_x$ MXene gas sensors with ultrahigh signal-to-noise ratio. *ACS nano* **2018**, *12*, 986–993.

[225] Yu, X.-f.; Li, Y.-c.; Cheng, J.-b.; Liu, Z.-b.; Li, Q.-z.; Li, W.-z.; Yang, X.; Xiao, B. Monolayer Ti_2CO_2: a promising candidate for NH_3 sensor or capturer with high sensitivity and selectivity. *ACS Applied Materials & interfaces* **2015**, *7*, 13707–13713.

[226] Naguib, M.; Come, J.; Dyatkin, B.; Presser, V.; Taberna, P.-L.; Simon, P.; Barsoum, M. W.; Gogotsi, Y. MXene: a promising transition metal carbide anode for lithium-ion batteries. *Electrochemistry Communications* **2012**, *16*, 61–64.

[227] Liang, X.; Garsuch, A.; Nazar, L. F. Sulfur cathodes based on conductive MXene nanosheets for high-performance lithium–sulfur batteries. *Angewandte Chemie International Edition* **2015**, *54*, 3907–3911.

[228] Wang, X.; Kajiyama, S.; Iinuma, H.; Hosono, E.; Oro, S.; Moriguchi, I.; Okubo, M.; Yamada, A. Pseudocapacitance of MXene nanosheets for high-power sodium-ion hybrid capacitors. *Nature Communications* **2015**, *6*, 6544.

[229] Naguib, M.; Kurtoglu, M.; Presser, V.; Lu, J.; Niu, J.; Heon, M.; Hultman, L.; Gogotsi, Y.; Barsoum, M. W. Two-dimensional nanocrystals produced by exfoliation of Ti_3AlC_2. *Advanced Materials* **2011**, *23*, 4248–4253.

[230] Ghidiu, M.; Barsoum, M. W. The $\{110\}$ reflection in X-ray diffraction of MXene films: Misinterpretation and measurement via non-standard orientation. *Journal of the American Ceramic Society* **2017**, *100*, 5395–5399.

[231] Ghidiu, M.; Kota, S.; Drozd, V.; Barsoum, M. W. Pressure-induced shear and interlayer expansion in Ti_3C_2 MXene in the presence of water. *Science Advances* **2018**, *4*, eaao6850.

[232] Ren, C. E.; Hatzell, K. B.; Alhabeb, M.; Ling, Z.; Mahmoud, K. A.; Gogotsi, Y. Charge-and size-selective ion sieving through $Ti_3C_2T_x$ MXene membranes. *The Journal of Physical Chemistry Letters* **2015**, *6*, 4026–4031.

[233] Xia, Y.; Mathis, T. S.; Zhao, M.-Q.; Anasori, B.; Dang, A.; Zhou, Z.; Cho, H.; Gogotsi, Y.; Yang, S. Thickness-independent capacitance of vertically aligned liquid-crystalline MXenes. *Nature* **2018**, *557*, 409.

[234] Henn, R.; Schnelle, W.; Kremer, R.; Simon, A. Bulk superconductivity at 10 K in the layered compounds $Y_2C_2I_2$ and $Y_2C_2Br_2$. *Physical Review Letters* **1996**, *77*, 374.

[235] Mattausch, H.; Kremer, R.; Simon, A. The polytypism and phase width of the yttrium carbide bromides 1T-$Y_2Br_2C_{1-x}$ and 3R-$Y_2Br_2C_{1-x}$. *Zeitschrift fur Anorganische und Allgemeine Chemie* **1995**, *621*, 1001–1006.

[236] Ahn, K.; Kremer, R. K.; Simon, A.; Marshall, W. G.; Puschnig, P.; Ambrosch-Draxl, C. Influence of pressure on the structure and electronic properties of the layered superconductor $Y_2C_2I_2$. *Journal of Physics: Condensed Matter* **2005**, *17*, S3121.

[237] Kauzlarich, S. M.; Hughbanks, T.; Corbett, J. D.; Klavins, P.; Shelton, R. N. Two extended metal chain compounds, yttrium iodide carbides (Y_4I_5C and $Y_6I_7C_2$). Synthesis, structure, properties, and bonding. *Inorganic Chemistry* **1988**, *27*, 1791–1797.

[238] Kauzlarich, S. M.; Payne, M. W.; Corbett, J. D. $Y_{10}I_{13}C_2$: a novel compound with chains of both carbon-centered and empty clusters. *Inorganic Chemistry* **1990**, *29*, 3777–3781.

[239] Schaloske, M. C.; Kienle, L.; Duppel, V.; Mattausch, H.; Simon, A. $SE_{19}(C_2)_3I_{34}$ (SE= Y, Gd): Verbindungen mit diskreten SE_6I_{12}-clustern und isolierten SE-atomen. *Zeitschrift für Anorganische und Allgemeine Chemie* **2009**, *1*, 188–195.

[240] Mattausch, H.; Borrmann, H.; Simon, A. Crystal structure of diyttrium diiodide dicarbide, $Y_2I_2C_2$. *Zeitschrift für Kristallographie* **1994**, *209*, 281–281.

[241] Hinz, D.; Meyer, G. Crystal structure of yttrium carbide iodide (10-4-18),$[Y_{10}(C_2)_2]I_{18}$. *Zeitschrift fur Kristallographie* **1995**, *210*, 957–957.

[242] Simon, A.; Bäcker, M.; Henn, R.; Felser, C.; Kremer, R.; Mattausch, H.; Yoshiasa, A. Supraleitung in seltenerdmetall-carbidhalogeniden des typs $SE_2X_2C_2$. *Zeitschrift für Anorganische und Allgemeine Chemie* **1996**, *622*, 123–137.

[243] Jongen, L.; Mudring, A.-V.; Meyer, G. The molecular solid $Sc_{24}C_{10}I_{30}$: A truncated, hollow T4 supertetrahedron of iodine filled with a T3 supertetrahedron of scandium that encapsulates the adamantoid cluster Sc_4C_{10}. *Angewandte Chemie International Edition* **2006**, *45*, 1886–1889.

[244] Dudis, D. S.; Corbett, J. D.; Hwu, S. J. Synthesis, characterization, and crystal structures of two scandium cluster carbides and a boride, $Sc_7X_{12}C$ (X= I, Br) and $Sc_7I_{12}B$. *Inorganic Chemistry* **1986**, *25*, 3434–3438.

[245] Hwu, S.-J.; Corbett, J. D. Metal-metal-bonded scandium cluster ($Sc_7Cl_{12}Z$) and infinite chain (Sc_4Cl_6Z) phases stabilized by interstitial boron or nitrogen (Z). *Journal of Solid State Chemistry* **1986**, *64*, 331–346.

[246] Dudis, D. S.; Corbett, J. D. Two scandium iodide carbides containing dicarbon units within scandium clusters: $Sc_6I_{11}C_2$ and $Sc_4I_6C_2$. Synthesis, structure, and the bonding of dicarbon. *Inorganic Chemistry* **1987**, *26*, 1933–1940.

[247] Hwu, S.-J.; Corbett, J. D.; Poeppelmeier, K. R. Interstitial atoms in metal-metal bonded arrays: The synthesis and characterization of heptascandium decachlorodicarbide, $Sc_7Cl_{10}C_2$, and comparison with the interstitial-free Sc_7Cl_{10}. *Journal of Solid State Chemistry* **1985**, *57*, 43–58.

[248] Smith, J. D.; Corbett, J. D. Four zirconium iodide cluster phases centered by boron, aluminum, or silicon. *Journal of the American Chemical Society* **1986**, *108*, 1927–1934.

[249] Smith, J. D.; Corbett, J. D. Stabilization of clusters by interstitial atoms. Three carbon-centered zirconium iodide clusters, $Zr_6I_{12}C$, $Zr_6I_{14}C$, and $MZr_6I_{14}C$ (M= K, Rb, or Cs). *Journal of the American Chemical Society* **1985**, *107*, 5704–5711.

[250] Ströbele, M.; Meyer, H.-J. The new binary tungsten iodide $W_{15}I_{47}$. *Zeitschrift für Anorganische und Allgemeine Chemie* **2010**, *636*, 62–66.

[251] Rietveld, H. M. The rietveld method. *Physica Scripta* **2014**, *89*, 098002.

[252] Glass, C. W.; Oganov, A. R.; Hansen, N. USPEX–Evolutionary crystal structure prediction. *Computer Physics Communications* **2006**, *175*, 713–720.

[253] Garcia, E.; Corbett, J. D.; Ford, J. E.; Vary, W. J. Low-temperature routes to new structures for yttrium, holmium, erbium, and thulium oxychlorides. *Inorganic Chemistry* **1985**, *24*, 494–498.

[254] Templeton, D.; Carter, G. F. The crystal structures of yttrium trichloride and similar compounds. *The Journal of Physical Chemistry* **1954**, *58*, 940–944.

[255] Zalkin, A.; Templeton, D. The crystal structures of YF_3 and related compounds. *Journal of the American Chemical Society* **1953**, *75*, 2453–2458.

[256] Shannon, R. t.; Prewitt, C. Revised values of effective ionic radii. *Acta Crystallographica Section B: Structural Crystallography and Crystal Chemistry* **1970**, *26*, 1046–1048.

[257] Mattausch, H.; Eger, R.; Simon, A. Das erste Gadoliniumcarbidfluorid: Gd_2CF_2. *Zeitschrift für Anorganische und Allgemeine Chemie* **1991**, *597*, 145–150.

[258] Cockcroft, J.; Kremer, R.; Mattausch, H.; Raju, N.; Simon, A. Structure and magnetic ordering of holmium carbide fluoride, Ho_2CF_2. *Journal of Alloys and Compounds* **1992**, *183*, 241–251.

[259] Come, J.; Naguib, M.; Rozier, P.; Barsoum, M. W.; Gogotsi, Y.; Taberna, P.-L.; Morcrette, M.; Simon, P. A non-aqueous asymmetric cell with a Ti_2C-based two-dimensional negative electrode. *Journal of the Electrochemical Society* **2012**, *159*, A1368–A1373.

[260] Heyd, J.; Scuseria, G. E. Assessment and validation of a screened Coulomb hybrid density functional. *The Journal of Chemical Physics* **2004**, *120*, 7274–7280.

[261] Albright, T. A.; Burdett, J. K.; Whangbo, M.-H. *Orbital interactions in chemistry*; John Wiley & Sons, 2013.

[262] Kuntz, K. L.; Wells, R. A.; Hu, J.; Yang, T.; Dong, B.; Guo, H.; Woomer, A. H.; Druffel, D. L.; Alabanza, A.; Tomnek, D.; Warren, S. C. Control of surface and edge oxidation on phosphorene. *ACS Applied Materials & Interfaces* **2017**, *9*, 9126–9135.

[263] Spitzer, S.; Schwartz, B.; Kuhn, M. Electrical properties of a native oxide on gallium phosphide. *Journal of The Electrochemical Society* **1973**, *120*, 669–672.

[264] Morita, M.; Ohmi, T. Characterization and control of native oxide on silicon. *Japanese Journal of Applied Physics* **1994**, *33*, 370–374.

[265] Poole, R. T.; Szajman, J.; Leckey, R. C. G.; Jenkin, J. G.; Liesegang, J. Electronic structure of the alkaline-earth fluorides studied by photoelectron spectroscopy. *Physical Review B* **1975**, *12*, 5872–5877.

[266] Vasquez, R. XPS Core level spectra of some Y compounds. *Journal of Electron Spectroscopy and Related Phenomena* **1990**, *50*, 167–170.

[267] Dubbe, A.; Wake, M.; Sadaoka, Y. Yttria/carbonate composite solid electrolytes for potentiometric CO_2 sensors. *Solid State Ionics* **1997**, *96*, 201–208.

[268] Fujimori, A.; Schlapbach, L. Electronic structure of yttrium hydride studied by X-ray photoemission spectroscopy. *Journal of Physics C: Solid State Physics* **1984**, *17*, 341.

[269] Mongstad, T.; Thgersen, A.; Subrahmanyam, A.; Karazhanov, S. The electronic state of thin films of yttrium, yttrium hydrides and yttrium oxide. *Solar Energy Materials and Solar Cells* **2014**, *128*, 270–274.

[270] Agarwal, M.; DeGuire, M. R.; Heuer, A. H. Synthesis of yttrium oxide thin films with and without the use of organic self-assembled monolayers. *Applied Physics Letters* **1997**, *71*, 891–893.

[271] Zhang, C. J.; Pinilla, S.; McEvoy, N.; Cullen, C. P.; Anasori, B.; Long, E.; Park, S.-H.; Seral-Ascaso, A.; Shmeliov, A.; Krishnan, D.; Morant, C.; Liu, X.; Duesberg, G. S.; Gogotsi, Y.; Nicolosi, V. Oxidation stability of colloidal two-dimensional titanium carbides (MXenes). *Chemistry of Materials* **2017**, *29*, 4848–4856.

[272] Li, G.; Jiang, K.; Zaman, S.; Xuan, J.; Wang, Z.; Geng, F. Ti_3C_2 sheets with an adjustable surface and feature sizes to regulate the chemical stability. *Inorganic Chemistry* **2019**, *58*, 9397–9403.

[273] Huang, S.; Mochalin, V. N. Hydrolysis of 2D transition-metal carbides (MXenes) in colloidal solutions. *Inorganic Chemistry* **2019**, *58*, 1958–1966.

[274] Chertopalov, S.; Mochalin, V. N. Environment-sensitive photoresponse of spontaneously partially oxidized Ti_3C_2 MXene thin films. *ACS Nano* **2018**, *12*, 6109–6116.

[275] Wang, X.; Garnero, C.; Rochard, G.; Magne, D.; Morisset, S.; Hurand, S.; Chartier, P.; Rousseau, J.; Cabioc'h, T.; Coutanceau, C.; Mauchamp, V.; Clrier, S. A new etching environment (FeF_3/HCl) for the synthesis of two-dimensional titanium carbide MXenes: a route towards selective reactivity vs. water. *Journal of Materials Chemistry A* **2017**, *5*, 22012–22023.

[276] Chae, Y.; Kim, S. J.; Cho, S.-Y.; Choi, J.; Maleski, K.; Lee, B.-J.; Jung, H.-T.; Gogotsi, Y.; Lee, Y.; Ahn, C. W. An investigation into the factors governing the oxidation of two-dimensional Ti_3C_2 MXene. *Nanoscale* **2019**, *11*, 8387–8393.

[277] Lotfi, R.; Naguib, M.; Yilmaz, D. E.; Nanda, J.; van Duin, A. C. T. A comparative study on the oxidation of two-dimensional Ti_3C_2 MXene structures in different environments. *Journal of Materials Chemistry A* **2018**, *6*, 12733–12743.

[278] Alhabeb, M.; Maleski, K.; Mathis, T. S.; Sarycheva, A.; Hatter, C. B.; Uzun, S.; Levitt, A.; Gogotsi, Y. Selective etching of silicon from Ti_3SiC_2 (MAX) to obtain 2D titanium carbide (MXene). *Angewandte Chemie International Edition* **2018**, *57*, 5444–5448.

[279] Ghidiu, M.; Lukatskaya, M. R.; Zhao, M.-Q.; Gogotsi, Y.; Barsoum, M. W. Conductive two-dimensional titanium carbide 'clay' with high volumetric capacitance. *Nature* **2014**, *516*, 78.

[280] Zhang, W. L.; Deng, L.; Liu, J.; Liu, Y.; Yin, J.; Zeng, H.; Zheng, W.; Zhang, A. Unveiling the critical role of surface oxidation of electroresponsive behaviors in two-dimensional $Ti_3C_2T_x$ MXenes. *The Journal of Physical Chemistry C* **2019**, *123*, 5479–5487.

[281] Khazaei, M.; Arai, M.; Sasaki, T.; Ranjbar, A.; Liang, Y.; Yunoki, S. OH-terminated two-dimensional transistion metal carbides and nitrides as ultralow work function materials. *Physical Review B* **2015**, *92*, 075411.

[282] Schultz, T.; Frey, N. C.; Hantanasirisakul, K.; Park, S.; May, S. J.; Shenoy, V. B.; Gogotsi, Y.; Koch, N. Surface termination dependent work function and electronic properties of $Ti_3C_2T_x$ MXene. *Chemistry of Materials* **2019**, *ASAP*, XX.

[283] Khazaei, M.; Ranjbar, A.; Arai, M.; Sasaki, T.; Yunoki, S. Electronic properties and applications of MXenes: a theoretical review. *Journal of Materials Chemistry C* **2017**, *5*, 2488–2503.

[284] Seh, Z. W.; Fredrickson, K. D.; Anasori, B.; Kibsgaard, J.; Strickler, A. L.; Lukatskaya, M. R.; Gogotsi, Y.; Jaramillo, T. F.; Vojvodic, A. Two-dimensional molybdenum carbide (MXene) as an efficient electrocatalyst for hydrogen evolution. *ACS Energy Letters* **2016**, *1*, 589–594.

[285] Trasatti, S. Work function, electronegativity, and electrochemical behaviour of metals: III. Electrolytic hydrogen evolution in acid solutions. *Journal of Electroanalytical Chemistry and Interfacial Electrochemistry* **1972**, *39*, 163–184.

[286] Tarascon, J.-M.; Armand, M. *Materials for sustainable energy: A collection of peer-reviewed research and review articles from Nature publishing group*; World Scientific, 2011; pp 171–179.

[287] Choi, J. W.; Aurbach, D. Promise and reality of post-lithium-ion batteries with high energy densities. *Nature Reviews Materials* **2016**, *1*, 16013.

[288] Slater, M. D.; Kim, D.; Lee, E.; Johnson, C. S. Sodium-ion batteries. *Advanced Functional Materials* **2013**, *23*, 947–958.

[289] Xu, C.; Li, B.; Du, H.; Kang, F. Energetic zinc ion chemistry: The rechargeable zinc ion battery. *Angewandte Chemie* **2012**, *124*, 957–959.

[290] Cathode materials for magnesium and magnesium-ion based batteries. *Coordination Chemistry Reviews* **2015**, *287*, 15–27.

[291] Bard, A. J.; Faulkner, L. R.; Leddy, J.; Zoski, C. G. *Electrochemical methods: fundamentals and applications*; wiley New York, 1980; Vol. 2.

[292] Ohzuku, T.; Iwakoshi, Y.; Sawai, K. Formation of lithium-graphite intercalation compounds in nonaqueous electrolytes and their application as a negative electrode for a lithium ion (shuttlecock) cell. *Journal of The Electrochemical Society* **1993**, *140*, 2490–2498.

[293] Shu, Z.; McMillan, R.; Murray, J. Electrochemical intercalation of lithium into graphite. *Journal of The Electrochemical Society* **1993**, *140*, 922–927.

[294] Besenhard, J.; Winter, M.; Yang, J.; Biberacher, W. Filming mechanism of lithium-carbon anodes in organic and inorganic electrolytes. *Journal of Power Sources* **1995**, *54*, 228–231.

[295] Dawes, S. B.; Ward, D. L.; Huang, R. H.; Dye, J. L. First electride crystal structure. *Journal of the American Chemical Society* **1986**, *108*, 3534–3535.

[296] Clearfield, A. Role of ion exchange in solid-state chemistry. *Chemical Reviews* **1988**, *88*, 125–148.

[297] Waser, R.; Dittmann, R.; Staikov, G.; Szot, K. Redox-based resistive switching memories–nanoionic mechanisms, prospects, and challenges. *Advanced Materials* **2009**, *21*, 2632–2663.

[298] Takahashi, Y.; Kijima, N.; Dokko, K.; Nishizawa, M.; Uchida, I.; Akimoto, J. Structure and electron density analysis of electrochemically and chemically delithiated $LiCoO_2$ single crystals. *Journal of Solid State Chemistry* **2007**, *180*, 313–321.

[299] Ohzuku, T.; Makimura, Y. Layered lithium insertion material of $LiNi_{1/2}Mn_{1/2}O_2$: A possible alternative to $LiCoO_2$ for advanced lithium-ion batteries. *Chemistry Letters* **2001**, *30*, 744–745.

[300] Nitta, N.; Wu, F.; Lee, J. T.; Yushin, G. Li-ion battery materials: present and future. *Materials Today* **2015**, *18*, 252–264.

[301] Beaulieu, L.; Eberman, K.; Turner, R.; Krause, L.; Dahn, J. Colossal reversible volume changes in lithium alloys. *Electrochemical and Solid-State Letters* **2001**, *4*, A137–A140.

[302] Schweidler, S.; de Biasi, L.; Schiele, A.; Hartmann, P.; Brezesinski, T.; Janek, J. Volume changes of graphite anodes revisited: A combined operando X-ray diffraction and in situ pressure analysis study. *The Journal of Physical Chemistry C* **2018**, *122*, 8829–8835.

[303] Kang, K.; Meng, Y. S.; Bréger, J.; Grey, C. P.; Ceder, G. Electrodes with high power and high capacity for rechargeable lithium batteries. *Science* **2006**, *311*, 977–980.

[304] Kang, B.; Ceder, G. Battery materials for ultrafast charging and discharging. *Nature* **2009**, *458*, 190.

[305] Smidstrup, S.; Pedersen, A.; Stokbro, K.; Jonsson, H. Improved initial guess for minimum energy path calculations. *The Journal of Chemical Physics* **2014**, *140*, 214106.

[306] Okubo, M.; Tanaka, Y.; Zhou, H.; Kudo, T.; Honma, I. Determination of activation energy for Li ion diffusion in electrodes. *The Journal of Physical Chemistry B* **2009**, *113*, 2840–2847.

[307] Toyoura, K.; Koyama, Y.; Kuwabara, A.; Oba, F.; Tanaka, I. First-principles approach to chemical diffusion of lithium atoms in a graphite intercalation compound. *Physical Review B* **2008**, *78*, 214303.

[308] Henkelman, G.; Uberuaga, B. P.; Jnsson, H. A climbing image nudged elastic band method for finding saddle points and minimum energy paths. *The Journal of Chemical Physics* **2000**, *113*, 9901–9904.

[309] Thackeray, M. Structural considerations of layered and spinel lithiated oxides for lithium ion batteries. *Journal of The Electrochemical Society* **1995**, *142*, 2558–2563.

[310] Vitins, G.; West, K. Lithium intercalation into layered $LiMnO_2$. *Journal of the Electrochemical Society* **1997**, *144*, 2587–2592.

[311] Reed, J.; Ceder, G.; Van Der Ven, A. Layered-to-spinel phase transition in Li_xMnO_2. *Electrochemical and Solid-State Letters* **2001**, *4*, A78–A81.

[312] Morgan, D.; Van der Ven, A.; Ceder, G. Li conductivity in Li_xMPO_4 (M= Mn, Fe, Co, Ni) olivine materials. *Electrochemical and Solid-State Letters* **2004**, *7*, A30–A32.

[313] Van der Ven, A.; Ceder, G. Lithium diffusion in layered Li_xCoO_2. *Electrochemical and Solid-State Letters* **2000**, *3*, 301–304.

[314] Hájek, B.; Karen, P.; Brožek, V. Investigation of the products of carbothermal reduction of yttrium oxide by the hydrolysis method. *Collection of Czechoslovak Chemical Communications* **1984**, *49*, 936–943.

[315] Ong, S. P.; Chevrier, V. L.; Hautier, G.; Jain, A.; Moore, C.; Kim, S.; Ma, X.; Ceder, G. Voltage, stability and diffusion barrier differences between sodium-ion and lithium-ion intercalation materials. *Energy & Environmental Science* **2011**, *4*, 3680–3688.

[316] Holcombe, C. E.; Carpenter, D. A. Identification of a new yttrium oxycarbide, Y_2OC. *Journal of the American Ceramic Society* **1981**, *64*, C82–C83.

[317] Atoji, M.; Kikuchi, M. Crystal structures of cubic and trigonal yttrium hypocarbides: A dimorphically interphased singlecrystal study. *The Journal of Chemical Physics* **1969**, *51*, 3863–3872.

[318] Soni, P.; Pagare, G.; Sanyal, S. P. Structural, high pressure and elastic properties of transition metal monocarbides: A FP-LAPW study. *Journal of Physics and Chemistry of Solids* **2011**, *72*, 810–816.

[319] Dunn, B.; Kamath, H.; Tarascon, J.-M. Electrical energy storage for the grid: A battery of choices. *Science* **2011**, *334*, 928–935.

[320] Kuzmina, O.; Bordes, E.; Schmauck, J.; Hunt, P. A.; Hallett, J. P.; Welton, T. Solubility of alkali metal halides in the ionic liquid $[C_4C_1im][OTf]$. *Physical Chemistry Chemical Physics* **2016**, *18*, 16161–16168.

[321] Davis, V. K. et al. Room-temperature cycling of metal fluoride electrodes: Liquid electrolytes for high-energy fluoride ion cells. *Science* **2018**, *362*, 1144–1148.

[322] Orman, H.; Wiseman, P. Cobalt (III) lithium oxide, $CoLiO_2$: structure refinement by powder neutron diffraction. *Acta Crystallographica Section C: Crystal Structure Communications* **1984**, *40*, 12–14.

[323] Park, J.; Hwang, J.-Y.; Lee, K. H.; Kim, S.-G.; Lee, K.; Kim, S. W. Tuning the spin-alignment of interstitial electrons in two-dimensional Y_2C electride via chemical pressure. *Journal of the American Chemical Society* **2017**, *139*, 17277–17280.

[324] Miller, D. J.; Biesinger, M. C.; McIntyre, N. S. Interactions of CO_2 and CO at fractional atmosphere pressures with iron and iron oxide surfaces: one possible mechanism for surface contamination? *Surface and Interface Analysis* **2002**, *33*, 299–305.

[325] Pertsin, A.; Pashunin, Y. Differential charging in XPS studies of polymer/metal interfaces. *Applied Surface Science* **1990**, *44*, 171–178.

[326] Fox, M. Optical properties of solids. 2002.

[327] Bohr, N. XXXVII. On the constitution of atoms and molecules. *The London, Edinburgh, and Dublin Philosophical Magazine and Journal of Science* **1913**, *26*, 476–502.

[328] Schrödinger, E. Die gegenwärtige Situation in der Quantenmechanik. *Naturwissenschaften* **1935**, *23*, 823–828.

[329] Fowler, R. H.; Nordheim, L. Electron emission in intense electric fields. *Proceedings of the Royal Society of London. Series A, Containing Papers of a Mathematical and Physical Character* **1928**, *119*, 173–181.

[330] Thomson, J. J. *Conduction of electricity through gases*; Watchmaker Publishing, 2005.

[331] Pfrommer, B. G.; Côté, M.; Louie, S. G.; Cohen, M. L. Relaxation of crystals with the quasi-Newton method. *Journal of Computational Physics* **1997**, *131*, 233–240.

[332] Marsman, M.; Paier, J.; Stroppa, A.; Kresse, G. Hybrid functionals applied to extended systems. *Journal of Physics: Condensed Matter* **2008**, *20*, 064201.

[333] Zhao, Y.; Lynch, B. J.; Truhlar, D. G. Development and assessment of a new hybrid density functional model for thermochemical kinetics. *The Journal of Physical Chemistry A* **2004**, *108*, 2715–2719.

[334] Laricchia, S.; Fabiano, E.; Sala, F. D. Semilocal and hybrid density embedding calculations of ground-state charge-transfer complexes. *The Journal of chemical physics* **2013**, *138*, 124112.

[335] Roothaan, C. C. J. New developments in molecular orbital theory. *Reviews of modern physics* **1951**, *23*, 69.

[336] Pople, J.; Nesbet, R. Self-consistent orbitals for radicals. *The Journal of Chemical Physics* **1954**, *22*, 571–572.

[337] McWeeny, R.; Diercksen, G. Self-consistent perturbation theory. II. Extension to open shells. *The Journal of Chemical Physics* **1968**, *49*, 4852–4856.

[338] Lin, J.; Qteish, A.; Payne, M.; Heine, V. Optimized and transferable nonlocal separable ab initio pseudopotentials. *Physical Review B* **1993**, *47*, 4174.

[339] Marzari, N.; Vanderbilt, D. Maximally localized generalized Wannier functions for composite energy bands. *Physical review B* **1997**, *56*, 12847.

[340] Neugebauer, J.; Scheffler, M. Adsorbate-substrate and adsorbate-adsorbate interactions of Na and K adlayers on Al (111). *Physical Review B* **1992**, *46*, 16067.

[341] Habermann, C.; Daane, A. The preparation and properties of distilled yttrium. *Journal of the Less Common Metals* **1963**, *5*, 134–139.

[342] Savvatimskiy, A. Measurements of the melting point of graphite and the properties of liquid carbon (a review for 1963–2003). *Carbon* **2005**, *43*, 1115–1142.

[343] Brewer, L., et al. *Chemistry and Metallurgy of Miscellaneous Materials: Thermodynamics*; McGraw-Hill New York, 1950; Vol. 19; p 193.

[344] Werner, P.-E.; Eriksson, L.; Westdahl, M. TREOR, a semi-exhaustive trial-and-error powder indexing program for all symmetries. *Journal of Applied Crystallography* **1985**, *18*, 367–370.

[345] Brandenburg, K.; Putz, H.; Match!, `http://www.crystalimpact.com/`.

[346] Version, P. 2.0. 3.0 Integrated X-ray Powder Diffraction Software. *Tokyo, Japan: Rigaku Corporation* **2011**, 196–8666.